UNIVERSITY OF CATANIA
Department of Chemical Sciences
International Ph.D. In Chemical Sciences – XXXII Cycle

Hyaluronic Acid – Metal Nanoparticles Hybrids for Wound Care and Regenerative Therapy

Viviana Carmela Linda Caruso

Thesis supervisors:

Prof. Cristina Satriano
Dr. Rosanna Inturri, Dr. Luciano Messina (Fidia Farmaceutici)
Prof. François Reniers (Université libre de Bruxelles, ULB)

PhD Coordinator:

Prof. Salvatore Sortino

“PON Dottorati Innovativi con caratterizzazione industriale 2016” - A.Y. 2018-2019

Acknowledgements

Firstly, I would like to express my sincere gratitude to my advisors Prof. Cristina Satriano, Dr. Luciano Messina and Prof. François Reniers for the support they provided so far to my PhD study and related research, for their patience, motivation, and immense knowledge.

A special thanks to Prof. François Reniers who provided me with the opportunity to join their team as an intern, and to access to the laboratory in the Université libre de Bruxelles and research facilities. My sincere thanks also go to Dr. Delphine Merche for the experimental support for plasma facilities to conduct the second part of this research and all the CHANI team because made me feel right at home.

Many thanks to Dr. Susanna Vaccaro for her support and because she provided me with the opportunity to develop the industrial part of the thesis.

I would like to thank Dr. Valentina Greco (Fidia Farmaceutici) for her precious contribution in the synthesis processes, my colleague Lorena Cucci (University of Catania) for her precious support for the biological measures and Dr. Rosanna Inturri (Fidia Farmaceutici) for her support in the microbiological assay.

Abstract

The skin wound treatment represents an important research area due to the essential roles of this tissue, which is the human's body largest organ. A new approach to tackle the wound healing process is the use of gold (AuNP) or silver (AgNP) nanoparticles as smart nanomedicine tools, thanks to their intrinsic therapeutic effects, such as the angiogenic regulation as well as the anti-inflammatory and antibacterial activity, respectively. Moreover, the nanoparticle conjugation with bioactive molecules is a promising strategy to set up multifunctional nanoplatforms with 'tunable' therapeutic action, where each component acts synergically with the others in modulating the biological response at the biointerface.

According to such premises, this industrial Ph.D. thesis deals with the investigation of newly developed hyaluronan-metal nanoparticle nanocomposite systems for improved performances in the wound care application in comparison with the market products.

Hyaluronic acid (HA) treatments are well known and have been used for tissue repair to treat general wounds, ulcers and bedsores, as well as for the topical treatment of burns. The industrial partner of this Ph.D. project is Fidia Farmaceutici that is, after fifty years of research on the field of hyaluronic acid, at the forefront in HA-related R&D, technological development, production and commercialization, not only in Italy but worldwide.

Plasma-based treatments enable one to efficiently synthesize or modify nanomaterials using eco-friendly and often single-step processes, thus considerably lowering labour investment and costs. As a result, the nanoparticle synthesis and their functionalization is more straightforward and can be carried out on a much larger scale, compared to other methods and procedures involving complex chemical treatments and processes.

The foreign partner of this Ph.D. project is the Université libre de Brussels (ULB), where the synthesis and characterization of gold and silver nanoparticles coated with hyaluronic acid at different molecular weights have been carried out at by plasma reduction methods, in comparison to the wet chemical reduction methods used in the research activity at the University of Catania.

Keywords: wound healing, metal nanoparticles, hyaluronic acid, plasma chemistry, antiangiogenic peptides, hybrid nanobiointerfaces.

List of Content

List of abbreviations

Abs	Absorbance
AFM	Atomic Force Microscopy
AgNP	Silver nanoparticle
ATCC	American Type Culture Collection
ATR - FTIR	Attenuated Total Reflectance – Fourier Transform Infrared Spectroscopy
AuNP	Gold nanoparticle
BHI	Brain Heart Infusion broth
CFU	Colony-Forming Unit
CHL	Chloramphenicol
CLSI	Clinical Laboratory Standards Institute
Da	Dalton
DC	Direct Current
DG	Deoxyglucose
DHEA	Dehydroepiandrosterone
DHT	5α-Dihydrotestosterone
DLS	Dynamic Light Scattering
DMSO	Dymethylsulfoxyde
ECM	Extracellular Matrix
FWHM	Full Width at Half Maximum
GAG	Glycosaminoglycan
GHHPHGK	GlycineHistidineHistidineProlineHistidineGlycineLysine
GPC	Gel Permeation Chromatography
HA	Hyaluronic Acid
HA1200	Hyaluronic Acid 1200 kDa
HA200	Hyaluronic Acid 200 kDa
HA700	Hyaluronic Acid 700 kDa
HMW	High Molecular Weight
HRGP	Histidine-Rich Glycoprotein
HTC116	Colorectal carcinoma
HUVEC	Human Umbilical Vein Endothelial Cells
HYAL	Hyaluronidase
IL-β	Interleukin - 1 beta

LSM	Laser Scanning Confocal Microscopy
LMW	Low Molecular Weight
MH	Mueller-Hinton
MIC	Minimal Inhibitory Concentration
MMP	Metalloproteinase
MW	Molecular Weight
MTT	3-(4,5-Dimethylthiazol-2-yl)-2,5-Diphenyltetrazolium Bromide
NM	Nanomaterial
NMR	Nuclear Magnetic Resonance
OD	Optical Density
P	Plasma
PC-3	Human Prostate Cancer Cell Line
PCS	Photon Correlation Spectroscopy
PEG	Poly(ethylene glycol)
PMAA	Poly(meth acrylic acid)
PMMA	Poly(methyl methacrylate)
PSD	Particle Size Distribution
PVA	Poly(vinyl alcohol)
PVP	N-Poly(vinylpyrrolidone)
QCM-D	Quartz Crystal Microbalance with Dissipation monitoring
ROS	Reactive oxygen species
RSD	Relative Standard Deviation
SD	Standard Deviation
SEC	Size Exclusion Chromatography
SH-SY5Y	Human Neuroblastoma Cell Line
SLB	Supported lipid bilayer
SPR	Surface Plasmon Resonance
SSD	Silver sulfadiazine
TBAB	Tetradecyl-trimethyl-ammonium bromide
TEM	Transmission Electron Microscopy
THF	Tetrahydrofuran
TNF-α	Tumour necrosis factor - Alfa
UV	Ultra violet
UV-vis	Ultra Violet - visible
WHO	World Health Organization
ZOI	Zone of Inhibition

CHAPTER 1

INTRODUCTION

1.1 MOTIVATION

Chronic wounds have emerged as a major cause of mortality, especially in patients with diabetes and other pathologies. Growing incidence of chronic wounds and associated pathologies along with the limitations of current therapies have established a strong need for novel and innovative approaches to accelerate wound healing.

Nanoparticles, especially inorganic metal nanoparticles, are promising candidates for addressing various pathological conditions, including wound healing. Nanotechnology-based diagnostics and treatments have achieved a new horizon in the arena of wound care due to its ability to deliver a plethora of therapeutics into the target site, and to target the complexity of the normal wound-healing process, cell type specificity, and plethora of regulating molecules as well as pathophysiology of chronic wounds.[1]

Many requirements must be fulfilled to form a working system applied *in vivo* for advanced wound healing. A crucial point is the pro-angiogenic response by the nano-wound care formulation that, at the same time, could reduce the wound infection. Indeed, wound infections impose a remarkable clinical challenge that has a considerable influence on morbidity and mortality of patients, influencing the cost of treatment.[1]

Another relevant issue is the setup of a low-cost, green and reliable methodology for the synthesis and functionalisation of the inorganic nanomedicine for addressing wounds. Plasma is a physical method that allows to synthetize metal nanoparticles at atmospheric pressure using microplasma electrochemistry (plasma-liquid electrochemistry or gas-liquid interface discharges).

Moreover, plasma chemistry may offer a simple, one-step, rapid and environment-compatible method to obtain biologically active nano-systems.

1.2 AIM OF THE THESIS

In this work, silver (AuNP) and gold (AuNP) nanoparticles functionalized with hyaluronic acid (HA) have been designed, synthesised and characterised by both physicochemical and biological investigations. The focus is on the setup of a reliable synthetic approach, by comparison of wet chemistry and plasma chemistry reduction methods, to fabricate multifunctional plasmonic nanoplatforms with tunable angiogenic properties, in view of potential application in wound healing.

In **chapter 2** we highlight the question of how does hyaluronic acid at different molecular weights influences the physicochemical properties of HA-conjugated metal nanoparticles. Specifically, silver or gold nanoparticles were synthesised in haluronan-based solutions with molecular weights ranging from 200 kDa to 1,200 kDa. UV-visible spectroscopy and dynamic light scatterning were used to scrutinise the HA@NP hybrids in terms respectively of optical and hydrodynamic diameters, as well as the stability against aggregation upon ageing and ionic strengths. The chemical structure at the nanoparticle-polymer interface and the fingerprint of the nanoparticle bioconjugation with HA were determined by ATR/FTIR. Moreover, the correlation between the intrinsic viscosity and the haluronan MWs were investigated by a Viscotek GPC/SEC system, with integrated refractive index viscometer and light scattering detectors.

In **chapter 3** we focus on the tunability of the anti-angiogenic properties of AuNP and AgNP for anticancer therapies. To this purpose, hyaluronic acid, which specifically interacts with CD-44 receptor that is overexpressed in several tumoral cell lines, was used as targeting agent for the surface functionalisation of the metal nanoparticles. The cellular uptake of HA-coated nanoparticles was investigated in human cancer cells of prostate (PC-3) or neuroblastoma (SH-SY5Y), where the CD-44 receptor is overexpressed or in quiescent state, respectively (Section 3.1). Moreover, as further step of complexity, we conjugated the pro-angiogenic low MW (200 kDa) hyaluronic acid with an anti-angiogenic peptide sequence (GHHPHGK). In that study, the HA@NP hybrids were synthesised either via plasma chemistry or by wet chemistry reduction and the samples tested in human umbelical vein endothelial cells (HUVEC) (Section 3.2).

In **chapter 4** the biophysical and biological study on the hybrid biointerface between the HA@NP systems and supported lipid bilayers (SLBs, used as model cell membranes) or actual cells is addressed. In particular, the perturbation upon the interaction with the HA-coated NPs (fabricated either via plasma or via chemical reduction) of the viscoelastic properties of pre-formed SLBs or of the cytoskeleton actin were scrutinised by QCM-D acoustic sensig or confocal microscopy imaginfg, respectively.

Finally, **chapter 5** tries to answer the question of how HA-functionalised gold and silver nanoparticles can be used as multifunctional platforms able to prompt at the same time a pro-angiogenic response and an antibacterial activity. The hybrid HA@NP systems, fabricated either via wet chemistry reduction or by plasma chemistry method were studied in comparison by spectroscopic (UV-visible, ATR/FTIR) and microscopic (TEM, AFM) analyses. The biological assays of cytotoxicity and antibacterial activity were performed in endothelial cells and in *Escherichia Coli*/*Stafilococcus Aureus* strains, respectively.

1.3 STATE OF THE ART

1.3.1 Wound healing and nanomedicine

1.3.1.1 Brief introduction to wound healing

Statistics indicate that chronic wounds affect around 6.5 million patients annually, with wound care and management incurring huge economic costs.[2] Conventionally, chronic wounds are addressed using various FDA-approved silver-based formulations and other biomaterials. However, the toxicity associated with these conventional approaches, along with the increased frequency of chronic wound cases, makes the development of alternative therapies for effective wound healing necessary.

One of the most important research fields, due to the crucial physiological and aesthetic role of skin, concerns the treatment of wounds.[3-5] With the increase in the world age population, the research has felt the necessity to find appropriate solutions in wound care and aesthetic field; moreover, unhealthy lifestyles such as unhealthy eating habits, sedentary life, stress and environmental factors such as pollutions lead to crescents diseases with implications in the skin health.[6]

In the last years, the aesthetic exigencies were to find less invasive skins treatments (compared to chemical peels and CO_2 lasers) in order to treat not only the aging signs but also wounds derivate from invasive surgical procedures or burns. [7]Hard-to-heal and chronic wounds typically present a huge challenge to the clinical team charged with their treatment. Wounds that are extremely painful and/or unsightly can have an extreme psychological impact on the patient, and this can be as crucial consideration as the complexities involved in managing the physical healing. While resource expenditure on hard-to-heal wounds can be quantified, quality of life is less easy to evaluate, but is clearly of paramount importance to the patient.[6]

A negative spiral may occur when the wound causes bring a negative emotional state which has an impact on wound healing and that, in turn, leads to further negative emotions. Social isolation may also occur if an individual lacks energy because of sleep deprivation. Sleep plays an important role in the healing process and lack of sleep can interfere with the immune system. Pain is usually reported as one of the main reasons why individuals with chronic wounds have sleep disturbances. Chronic wounds also affect an individual’s ability to perform activities of daily living, further contributing to social isolation. It has been reported that individuals avoid certain activities such as shopping, walking or exercising because they cause or exacerbate pain.[8]

Cutaneous wound healing is an essential physiological process consisting of the collaboration of many cell strains and their products. Regeneration and tissue repair processes consist of a sequence of molecular and cellular events which occur after the onset of a tissue lesion to restore the damaged tissue. The stages of wound healing (**Figure 1.1**) proceed in an organized way and follow four processes: haemostasis, inflammation, proliferation and maturation.[9]

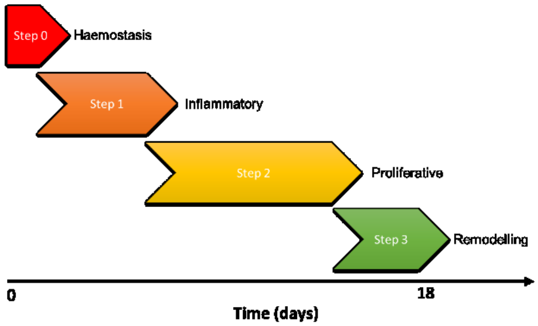

Figure 1.1. Sequential illustration of the stages involved in tissue repair.

In the first step of **haemostasis**, the lesioned blood vessels contract to restrict the blood flow. Next, platelets express sticky glycoproteins on their cell membranes that allow them to aggregate, forming a mass.[10]

In the vascular **inflammatory** response the coagulation is the first step consisting of the aggregation of thrombocytes and platelets in a fibrin network~~.~~ The fibrin network, in addition to re-establishing homeostasis and forming a barrier against the invasion of microorganisms, organizes the necessary temporary matrix for cell migration, restores the skin’s function as a protective barrier, maintaining the skin's integrity.[11] Immediately after a blood vessel is breached, the vasodilatation step takes place in order to prevent blood loss and to collect inflammatory cells and factors in the area. This vasoconstriction lasts five to ten minutes and is followed by vasodilation in which histamine makes blood vessels porous, allowing the tissue to become oedematous; increased porosity of blood vessels also facilitates the entry of inflammatory cells like leukocytes into the wound site from the bloodstream.[12, 13, 14-17] Because inflammation plays key roles in fighting infection, clearing debris and inducing the proliferation phase, it is a necessary part of healing. However, inflammation can lead to tissue damage if it lasts too long.[18]Thus the reduction of inflammation is frequently a goal in therapeutic settings.[19]

The next step is the **proliferative stage** and it aims to diminish the lesioned tissue area by contraction and fibroplasia, establishing a viable epithelial barrier to activate keratinocytes. This stage is responsible for the closure of the lesion itself, which includes angiogenesis, fibroplasia, and re-epithelialization. Angiogenesis is the physiological process through which new blood vessels form from pre-existing vessels; because of the activity of fibroblasts and epithelial cells requires oxygen and nutrients, angiogenesis is imperative for other stages in wound healing, like epidermal and fibroblast migration.[10, 11 12-16, 20, 21] Simultaneously with angiogenesis, fibroblasts begin accumulating in the wound site Granulation tissue consists of new blood vessels, fibroblasts, inflammatory cells, endothelial cells, myofibroblasts, and the components of a new, provisional extracellular matrix (ECM). The formation of granulation tissue into an open wound allows the re-epithelialization phase to take place, as epithelial cells migrate across the new tissue to form a barrier between the wound and the environment. Basal keratinocytes from the wound edges and dermal appendages such as hair follicles, sweat glands and sebaceous (oil) glands are the main cells responsible for the epithelialization phase of wound healing.[10]

Contraction is a key phase of wound healing (Remodelling, Figure 1.1). Contraction commences approximately a week after wounding when fibroblasts have differentiated into myofibroblasts.[10, 21] Myofibroblasts, which are similar to smooth muscle cells, are responsible for contraction.[22] These events signal the onset of the maturation stage of wound healing.

When the levels of collagen production and degradation equalize, the **maturation phase** of tissue repair is said to have begun (Remodelling, Figure 1.1). During maturation originally disorganized collagen fibres are rearranged, cross-linked, and aligned along tension lines. The phases of wound healing normally progress in a predictable, timely manner; if they do not, healing may progress inappropriately to either a chronic wound such as a venous ulcer or pathological scarring such as a keloid scar.[22]

The use of hyaluronic acid to modulate the wounds regeneration is becoming increasingly popular to improve the wound repair, decrease the healing time, the inflammation and improve the appearance of the wound by modulating the healing process. For example, the application of a dressing consisting of low molecular weight hyaluronic acid (commercial product example, Hyalofill-F) on the bottom of the lesion, determines both the formation of well-vascularized granulation tissue and marked macroscopic proliferation margins.[23]

In fact, in the proliferation phase to form granulation tissue, hyaluronic acid (synthesized mainly by fibroblasts) allows the diffusion of nutrients and the elimination of waste products. Hyaluronic acid facilitates the migration and proliferation of fibroblasts and keratinocytes and represents a reservoir of growth factors. This is due to the ability of hyaluronic acid to absorb water, maintain wound moisture and limit cellular adhesion to extracellular matrix molecules. This matrix and fibroblasts maintain a bidirectional interaction, since fibroblasts participate in the synthesis and remodelling of the extracellular matrix and this modulates the activity of these cells. In addition, it has been demonstrated that degradation products of hyaluronic acid are pro-angiogenic. Subsequent remodelling of granulation tissue involves lowering hyaluronic levels and increasing the proportion of other proteoglycans and collagen to improve tissue resistance and elasticity.[7]

There are different commercial solutions such as Hyalosilver (Fidia Farmaceutici S.p.A, Italy) that allow to treat chronic wounds using the hyaluronic acid together with the metal silver. In a recent study of Gazzabin et al[23], tests this product on 25 patients with chronic wound studying the synergic effect of the hyaluronic acid, which promote wound healing, repair and angiogenesis, and metal silver with the known antibacterial properties. At the start of the study, patients presented with wounds with moderate exudate (76%), odour (72%), while erythema was present in the periwound skin in 48% of patients. All patients presented with at least one sign of bacterial colonisation at baseline, the most relevant of which was reduced or delayed wound healing (92%), changes in granulation tissue (72%) and smelly exudate (56%). The results of this study show improved neoangiogenesis (and consequently blood flow which is useful in controlling bacterial load); the signs of bacterial colonisation (smell, exudate and erythema of the periwound skin) at the end of the 28 days of treatment (with the exception of two cases were exudate did not modify against baseline) decrease. At the end of the 28 days of treatment, all wounds were odourless.

A study published in the International Society For Pharmacoeconomics and Outcomes Research's *Value in Health* journal[24] shows the economic impact and full burden of chronic nonhealing wounds in the National United States Medicare population. The study analysed the Medicare 5% Limited Data Set for CY2014 to determine the cost of chronic wound care for Medicare beneficiaries in aggregate, by wound type, and by setting. Chronic nonhealing wounds impact nearly 15% of Medicare beneficiaries (8.2 million) for more than suggested by previous studies. A conservative estimate of the annual cost is $28 billion when the wound is the primary diagnosis on the claim. When the analysis included wounds as a secondary diagnosis, the cost for wounds is conservatively estimated at $31.7 billion. The highest cost estimates regarding the site of service were for hospital outpatients ($9.9-$11.4 billion) demonstrating a major shift in costs from hospital in patient to outpatient settings. Including the cost of infections, the most expensive chronic wounds were surgical wounds ($11.7 to $13 billion) and diabetic foot ulcers ($6.2 to $6.9 billion). On an individual wound basis, mean Medicare spending per wound was $3,415 to $3,859. The most expensive wounds per beneficiary were arterial ulcers ($9,105 to $9,418) followed by pressure ulcers ($3,696 to $4,436). Surgical infections were the largest prevalence category (4.0%), followed by diabetic wound infections (3.4%).[25]

Moreover, in the work of Nussbaum et al.[24], it is possible to observe that the chronic wounds (organized into 12 broad wound categories: arterial ulcers, chronic ulcers, diabetic foot ulcers, diabetic infections, pressure ulcers, skin disorders, skin infections, surgical wounds, surgical infections, traumatic wounds, venous ulcers, and venous infections) afflict female and male over 75 years old (19.7% and 19.6 %, respectively); also in the case of the surgical wounds and diabetic wounds the percent is homogeneous for both male and female cases.

Multiple factors can lead to impaired wound healing. In general terms, the factors that influence the reparation can be categorized into local and systemic. Local factors are those that influence directly the characteristics of the wound itself such as sufficient oxygenation of the wound tissues, bacterial infection, the presence of foreign body into the wound and venous sufficiency.[26]

The systemic factors are the overall health or disease state of the individual that affect his or her ability to heal. The age, for example, is an important systemic factor, in the population of over 60 years is growing faster than any other age group (World Health Organization [WHO, www.who.int/topics/ageing]), and increased age is a major risk factor for impaired wound healing.[27] With the increase in age, it is observable a delayed wound healing associated with an altered inflammatory response, such as delayed T-cell infiltration into the wound area with alterations in chemokine production and reduced macrophage phagocytic capacity.[28] Delayed re-epithelialization, collagen synthesis, and angiogenesis have also been observed in aged mice as compared with young mice.[29] Moreover, with the increase in age, the level of hyaluronic acid, indispensable in the wound healing process, reduces on the skins and compartments in the sub skin tissue as hyaluronan-binding proteins altering the histolocalization of hyaluronan and the wound healing process speed.[30] Also, sex hormones play a role in age-related wound-healing deficits. Compared with females, males have been shown to have delayed healing of acute wounds. A partial explanation for this is that the female estrogens (estrone and 17β-estradiol), male androgens (testosterone and 5α-dihydrotestosterone, DHT), and their steroid precursor dehydroepiandrosterone (DHEA) appear to have significant effects on the wound-healing process.[31] Moreover, studies in both humans and animals have demonstrated that psychological stress causes a substantial delay in wound healing. Caregivers of peoples with Alzheimer's and students undergoing academic stress during examinations demonstrated delayed wound healing.[32, 33] Diabetes affects hundreds of millions of people worldwide. Diabetic individuals exhibit a documented impairment in the healing of acute wounds. Moreover, this population is prone to develop chronic non-healing diabetic foot ulcers (DFUs), which are estimated to occur in 15% of all persons with diabetes. DFUs are a serious complication of diabetes, and precede 84% of all diabetes-related lower leg amputations.[34] Other factors which afflict wound healing are medications such as chemotherapeutics[35], obesity[36], alcohol consumption[37], smoking[38] and nutrition.[39]

1.3.1.2. Hyaluronic acid

Hyaluronic acid or hyaluronan (HA) polymers exist in varying lengths, and each molecular size range plays a key role in all wound healing phases. In brief, long, heavy HA molecules ($> 5 \cdot 10^5$ Da) are space-filling molecules with regulatory and structural functions and anti-angiogenic properties; when HA exists in high concentrations in this form, it creates a porous scaffolding network, allowing for select diffusion of cells and proteins, creating pathways for cell migration.[40] This is a key feature of HA, as cell migration and proliferation is essential to successful wound healing.[41]

Instead, small HA fragments are involved in angiogenesis, inflammation and immunostimulation;[42] smaller molecular size HA fragments, also encourage cell migration, with very short, low-weight, HA fragments inducing chemotaxis and medium-sized HA chains stimulating inflammatory cytokines expression.[42]

HA catabolism primarily occurs in two main ways, through six hyaluronidases (HYALs) and reactive oxygen species (ROS). HYALs are responsible for altering the various HA sizes needed during each wound healing phase.[42] HYAL-induced breakdown is quite systematic in contrast to the ROS catabolism, which is often induced extrinsically by UV[43] or intrinsically by neutrophils.[44] In addition to HA's unique structural properties, the cell surface interactions are crucial to understand HA's role in wound healing, as HA's size and shape dictates its different roles and interactions at each wound stage. During the inflammatory phase of wound healing, HA synthesis increases rapidly.[45] Upon breach of the skin large, heavy molecular size HA fragments are synthesised from platelets and available HA in the bloodstream.[42] These HA fragments are able to bind to fibrinogen to commence the extrinsic clotting pathway.[43] Because of the large amounts of HA released at wounding, the wound site is saturated with fluid leading to oedema.[44] HA's hydrophilic properties causes swelling of the tissue surrounding the wound, creating a porous framework for cells to migrate to the injury site.[46] Edema can be observed macroscopically in this initial stage of wound healing, allowing for microscopic chemotaxis of inflammatory cells. This inflammatory process is driven by the primary cytokines tumour necrosis factor-alpha (TNF-α), interleukin-1 beta (IL-1β) and IL-8 and is stimulated when concentrations of HA are high. These inflammatory cytokines increase blood vessel dilation, allowing increased cellular recruitment to the wound.[47] This vasodilation presents as heat and redness, serving as a clinical indicator of wound inflammation and progression. Inflammation and its associated symptoms are essential for successful wound repair.[42]

Conversely, HA also has a role in reducing and moderating the inflammatory response, through its interaction with the hyaladherin TNFstimulated gene-6 (TSG-6).[48] TSG-6 is stimulated by inflammatory cytokines IL-1 and TNF-α, causing fibroblasts and another inflammatory expression of the TSG-6 protein. Once expressed by cells, TSG-6 proteins are retained in HA-rich environments, binding to high molecular weight HA polymers which form heavy chains. These heavy HA chains prevent inflammation by inhibiting neutrophil migration and inhibition of plasmin through negative feedback loops.[49] Following on from the late inflammatory phase, the proliferative phase of wound healing marks the arrival of fibroblast migration. These dermal cells are drawn to wound tissue by small HA fragments (6–20 saccharides) and growth factors. Fibroblasts, create collagen and glycosaminoglycans (GAGs) (including HA), constructing and anchoring the newly formed extracellular matrix (ECM). The developing ECM is visibly identifiable as granulation tissue, displaying the structural properties of HA. With collagen and elastin providing the fibrous scaffolding, HA ’fills in the gaps’ to form a cushioning gel.[49] As shown during the inflammatory phase of wound healing, long, heavy HA chains form this gel because of HA’s hydrophilic nature. Upon saturation, HA displays the elastic recoil properties similar to cartilage.[40] This malleability is an important clinical feature of granulation tissue, as wound healing often occurs in areas of high movement or pressure that is joints, plantar surface of feet. Without HA’s microscopic, hydrophilic and porous networking abilities, the macroscopic granulation tissue would not able to hold its shape to allow for normal wound healing. HA contributes to this process by its short chain lengths called oligomers, which are as small as 6–20 molecules in length.[42] These oligomers bind to the hyaladherin CD44 and act as stimulating fragments for matrix metalloproteinases (MMPs).[50] The MMPs are essential for new capillary sprouting by breaking down the basement membrane of the wound. This allows for new capillary buds to sprout from existing ones. Borgognoni et al.[51] studied low weight (short-chain) HA and its effects on angiogenesis. In their study, primary (sutured) and secondary (open) wounds were created in rats. Both groups were treated with HA gel. The results showed an increased microvasculature compared with control groups, but only wounds healing by secondary intention demonstrated accelerated healing. The final component of the proliferative phase of wound healing is epithelialisation which begins very early after wounding.[52] The skin contains most of the body’s HA, which is concentrated in the deeper, intercellular layers (basal stratum) of the epidermis as well as in the dermis. The main cell type in this basal layer is the keratinocyte, which expresses hyaladherin CD44 in large amounts.[50] In the skin, HA functions to hydrate the basal stratum, creating the aforementioned porous structures for nutrient channelling. Upon wounding, keratinocytes and their HA structures are torn apart, commencing the inflammatory phase of wound healing. Through CD44 interactions, keratinocytes migrate to the wound site, collecting at wound edges. Keratinocytes then form a delicate cover over the new wound from the wound borders. These cells then ’leapfrog’ over each other to form a cover of epithelial cells over the new wound. These new cells then differentiate to create the various epidermal skin layers, providing a protective barrier against infection and fluid loss.[49]

In the scientific literature, there is an increasing interest in hyaluronic acid conjugate to small molecules[53] and peptide[54] to improve the biological activity of the compounds. Curcumin is a promising wound healing agent thanks to its antioxidant,[55] anti-inflammatory[56] and antimicrobial[57] properties but its clinical application is limited due to hydrophobicity and lack of stability. Results show that the conjugate accelerates healing by increasing skin penetration and dermal localization of curcumin; it also reduces the scar formation due to the combined effect of HA and curcumin.[58]

Ongoing studies on the hyaluronic acid-carnosine conjugate show that this preparation offers the bio-pharmacological properties of both compounds. When the carnosine reaches the biological fluids, it will be rapidly destroyed by the serum carnosinase. The conjugate is characterized by the presence of a covalent amide bond between carnosine and hyaluronic acid, which is not immediately hydrolysable; carnosine, in its conjugated form, is therefore more resistant to the action of serum carnosinase and the conjugate maintains the carnosine linked and intact for a period of time which is sufficient in order to allow the same carnosine to reach the site where it will exert its action, giving a technical effect of slow release. Carnosine, in fact, has important biological properties such as anti-radical and anti-peroxidative, in some cases it prevents cataract,[59] anti-inflammatory activity (demonstrated in tissues of the digestive system, in the eyes and skin).[60] This bio-conjugate is studied in vivo for the treatment of the arthritis.[61]

1.3.2. Nanomedicine

Innovative methods for treating impaired and hard-to-heal wounds are needed. Novel strategies are needed for faster healing by reducing infection, moisturizing the wound, stimulating the healing mechanisms, speeding up the wound closure and reducing scar formation. Nanotechnology-based therapy has recently announced itself as a possible next-generation therapy that is able to advance wound healing to cure chronic wounds. [62] Nanomaterials are defined material with a size between 1 and 100 nm.[63]

Currently, it is possible to distinguish two types of Nanomaterials (NMs) for wound-healing therapy. NMs which are able to heal due to the features of nano-scaled material or NMs as cargo for delivering therapeutic agents.[64]

Nanotechnology-based products used in wound healing were divided into five groups according to NM composition: polymer, carbon-based, lipids-contained, ceramic, metal and metal oxide nanoparticles and different types of scaffolds with embedded NMs. Thanks to their optic and biological properties, the high surface/volume ratio and the possibility to conjugate with other therapeutics, metal nanoparticles are one of the most studied systems for the wound healing treatment, in fact about the 39% of the publication concerning the application of nanomaterials in wound healing concerns NP.[62]

In particular, silver (AgNP) and gold nanoparticles (AuNP) are largely studied thanks to their therapeutic effects on the wound healing (such as antibacterial[65] and anti-inflammatory activity[66]) and their wide range activity in different phases of wound healing modulating both inflammation and proliferation phases.[67]

1.3.2.1. Gold and silver nanoparticles in wound healing

Recently, a nanomedicine-based approach for the skin wound treatments based on the metal nanoparticles has emerged. In particular, silver (AgNP) and gold (AuNP) NP have been demonstrated to exhibit significant therapeutic effects on wound healing.[68] Pharmaceutical formulation based on NP are largely employed in the wound treatment protocols. Some of the properties exhibited by the different metal NP by the application to wounds are: the antibiotic activity,[69] the capability of targeted drug release,[70] cytokine regulation,[71, 72] and antioxidant activity.[73] Moreover, NP used in the wound healing treatments could provide the drug delivery to a selected target and they lead to permeabilize the stratum corneum.[74]

Silver has been used for decades in a variety of forms (metallic silver, silver nitrate, silver sulfadiazine) for the treatment of burns, open wounds, and several chronic infected wounds.[75]

Recently, due to the increase in antibiotic-resistant pathogenic bacteria and limitations on the use of antibiotics, the use of silver-based topical products has gained popularity, mainly in the management of open wounds.[76] Nanotechnology is used to modify silver in materials at the nano-scale dimension, resulting in a change of its chemical, physical and optical properties. This has consequences in improving tissue penetration and modifies its function at a cellular level.[77] AgNP are clusters of silver atoms ranging in diameter from 1 to 100 nm, which have gained interest as antibacterial agents.[78] The direct administration of AgNP to wounds shows efficient antimicrobial activity compared to other conventional formulations; their extremely large surface area to volume ratio provides better contact with microorganisms.

The preferred attack of the NP to the respiratory chain and cell division mechanism drives to cell death. Furthermore, NP could also release silver ions (Ag^+) enhancing their bactericidal activity.[75] The three common mechanisms of action on bacteria proposed are: (1) uptake of free Ag^+ ions followed by disruption of ATP production and DNA replication, (2) AgNP and Ag^+ generation of reactive oxygen species (ROS) and (3) AgNP direct damage to the cell.[79] Consequently, AgNP are efficient even at a very low concentration, which minimizes the chance for tissue toxicity due to silver delivery. *In vitro*, AgNP have shown antimicrobial activity against strains of Bacillus subtilis, Escherichia Coli and Staphylococcus aureus, among other important pathogens that colonize skin.[79, 80] In an interesting study, Tian et al. (2007)[81] investigated the wound-healing properties of AgNP in a thermal injury animal model. The treatment with AgNP shows a positive and therapeutic effect thanks to their antimicrobial properties and the reduction of wound inflammation through cytokine modulation; it was established the link between the dose-dependent treatment and the rapid healing and the improvement of the aesthetic and cosmetic appearance.[81] Additionally, the work of Adhya et al. (2014)[82] showed the effectiveness of topical silver sulfadiazine (SSD) which was compared with the nano-crystalline silver hydrogel in burn wounds treatment. They concluded that AgNP can be as effective and even superior to SSD for burn wound treatment, particularly 2nd-degree burns.

A controversial point regarding the use of AgNP is their potential toxicity. For example, the safety of AgNP in the medical field is critically discussed by Chaloupka et al. (2010)[78]. Several investigations have demonstrated, in vitro and animal models, that AgNP can exhibit a significant level of toxicity. Additionally, long-term treatment with this nanosystem is correlated to the increase in argyremia incidence in rats.[78] It is important to note that the potential toxicity of AgNP is not only related to metal accumulation, but also associated with the synthetic method used to produce the NP.[83] In this sense, conventional syntheses of AgNP use toxic precursors and toxic solvents (having toxic effects in humans and the environment), limiting their full application. Interestingly, safer NP synthesis is well-established under green chemistry precepts which eliminates the toxicity arising from conventional approaches.[84]

Similar to AgNP, AuNP have unique optical properties. They have the ability to resonantly scatter visible and near-infrared light upon the excitation of their surface plasmon oscillation. Interestingly, the scattered light intensity is sensitive to the size and shape of the particles.[85] Due to these important properties, AuNP are promising materials as biosensors, biologically active materials, and diagnostic agents (especially in cancer diagnosis).[86] In the field of wound healing, cutaneous wounds, diabetic wound tissue, and rheumatoid arthritis can be treated with AuNP thanks to their anti-inflammatory properties;[73] they are not toxic to human dermal fibroblasts and normal human epidermal keratinocytes and exert the anti-inflammatory activity via inhibition of IL-6, IL-12 and TNF- α level.[87] AuNP have potent antioxidant effects and free radicals such as DPPH (2,2-diphenyl-l-picrylhydrazyl), OH (hydroxyl), H_2O_2 (hydrogen peroxide), and NO (nitric oxide)[73] are effectively quenched. The antioxidant activity of the AuNP concerning free radical depends significantly on the specific surface.[88] Spherical AuNP have a large surface area, electron acceptors and interact with ROS in order to scavenge or deactivate them. As a result, AuNP is an important antioxidant agent and could consequently play a key role in wound healing.[89]

The nano-hybrid system formed by AuNP with other bioactive molecules has resulted in incredible progress in the wound care field. An example is the nano-system obtained by combining AuNP with epigallocatechin gallate and α-lipoic acid that significantly accelerated wound healing in mice. The authors attributed the healing results mainly to the antioxidant effect of the actives.[90] It was evaluated the efficacy of a similar formulation (AuNP comprising also epigallocatechin gallate and α-lipoic acid) in the expression of the receptor for advanced glycation of end-products whose role in diabetes cutaneous wounds may be determinant. The results indicated that the topical application of the product accelerated wound healing on diabetic mouse skin and decreased the receptor expression. This material showed great potential in diabetic wound healing because it can significantly accelerate the healing through angiogenesis regulation and anti-inflammatory effects. These results were attributed to the receptor blockade triggered by anti-oxidant agents and AuNP.[73]

1.3.2.2. Introduction to metal nanoparticles fabrication and surface tailoring approaches

A large number of approaches were for the synthesis of gold and silver nanoparticles. These methods can be grouped into three approaches: chemical, physical and biological synthesis.

Wet chemical methods for the preparation of colloidal metal are “bottom-up” processes based on the chemical reduction of the metal salts, electrochemical pathways, or the controlled decomposition of metastable organometallic compounds. Particle size and morphology of the metal nanoparticles are typically tuned by using different reducing agents and stabilizers.[91]

The most popular chemical method of preparing 20 nm gold metal colloids dispersed in water is the reduction of $AuCl_4^-$ in a boiling sodium citrate solution. This method was invented by Turkevich et al. in 1951.[92] The metal salt is reduced to give zerovalent metal atoms in the embryonic stage of nucleation. The citrate acts both to reduce the metal cation and as capping agent, preventing aggregation of the particles and stabilizing the resulting nanoparticles by electrostatic and/or physical repulsion. Also, citrate plays a role in determining the growth of the particles controlling the size and shape of the nanoparticle.[93]

Since then, the Turkevich’s method, has been improved[94-96] and extended to other metals, including silver.[96]

Moreover, other chemical approaches are based on the electrochemical and sonochemical methods, polyol methods, solvent-reduction methods, microemulsion techniques and template methods.

A variety of physical methods have been used for the synthesis of metal nanoparticles, including plasma reduction, thermal reduction, photochemical reduction, radiolysis, laser ablation and microwave treatment. [97, 98]

As a special category of plasma being confined within submillimeter scale in at least one dimension, microplasma has attracted tremendous interests for nanofabrication due to their unique characteristics;[99] in fact, microplasma allows to obtain NMs by direct reduction of the metal salts in solution at atmospheric pressure.[100]

Biological methods of nanoparticles synthesis utilize extracts from bio-organisms as reductant, capping agents or both. Such extracts can include microorganisms, proteins, amino acids, polysaccharides, and vitamins.[101] These approaches have been suggested as possible eco-friendly alternatives to chemical and physical methods, to synthesize gold and silver nanoparticles without the use of any harsh, toxic and expensive chemical substances.[102]

The NP functionalization allows to merge the physicochemical/biological properties of the carrier (NP) to the therapeutic compound, modulating the final biological effect [103]. The conjugation of NPs with a bioactive molecule (peptides, proteins, nucleic acids, polymers, or small-molecule) that binds to receptors found on cells can provide to an enhanced effect on wound healing leading to better control on the wound closure, contrast a prolonged inflammation stage and the bacterial infections.[90]

The functionalization of the surface of the gold and silver nanoparticles allows for the surface structure tailoring, the controlled change of morphology and charge (surface potential) of the nanoparticles themselves, influencing the nanomaterial response to hybrid biointerfaces with the biological environment [103].

In general, the strategies for the conjugation of nanoparticles with biomolecules can be classified according to a pure physical adsorption (physisorption) or a covalent derivatization (chemisorption) mechanism.

While in the physisorption of bioactive molecules are involved weak interaction (such as electrostatic and hydrophobic interactions, Van der

Waals and hydrogen bonds) in the chemical absorption there is a strong interaction between ligands and NP.

A non-covalent approach for the surface functionalization has several advantages such as easy maintenance of conformational degrees of freedom, reversible interaction with the surface, can be used to trigger the adsorption release of biomolecules on the surface of the material; enhanced stability for the selective cell and nuclear targeting because the surface of the material can be adapted to have a more precise interaction with the biomolecule [104]

1.3.2.3. Wet chemistry methods for the synthesis and functionalization of metal nanoparticles

The synthesis of noble metal nanoparticles (NPs) dates back to the mid-nineteenth century. Due to their unique properties, the interest of the scientists to find new preparation methods is increasing in order to investigate their potential applications in different fields such as: catalysis, biology, optics, electronics, solar cells, sensing and medicine.[105, 106]

Metal NP can be synthetized by different approaches classified in three wide-classes: chemical, physical and biological. The wet chemical methods for the preparation of colloidal metal are based on the chemical reduction of the metal salts, electrochemical pathways, or the controlled decomposition of metastable organometallic compounds and they are considered as “bottom-up” processes. The first scientific report describing the production of gold nanoparticles dates 1857, when Michael Faraday found that the ‘‘fine particles’’ formed from the reduction of gold chloride solution by phosphorus could be stabilized by the addition of carbon disulphide, resulting in a ‘‘beautiful ruby fluid’’.[107]

Over the past 150 years, plenty of solution-phase methods have been developed for preparing metal colloids either in aqueous or in organic phase. The most popular method of preparing 20 nm gold metal colloids dispersed in water is the reduction of $AuCl_4^-$ in a boiling sodium citrate solution. This method was developed by Turkevich et al.[108] in 1951. The metal salt is reduced to give zerovalent metal atoms in the embryonic stage of nucleation. These can collide in solution with further metal ions, metal atoms, or clusters to form an irreversible "seed" of stable metal nuclei.[109] These clusters eventually lead to the formation of metallic colloidal particles. Several mechanisms have been proposed depending on the reduction method such as LaMer'growth[110], Ostwald ripening,[96] Polte's model,[111] Pong's model.[112]

Since then, the Turkevich's method, has been improved[94, 95] and extended to other metals, including silver.[96] The citrate acts both to reduce the metal cation and as capping agent, preventing aggregation of the particles and stabilizing the resulting nanoparticles by electrostatic and/or physical repulsion. Also, citrate plays a role on determining the growth of the particles controlling the size and shape of the nanoparticle.[93] Since then, the Turkevich's method has been improved and extended to other metal, including silver.[113]

The reducing agents, besides to reduce the metal cations, can act as capping agent preserving NP from the aggregation during the aging time. The use of the capping agent can stabilize the colloidal suspension by electrostatic and/or physical repulsion. The main classes of protective groups are: polymers and block copolymers such as poly(vinylalcohol) (PVA), N-poly(vinylpyrrolidone) (PVP), poly(ethyleneglycol) (PEG), poly(methacrylic acid) (PMAA) and polymethylmethacrylate (PMMA); [114] P, N, S donors (e.g., phosphines, amines, thioethers);[115] solvents such as THF;[116] long-chain alcohols;[117] surfactants[118] and organometallics.[119] Particle size and morphology of the metal nanoparticles are typically tuned by using different reducing agents and stabilizers.[119]

However, the synthesis of citrate-capped AuNP is usually carried out at high temperatures, close to the boiling temperature of water; the hard reaction conditions (organic solvents, high temperature and denaturant agents) limit the NP biological applications and the possibility to use biological small molecules or polymers in the reaction mixture as capping agents. It is well known that biological molecules and polymers degrade at high temperature; accordingly with the HA degradation in solution at a temperature higher than 40 °C,[120] the using of HA as capping agent for the NP synthesis requires temperature up to 25 °C.

Suvarna et al.[121] develop a synthesis of AuNP using 2-deoxy-D-glucose (2DG) as capping and reducing agent. The reaction (Equation 1.1) was conducted at 25 °C, under stirring and in basic conditions. This study demonstrates that 2DG capped AuNP are suitable candidates for theranostic application; they show high cytotoxicity (cell viability < 80% for 2DG-AuNP 80 µM) on HTC116 (colorectal carcinoma) and HepG2 (hepatocellular carcinoma). Thus, the reaction (equation 1.1) previously described was studied in this work in order to obtain HA coated AuNP (HA-AuNP) by wet chemical reduction.

$$2Au^{3+} + 3C_6H_{12}O_6 + 6OH^- \xrightarrow{T=25°C} 3C_6H_{12}O_7 + 3H_2O + 2Au^0 \quad (1.1)$$

The use of strong reducing agents such as sodium citrate, ascorbate, sodium borohydride, elemental hydrogen, polyol process, Tollens reagent, N,N-dimethylformamide, and poly (ethylene glycol)-block copolymers are used for the reduction of the metal salt (Au^{3+} or Ag^+) in aqueous or non-aqueous solutions.[103] Several studies showed that strong reductants such as sodium borohydride result in small monodisperse particles, but also less control of the reaction can lead to the generation of larger particles.[122] However, it is true that particle size and morphology of the metal NP are typically tuned by using different reducing agents and stabilizers[123] and small changes in synthetic factors lead to dramatic modifications in NP stability, self-assembly patterns, average size and size distribution width.[124]

AgNP can be easily synthetized using sodium borohydride as reducing agent.[125, 126] The reaction (Equation 1.2) is conducted in an ice bath on a stir plate for 45 minutes. This reaction is used in order to obtain “bare” AgNP in solution without any capping agents.

$$Ag^+ + [BH_4]^- + 3H_2O \xrightarrow{ice\ bath} Ag^0 + H_3BO_3 + 3.5\ H_2 \quad (1.2)$$

In addition to the aforementioned method, the metal NP can be synthetized by physical methods such as thermal reduction[127] and photochemical reduction,[128] radiolysis and laser ablation.[129]

1.3.2.4. Plasma chemistry methods for the synthesis and functionalization of metal nanoparticles

Plasma is the fourth state of the matter and it was studied and defined for the first time in the early 1920’s by Langmuir with these words “the ionized gas contains ions and electrons in about equal numbers so that the resultant space charge is very small. We shall use the name plasma to describe this region containing balanced charges of ions and electrons”.[130] When the applied energy to gas is sufficient to eject an electron from collisions between molecules and atoms it is possible to obtain the plasma.

Plasma is the main state of the universe, in fact it is composed by 99.999% of plasma; (all stars, the interplanetary, interstellar and intergalactic medium and the Earth ionosphere are constituted by plasma).[131]

Plasmas can be defined as partially ionized gases, characterized by different electrons, ions and neutral species densities but it is globally electrically neutral (Equation 1.3).

$$n_e + \sum\nolimits_A qn\,(A^{q^-}) = \sum\nolimits_C pn\,(C^{p^+}) \tag{1.3}$$

where n_e is the electron density (m^{-3}), $n\ (A^{q^-})$ is the negative ion density (m^{-3}), $n\ (C^{p^+})$ is the positive ion density (m^{-3}). The parameter that defines the density of the charged particles in plasma is the degree of ionization of the gas. It specifies the fraction of the particles in the gaseous phase, which are ionized. The degree of ionization, α, is defined as (Equation 1.4):[132]

$$\alpha = \frac{n_i}{n_i + n_0} = \frac{n_e}{n_e + n_0} \tag{1.4}$$

The equality between the two expressions of the degree of ionization (α), in Eq. 1.4, is true only in the case of global electro-neutrality in the state of plasma. This charge compensation phenomenon can be directly related to the Debye length concept that represents the distance in which each charge is surrounded and screened by charges of opposite sign.[133] The electro-neutrality is achieved at a greater distance than the Debye length that characterize the ion interaction zone. It is defined by Equation 1.5:

$$\lambda_d = \sqrt{\frac{\varepsilon_0\, k_B\, T_e}{n_e\, e^2}} \tag{1.5}$$

where λ_d is the Debye length (in m), ε_0 is the permittivity of vacuum ($8.85 \cdot 10^{-12}$ C^2 J^{-1} m^{-1}), k_B is the Boltzmann constant ($1.38 \cdot 10^{-23}$ J K^{-1}), T_e is the electron temperature (in K), n_e is the electron density (in m^{-3}) and e is the electron charge ($1.602 \cdot 10^{-19}$ C). As indicated by Equation 1.5, the Debye length decreases with the increase of the electron density. An ionized gas is considered as a plasma only if the density of the charged particles is large enough such that $\lambda_d << L$, where L is the dimension of the system.[132]

Microscale plasmas are a special class of electrical discharges where at least one dimension is reduced to sub-millimeter scales. Microplasmas have been found to be uniquely characterized by high-pressure stability, non-equilibrium thermodynamics, high electron densities and excimer generation.[134]

From early attempts at characterizing earth's atmosphere to recently developed medical treatments, plasma-liquid interactions have been of significant interest to the scientific community. Modern low-temperature plasma sources, such as the micro hollow cathode, allow a stable chemical treatment of aqueous systems at atmospheric pressure.[135] For example, DC microplasma jets have recently been used to synthesize metallic nanoparticles in aqueous solution,[136] and atmospheric pressure plasma jets have been used for a variety of medical purposes, including sterilization and wound healing.[137] A pressure of 10^5 Pa is a favourable condition for the synthesis of the nanoparticles.[105] Indeed, the passage from a reduced pressure to the atmospheric pressure causes a decrease in the electrons mean free path and an increase in the collisions. However, it also involves the increase in the charged species densities and the formation of a thermal equilibrium. To offset this effect, it is possible to reduce the size of the plasma.[138]

The increase in the electronic temperature associated to the increase in the density at atmospheric pressure can be controlled through the two quantities, P_{heat} and P_{cool}, defined by Equations 1.6 and 1.7, respectively.

$$\frac{P_{heat}}{V} = \varepsilon(T_e)n_g n_e K_e(T_e) \tag{1.6}$$

Where ε is the average energy exchanged in each collision and P_{heat}/V is the power density transferred as thermal energy, n_g and n_e (in mol/L) are respectively the gas density and the electron density, K_e is the collision rate and T_e (in K) is an effective electron temperature.

$$\frac{P_{cool}}{V} \propto n_g \frac{{T_g}^{3/2}}{pD^2} \tag{1.7}$$

Where P_{cool}/V is the power loss per unit volume, T_g (in K) is the temperature of the neutral gas atoms, D is a parameter that refers to the size of a microplasma in one dimension and p (in atm) is the pressure. For a plasma at steady state (for example no gas flow), the power transferred to the gas must be equal to the power lost through conduction; therefore, we can equalize Equations 1.6 to Equation 1.7 and obtain the following relationship (Equation 1.8):[139]

$$D^2 \propto \frac{T_g^{3/2}}{p\varepsilon(T_e)n_e K_e(T_e)} \qquad\qquad p \propto \frac{T_g^{3/2}}{D^2\varepsilon(T_e)n_e K_e(T_e)} \tag{1.8}$$

The relationships found in Equation 1.8 can be used for a basic analysis of the effect of confinement on plasmas. In Figure 1.2, the pressure (p) is plotted as a function of the dimension of a plasma (D) where the thermal equilibrium limit (i.e., $T_e = T_g$) is indicated by the red curve; the non-equilibrium regime ($T_e > T_g$) is the area below the red curve indicated in grey. Near the thermal equilibrium curve, defined as the range of $T_g = 0.1T_e$ to $T_e = T_g$, the plasma is likely to undergo thermal instabilities.[134]

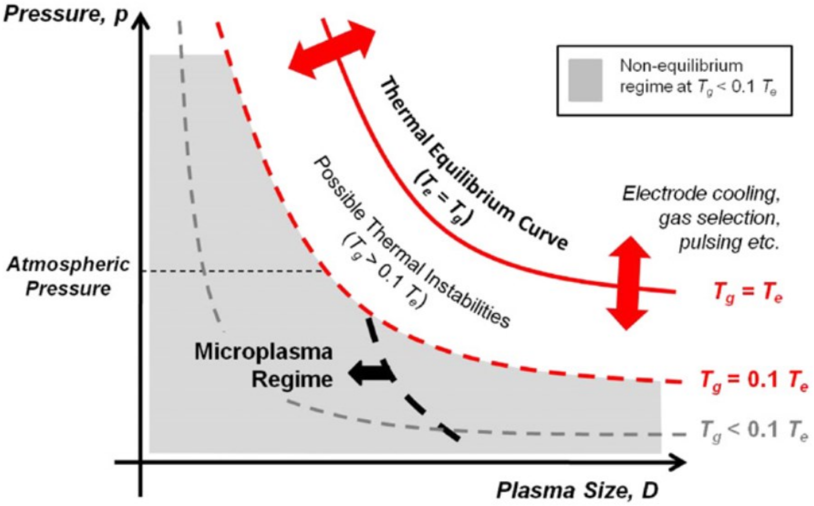

Figure 1.2. *Regimes of plasma operation as a function of the pressure (p) and its physical size in one dimension (D). The transition from non-equilibrium to thermal equilibrium is indicated by the solid or dashed lines*[134]

As indicated by Equation 1.2, reducing the size of the plasma at constant pressure (i.e. moving left from our starting point along the x-axis) results in a decrease in the gas temperature and/or an increase in the electron temperature (since both K_e and ε increase with T_e). Overall, this analysis illustrates that one of the most notable and interesting properties of microplasmas is the possibility to control two system temperatures separately (electron and gas temperature) simply by reducing the size of the plasma[134, 140]. Therefore, microplasma can be defined as "a particular type of electrical discharge produced in a system where one of the dimensions is reduced to a submillimeter scale"; it is characterized by a high electronic density with high energy (5-10 eV) that produces lots of reactive species both in the gas and in the liquid phase[105, 141].

Thanks to all the properties, one of the most recent physical methods for the synthesis of noble NPs is the atmospheric microplasma electrochemistry (plasma-liquid electrochemistry or gas-liquid interface discharges). This method is reliable and attractive thanks to its advantage in metal NP production such as rapidity and environment-compatibility (toxic-reducing agents or stabilizers such as $NaBH_4$ and TBAB Tetradecyl-trimethyl-ammonium bromide are not necessary anymore).[105, 142, 143] Therefore, the increased scientific interest leads to many studies concerning it.[105, 144]

Huang et al.[144] studied the particle size and the particle size distribution (PSD) of fructose capped AuNP synthesized by atmospheric microplasma electrochemistry under different experimental conditions (variation of current, temperature, and stirring or not). Summarizing, they found that: (1) the increase of the temperature led to bigger NPs, (2) as a result of the current increasing, more electrons were injected into the solution to reduce the Au^{3+} and more AuNP, with smaller size, were produced under the effect of the electrostatic repulsion of the charged AuNP. Stirring decreased the residence time of AuNP at the interfacial region and led to the production of AuNP with small and uniform size.

De Vos et al.[105] compared the aqueous reduction of $AgNO_3$ and HAuCl4 at a plasma-aqueous interface in the presence of a stabilizer, polyvinyl alcohol (PVA). Ag and AuNP were small (less than 20 nm), spherical and non-agglomerated when they were synthesized in the presence of the stabilizing agent (PVA) at a weight percent of 1%. The effect of the discharge current and the process time on the concentration and size of the NP was studied. The NP concentration exhibited a linear dependence on the charge injected, except at longer processing time that correspond to large amounts of charge transferred. The amount of charge injected was found to correlate well with the dependences on discharge current and process time, but was different for the two metal salts. This was partially explained by the number of electrons needed for each reduction reaction, three electrons were needed to reduce the Au ions as compared to Ag (Equation 1.9 and Equation 1.10), but also by the differences in the reaction mechanisms.

$$Ag^{+}_{(aq)} + 1e^{-} \rightarrow Ag_{(s)} \qquad E°=0.7996\ V\ versus\ SHE \qquad (1.9)$$

$$AuCl_4{}^{-}_{(aq)} + 3e^{-} \rightarrow Au_{(s)} + 4Cl^{-}_{(aq)} \qquad E°=1.002\ V\ versus\ SHE \qquad (1.10)$$

In fact, it was found that AuNP were prevalently obtained through reduction of $HAuCl_4$ by hydrogen peroxide (H_2O_2). [105] Indeed, the electrical discharges in contact with water could produce numerous reactive species by chemical dissociation, including atomic oxygen ($O^{\bullet}$), $H^{\bullet}$, and $OH^{\bullet}$. Recombination of $OH^{\bullet}$ can lead to the formation of H_2O_2 (Equation 1.11):

$$2OH^{\bullet} \rightarrow H_2O_2 \qquad (1.11)$$

The reduction reaction of gold by hydrogen peroxide is written in Equation 1.12, which as a positive potential, meaning that it is thermodynamically spontaneous. On the contrary, the reduction of Ag^{+} by H_2O_2 was found thermodynamically unfavourable.

$$2[AuCl_4]^{-}_{(aq)} + 3H_2O_{2(l)} \rightarrow 2Au_{(s)} + 8Cl^{-}_{(aq)} + 3O_{2\,(g)} + 6H^{+}_{(aq)} \qquad \Delta E = 0.449\ V \qquad (1.12)$$

Biological methods of nanoparticles synthesis utilize extracts from bio-organisms as reductant, capping agents or both. Such extracts can include microorganisms, proteins, amino acids, polysaccharides, and vitamins.[145]

These biological methods have been studied as possible eco-friendly alternatives to chemical and physical methods, to synthesize gold and silver nanoparticles without the use of any harsh, toxic and expensive chemical substances.[146]

1.3.3. Physicochemical characterization of nanoparticles (bulk and surface) and biophysical methods for the hybrid biointerface

1.3.3.1. UV visible (UV-vis) spectroscopy

Any elementary particle (atom, ion or molecule) has several energetic states. The ground state, which is the lowest energy state, is the most occupied at room temperature. However, if the particle is subjected to electromagnetic radiation and the energy of the associated photon is exactly equal to the energy difference between the fundamental level and the higher level, it will be able to absorb the energy of this photon and to pass to the excited state. After a short time (between 10^{-6} and 10^{-9} s), the particle will return to the ground state releasing the energy excess in the form of a photon or heat. The absorption spectrum is represented as the transmittance or absorbance as a function of the wavelength (Abs), the frequency (ν) or the wavenumber ($\bar{\nu}$). Transmittance is defined as the fraction of incident radiation that is transmitted by the sample *(Equation 1.13).* It is usually expressed as a percentage. Absorbance is defined as the fraction of incident radiation that is absorbed by the sample *(Equation 1.14).*[147]

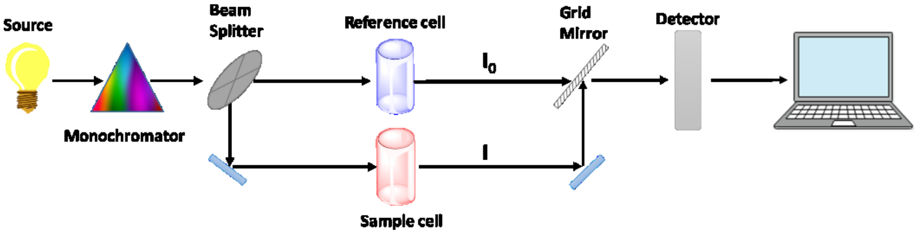

Figure 1.3. *Scheme of UV-Vis spectrophotometer.*

$$T = \frac{I}{I_0} \tag{1.13}$$

$$Abs = log\frac{I_0}{I} \tag{1.14}$$

Where $I_0$is the intensity of the incident radiation and I is the intensity of the transmitted radiation (Figure 1.3). The equation shows the relation between absorbance and transmittance (Equation 1.15):

$$Abs = -log\mathrm{T} \tag{1.15}$$

The absorbance is correlated to the concentration of the analyte by the Beer-Lambert law (*Equation 1.16*):

$$Abs = \varepsilon \cdot b \cdot C \tag{1.16}$$

where ε is the molar absorption coefficient of the analyte (in L mol^{-1} cm^{-1}), b is the length of the optical path (in cm) and C is the concentration (in mol L^{-1}). The validity area of the Beer-Lambert law is limited. The Beer-Lambert law can be applied when the absorbance is linearly correlated to the variation of the concentration of the analyte.[148]

In 1908, Gustav Mie proposed a solution to Maxwell's equations to explain the phenomenon of surface plasmon resonance (SPR) that characterizes metallic nanoparticles.[34] If the nanoparticles are exposed to electromagnetic radiation, the conduction electrons of the metal interact with the electrical component of the light causing the collective oscillation of the electrons Figure 1.4. The oscillation energy is dependent on the electronic density, the size and the shape of the nanoparticles and can be correlated to the wavelength[35].

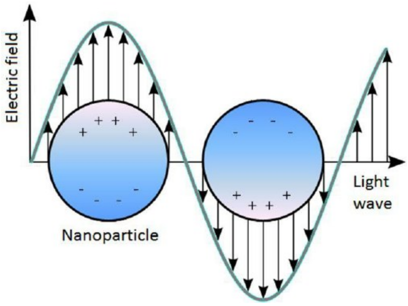

Figure 1.4. *Representation of the SPR phenomenon.*[149]

As above indicated, SP corresponds to an interaction between matter and the electromagnetic field of the light. Thus, the exact analysis of SP implies the solution of the Maxwell equations with the appropriate boundary conditions. The solution of these equations is only possible for certain conditions and even in this case, the results are mathematical series that do not explain what are SP. A metallic NP can be described as a lattice of ionic cores with conduction electron moving almost freely inside the NP (the Fermi sea) as Figure 1.5 illustrates. When the particle is illuminated, the electromagnetic field of the light exerts a force on these conduction electrons moving them towards the NP surface. As these electrons are confined inside the NP, negative charge will be accumulated in one side and positive charge in the opposite one, creating an electric dipole. This dipole generates an electric field inside the NP opposite to the light one that will force the electrons to return to the equilibrium position (Figure 1.5). If the electrons are displaced from the equilibrium position and the field is later removed, they will oscillate with a certain frequency that is called the resonant frequency; in the case of SP it is named the plasmonic frequency. Actually, the electron movement inside the NP exhibits some damping degree. The ionic cores and the NP surface partially damp the electron oscillations. Thus, the system is similar to linear oscillator with some damping.[147]

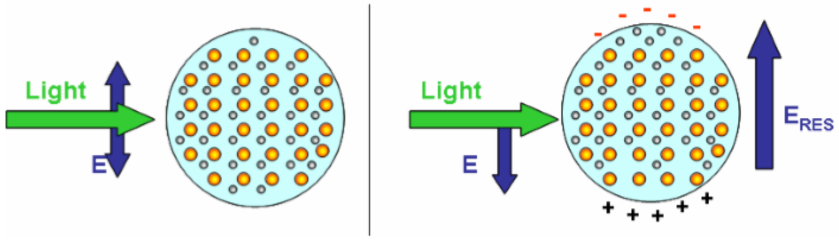

Figure 1.5. *Scheme of the light interaction with a metallic NP. The electric field of the light induces the movement of conduction electrons which accumulate on the NP surface creating an electric dipole. This charge accumulation creates an electric field opposite to than that of the light.*[147]

An accurate calculation of the SP and the associated light absorption requires solving the Maxwell equations at the NP region using the proper boundary conditions. The analytic solution can be obtained only for certain geometries and it was developed by Gustav Mie in the early 1900. Mie introduced spherical coordinates system, used the dimensionless size parameter $x = 2\pi mR/\lambda_0$, where R is the particle radio, m is the real refractive index and λ_0 is the incident wavelength. For the solutions of electromagnetic fields Mie introduced the extinction, absorption and scattering diffusion efficiencies, Q_{ext}, Q_{abs} and Q_{sca} (Equation 1.17, Equation 1.18 and Equation 1.19) known as Mie efficiencies of a spherical NP with area πR^2, these efficiencies are the cross-section of extinction, absorption and scattering normalized per area unit and it is given by the following expressions:[150, 151]

$$Q_{ext} = \frac{\sigma_{ext}}{\pi R^2} = \frac{2}{x^2} \sum_{n=0}^{\infty} (2n+1)\, \mathbf{R}\, (\mathrm{a}_n + b_n) \tag{1.17}$$

$$Q_{sca} = \frac{\sigma_{sca}}{\pi R^2} = \frac{2}{x^2} \sum_{n=0}^{\infty} (2n+1)\, (|\mathrm{a}_n| + |b_n|) \tag{1.18}$$

$$Q_{abs} = Q_{ext} - Q_{sca} \tag{1.19}$$

$$a_n = \frac{\psi_n(x)\psi'_n(mx) - m\psi_n(mx)\psi'_n(x)}{\xi(x)\psi'_n(mx) - m\psi_n(mx)\xi'_n(x)} \tag{1.20}$$

$$b_n = \frac{m\psi_n(x)\psi'_n(mx) - \psi_n(mx)\psi'_n(x)}{m\xi(x)\psi'_n(mx) - \psi_n(mx)\xi'_n(x)} \tag{1.21}$$

where $\psi_n(x)$ and $\xi(x)$ represent the Riccati-Bessel functions and it is described by the following expression (Equation 1.22 and Equation 1.23).

$$\psi_n(x) = \frac{\sqrt{nx}}{2} J_{n+\frac{1}{2}}(x) \tag{1.22}$$

$$\xi_n(x) = \sqrt{\frac{nx}{2}} \left[J_{n+\frac{1}{2}}(x) + iY_{n+\frac{1}{2}}(x) \right] \tag{1.23}$$

J_n and $Y_n(x)$ are the Bessel functions of first and second kind respectively.[150, 152, 153]

Thus, Mie's theory was based on many approximations; it was only applied to a spherical, homogeneous and isolated particle. Today, we speak about "Generalized Mie’s Theory" because, taking into account real systems, it was necessary to consider the non-sphericity of the particles, the inhomogeneity of the medium, the solvation and the aggregation[36].

The full width at half maximum wavelength and the intensity of the spectroscopic peak are influenced by the different characteristics of the system. In fact, a wide size distribution affects the full width at half maximum wavelength increase and when the particles are not spherical (particular geometric shapes or simple deformations) the intensity of the signal decrease due to luminescent anisotropy. Aggregation can also play a role by increasing the wavelength and varying absorbance.[37]

1.3.3.2. Attenuated Total Reflectance Fourier Transformed Infrared Spectroscopy (ATR-FTIR)

Internal-reflection spectroscopy is a technique that allows to obtain IR spectra of samples such as solids of limited solubility, films, threads, pastes, adhesives, and powders.[154]

The principle is that when a beam of radiation passes from a denser to a less dense medium, reflection occurs: the fraction of the incident beam reflected increases as the angle of incidence becomes larger; beyond a certain critical angle, reflection is complete. During the reflection process, the beam penetrates a small distance into the less dense medium before reflection occurs. The depth of penetration, which varies from a fraction of a wavelength up to several wavelengths, depends on the wavelength, the index of refraction of the two materials, and the angle of the beam with respect to the interface. The penetrating radiation is called the *evanescent wave*. When the less dense medium absorbs the evanescent radiation at different wavelengths, attenuation of the beam occurs and this phenomenon is known as attenuated total reflectance (ATR). The resulting ATR spectrum resembles that of a conventional IR spectrum but it is possible to notice some differences, although the same bands are observed, their relative intensities differ.[148]

In an apparatus for ATR measurements the sample (Figure 1.5) is placed on opposite sides of a transparent crystalline material of high refractive index. The incident radiation undergoes multiple internal reflections before passing from the crystal to the detector. Absorption and attenuation take place at each of these reflections.[155]

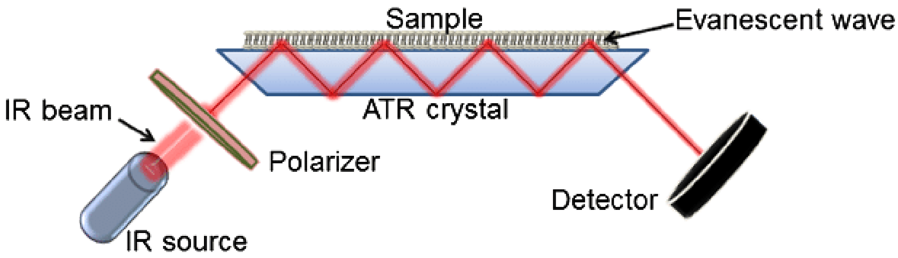

Figure 1.5. *Schematic representation of an ATR-FTIR system.*[155]

With ATR spectra, the absorbance, although dependent on the angle of incidence, are independent of sample thickness, because the radiation penetrates only a few micrometres into the sample. The effective penetration depth d_p depends on the wavelength of the beam, the refractive indexes of the crystal and the sample, and the beam angle. The penetration depth can be calculated from Equation 1.24.

$$d_p = \frac{\lambda_c}{2\pi\left[sen^2\theta - (n_s/n_c)^2\right]^{1/2}} \tag{1.24}$$

where λ_c is the wavelength in the crystal, θ is the angle of incidence, and n_s and n_c are the refractive indexes of the sample and crystal, respectively. It is important to notice that the effective penetration depth can be modulated by changing the crystal material, the angle of incidence, or both. [156]

One of the major advantages of ATR spectroscopy is that absorption spectra are readily obtainable on a wide variety of sample types with a simple preparation. It is possible to analyse polymers, rubbers, and other solids and to obtain IR spectra independent from the solvent IR contribute and from the sample preparation. Pastes, powders, or suspensions can be handled in a similar way. Aqueous solutions can also be accommodated provided the crystal is not water soluble. There are even ATR flow cells available.[148]

1.3.3.3. Dynamic Light Scattering (DLS)

Dynamic Light Scattering (DLS) also called Photon Correlation Spectroscopy (PCS) is a powerful technique, which allows to obtain, in a few minutes, information about the nanoparticle dimensions with diameters between few nanometres and about 5µm. The DLS technique involves the measurement of the Doppler broadening of the Rayleigh light because of the Brownian motion (translation diffusion) of the particles. This thermic motion leads to temporal fluctuations in the intensity of diffusion and a broadening of the Rayleigh line. As the Rayleigh line has a Lorentzian shape the Fourier transform is an exponential decay and the exponential decay constant τ (Equation 1.25*)* is directly related to the translational diffusion coefficient D_T of the isotropic, spherical particles (in Brownian motion).

$$\tau = D_T q^2 \tag{1.25}$$

In the Equation 1.25 and Equation 1.26 q is the diffusion vector modulus

$$q = \frac{4\pi n}{\lambda} sen\left(\frac{\theta}{2}\right) \tag{1.26}$$

where n is the refraction index of the suspension liquid, θ is the diffusion angle and λ is the wavelength of the laser radiation. For spherical particles, it is possible to calculate the hydrodynamic size d_h using the translational diffusion coefficient (D_T) and the Stokes-Einstein relation (Equation 1.27):

$$d_h = \frac{kT}{3\pi\eta D_T} \tag{1.27}$$

where k is the Boltzmann constant, T is the temperature (in K) and η is the medium viscosity. It is possible to use this last equation (Equation 1.27) for spherical particles which do not interact with each other's; for not spherical particles, it is possible to calculate the hydrodynamic size of a hypothetic sphere which has the same translational diffusion coefficient D_T of the not spherical one.

The instrument consisting of a laser source, a sample cell and a photodetector. The most common laser sources are: He-Ne (632.8 nm), Ar^+ (488 and 514.5 nm), diode laser (650 nm). The diffused radiation is measured with an angle θ (often 90°) from the incident beam. The most common photodetector is a photomultiplier, his signal can be elaborated using photon counting techniques or considering the analogic photocurrent.

1.3.3.4. Viscotek in GPC/SEC

Viscotek is an instrumental system used to scrutinize the viscoelastic properties of HA and to measure the intrinsic viscosity. The measure of the intrinsic viscosity is independent on the solvent viscosity but dependent on the polymer structure. Intrinsic viscosity is defined as (Equation 1.28):

$$[\mu] = \lim_{c \to 0} \frac{\eta_{spec}}{c} \tag{1.28}$$

where $\eta_{spec}$is the specific viscosity ($\eta_{\mathrm{spec}} = \frac{\mu_{solv} - \eta_{solution}}{\mu_{solv}}$) and c is the concentration; moreover, intrinsic viscosity is a dimensionless measure.

Molecular weight calculation allows to verify the intrinsic viscosity value, in fact, the Mark–Houwink equation (Equation 1.29) gives an empirical relation between intrinsic viscosity and molecular weight:

$$[\mu] = KM^a \tag{1.29}$$

where a and K are empirical constants.

From this equation, the molecular weight of a polymer can be determined from the intrinsic viscosity and vice versa. Intrinsic viscosity of the hyaluronic acid is about 5.4 for 200 kDa, about 14 for 700 kDa and 15-17 for 1000 kDa.[157]

Viscotek system is a method that allows to characterize the synthetic and natural linear polymers as well as proteins. In a single run, it is possible to obtain the molecular weight, the size, the intrinsic viscosity and structure of a biopolymer as well as to characterize copolymers, conjugates and branching. This instrument consists in three detectors: a light scattering enables absolute molecular weight calculation, independent of structure and sample retention volume; a viscometer probe the very structure of a molecule to give a sample's intrinsic viscosity and a refractive index detector which measures sample concentration.

1.3.3.5. Atomic Force Microscopy (AFM)

The atomic force microscope was invented in 1986.[158] This technique permits the resolution of individual atoms on both conducting and insulating surfaces. In this procedure, a flexible force-sensing cantilever stylus is scanned in a raster pattern over the surface of the sample. The force acting between the cantilever and the sample surface causes minute deflections of the cantilever, which are detected by optical means. The motion of the tip is achieved thanks to a piezoelectric tube. During a scan, the force on the tip is held constant by the up-and-down motion of the tip, which then provides the topographic information. The advantage of the AFM is that it applies to nonconducting samples.[159]

Figure 1.6 shows schematically the most common method of detecting the deflection of the cantilever holding the tip. A laser beam is reflected off a spot on the cantilever to a segmented photodiode that detects the motion of the probe. The output from the photodiode then controls the force applied to the tip so that it remains constant. The movement system is a tubular piezoelectric device that moves the sample in x, y and z directions under the tip. The signal from the laser beam detector is then fed back into the sample piezoelectric transducer, which causes the sample to move up and down, maintaining a constant force between the tip and the sample.[148]

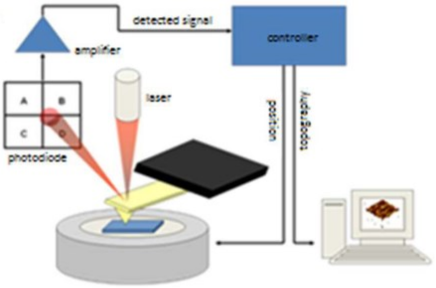

Figure 1.6. *Schematic representation of an AFM system.*[160]

The performance of an atomic force microscope depends on the physical characteristics of the cantilever and tip critically. In early AFMs, cantilevers were cut from metal foil and tips were made from crushed diamond particles. The tips were painstakingly manually glued to the cantilevers. The most common cantilever-tip assemblies in use today are micro-machined from monolithic silicon; the cantilevers and tips arc remarkably small (ideally a single atom at the tip apex).[148]

Three modes are commonly used in AFM: contact mode, noncontact mode and tapping mode. In the first one, the tip is in constant contact with the surface of the sample. The majority of AFM measurements are made under ambient pressure conditions or in liquids, and surface tension forces from adsorbed gases or from the liquid layer which may pull the tip downward. These forces, although quite small, may be large enough to damage the sample surface and distort the image. This problem is particularly bothersome with softer materials, such as biological samples, polymers and even some seemingly hard materials, such as silicon wafers. In addition. Many samples can trap electrostatic charges, which can contribute to an attractive force between the probe and the sample. This can lead to additional frictional forces as the tip moves over the sample which dulls the tip and damage the sample.[161, 162]

In the noncontact mode, the tip hovers a few nanometres above the sample surface. Attractive van der Waals forces between the tip and the sample are detected by the tip scans over the surface. These forces are substantially weaker than those detected in contact-mode AFM. Hence, the tip is oscillated and alternate current detection techniques are used to recover the small signals.[163]

The problem of surface damage can be largely overcome by using the tapping mode in which the tip contacts on the surface periodically for only a brief time and then is removed from the surface. In this tapping mode operation, the cantilever oscillates at a frequency of a few hundreds of kHz. This technique has been used successfully to image a wide variety of materials that have been difficult or impossible to image by the ordinary contact mode such as hydrogels or biological samples. AFM in tapping mode provides a powerful instrument for visualization and quantitative characterization of native biomaterials with manometer spatial resolution. AFM has been used to characterize the morphology and mechanical properties (e.g., stiffness, adhesion) of biomaterials, such as natural nanoparticles secreted from ivy,[164] peptide-assembled nanoparticles,[165] and wet adhesive inspired by mussels and geckos.[166]

Particularly, in recent years, the peak force tapping AFM imaging mode, has shown potent capabilities for simultaneously obtaining multiple mechanical parameters of diverse biological samples, including cells,[167] viruses,[168] membrane proteins[169] and biointerfaces[170] and to reveal the dynamic changes of morphology and mechanics of peptide-assembled nanofibrillar hydrogels.[171]

Using the AFM is possible to visualize metal nanoparticles and groups of particles and, unlike other microscopy techniques the AFM offers visualization in three dimensions; thanks to this technique it is possible to have precious information about the size, shape and the chemical hindrance of the particles.[172, 173]

Despite the advantages, a serious disadvantage of the AFM technique is that many artefacts can appear in AFM images which are difficult to recognize even by experienced users. An image artefact is defined as any feature which appears in the image which is not present in the original probed object. Artefacts can occur for several reasons, including finite tip dimensions, creep and hysteresis of piezo-scanner, thermal gradients, vibrations and the electronics (feedback circuits) and can be influenced by the sample preparation techniques and external factors (electromagnetic and mechanical noise and so on).[174]

The most frequently encountered artefacts are (**Figure 1.7**): edge overshoot, edge elevation, thermal drift and piezoelectric creep, external and internal noise, light interference artefact, friction-related artifacts.[175]

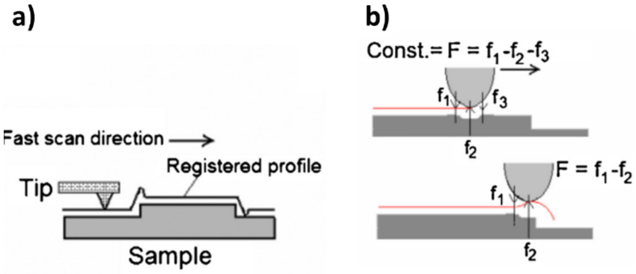

Figure 1.7. *Drawing explaining the origin of a) edge overshoots b) the elevation effect*[174]

It is clear that the key components of AFM data analysis are the modelling and characterization of the tip and sample artefact sources for use in subsequent deconvolution algorithms. In general, when modelling of the AFM data provides the output of a linear time-invariant system and when the sample surface involves sharp nanoscale features, the surface measured by the AFM can be interpreted as the convolution of the sample with a transfer function that depends on the properties of the tip. When the tip properties are accurately known, the true image can be reconstructed by a deconvolution of the measured surface.[176]

1.3.3.6. Transmission Electron Microscopy (TEM)

While optical microscopy is based on the interactions between light and the reflected photons detection, electron microscopy is based on the interaction between an incident electron beam and the sample surface, generating numerous physical phenomena such as the emission of X-photons, backscattered electrons, secondary electrons or Auger electrons, as shown in *Figure 1.8*.

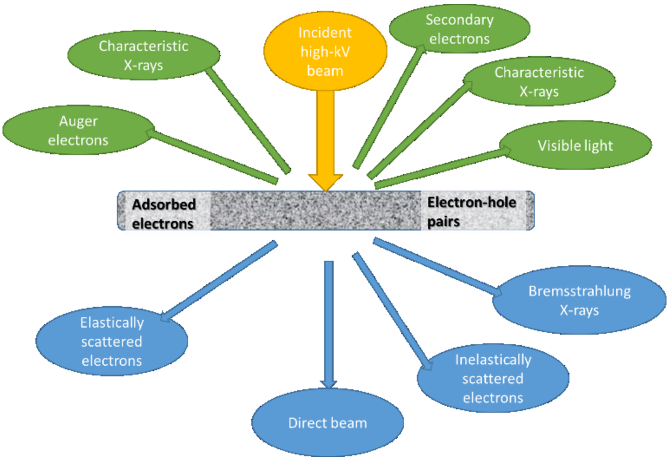

Figure 1.8. *Signals generated when a high-energy beam of electrons interacts with a thin surface.*

Scanning electron microscopy (SEM) defines the sample topography analysing particles and radiation. It focuses mainly on backscattered electrons, secondary electrons, Auger electrons and X photons. On the other hand, transmission electron microscopy (TEM) focuses on diffracted and/or transmitted electrons. What mainly distinguishes TEM and SEM is the position of the sample in the microscope structure. In fact, the analysis of the transmitted electrons is possible only if the incident ray passes through the sample. The electrons are accelerated by a voltage of 100 to 300 kV before reaching the sample. The schematic representation of TEM, the position of the lenses and apertures are shown in Figure 1.9.

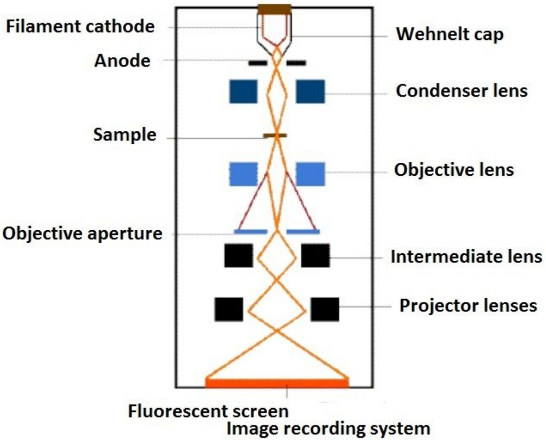

Figure 1.9. *Schematic representation of the TEM.*[177]

The primary electron beam is generated by the electron gun. Its operation is based on the thermoelectric effect or on the field effect: in the first case, the tungsten or lanthanum hexaboride (LaB_6) is heated by the Joule effect and in the second case, the final piece of the cathode is subjected to a very intense electric field which reduces the energy barrier and allows the direct extraction of electrons.

The complex lenses system allows to improve the resolution of the microscope and to correct the various optical aberrations. TEM is composed of three diaphragms (condenser, objective and selected area): the first enables to limit the convergence angle of the incident beam, the second defines the imaging or diffraction observation modality and the third allows to individualize the sample region to study. In this work, the HA@NP (plasma synthesis) were drop-casted from the processed solutions onto carbon-coated copper grids. The morphology, composition, and size of the HA@NP (plasma synthesis) have been evaluated by TEM using Philips CM20 microscope operated at 200 kV with a tungsten electron gun in the 4MAT laboratory (Materials Engineering, Characterization, Synthesis and Recycling), Université libre de Bruxelles (ULB).

1.3.3.7. Quartz Crystal Microbalance with Dissipation Monitoring (QCM-D)

HA is widely distributed but mainly localized to the extracellular matrix and body fluids. It contributes to the viscoelasticity of the fluids and elasticity in connective tissues, which absorbs mechanical stress, for example, between cartilage and cartilage surfaces.[178]

Hyaluronic acid is a non-Newtonian fluid and shows pseudoplastic and viscoelastic behaviour.[179] Viscoelastic materials exhibit both viscous and elastic characteristics when undergoing deformation; viscoelastic models are used to explain viscoelastic materials behaviour. Dynamic viscosity of a fluid expresses its resistance to shearing flows, where adjacent layers move parallel to each other with different speeds.

The friction force is found to be proportional to the speed u and the area A of each plate, and inversely proportional to their separation y (Equation 1.30):

$$F_a = \mu A \frac{u}{y} \tag{1.30}$$

where μ (in mPa · s) is the dynamic viscosity of the fluid.

Hyaluronic acid 700 kDa dynamic viscosity reported by Bonnevie et al.[180] is 170 mPa s (1% w/v at 20°C); dynamic viscosity of hyaluronic acid 200 kDa 1% w/v at 20°C is 100 mPa s.[181]

The dynamic viscosity of the hyaluronic acid at the different molecular weights used in this study was investigated with Quartz crystal microbalance with dissipation monitoring (QCM-D). The QCM-D technology is a real-time surface sensitive technique to monitor and characterize thin films on a surface in terms of adsorption, desorption, molecular interactions and structural properties. With the QCM-D technology, two parameters, frequency (related to mass/thickness) and dissipation (related to rigidity), are monitored simultaneously, in real-time, as molecular layers form on the sensor surface. The QCM-D instrument consists in electro-mechanical transducer with two electrodes, which are sensitive to the deposition of mass or to contact with liquid. The quartz crystal has a resonance frequency determined by its geometry, in particular, by its thickness. The crystal is stimulated by an alternating current voltage between its electrodes and, as a consequence, the crystal vibrates producing shear waves.

When the crystal is in contact with a mass or liquid, its resonance frequency changes according to the Sauerbrey equation (Equation 1.31):[182]

$$\Delta m = -\frac{C \cdot \Delta f}{n} \tag{1.31}$$

where C (17.8 ng·cm^{-2}·Hz^{-1}, when n = 1, f_0= 5 MHz) is the constant (describing surface area, density and shear modulus of quartz resonator) and n is the overtone number.

The dissipation factor D is proportional to the power dissipation of the oscillating system (Equation 1.32) and gives important information about the rigidity of the adsorbed layer:

$$D = \frac{E_{Diss}}{2\pi \cdot E_{Stor}} \tag{1.32}$$

where E_{Diss} is the energy dissipated during one oscillation and E_{Stor} is the energy stored in the oscillation system.[183]

For rigid, thin and evenly distributed films the Sauerbrey relation is a good estimation in cases when the change in the dissipation factor $\Delta D < 1 \cdot 10^{-6}$ for 10 Hz frequency shift (Δf). In these cases, the Sauerbrey equation can be used for adsorbed mass calculations. In the case of viscoelastic or soft films, the Sauerbrey relation underestimates the mass, since the film is not fully coupled to the motion of the sensor surface and the system energy dissipation increases. In cases when $\Delta D/\Delta f > 1 \cdot 10^{-6}/10\,Hz$, a viscoelastic modelling has to be used. In the Voigt viscoelastic model f and D depend on the density, thickness, elastic shear modulus and shear viscosity of the adsorbed layer. The analysis software QTools contains both the Voigt viscoelastic models, the Maxwell model and the Sauerbrey relation, thus allowing to the characterization of soft and rigid films. It enables quantification of the film in terms of mass, thickness, water content, density and viscoelastic properties (dynamic viscosity).[184]

Due to the interaction between surface and HA large elongated molecules, a large Δf due to mass deposition and large ΔD due to viscoelastic film formation can be expected.[185]

1.3.3.8. Laser Scanning Confocal Microscopy (LSM)

The principle of confocal imaging was patented in 1957 by Marvin Minsky.[186] Confocal microscopy (LSM) is an optical technique used for the acquisition of the three-dimensional images about the study of isolating or in situ biological structures. The optical sections of a biological system in the collection of a series of images of parallel planes, moving the focus of the lens along an axis coinciding with the light propagation axis. To obtain a perfect representation of a single sample plane, you should ideally collect only the light coming from that particular plane; however, even the overlying and underlying planes emit light, there is a loss of image sharpness. The key to the success of the confocal technique is the removal of hole interferences from the adjacent planes to the one that is focused, through the use of the so-called pinhole. Confocal microscopy uses a very intense light source, the laser, to excite molecules. The light emitted by the fluorochromes excited by the laser is captured by the lenses, crosses the dichroic mirror and reaches the photomultiplier, which transforms the light intensity into an electric signal of proportional intensity. Between the dichroic mirror and the photomultiplier, the light beam passes through a diaphragm, or pinhole, which embraces the light coming from the out-of-focus areas to reach the photomultiplier (Figure 1.10). In this way, only the light signal on the focus plane is recorded and used in the formation of the final image. The result is an image that is not very disturbed by the diffusion of light in the non-focused area. In fact, in addition to the pinhole for the light emitted, a pinhole is also used for the excitation light, so as to illuminate only a microscopic portion of the sample, increasing the contrast. To obtain the representation not of a microscopic portion of the sample but of an entire plane, the light beam is moved along the sample from point to point, so that the whole plane located at the desired depth is illuminated by the light beam according to a precise sequence. This process is called scanning. To increase the speed of image acquisition, some microscopes move the light beam by moving mirrors that direct the incident light towards the sample in a regular scan. These mirrors make the image reconstruction possible in less than a second. The electrical signal output from the photomultiplier is then digitized and sent to a computer that records the intensity values measured for each point. These values are used to reconstruct the image: each point corresponds to a pixel of the screen, and the luminous intensity of the point will be represented by a corresponding shade of grey. The combination of all the individual pixels, corresponding to points marked by the laser beam in the sample, will thus give the final image.

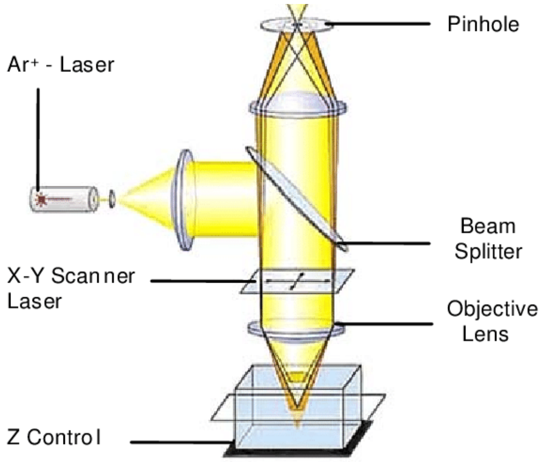

***Figure 1.10.** Optical scheme of laser confocal microscope*[187]

Due to its optical sectioning ability, LSM is a unique method to locate NP in the skin [188-190] but also to investigate the cellular uptake and localization of the NP inside the cells.

The work of Klingberg et al.[191] shows the application of the LSM on the study of the uptake of gold nanoparticles in primary human endothelial cells. HUVECs were cultured for 24 h in medium with citrate-AuNP in a concentration range of 1.25–10 µg mL^{-1}. The membrane-staining experiments showed that AuNP were predominantly located within the cell, and only a few AuNP located near or on the cell membrane.

A recent work of Li et al.[192] studied the cellular uptake on HUVEC and macrophages cell lines of the curcumin-loaded chitosan nanoparticles (Cur-CS-NPs) and explored their potential to accelerate diabetic wound healing. LSM images showed that Cur-CS-NPs accelerated internalization of Cur, moreover, the green fluorescence intensity emitted by Cur-CS-NPs was gradually enhanced with the extension of incubation time, indicating that the uptake of Cur-CS-NPs was time-dependent.

Moreover, LSM images can be useful in order to quantify the nanoparticle uptake (by 3D fluorescence microscopy). In fact, in the work of Torrano et al.[193] this method was used in order to investigate the silica nanoparticles uptake on human vascular endothelial cells (HUVEC) in comparison with a cancer cell line derived from the cervix carcinoma (HeLa). Finally, after 48 h, the particles that form smaller agglomerates (30 nm) nanoparticles, are internalized more efficiently by endothelial cells.

CHAPTER 2

EXPLORING THE RELATIONSHIP OF HYALURONIC ACID MOLECULAR WEIGHT AND NANOPARTICLE SURFACE TAILORING

MOTIVATION OF THE STUDY

In recent years, the use of nanoparticles, particularly metal nanoparticles, has expanded tremendously in biomedical field-related research.

Nanoparticles are available in different sizes and shapes, due to their ability to react and agglomerate with other nanoparticles in their surroundings. Metal nanoparticles can exhibit exceptional optical properties, making them capable of producing platforms suitable for imaging applications. For instance, silver (AgNP) and gold (AuNP) nanoparticles can be used simoultaneous in diagnosis and therapeutics (i.e., theranostics), due to their unique properties of controlled small size, large surface area to volume ratio, stability over high temperatures, high reactivity to the living cells and translocation into the cells, etc.

In this study we addressed the bioconjugation of silver and gold nanoparticles with hyaluronic acid by a one-pot synthetic approach where the metal salt ($HAuCl_4$ or $AgNO_3$), dissolved in the hyaluronan aqueous solution, is reduced by the corresponding reducing agent (glucose or sodium borohydride). It is to note that HA can act both as stabilising capping agent and as co-reducing agent at the used experimental conditions. The focus of this work was to scrutinise the effect of the polymer molecular weight on the physico-chemical properties of nanoparticle size (both optical and hydrodynamic diameter), colloidal stability against aggregation and intrinsic viscosity. To this purpose, three different polymer sizes, i.e. low MW (200 kDa), medium MW (700 kDa) and high MW (1,200 kDa) were used.

HYALURONAN-WRAPPED SILVER AND GOLD NANOPARTICLES: EXPLORING THE RELATIONSHIP BETWEEN THE POLYMER MOLECULAR WEIGHT AND THE NANOPARTICLE SURFACE TAILORING

Abstract

The bioconjugation of metal nanoparticles represents an attractive route for the fabrication of multifaceted nanoplatforms that merge the unique plasmonic features of the nanomaterial to the biocompatibility and targeting properties of the biomolecules used to tailor the NP surface. Hyaluronic acid, or hyaluronan, is an endogenous component of the extracellular matrix, and has excellent biological characteristics such as biodegradability, non-toxicity, and receptor-binding properties.

In this work, we developed an easy and green approach based on a wet chemical reduction method for the one-pot synthesis and bioconjugation of silver and gold nanoparticles with HA polymers of molecular size ranging from low (200 kDa) to high (1,200 kDa) molecular weight.

The as prepared HA@NP hybrids were characterized by using UV-visible and attenuated total reflectance-Fourier transformed infrared spectroscopies, to scrutinize respectively the optical response and the conformational structure at the polymer-metal interface, as well as by dynamic light scattering, to get insight into the hydrodynamic size and stability upon aging of the NPs. Moreover, intrinsic viscosity values were determined by Viscotek GPC/SEC system, with integrated refractive index viscometer and light scattering detectors. Results pointed out to the tunability of nanoparticle size and ionic strength-dependent aggregation by the different molecular weights of hyaluronic acid.

1. Introduction

Application of nanomaterials has gained a keen interest in research, especially in the area of medicine and biology. In particular, metal nanoparticles such as gold (AuNP) and silver (AgNP), either alone or in association with other bioactive molecules, have been largely investigated thanks to their peculiar physicochemical[194] and biological properties.[103]

The application of green chemistry in the nano-science and technology is very important in the area of the preparation of various materials. Indeed, green chemistry for metal nanoparticles fabrication is nowadays the torch bearing field of sustainable research. Advantages of green nanoparticle synthesis over chemical-based synthesis are its nearly zero toxicity with wider applications in different areas of science such as medicine, biology, chemistry, among others. [195-198]

Because of cheaper cost, wide availability, enhanced effectivity and fewer side effects, polysaccharides have successfully replaced the position of chemical reducing agents in nanoparticle synthesis.

Following this path, recently, nanoparticle syntheses were developed under mild and environmentally friendly conditions using biocompatible reagents such as mono- and poly-saccharides, in order to obtain, in high yields, nanoparticles with controlled size and shape.

Polysaccharides are natural biopolymers that have been recognized to be the most promising hosts for the synthesis of metallic nanoparticles because of their outstanding biocompatible and biodegradable properties. Polysaccharides are diverse in size and molecular chains, making them suitable for the reduction and stabilization of the nanoparticles.[199, 200]

As examples from literature, glucose and 2-deoxy-glucose capped-AuNP were synthetized for application in theranostic[201] and in the work of Engelbrekt et al.[202], glucose and starch were used as the reducing and stabilizing agents, obtaining AuNP for bioelectrochemistry applications; in the work of Castro-Guerrero et al[203] AuNP were synthesized at room temperature and atmospheric pressure using fructose, a common and non-toxic monosaccharide. Likewise, there are green protocols which use starch,[204] fructose[205] or sucrose[206] for the synthesis of AgNP or which decreases the use and concentration of toxic reagents.

Hyaluronic acid is a major glycosaminoglycan of the extracellular matrix of the skin, mucosal tissue, joints, eyes, and many other organs and tissues.[207] Hyaluronic acid is a biopolymer that exhibits different biological properties depending on the molecular weight (MW). For instance, HA has been shown to have differential signaling based on its molecular weight, namely pro-inflammatory response for low-MW HA or anti-angiogenic for high-MW HA.[208] Other than the biological effects, also the nanoparticle stabilisation is connected to the molecular weight. In fact, long chains of polymers are known to provide steric stabilization for nanoparticles, with the increase in molecular weight producing two counteracting effects: a decrease in the diffusion rate of chains and an increase in the physical adsorption of the polymer.[209]

The interaction of HA with metal nanoparticles may lead to interesting new nanocomposites for nanomedicine applications. In fact, HA, which is a linear anionic polymer, has biocompatibility, biodegradability, non-immunogenicity, non-inflammatory, and non-toxicity properties. Nanometer-sized HA nanomedicines can selectively deliver drugs or other molecules into tumor sites via their enhanced permeability and retention (EPR) effect. In addition, HA can interact with overexpressed receptors in cancer cells such as cluster determinant 44 (CD44) and receptor for HA-mediated motility and be degraded by a family of enzymes called hyaluronidase (HAdase) to release drugs or molecules.[210]

To fabricate HA-coated AgNPs or AuNPs, typically the hyaluronan solution is mixed with the nanoparticle dispersion.[210, 211] Zhang et al. synthetized HA-coated AgNPs by reduction of HA-Ag^+ with $NaBH_4$ at room temperature.[212] To the best of our knowledge, there are no reports on the reduction of HA-Au^{3+} analogous.

In this work, an eco-friendly chemical method based on HA was successfully used for the preparation of hyaluronan-capped silver nanoparticles (HA@Ag) and gold nanoparticles (HA@Au). To span a polymer molecular size range from low MW to high MW, such a green synthesis of silver and gold nanoparticles was achieved by using the hyaluronic acid at the three different molecular weighs of 200, 700 and 1,200 kDa.

2. Materials and Methods

2.1. Chemicals

Sodium hydroxide (NaOH) was purchased by Honeywell Fluka (USA). Silver nitrate ($AgNO_3$), sodium borohydride ($NaBH_4$), D-(+)-glucose, tetrachloroauric (III) acid trihydrate ($HAuCl_4 \cdot 3H_2O$), purity ≥ 99.9 %, sodium chloride (NaCl), sodium nitrate ($NaNO_3$) and sodium azide (NaN_3) were purchased by Sigma Aldrich (USA). All chemicals were with purity ≥ 99 %. Water was deionized (resistivity > 18.2 mΩ cm at 25 °C) and purified using a milli-Q unit (Milli-Q plus, Millipore, France). Glassware was cleaned with aqua regia (HCl: HNO_3, 1:3 volume ratio) and rinsed with water immediately before starting the use.

2.2. Hyaluronic acid biosynthesis and characterisation

Hyaluronic acid powders at low (~200 kDa) and high (~700 kDa and ~1,200 kDa) molecular weight were produced by bacterial cultures, followed by purification and freeze-drying, according to patented protocols of Fidia Farmaceutici S.p.A. (Italy).[213] Briefly, *Bacillus megaterium* was used to express episomal plasmid vectors (pT7-RNAP and pPT7) in the presence of T7 promoter.[213]

To determine the molecular weight and intrinsic viscosity of the different hyaluronan batches, a viscosimeter Viscotek system with GPC/SEC multi-detectors (Malvern Instrument, UK) was used. To prepare the samples for the Viscotek analyses, HA powders were dissolved in water at the concentration of 2 mg/mL, and left under stirring overnight in order to have the complete dissolution of the biopolymer. For the studies of degradation against aging in basic conditions, the stock HA solution was prepared in 7 mM NaOH and two aliquots were stored respectively at room temperature in controlled laboratory environment and in the fridge at 4°C during one month. To run the experiment with the Viscotek, the stocks HA solution were diluted to 0.2 mg/mL in the Viscotek buffer (NaCl 0.3 M, pH 7); these solutions were filtered with 0.22 µm pore size syringe filter and thus injected into the viscosimeter injector loop. The chromatographic runs were carried out in isocratic elution of $NaNO_3$ (0.1 M) and NaN_3 (0.5 g L^{-1}) for 30 minutes.

2.3. Synthesis of HA@Ag and HA@Au by wet-chemistry reduction.

Hyaluronan-conjugated silver and gold nanoparticles were fabricated by using a chemical reduction method modified from Mavani et al.[125] for AgNP and from Suvarna et al.[201] for AuNP, respectively. The HA polymer was added to the reaction mixture containing the metallic precursor salts (respectively $AgNO_3$ for AgNP and $HAuCl_4$ for AuNP) in the tripartite role of co-solvent, co-reducing and stabilising agent. For the synthesis of HA-coated silver nanoparticles (HA@Ag), the aqueous solution of $AgNO_3$ was reduced with $NaBH_4$ in the presence of HA, acting both as co-reducer and capping agent (Figure 2.1), according to the reaction in Equation 2.1:

$$Ag^+ + [BH_4]^- + 3H_2O \xrightarrow{ice\ bath} Ag^0 + H_3BO_3 + 3.5\ H_2 \qquad (2.1)$$

Briefly, a solution of $AgNO_3$ 0.5 mM ($AgNO_3$ final concentration = 0.03 mM) was added to a solution 0.2 % (w/v) of HA200 (or HA700 or HA1200) under magnetic stirring in an ice bath. Then, a freshly prepared aqueous $NaBH_4$ solution 100 mM was added dropwise over 5 minutes ($NaBH_4$ final concentration = 0.6 mM). The initially colourless solution became yellow and was stirred in ice bath for 105 minutes (Fig. 2.1a). The synthesis of bare, borohydride-capped AgNPs was carried out using the method of Mavani et al. [125]. In an Erlenmeyer flask was added a 2 mM solution of $NaBH_4$. A magnetic stir bar was added and the flask was placed in an ice bath on a stir plate. Ice bath was used to slow down the reaction temperature and give better control over final particle size/shape [214]. A 1 mM solution of $AgNO_3$ was dripped into the stirred $NaBH_4$ solution at approximately 1 drop per second. The initially colourless solution became yellow and was stirred in ice bath for 45 minutes.

Figure 2.1. *A representative picture of the wet chemical reduction synthesis and bioconjugation with HA of: (a) AgNP, (b) AuNP.*

For the synthesis of HA-coated gold nanoparticles (HA@Au), NaOH 7 mM and glucose 5 mM were added to an aqueous $HAuCl_4$ solution 0.5 mM. The reaction mixture was maintained under stirring and at controlled temperature of 25°C using Eppendorf ThermoMixer (Fig. 2.1b), in order to improve the experimental repeatability of the reaction, given in Equation 2.2:

$$2Au^{3+} + 3C_6H_{12}O_6 + 6OH^- \xrightarrow{T=25°C} 3C_6H_{12}O_7 + 3H_2O + 2Au^0 \tag{2.2}$$

The HA-capped gold nanoparticles were formed approximately in 1 minute. As to the bare, glucose-capped AuNPs, the same reaction of Eq. 2 was conducted in water instead of HA 0.2% aqueous solution.

For both HA@Ag and HA@Au hybrids, the as prepared colloidal dispersions were concentrated by two repeated centrifugation steps (4 minutes; 9391 xg; 15 °C) in a Eppendorf Centrifuge (5417R, FA453011 Rotor, Italy), with washing with milliQ water in between the two centrifugations. 0.5 mL Amicon Ultra centrifugal filters (Merk Millipore, USA) were used, with a molecular weight cut-off of 30 kDa. As to the reference bare AuNP and AgNP samples, the pellets were obtained by double centrifugation and washing in Eppendorf at 6010xg for 15 minutes for AuNP and at 11766xg for 20 minutes for AgNP, respectively.

2.4. UV-Visible spectroscopy

UV-Vis spectra were recorded at 25°C using Lambda2S spectrophotometer (Perkin Elmer, USA). The measurements were performed into a 3 mL quartz cuvette with a 1 cm path length or into 300 µL quartz cuvette with 0.1 cm path length. After each synthesis and pellet preparation, UV-Vis spectrum was recorded in order to check the NP spectrum in terms of absorbance and maximum wavelength. For the replicated UV-visible spectra from three independent syntheses, the percent of relative standard deviation (% RSD), was calculated, as given in Equation 2.3:

$$\%RSD = \frac{SD}{\bar{x}} \cdot 100 \qquad (2.3)$$

where $\bar{x}$ the average value of the measured variable, and SD is the standard deviation. We used this parameter as statistical tool to evaluate the reproducibility of the syntheses.

The optical parameters of the wavelength at the maximum of plasmon absorbance (λ_{max}) and the corresponding Abs values were used to calculate the optical diameter (d_O, in nm) and the molar extinction coefficient (ε, in L mol^{-1} cm^{-1}), according to eq.s (2.4)-(2.6) for AgNP[215] and eqs. (2.7) and (2.8) for AuNP [216, 217]:

$$d_O = \left(\frac{1-\lambda_{\mathrm{max}}}{a}\right)^{-\frac{1}{b}} \qquad \text{for } 8< d <20 \text{ nm} \qquad (2.4)$$

$$d_O = \left(\frac{\lambda_{max}-a}{b}\right)^{0.5} \qquad \text{for } 20< d <100 \text{ nm} \qquad (2.5)$$

$$\varepsilon = \varepsilon^0 + Ae^{Rd} \qquad \text{for } 8< d <30 \text{ nm} \qquad (2.6)$$

where a and b are constants (a=405 and b=1.5 in eq.4; a=397 and b=9.58· 10^{-3} in eq.5) as well as A and R (A=6.984 · 10^{8}; R=0.104).

$$d_O = \frac{\lambda_{max}-515.04}{0.3647} \qquad (2.7)$$

$$\varepsilon = Bd^{\gamma} \qquad (2.8)$$

where B and γ are two constants (B = $4.7 \cdot 10^4$ and γ=3.30 for d_O≤ 85 nm; B = $1.6 \cdot 10^8$; γ=1.47 for d_O > 85 nm).

2.5. Dynamic light scattering characterization

DLS measurement were obtained at 25°C using dynamic light scattering particle size distribution analyzer (DLS, HORIBA LB-550, USA) with a light source 650 nm (laser diode, 5 mW and a photo multiplier tube detector). The measurements were performed into a 3 mL quartz cuvette with a 1 cm path length. After each synthesis and pellet preparation, DLS measurements were carried out in order to investigate the NP hydrodynamic size.

2.6. Flocculation experiment

Gradual addition of NaCl concentrated solution (5 M) was added to the NP pellet suspensions. Sequential additions (50, 100, 200, 300, 400, 500 and 600 mM) of NaCl were carried out until complete NP aggregation was reached. Before and after every addition, UV-visible spectra of the samples were recorded using Lambda2S spectrophotometer (Perkin Elmer, USA).

2.7. ATR-FTIR spectra

The silicon wafers are cut in a surface of 0.8 cm x 1 cm and washed with methanol and iso-octane. 100 µL of sample (HA, NP or HA@NP) was putted on the cleaned silicon surface and left to dry at room temperature. The ATR-FTIR spectra was recorded using Spectrum Two™ FTIR Spectrometer (Perkin Elmer, USA).

3. Results and Discussion

The successfully formation of colloidal dispersions of metal nanoparticles was demonstrated by UV-visible spectroscopy analyses (Figure 2.2), which also evidenced differences among the three different molecular weights of HA used, namely, 200 kDa (HA200), 700 kDa (HA700) and 1,200 kDa (HA1200), respectively.

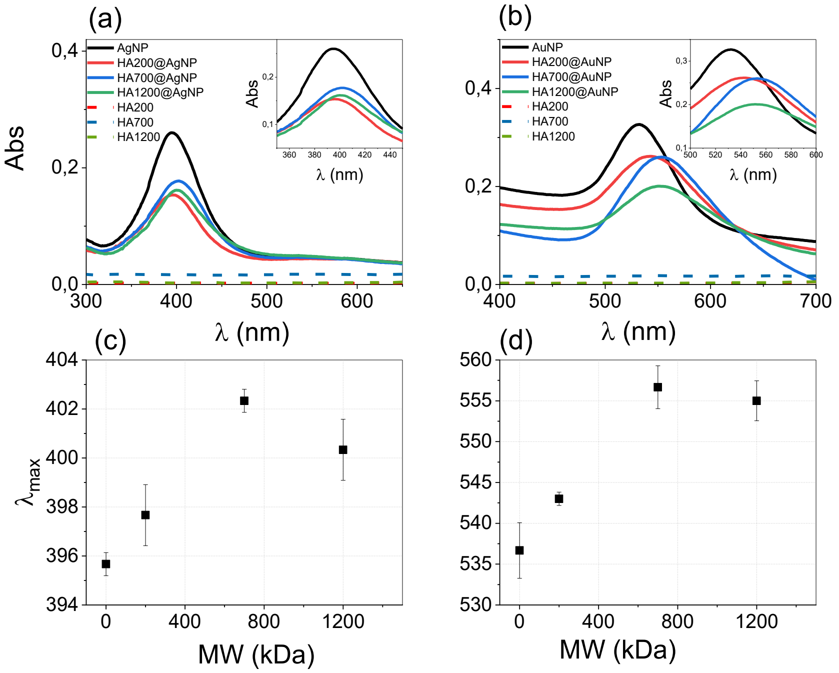

Figure 2.2. *UV-visible spectra of as prepared AgNP (a) and AuNP (b) samples, both bare and HA-capped nanoparticles. In (c) and (d) the wavelengths at the maximum of absorbance of the plasmon band (λmax) is displayed as function of the MWs for HA@Ag (c) and HA@Au(d), respectively. Spectra from three repeated syntheses were performed and results are shown as average λmax ± SD.*

According to eqs. from 2.4 to 2.7 for spherical metal nanoparticles, the wavelength at the maximum of absorbance of the plasmon band can be used to calculate the optical size of the HA-capped nanoparticles.

In the case of HA@Ag samples, with peaks centred in the 400-410 nm range (Fig. 2.2a) diameters approximately of 12 nm for HA200@Ag (similar to the bare AgNP, ~ 10 nm in size), ~22 nm for HA700@Ag and ~ 20 nm for HA1200@Ag were determined, respectively.

Similarly, the spectra of HA@Au samples, with plasmon peaks ranging from 535 nm to 550 nm (Fig.2.2b) correspond to spherical gold nanoparticles having diameters respectively of 70 nm, 121 nm and 118 nm for HA200@Au, HA700@Au and HA1200@Au, which are all significantly larger than the bare AuNP (~60 nm in size).

Significant differences in the plasmon peak were found in the spectra of HA-capped nanoparticles in comparison with those of reference bare NPs not only in terms of red shifts ($\Delta\lambda_{max}$ >0), but also for hypochromic effect (ΔAbs <0) and peak broadening, as measured by the increase of the full width at half maximum (ΔFWHM>0) (Table 2.1).

Table 2.1. UV-visible parameters of wavelength at the maximum of absorbance (λ_{max}), absorbance at the plasmon peak (Abs) and full width at half maximum (FWHM) for bare and HA-capped AgNPs and AuNPs with the three MWs of hyaluronan used. Values are the average from three spectra recorded for independent syntheses; in the brackets, percentage of relative standard deviation is shown.

	HA MW (kDa)	**λ_{max} (nm)± SD (% RSD)**	**Abs ± SD (%RSD)**	**FWHM± SD (% RSD)**
AgNP	0	396 ± 1 (0.4)	0.25 ± 0.01 (3)	68 ± 1 (2)
	200	398 ± 1 (0.1)	0.15 ± 0.01 (2)	65 ± 3 (4)
	700	402 ± 1 (0.2)	0.17 ± 0.01 (3)	80 ± 2 (3)
	1200	401 ± 1 (0.2)	0.16 ± 0.01 (3)	76 ± 1 (2)
AuNP	0	537 ± 1 (0.2)	0.27 ± 0.04 (1)	55 ± 2 (3)
	200	541 ± 1 (0.3)	0.21 ± 0.01 (2)	70 ± 2 (2)
	700	556 ± 3 (0.6)	0.19 ± 0.01 (2)	97 ± 5 (5)
	1200	555 ± 1 (0.2)	0.13 ± 0.01 (4)	63 ± 1 (2)

Specifically, for HA@Ag, a similar decrease in the absorbance of the plasmon peak (ΔAbs ~ -36%) was observed for all three MWs of HA used. On the other hand, for HA@Au samples, a MW-dependent trend was found, with ΔAbs of about -26% for both 200kDa and 700 kDa HA and

ΔAbs ~ -52% for 1200 kDa HA, respectively. As to the plasmon red-shift for the hybrid HA@NP samples with respect to the corresponding reference bare NPs, a nanoparticle-specific behaviour was detected, with a narrow range spanned by AgNPs (Fig. 2.2c) than AuNPs (Fig. 2.2d). To note, the largest red-shifts were found for both HA700- and HA1200-coated NPs ($\Delta\lambda_{max}$ ~5 nm for Ag and $\Delta\lambda_{max}$ ~20 nm for Au, respectively), whereas HA200-coated NPs exhibited a limited shift of few nm, i.e., $\Delta\lambda_{max}$ ~2 nm for Ag and $\Delta\lambda_{max}$ ~4 nm for Au, respectively (see Table 2.1). Finally, the measured FWHM (Table 2.1) did not change appreciably for HA200@Ag but significantly increased (ΔFWHM ~ +10 nm) for both HA700@Ag and HA1200@Ag, respectively. On the contrary, for HA@Au hybrids, an increase of FWHM with respect to bare AuNPs for increasing MWs of HA was found in the case of HA 200 kDa (ΔFWHM ~ +15 nm) and HA 700 kDa (ΔFWHM ~ +42 nm), instead for HA 1,200 kDa the lowest plasmon peak broadening (ΔFWHM ~ +8 nm) was found. In general, the broadening of the plasmonic peak FWHM in the presence of hyaluronic acid suggests the increase of polydispersity index of the colloidal dispersion, which thus consists of a population of several size distributions.[218, 219]

To note, the calculated values of %RSD given in Table 2.1 confirm the high reproducibility of the synthetic approach for the nanoparticle preparation, with a good level of similarity among the different samples from repeated syntheses in independent experiments.

Taken together, these results can be indicative of an actual coating of the metal nanoparticle by HA, with the resulting increase in the nanoparticle optical diameter due to the wrapping of the metal core by the hyaluronan polymer chains.[220, 221]

In particular, the hypocromic and red shifts as well as the plasmon peak broadening, point to a general increase in the particle size (that correspond to the decrease in the nanoparticle molar concentration) as well as to the increase in the dispersity index by the increase of the hyaluronan molecular weight.

Of course, the molecular weight of the hyaluronan is expected to have a role in the mechanism of seeds formation and growth that occurs during the reduction reaction. Indeed, various experimental evidences show that the polymer MW influences the yield, the morphology and size distribution adopted by metal nanoparticles.[216]

For instance, Zhang et al. measured a plasmon peak red-shift of $\Delta\lambda_{max} \sim 6$ nm for AgNP coated with 22 kDa HA with respect to the bare, citrate-capped AgNP (λ_{max} = 390 nm).[212] Similarly, a red shift of $\Delta\lambda_{max} \sim 10$ nm was found for hyaluronan (100 kDa)-reduced silver nanoparticles with respect to glucose-reduced AgNP.[222] Finally, Hien et al. found in HA-capped AuNPs synthesised by using a γ-irradiation method that the average diameters determined by TEM of AuNPs were of 10.2, 7.0, 6.0 and 5.5 nm for HA concentrations of 0.05, 0.1, 0.2 and 0.4%, respectively.[223]

In physiological solution, the backbone of a hyaluronan molecule is stiffened by a combination of the chemical structure of the disaccharide, internal hydrogen bonds, and interactions with the solvent. However, the OH and $-COO^-$ groups on the HA side chains are expected to have a high affinity with the metal ion precursors, i.e., Ag^+ [224] or Au^{3+}.[225-227] Therefore, the differences found for HA@Ag and HA@Au can be related to different HA-assisted growth paths ongoing during the synthesis for the AuNP or the AgNP seeds and/or the partial nanoparticle aggregation.

Since the reproducibility and the stability against aggregation are crucial factors to set the optimal conditions for the synthesis and purification of metal-based nanoparticles, we investigated the pellets obtained after two centrifugation steps with water washing in between and at the end (see Materials and Methods). The UV-visible spectra of the pellets in Figure 2.3 show that the red-shifts ($\Delta\lambda_{max}$ ~10 nm for HA@Ag and $\Delta\lambda_{max}$ ~20 nm for HA@Au, respectively) found in the as prepared HA-capped NPs with respect to the corresponding bare NPs were substantially maintained.

To note, in the case of HA1200@Au pellet, a further red-shift ($\Delta\lambda_{max} \sim$ 10 nm) compared to the as prepared sample (i.e., before the centrifugation and rinsing steps) points most likely to a partial aggregation of the nanoparticle. This finding can be related to the nanoparticle purification procedure, which rinsed off part of the stabilising polymer shell that coated the metallic core in the nanoparticle suspension. Such a phenomenon, given by the sum of the contributions from both gravitational and centrifugal forces, is expected to have a major effect on the longer and 'heavier' polymer chains of HA 1,200 kDa than in the case of HA 200 kDa and 700 kDa, respectively. In the case of AgNP, the likely presence of Ag^+ species at the nanoparticle surface[228] allowed for a more stable anchoring of HA capping layer, due to the electrostatic interaction between the metal cation and the negatively charged O^- and COO^- -rich groups of hyaluronan.

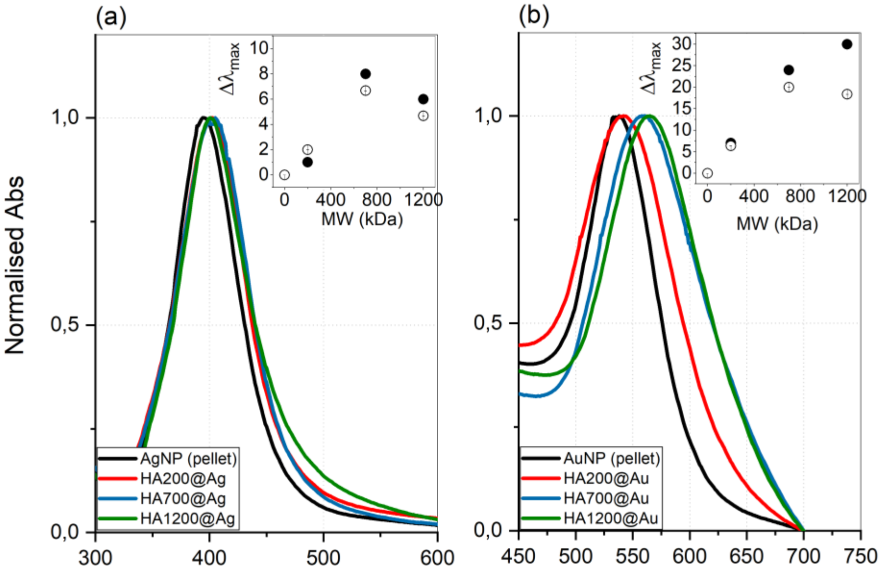

Figure 2.3. *UV-visible spectra with normalised absorbance for the pellet samples resuspended in water for bare NP and HA@NP samples of AgNP (a) and AuNP (b). In the inset: the wavelengths at the maximum of absorbance plotted versus the HA MWs for the pellets (solid symbols) in the comparison with the corresponding as prepared dispersion (open symbols).*

The NP optical size (d_0) and the concentration (in mol/L) were calculated, according to Eq.s (2.4)-(2.8) given in Materials and Methods, by using the λ_{max} and the corresponding Abs values for the plasmon peak of the various pellet samples. The values reported in Table 2.2 show that the optical size slightly increased in comparison with the bare NPs for HA200-coated NP (+1 nm for HA200@Ag and +7 nm for HA200@Au, respectively), whereas the diameter size was approximately doubled for the AgNP and AuNP coated by the high-MW (700 kDa and 1,200 kDa) hyaluronan.

Table 2.2. *UV-visible parameters from the pellet-NP UV-Visible spectra.*

	MW (kDa)	λ_{max} (nm)	FWHM (nm)	d_0 (nm)	[nM]	NP/mL[(a)]
AgNP	0	395	68	12	5.64	$6.33 \cdot 10^7$
	200	396	62	13	5.92	$5.23 \cdot 10^7$
	700	403	60	25	1.00	$1.24 \cdot 10^6$
	1200	401	67	20	1.66	$4.03 \cdot 10^6$
AuNP	0	535	87	66	0.28	$1.96 \cdot 10^4$
	200	542	117	73	0.17	$8.30 \cdot 10^3$
	700	559	104	123	0.04	$3.66 \cdot 10^2$
	1200	565	108	134	0.05	$3.87 \cdot 10^2$

[a] As calculated according to the volume of a spherical nanoparticle, with a fcc unit cell of 0.407 nm for AgNP[229] and 0.408 nm for AuNP[230] in length; and using $N_{mol}/NP = 4 \cdot (V/V_{cell} \cdot N_A)$ (N_A = Avogadro's constant; 4 atoms/unit cell) to the molar concentration, $c = (NP/mL) \cdot N_{mol}/NP$.

The trend in the changes of calculated optical diameters were in good agreement with the measured (by DLS) hydrodynamic size of the nanoparticles (Figure 2.4). To note, the hydrodynamic size of bare nanoparticles, respectively of 32±2 nm for AgNP and 57 ± 1 nm for AuNP, increased as the MW of the hyaluronan used for the bioconjugation increased (~ 100 nm for HA200@NP and ~ 200 nm for HA700@NP and HA1200@NP, respectively), for both silver and gold nanoparticles. Figure 2.4 also evidences a larger difference between the hydrodynamic size and the optical size in the case of HA@AgNP.

Such an increase of the nanoparticle size with the increase of the HA molecular weight is well-known from literature, for instance Shimmin et al[220] demonstrated a linear correlation between molecular weight of the stabilising polymer shell and the hydrodynamic size of the nanoparticle, as expected by the steric stabilisation mechanism of colloids against aggregation.[231]

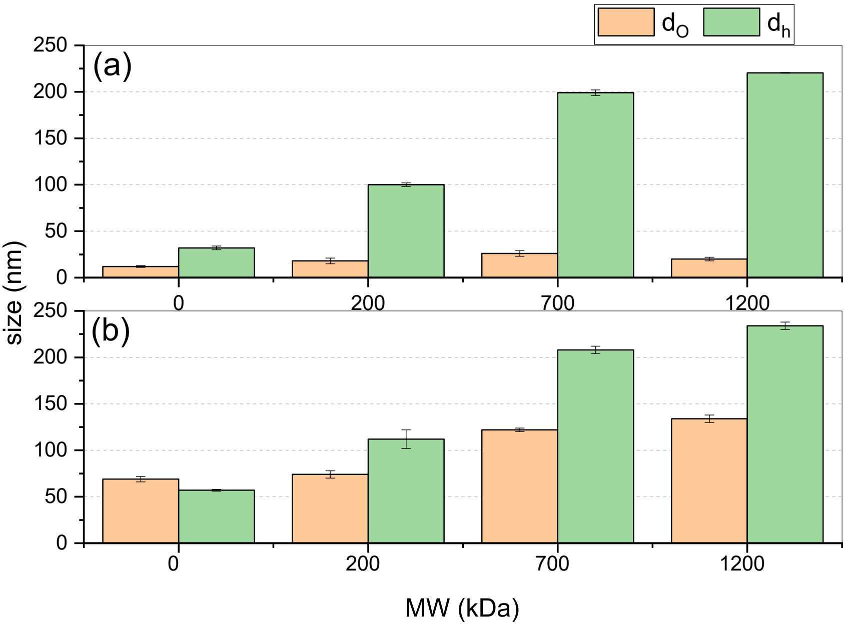

Figure 2.4. *Optical and hydrodynamic diameter measured for the pellets for silver (a) and gold (b) nanoparticles, both bare (MW=0) and HA-conjugated (MW=200, 700 and 1,200 kDa) samples.*

To confirm the efficiency of the purification process performed through the centrifugation and water rinsing steps, the pH of the suspensions of as prepared and re-suspended pellets were measured.

Table 2.3 shows that the measured pH values for the as prepared dispersions were in the range of 5.58-6.18 for AgNPs and of 8.12-8.58 for AuNPs, respectively. After the purification, all the colloidal suspensions exhibited a value close to neutrality.

Table 2.3. *pH value of the as prepared and pellet dispersion*

	HA MW (kDa)	**pH (as prep)**	**pH (pellets)**
AgNP	0	5.58	6.89
	200	5.76	7.04
	700	6.18	7.10
	1200	6.16	7.15
AuNP	0	8.58	7.41
	200	8.12	7.44
	700	8.22	7.51
	1200	8.36	7.48

This finding was remarkable to demonstrate the efficiency of the purification procedure to rinse off unreacted and/or excess chemicals (e.g., the sodium hydroxide used for the basic conditions to synthesise the AuNPs). Moreover, the evidence of minor changes fund in the pH before and after the washing steps, confirmed the suitability of the approach for the synthesis and purification of the NPs. Indeed, it is known that pH may affect the stability of polymer-coated NPs by inducing changes both in the nanoparticle size and/or in the degradation of the macromolecule chains.

Generally, basic conditions are known to favour a shrinking in the nanoparticle size, with a corresponding change in the plasmonic peak features. For instance, AgNPs synthesised by using a polyphenol and alkaloid-based extract exhibited a diameter change from 30 nm to 130 nm as the pH increased from 2 to 8, due to the tuning of reducing mechanism involving the hydroxyl groups.[232] As to the stability of the hyaluronan polymer against pH changes, Chen et al. found that high MW HA (1,000 kDa) investigated at different pH, quickly degraded at pH = 4, whereas the maximum stability was detected in the pH range of 6-8.[233]

To note, in basic condition and room temperature (22°C-25°C), HA is rapidly hydrolysed with a consequent decrease in molecular weight and intrinsic viscosity. [234] The degradation of hyaluronan of the different molecular weights measured for fresh solutions (before degradation) was studied in aqueous solutions by Viscotek determination of molecular mass and intrinsic viscosity (η) parameters. The solutions were stored either at laboratory (r.t., 25°C) or refrigerator (4°C) temperatures during four weeks (Figure 2.5).

Already after 1 week, the average molecular weight decreased by 30% (25°C) or 3% (4°C) for 700 kDa (Fig. 2.5b) and by 10% (25°C) or 7% (4°C) for 1,200 kDa hyaluronan (Fig. 2.5c). Accordingly, the average intrinsic viscosity decreased respectively by 22% (25°C) or 0.5% (4°C) for 700 kDa and by 24% (25°C) or 8% (4°C) for 1,200 kDa HA, respectively. On the contrary, only a minor decrease of the average MW by 2% (25°C) or 0.08% (4°C) was found for 200 kDa HA (Fig. 2.5a), corresponding to the η decrease by 7% (25°C) or 2 % (4°C).

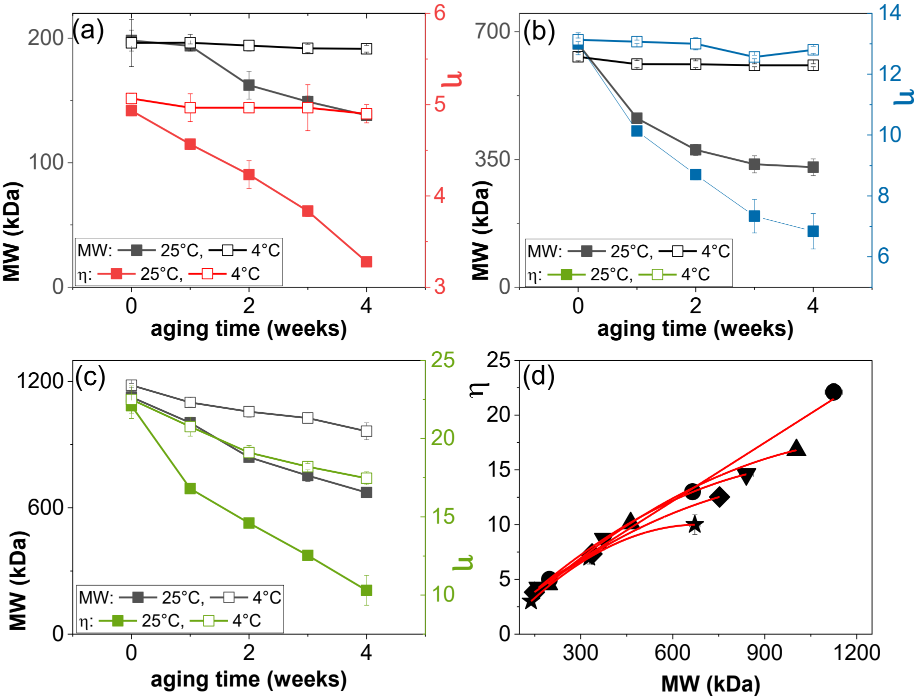

Figure 2.5. *(a-c): Viscotek results of average molecular weight (MW, left hand side axis) and average intrinsic viscosity (η, right hand side axis) for HA aged up to 4 weeks at room temperature (solid symbols) or in the refrigerator (open symbols): (a) 200 kDa, (b) 700 kDa, (c) 1,200 kDa. In panel d) the plots of the intrinsic viscosity against the molecular weight for fresh (t=0) and aged (t=1,2,3 and 4 weeks) samples (black scattered plot = experimental data points; red line = curve fit).*

During the following three weeks of aging a progressive degradation occurred, as evidenced by the decrease in both the average molecular weight and the average intrinsic viscosity for the all the three hyaluronan polymers studied. To note, the linear correlation between MW and η observed for the fresh samples changed to more complex curve fit functions at increasing aging times (Fig. 2.5d).

Figure 2.6 shows the comparison of the plasmon peak features between HA@Ag (Fig. 2.6a) and HA@Au (Fig. 2.6b), in terms of the variation in λ_{max} ($\Delta\lambda_{max}$), absorbance (ΔAbs) and FWHM (ΔFWHM) as a function of the aging time (up to 15 days). In general, the dispersions in both cases were quite stable, since the overall variation in $\Delta\lambda_{max}$, ΔAbs and ΔFWHM were respectively less than 1 nm, 0.7 and 10 nm, with respect to the freshly synthesised suspension. However, significant differences were found for silver and gold dispersions upon aging.

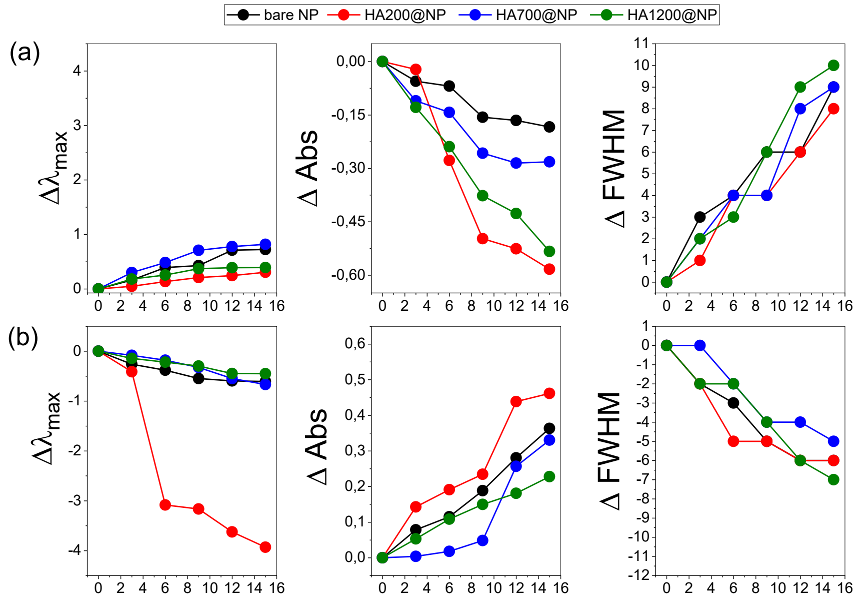

Figure 2.6. (a) $\Delta\lambda_{max}$, ΔAbs, and ΔFWHM for bare and HA-coated AgNPs and (b) $\Delta\lambda_{max}$, ΔAbs, and ΔFWHM for bare and HA-coated AuNPs as a function of the aging time (0, 3, 6, 9, 12, 15 days).

Upon ageing, both bare and HA-coated AgNPs likely form larger aggregates, in comparison with as prepared suspension, with a broader distribution in size, as evidenced by the red shifts, ipochromic shifts, and plasmonic peak broadening.[235] No significant differences among the three MWs tested were found. Conversely, for the aged AuNPs, a blue-shift (especially evident for the low MW HA-capped AuNP), together with an hyperchromic shift and a narrowing in the plasmon band were found.

In particular, AuNP initially shows a broad peak which indicates populations of various sizes at the initial growth stages but, after 15 days of aging, the narrower and sharper absorption peak point to smaller and stable NPs in colloidal form.[236] It is likely that the big and not stable fresh NPs stuck on the inner walls of the vial; however, other than this effect, the increase in the absorbance suggest that, during the aging time, a further NP nucleation occurred leading to formation of smaller NP (corresponding to the decrease in FWHM). These findings of the HA on the NP size evolution suggest a digestive ripening effect for gold,[237] by which the size of the NP decreased prompted by the interaction with the hyaluronan chains, and an Ostwald type growth for silver,[238] likely due to a lower level of interaction between the polysaccharide chains and the metal atoms.

The flocculation assay was conducted in order to investigate the protection activity of the HA chain on the NP aggregation after electrolyte addition and the results are showed in Figure 2.7. The gradual addition of NaCl, from 50 mM to 0.6 M, to the suspension of bare nanoparticles of silver (Fig. 5a, 0.34 nM = $3.2 \cdot 10^6$ AgNP/mL) or gold (Fig 5c, 0.04 nM = $7 \cdot 10^3$ AuNP/mL) showed that the disappearance of the plasmon band, i.e., complete aggregation of the nanoparticles, was reached for the NaCl addition at the concentration of 0.6 μM for AgNP and 0.5 μM for AuNP, respectively.

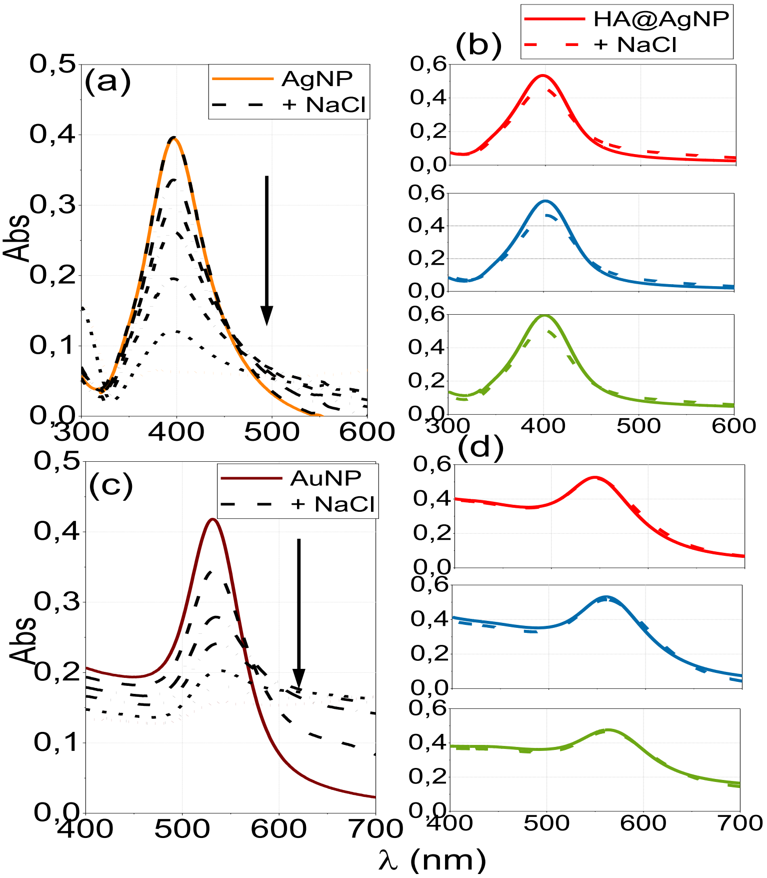

Figure 2.7. *UV-visible spectra of bare AgNP (a) or AuNP (c) before (solid line) and after (dashed lines) the gradual addition of a concentrated NaCl aqueous solution in the concentration range from 50 mM to 0.6 M. UV-visible spectra of HA HA-coated AgNP (b) or AuNP (d) nanoparticles before (solid line) and after (dashed lines) addition of 0.6 M NaCl to HA200@NP (red curves; 0.34 nM = 3.2 ·* 10^6 *AgNP/mL or 0.11 nM = 4 ·* 10^3 *AuNP/mL), HA700@NP (blue curves, 0.12 nM = 2.8 ·* 10^5 *AgNP/mL or 0.06 nM = 6 ·* 10^2 *AuNP/mL) and HA1200@NP (green curves, 0.10 nM = 1.6 ·* 10^5 *AgNP/mL or 0.05 nM = 4 ·* 10^2 *AuNP/mL).*

The direct addition of the same NaCl concentration to the HA@NP samples (Fig 2.7b and Fig. 2.7d) confirmed the actual surface decoration of the nanoparticles by the hyaluronan polymer chains, since minimal changes in the plasmon bands, with the absorbance decrease of about 15-16% for HA@Ag and of about 1-3% for HA@Au were found, respectively.

To note, no differences were found for the three different MWs of HA used.

The flocculation process occurs when the addition of an electrolyte to the suspension leads to the neutralization of the superficial NP charge forming big aggregate.[239] This protection effect of the polymer against flocculation is known in the literature in fact, the work of Lin et al.[240] shows that uncharged polymers such as PVP and charged polymer such as Arabic gum, stabilize efficiently AgNP against aggregation after electrolyte addition (0.1 M, $NaNO_3$); likewise, the work of Gangula et al.[241] shows that polymers such as PVA stabilize efficiently AuNP against aggregation after thiourea addition.

The nanoparticle stability against aggregation induced by addition of a strong electrolyte (NaCl) to the nanoparticles suspension was monitored by DLS measurements (Table 2.4) that confirmed the UV-visible results.

In fact, the direct addition of NaCl did not affect significantly the HA@NP diameter, with an increase of the particle size ranged between 2 % and 10 % for HA@Au and between 6 % and 7 % for HA@Ag.

The bare nanoparticles exhibited a size increase percent of 67 % and 46 % for AgNP and AuNP, respectively. These results confirmed the stabilising action of the HA coating shell around the nanoparticles against electrolyte addition.

Table 2.4. *DLS measurements of the hydrodynamic size of silver (0.6 nM-0.1 nM) and gold nanoparticles (0.03 nM-0.005 nM) before and after the direct addition of 0.6 M NaCl.*

	D (nm) ± SD	**D (nm)+ NaCl ± SD**
AgNP	36 ± 1	111 ± 7
HA200@Ag	113 ± 2	122 ± 2
HA700@Ag	208 ± 6	223 ± 5
HA1200@Ag	227 ± 3	243 ± 2
AuNP	62 ± 1	113 ± 11
HA200@Au	105 ± 3	119 ± 1
HA700@Au	217 ± 2	220 ± 2
HA1200@Au	240 ± 8	250 ± 7

The ATR-FTIR spectra of hybrid HA@NP samples are shown in Figure 2.8, the reference samples of bare NPs and HA (200 kDa, 700 kDa and 1,200 kDa) are included for comparison. The complete list of IR bands and their assignation is reported in Table 2.5.

For both HA@Ag (Fig. 2.8a) and HA@Au (Fig. 2.8b) samples, the characteristic IR bands of HA were found, including the OH and NH stretching (at about 3400-3200 cm^{-1}), the CH$_2$ symmetric stretching (at 2950-2850 cm^{-1}), the C=O stretching and N–H bending (1600-1500 cm^{-1}), the CH$_2$ bending (at about 1480-1350 cm^{-1}) and the C–O-C stretching of proteoglycan sugar rings (at 1140-985 cm^{-1}).[242]

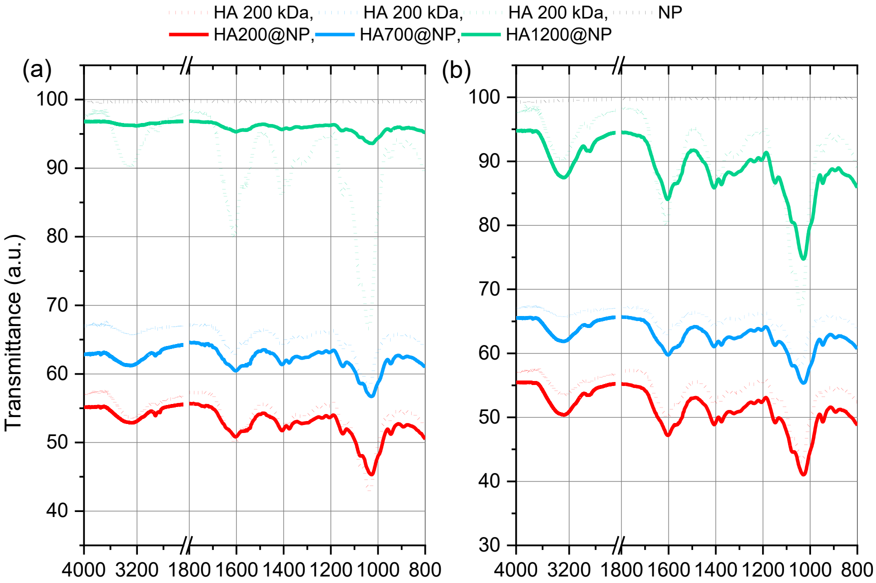

Figure 2.8. *IR/ATR spectra of the HA@NP samples (solid lines) in the comparison with the HA samples (dashed lines) at the three MWs (red: 200 kDa; blue: 700 kDa; green: 1,200 kDa): (a) HA@Ag, (b) HA@Au.*

To note, the –OH stretching found at 3280 cm^{-1} in the three ATR-FTIR spectra of HA 200 kDa, HA 700 kDa and HA 1,200 kDa, exhibited a shift in the spectra of HA@NP samples (Table 2.5). [242] Similarly, the signals of -

C=0 stretching and –NH bending (at about 1600-1500 cm^{-1}) in HA@NP were slightly shifted compared to HA samples, suggesting the occurrence of a interaction between the HA polymer chains and NPs.[243-245]

Table 2.5. *Peak position (cm^{-1}) of the characteristic transmittance spectra of the hyaluronic acid.*

	-OH/-NH stetch.	**-CH$_2$ stretch.**	**-C=0 stretch. –NH bend.**	**-CH$_2$ bend.**	**C-O-C stretch.**
HA200	3279	2890	1603	1399	1033
HA700	3288	2910	1613	1419	1043
HA1200	3307	2882	1612	1413	1033
AgNP	-	-	-	-	-
HA200@Ag	3311	2923	1605	1408	1027
HA700@Ag	3300	2923	1605	1408	1027
HA1200@Ag	3305	2923	1605	1408	1022
AuNP	-	-	-	-	-
HA200@Au	3277	2905	1605	1409	1027
HA700@Au	3279	2905	1605	1406	1029
HA1200@Au	3279	2905	1603	1409	1027

4. Conclusions

In this work, hyaluronic acid-capped gold and silver spherical nanoparticles were synthetized by using a reproducible and green chemical method of metal salt reduction by sodium borohydride (for AgNP) or by glucose (in basic environment, for AuNP), respectively.

The optical characterisation of the plasmonic band revealed significant differences in the HA@NP systems with respect to the bare NPs. A general increase in the nanoparticle size, due to the actual formation of core-shell metal-polymer hybrids was obtained. Moreover, for increasing hyaluronan MWs, a quasi-linear trend was found in hypochromic shifts, red-shifts and peak broadening effects. Such an effect, more evident for HA@Au than for HA@Ag, highlighted a significant manifold role of the hyaluronan polymer, which played an active role during the synthesis as solvent, capping and co-reducing agent.

The characterisation of the hydrodynamic diameter by DLS also pointed to the major effect of the hyaluronan molecular weigtht in influencing the yield, the morphology and the size distribution of the hybrid core-shell polymer-metal nanoparticles. ATR-FTIR confirmed a strong interaction between the hyaluronan chains and the metal core of the nanoparticles, as quantified by the significant shifts measured in the HA-characteristics vibrational bands.

Metal-specific effects were observed in studies of stability upon ageing, with a size evolution of the HA-capped nanoparticles indicative of an Ostwald type growth for HA@Ag and a digestive ripening effect for HA@Au (especially evident for the low MW HA-capped NPs), respectively. These results were very promising for the setup of syhthesis conditions for stable hyaluronan-capped metal nanoparticles of gold or silver with tunable size and controlled thickness of the HA shell around the metallic core, which can be of high interest in theranostic applications.

CHAPTER 3

ANTI-ANGIOGENIC HYBRID ASSEMBLIES OF HYALURONIC ACID AND METAL NANOPARTICLES

MOTIVATION OF THE STUDY

New growth in the vascular network is important since the proliferation, as well as metastatic spread, of cancer cells, depends on an adequate supply of oxygen and nutrients and the removal of waste products.

The angiogenesis process is involved in the cutaneous wound repair because in the wound healing process the nutrients and the defence, indispensable for the newly formed tissues, are transported by the new capillary in the injury. The modulation of this process has a key role to reduce both morbidity and mortality from carcinomas and to control healing of the injury reducing inflammation and the adhesion tissue formation.

The hyaluronic acid plays a key on the angiogenesis process, in fact, different sizes of HA exhibit distinctly different biological functions: high molecular weight (HMW) HA (> 500 kDa) is space-filling, anti-angiogenic and immunosuppressive and low molecular weight (LMW) HA with (< 500 kDa) is pro-angiogenic and immuno-stimulator. Moreover, HA has intrinsic targeting properties, since it exhibits a specific binding to CD-44 receptor, which is overexpressed in some tumour cells.

The association of HMW-HA (such as 700 kDa and 1,200 kDa) and LMW-HA (as the 200 kDa) with AgNP (antibacterial) or AuNP (anti-angiogenic) and/or an anti-angiogenic peptide (e.g., the GHHPHGK sequence) leads to new hybrids systems with tunable anti-angiogenic properties, for application in theranostics and in the wound healing process.

In the first part of this chapter (section 3.1) is reported the investigation on the the anticancer activity of HA@NP hybrid systems on two tumour cell lines, namely neuroblastoma (SH-SY5Y) and prostate (PC-3) cells, which do not express and overexpress the CD44 receptor, respectively. Hyaluronan-wrapped silver or gold nanoparticles were obtained by wet chemical synthesis with HA at the two molecular weights of 200 and 700 kDa; cellular assays of cell viability assays and confocal cell imaging were performed.

In the second part (section 3.2), AgNP and AuNP synthesized either by wet chemical reduction or microplasma methods in the presence of the pro-angiogenic LMW HA (200 kDa, HA200) or its conjugate with the anti-angiogenic GHHPHGK peptide (HA 200kDa, HA200GHHPHGK) were tested for cytotoxicity in endothelial cells (HUVEC line). In parallel, the antimicrobial activity of these systems was examined by microbiological studies on pathogenic bacteria strains of *Escherichia Coli* (ATCC 9637) and *Stafilococcus Aureus (*ATCC 29231), to investigate their antioxidant and antibacterial synergic effects and their possible applications on the wound healing process.

Section 3.1: SILVER AND GOLD NANOPARTICLES DECORATED WITH HYALURONIC ACID FOR TARGETED TUMOUR CELL THERAPY

Abstract

In this work, metallic nanoparticles of silver and gold, bioconjugated with hyaluronic acid at low (200 kDa) or high (700 kDa) molecular weight, were fabricated for cancer cells targeting and therapy. HA is a polymer capable of binding the CD-44 cell surface receptor, often overexpressed on the surface of cancer cells. The HA-conjugated nanoparticles were synthesised in aqueous hyaluronan solution by chemical reduction using borohydride or glucose as main reducing agents for the precursor metal salt of $AgNO_3$ or $HAuCl_4$, respectively. The bioconjugated nanoparticles were scrutinised by UV-visible spectroscopy and dynamic light scattering analyses, to study the plasmonic properties and the hydrodynamic size, respectively. Viability assays and confocal cell imaging were performed on two tumour cell lines, namely neuroblastoma (SH-SY5Y) and prostate (PC-3) cells, which do not express and overexpress the CD44 receptor, respectively. The results pointed to the promising potentialities of the developed nanoplatforms for selective targeting and dose-dependent cytotoxicity in cancer therapy.

1. Introduction

Rapid advances and emerging technologies in nanoscale systems, particularly nanoparticles, are having a profound impact on cancer diagnosis, treatment and monitoring, because of their ability to detect cancer cells, provide chemotherapeutic agents and monitor treatment response[246]. Nanometer-sized drug delivery systems with the ability to cross the biological barriers that they may encounter by moving towards the target tissue or organ[247] allow to increase the specificity of the therapy decreasing the toxicity of the traditional treatments and avoiding adverse effects on non-target tissues.[246] Examples include PEGylated liposomal doxorubicin or albumin-bound Paclitaxel, approved in USA for the treatment of refractory ovarian carcinoma and Kaposi's sarcoma or metastatic breast cancer, respectively.[248]

In recent years, new therapeutic approaches have been developed, based on the use of nanoparticles for theranostic applications, i.e., able to simultaneously carry out diagnosis and therapy by identifying individual tumour cells.[103] Among the various classes of theranostic nanomaterials, metal nanoparticles have been widely exploited for use in many different areas, especially in medicine, since they are prospective candidates for making a new class of anticancer agents[249], with numerous benefits, including improved efficacy, bioavailability and dose–response, targeting ability, personalization of the therapy, and safety, compared to conventional medicines as well as the ability to facilitate controlled drug release.[250] Indeed, metal nanoparticles, in addition to their enhanced absorption and scattering, show good biocompatibility, high stability against oxidative dissolution, easy synthesis[251] and conjugation to a variety of biomolecular ligands, antibodies, and other targeting moieties, making them suitable for use in biochemical sensing and detection, medical diagnostics, and therapeutic applications.[152]

In particular, silver nanoparticles and gold nanoparticles exhibit extensive application in anticancer agents, molecular imaging, and drug carriers. AgNPs and AuNPs have unique optical properties, originating from the excitation of surface plasmon (SP) resonance[252] that can be used in various applications such as sensing, detecting, and imaging.[253] Moreover, silver and gold nanoparticles have intrinsic biological properties that make their use especially promising to obtain multifunctional hybrid nanoplatforms.[103] Accumulated evidence shows that AgNPs can be used as a promising candidate in chemotherapy, photosensitizers and/or radiosensitizers, biodiagnostics, bioimaging, transfection vectors, and antiviral agents; some of these have been entered into clinic trials. Silver nanoparticles have the ability to generate more ionic silver, to increase the production of reactive oxygen species, and to deliver more efficiently ionic silver to small surfaces. Silver has also been used as a vector for anticancer drugs or for locating tumour cells and destroying them by photothermal treatment.[254] The antitumor activity of silver nanoparticles depends on the alteration of the cellular morphology and metabolic activity, the oxidative stress due to damage to the mitochondria and to the production of ROS, resulting in the damage to DNA and subsequent death of the tumour cells.[255] Another mechanism silver nanoparticle-induced anticancer is the process of cellular autophagy.[256] Silver has also been shown to exhibit antiangiogenic effects.[257] *In vitro* experiments with bovine retinal epithelial cells (BREC) and in a matrigel plug assay in vivo, AgNPs of 40 nm in size inhibited the cell proliferation and migration in the vascular endothelial growth factor (VEGF)-induced angiogenesis process. Furthermore, tumour bearing mice injected with AgNPs demonstrated a reduction of ascites production (65%) and tumour progression.[258]

Colloidal gold nanoparticles have unique antiangiogenic properties and have been applied in a variety of cancers for cancer diagnosis, imaging and especially treatment.[152] AuNPs have become an important alternative as imaging agents due to their potential non cytotoxic, facile immunotargeting as well as due to their non susceptibility to photobleaching or chemical/thermal denaturation, a problem commonly associated with dyes.[259] The very first step in the angiogenic cascade involves ligand binding to VEGFRs on endothelial cells that lead to receptor phosphorylation and initiates the signalling events.[260] 'Naked' gold nanoparticles directly bound heparin-binding growth factors (presumably through cysteine residues of the heparin-binding domain) and inhibited growth factor mediated signalling in vitro and VEGF induced angiogenesis *in vivo*.[261]

Surface size but not surface charge was shown to play a large role in the therapeutic effect of AuNPs.[152] When fabricated in certain geometries, the plasmon resonances of AuNP can be tuned to near infrared (NIR) wavelengths, where light penetrates deepest within human tissues due to minimal absorbance by native tissue chromophores. Gold nanoparticles fabricated to have strong absorption cross sections in the NIR wavelength, properly functionalized to recognize receptors present in pathological tissues, can accumulate in diseased tissues and through phototherapy they can absorb light energy converting it into thermal energy, thus destroying diseased cells. NIR-activatable gold nanoparticles have many advantages for clinical applications, such as the inertness of gold noble metal that does not react with biological tissues, the low long-term toxicity, the size tunability to get within size regimens that permit tumour-specific accumulation via the enhanced permeability retention (EPR) effect based on average vascular fenestrations of 60–400 nm in tumours, the surface bioconjugation for tumour-specific targeting [262].

The targeting and biocompatibility of silver and gold nanoparticles can be improved by the bioconjugation with biopolymers such as polysaccharides [263]. Hyaluronic acid, or hyaluronan (HA), is a linear polysaccharide composed of repeating disaccharide unit of D-glucuronic acid and N-acetyl-D-glucosamine, that are linked together through alternating β-1,4 and β-1,3 glycosidic bonds [250, 264]. As a pericellular matrix, it may have effects on ion flux which are important in cellular signalling through membrane ion channels [265]. In inflammation, hyaluronan may also have a moderating effect through free-radical scavenging [266, 267], antioxidant effect [268] as well as through exclusion of tissue degrading enzymes from the immediate cellular environment and from other structural components of the extracellular matrix [266]. The physical properties of HA include its compressive stress, compressive modulus, storage and loss modulus, porosity, swelling rate, degradation rate and density [269]. HA is also known to play a role in promoting cell proliferation, differentiation and migration by binding with cells with specific interactions [270].

These processes indeed are mediated by proteins, known as hyaladherins, that act as cellular receptors for HA.[271] In particular, CD44 is the best characterized transmembrane HA receptor; it is expressed on the surface of several cells such as leucocytes, fibroblasts, keratinocytes and epithelial and endothelial cells and it is also involved in different cellular processes (cell adhesion, migration, proliferation and activation as well as

HA degradation and uptake) [270, 272]. Based on current knowledge, CD44 is considered to be the primary HA receptor on most cell types [270, 273].

Since the discovery that the receptor is over-expressed in a variety of solid tumours, such as pancreatic, breast and lung cancer, many studies have focused on methods for targeting CD44 in an attempt to improve drug delivery and discrimination between healthy and malignant tissue, while reducing residual toxicity [271]. Experimental evidences showed that CD44 is the most effective membrane protein to bind hyaluronic acid, thus HA has been extensively used in developing nanocarriers that demonstrate preferential tumour accumulation and increased cell uptake in cancer cells [271]. One of the earliest evidence for effective delivery by HA modified carriers to tumour cells was demonstrated by Eliaz et al. [274]. Successively, several approaches of nanoparticle formulations have been developed that take advantage of the CD44 -targeting properties of HA, including the chemical conjugation of HA to pre-formed lipid-based nanocarriers, for the active targeting of small or large active molecules for the treatment of cancer [275], and self-assembling nanosystems for targeted siRNA delivery [276].

The interaction between hyaluronic acid and CD44 influences the adhesion to the components of the extracellular matrix and is involved in aggregation, stimulation, proliferation, cell migration and angiogenesis [277]. The link between hyaluronic acid and the CD44 adhesion molecule can initiate a series of events that begin with matrix adherence modifications and continue with the activation of other molecules (such as growth factors), degradation of the matrix itself, angiogenesis, vessel permeation, extravasation [278]. All these steps are necessary in the initiation of the metastatic pathway [279, 280]. It has been demonstrated that, from an oncological point of view, CD44 has a considerable importance in the study of progression and tumour invasiveness. An invasive tumour in fact, to expand, attacks the extracellular matrix of the surrounding tissues and CD44 together with hyaluronic acid certainly play a decisive role in the various cellular pathways [281].

HA plays an important role in certain pathologies, including the cancer. An increase in HA synthesis has indeed been considered in several malignant tumours, such as colon carcinoma and breast cancer [282, 283]. HA promotes the adhesion and migration of tumour cells [284] and forms a protective barrier around them, thus allowing their survival [285]. At the base of this double nature of hyaluronic acid is the difference between the molecular weight of the various residues that are considered: different molecules of HA have different functions [286]. Therefore, it is possible to state that: *i)* the high molecular weight polymer, i.e., MW > 1000 kDa, is found in physiological conditions in the extracellular matrix [287] and it's antiangiogenic and immunosuppressive [288]; *ii)* residues with lower molecular weights are associated with pathological conditions and above all with cancer [289] and can be inducers of inflammation and angiogenesis [288].

A very particular behaviour has been noted for HA oligomers, consisting of a very low number of repetitions of the HA constituent dimer (3-10 repetitions). They are in fact able to inhibit tumour proliferation *in vivo* [290], to induce apoptosis [291] and revert resistance to chemotherapy [292] following the link with CD44 receptor. High molecular weight HA does not seem to be involved in gene expression and only low/intermediate MW HA (20-450 kDa) is known to promote gene expression in macrophages, endothelial cells, eosinophils and certain epithelial cells [293].

In this work, we functionalised silver and gold nanoparticles with low (200 kDa) and high (700 kDA) molecular weight hyaluronan to test their interactions with two human cancer derived cell lines, namely neuroblastoma (SH-SY5Y) and prostate cancer (PC-3) cells.

2. Materials and methods

2.1 Chemicals

Hyaluronic acid at molecular weights (MW) of 200 kDa (hereinafter named HA200) and 700 kDa (hereinafter named HA700) were provided by Fidia Farmaceutici spa (Italy). Silver nitrate ($AgNO_3$) purity ≥ 99%, sodium borohydride ($NaBH_4$) purity ≥ 99.0 %, D-(+)-glucose purity ≥ 99.5%, gold (III) chloride trihydrate ($HAuCl_4$) purity ≥ 99.9 %, and sodium hydroxide (NaOH), were purchased by Sigma-Aldrich. 3-(4,5-dimethylthiazol-2-yl)-2,5-diphenyltetrazolium bromide (MTT reagent), Dulbecco's modified eagle medium (DMEM F-12) high glucose, RPMI-1640 and fetal bovine serum (FBS) were purchased from Sigma-Aldrich (St. Louis, MO). Ultrapure Milli-Q water was used (18.2 mΩ·cm at 25 °C, Millipore).

2.2 Synthesis of bare and HA-conjugated AgNP and AuNP

Bare metal NPs were synthesized by using ultrapure water as solvent, according to eq. 3.1.1 for silver [126] and eq. 3.1.2 for gold, [294] respectively:

$$Ag^+ + [BH_4]^- + 3H_2O \xrightarrow{ice\ bath} Ag^0 + H_3BO_3 + 3.5\ H_2 \qquad (3.1.1)$$

$$2Au^{3+} + 3C_6H_{12}O_6 + 6OH^- \xrightarrow{T=25°C} 3C_6H_{12}O_7 + 3H_2O + 2Au^0 \qquad (3.1.2)$$

As to the synthesis of bare AgNP in MilliQ-H_2O, 15 mL of 2 mM $NaBH_4$ (final concentration 1.71 mM) were placed in the ice bath under constant magnetic stirring and 2.5 mL of 1 mM $AgNO_3$ (final concentration 0.14 mM) were added dropwise. The reaction mixture changes from colourless to yellow after the addition of $AgNO_3$ and remains in an ice bath, under magnetic stirring, for 1 hour and 45 min. The synthesis produces AgNPs with a plasmonic peak centred approximately at 386 nm. The silver nanoparticles were estimated to be 10 to 20 nm in diameter.[125] As to the synthesis of bare AuNP in MilliQ-H_2O, the following aqueous stock solutions were prepared at room temperature: 1.0 mM chloroauric acid (prepared by adding 5 µL of 1 M of $HAuCl_4$ to 995 µL of H_2O-MilliQ), 100 mM sodium hydroxide (160.0 mg, corresponding to 4.0 mmol of NaOH dissolved in 40 mL MilliQ-H_2O), and 100 mM glucose (0.180 g of $C_6H_{12}O_6$ dissolved in 10 mL of MilliQ-H_2O).

Briefly, 0.1 mL of 1 mM $HAuCl_4$ (final concentration 0.5 mM) was diluted in 0.79 mL of MilliQ-H_2O, added with 0.07 mL of 100 mM NaOH (final concentration 7 mM) for basic condition and 0.05 mL of 100 mM glucose (final concentration 5 mM) as a reducing agent. The synthesis produces a particles with a plasmonic peak centred at 540-560 nm, according to literature reference. [294] As to the synthesis of HA-conjugated NPs, firstly the hyaluronic acid was dissolved in MilliQ-H_2O: 10 mg of HA200 or HA700 were weighed and solubilised in 2.5 mL of MilliQ-H_2O, under constant magnetic stirring for 2 h, to obtain the 0.4% (w/v) stock solution.

For the synthesis of HA-conjugated AgNP, HA200 (or HA700) stock solution 0.4 % (w/v) was placed in a beaker in ice bath on a stir plate (final concentration in the mixture reaction of 0.2 w/v) and $AgNO_3$ (2.5 mL, 1.66 mM) was added under vigorous stirring, at the final silver salt concentration of 0.79 mM. After 5 min, a 250 µL volume of 200 mM $NaBH_4$ were added dropwise and the solution (final concentration = 9.5 mM). As soon as the colour changed from colourless to yellowish brown, the beaker was placed immediately out of the ice. Typically, hyaluronan-capped silver nanoparticles with a plasmonic peak approximately at 395 nm were obtained, according to literature data.[295]

For the synthesis of HA-conjugated AuNP, the HA200 (or HA700) stock solution 0.4 % (w/v) (final concentration in the mixture reaction of 0.2 w/v), was placed in Eppendorf ThermoMixer at controlled temperature of 25°C. Briefly, 0.1 mL of $HAuCl_4$ 1 mM (final concentration = 0.5 mM) was added to 0.79 mL of HA 200 (or HA 700). Finally, to obtained solution were added 0.07 mL of 100 mM NaOH (final concentration = 7 mM) for basic condition and 0.05 mL of 100 mM glucose (final concentration = 5 mM) as a reducing agent. The AuNPs were formed immediately.[294]

2.3 UV–visible (UV-vis) spectroscopy and dynamic light scattering (DLS) analysis

UV-vis spectroscopy was performed on the aqueous dispersions of AuNPs e AgNPs, in quartz cuvettes with 0.5 and 0.1 cm optical path length on a Perkin Elmer UV-vis spectrometer (Lambda 2S). The dynamic light scattering (Horiba LB-550) is used to characterize the surface charge and the size distribution of the nanoparticles and the results were presented as the mean of at least three measurements.

2.4 Cell cultures and maintenance

Human neuroblastoma SH-SY5Y and prostate cancer cells (PC3) cell lines were cultured in 25 cm2 plastic flasks in DMEM F-12 and RPMI-1640, respectively. Both mediums were supplemented with 10% v/v foetal bovine serum (FBS), and contained 2 mM L-glutamine, 50 IU/mL penicillin and 50 µg/mL streptomycin. Cells were grown in tissue-culture treated Corning® flasks (Sigma-Aldrich, St. Louis, MO) in an incubator (Heraeus Hera Cell 150C incubator), under a humidified atmosphere at 37°C in 5% CO_2. For the cellular treatments, the day before the experiment cells were seeded in full medium on TPP® tissue culture plates (Sigma-Aldrich, St. Louis, MO). The HA-conjugated silver and gold nanoparticle samples were concentrated 5 times up to the final HA concentration of 1% w/v (‘pellet 3’) or, in the case of the bare AgNP and AuNP reference samples, up to the maximum washing by centrifugation steps to avoid aggregation (typically ‘pellet 2’ samples), and added to the cells in culture medium at the desired final concentration for incubation times of 90 min (confocal microscopy experiments) or 24 h (cell viability assays), respectively.

2.5 Cell viability assay

For MTT assay, cells were seeded at a density respectively of 12,000 cells/well and and10,000 cells/well respectively for SH-SY5Y and PC3 and maintained in their respective complete media in standard culture condition. The day after cells were washed with 1 % FBS-supplemented medium and treated with samples (HA-conjugated NPs and bare NPs) with a 10X dilution of pellet samples. After 24 h of incubation, cells were washed with buffer and treated with 5 mg/mL of 3-(4,5-Dimethyl-2-thiazolyl)-2,5-diphenyl-2H-tetrazolium Bromide (Applichem) at 37 °C for 90 minutes. At this stage, the formazan salts formed by succinate dehydrogenase activity in live cells, were solubilized with DMSO and quantified spectrophotometrically by a Synergy 2 microplate readers (BioTek), by the absorbance value at 570 nm of wavelength. All conditions were measured in triplicate and results were expressed as % of viable cells over the negative control (i.e., untreated cells).

2.6 Confocal microscopy analysis

For LSM live cell imaging analysis, cells were seeded at a density of 25.000 cells/well in 12 mm glass bottom dishes (Willco Wells, Amsterdam). The day after cells were washed with 1 % FBS-supplemented medium, and treated with HA-conjugated NP and bare NP samples for 90 min. During the last 20 min of the total treatment period, the cells were stained with LysoTracker Red (150 nM), a red-fluorescent dye for labelling and tracking acidic lysosome organelles in live cells and Hoechst (1 µg/mL) for fixed and live cell fluorescent staining of DNA and nuclei in cellular imaging technique. Cells were rinsed with fresh PBS and cellular fixation was performed with high purity paraformaldehyde (4% w/v) in PBS. For the straining of cytoskeleton actin, cells were permeabilized with 0.02% w/v Triton X-100 with 10% bovine serum albumin (BSA) and treated with a high-affinity F-actin probe, conjugated to green-fluorescent Alexa Fluor® 488 dye (ActinGreen™ 488 ReadyProbes® Reagent, TermoFisher). LSM imaging was performed with an Olympus FV1000 confocal laser scanning microscope (Olympus, Shinjuku, Japan), equipped with diode UV (405 nm, 50 mW), multiline Argon (457, 488, 515 nm, total 30 mW), HeNe(G) (543 nm, 1 mW) and HeNe(R) (633 nm, 1 mW) lasers. An oil immersion objective (60xO PLAPO) and spectral filtering systems were used. The detector gain was fixed at a constant value and images were collected, in sequential mode randomly all through the area of the well. The image analysis was carried out using Huygens Essential software (by Scientific Volume Imaging B.V., The Netherlands). The statistical analysis was performed with ImageJ software and one-way ANOVA test.

3. Results and discussions

The bioconjugate nanoparticles, in the comparison with the bare NP, were analysed by UV-Visible spectroscopy (UV-vis) and dynamic light scattering (DLS), respectively.

Figure 1 shows a strong resonance at approximately 394 nm and 531, respectively, for Ag (Fig. 3.1.1a) and Au (Fig. 3.1.1d) nanoparticles in the water solution, due to the excitation of surface plasmon vibrations [296]. The surface plasmon resonance bands are almost unchanged for AgNP-HA hybrids, whereas a red-shift is observed for AuNP-HA samples.

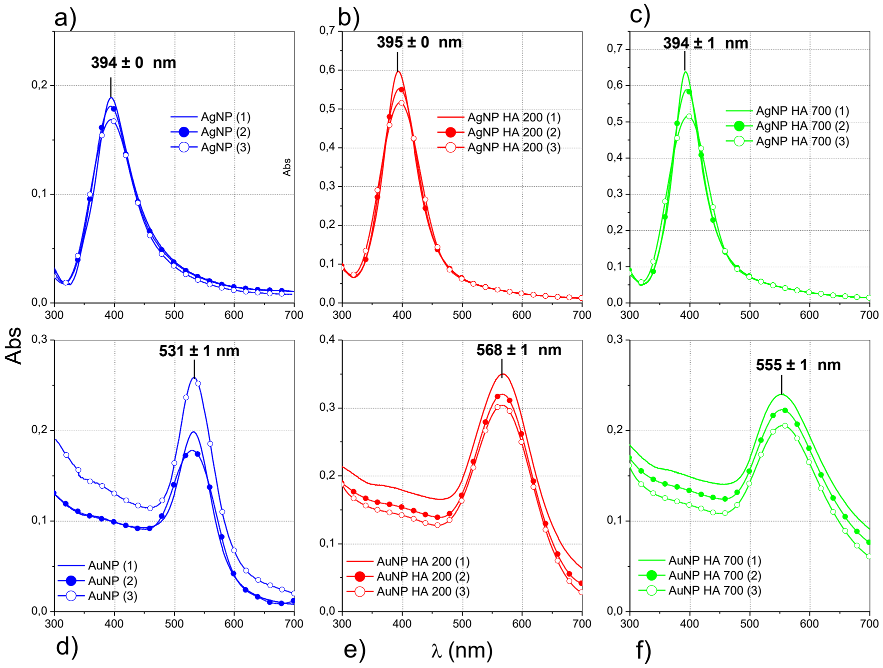

Figure 3.1.1. *UV-vis spectra of AgNP (a-c) and AuNP (d-f) systems for as prepared ('fresh') samples of bare (a,d), HA200-conjugated (b,e) and HA700-conjugated (c,f) nanoparticles. Each panel displays the spectra from three repeated syntheses.*

In particular, the plasmon shift approximately at 568 nm for AuNP-HA200 and 555 nm for AuNP-HA700, respectively. This shift can be explained by the interaction between the hyaluronan chains and the particles, which influences the surface plasmon resonance band for gold more than silver. The spectral parameters of the plasmon band, in terms of the full width at half maximum (FWHM), wavelength (λ_{max}) and absorbance (A_{max}) at the maximum for repeated syntheses (Table 3.1.1) highlight a good level of reproducibility and, in general, the formation of monodisperse colloidal suspension, as evidenced by FWHM values according to literature data. [219]

Table 3.1.1. *Optical parameters (full width at half maximum, wavelength and absorbance at the maximum) from the UV-vis spectra of AgNP and AuNP, bare and HA-conjugated samples. Averaged and standard deviation values from three repeated syntheses of each sample*

Sample	**FWHM (nm) ± S.D. (nm)**	**$\lambda_{average}$ ± S.D. (nm)**	**$Abs_{average}$ ± S.D. (nm)**
AgNP	75 ± 4	394 ± 0	0.19 ± 0.01
AgNP-HA200	66 ± 7	395 ± 1	0.56 ± 0.04
AgNP-HA700	61 ± 8	394 ± 1	0.58 ± 0.06
AuNP	61 ± 4	531 ± 1	0.21 ± 0.04
AuNP-HA200	88 ± 5	568 ± 1	0.324 ± 0.02
AuNP-HA700	95 ± 3	555 ± 1	0.22 ± 0.02

The as prepared dispersions were further purified by centrifugation and washing, both to remove the excess of unreacted reducing agent (typically the metal salt to reducing agent mole ratio is respectively of 1:12 for AgNP and 1:10 for AuNP, see Materials and Methods section) and to concentrate the nanoparticle systems.

Noteworthy, the UV-vis spectra of recovered pellets for Ag and Au nanoparticle solutions (Figure 3.1.2) show small shifts in the plasmon wavelength at maximum absorbance in comparison to the as prepared solutions. On the other hand, the freshly prepared pellets of AgNP-HA exhibit a red shift (about 5 nm for both AgNP-HA200 and AgNP-HA700, t=0), while the opposite trend is found in the case of hyaluronan-capped gold nanoparticles, with a blue shift of about 8 nm for AuNP-HA200 and ~6 nm for AuNP-HA700, respectively. These effects can be explained in terms of different effects of the HA on the nanoparticle size evolution, namely a digestive ripening effect for gold [297], by which the size of the NPs decreases prompted by the interaction with the hyaluronan chains, and an Ostwald type growth for silver [238], likely due to a lower level of interactions between the polysaccharide chains and the metal atoms.

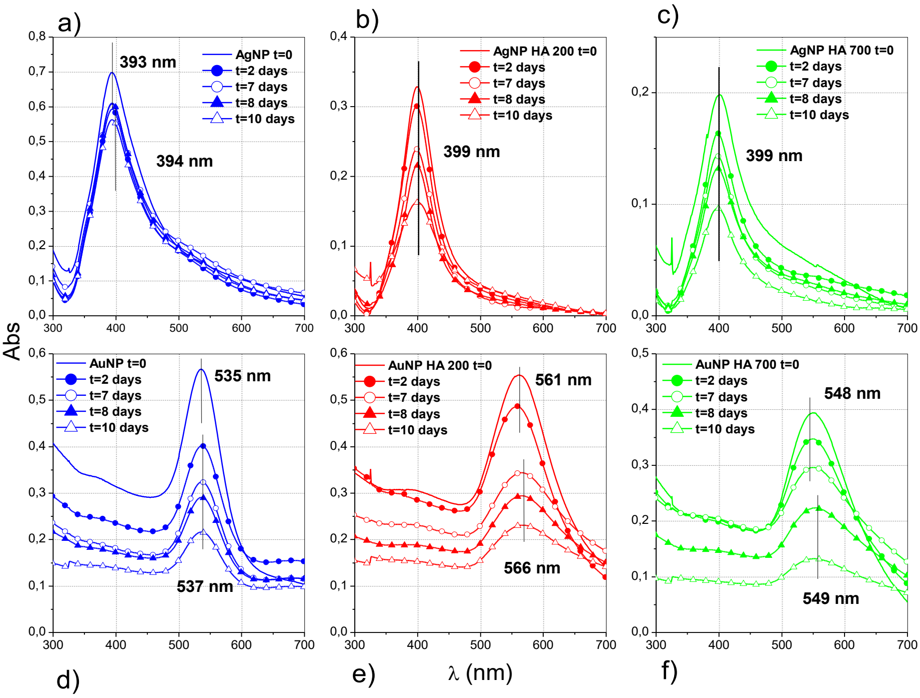

Figure 3.1.2. *UV-vis spectra of AgNP (a-c) and AuNP (d-f) systems for the pellets '2' (a,d: bare NPs) or pellets '3' (b,e: HA200-conjugated NPs; c,f: HA700-conjugated NPs) resuspended in ultrapure MilliQ water after the centrifugation and rinsing steps. Each panel displays the spectra recorded at increasing ageing times since the pellet resuspension up to 10 days.*

The UV-vis spectra of resuspended pellets for Ag and Au nanoparticle solutions, as well as those of the corresponding HA-conjugated samples, remain almost unchanged over two weeks when stored at 4 °C in the darkness, indicating the nanoparticle size distribution in water is rather stable. As to AuNP-HA, especially for the 200 kDa hyaluronan-conjugated samples, a general red-shift, together with a peak broadening and a decrease in absorbance values is observed (Figure 3.1.2 and Table 3.1.2).

Table 3.1.2. *Optical parameters (full width at half maximum, wavelength and absorbance at the maximum) measured from the UV-vis spectra of AgNP and AuNP, bare and HA-conjugated samples for the pellets '2' (bare NPs) or pellets '3' (HA-conjugated NP) immediately after the resuspension in ultrapure MilliQ water (t=0) and at increasing ageing times (up to t=10 days). The difference with respect to the freshly prepared pellets (t=0) for FWHM and* λ*, as well as the relative percentage variation in Abs are reported for comparison.*

Sample	FWHM (ΔFWHM), nm	λ_{max} ($\Delta\lambda_{max}$), nm	Abs$_{max}$ (-ΔAbs$_{rel}$, %), nm
AgNP (t = 0)	**55 (0)**	**393 (0)**	**0.698 (0)**
AgNP (t = 2 days)	60 (5)	393 (0)	0.593 (15%)
AgNP (t = 7 days)	60 (5)	394 (1)	0.608 (13%)
AgNP (t = 8 days)	60 (5)	394 (1)	0.615 (12%)
AgNP (t = 10 days)	**60 (5)**	**394 (1)**	**0.563 (19%)**
AgNP-HA200 (t = 0)	**62 (0)**	**399 (0)**	**0.330 (0)**
AgNP-HA200 (t = 2 days)	61 (-1)	399 (0)	0.300 (9%)
AgNP-HA200 (t = 7 days)	61 (-1)	399 (0)	0.238 (28%)
AgNP-HA200 (t = 8 days)	54 (-8)	399 (0)	0.216 (34 %)
AgNP-HA200 (t = 10 days)	**62 (0)**	**399 (0)**	**0.163 (50%)**
AgNP-HA700 (t = 0)	72 (0	**399 (0)**	**0.196 (0)**
AgNP-HA700 (t = 2 days)	71 (-1)	399 (0)	0.163 (17%)
AgNP-HA700 (t = 7 days)	71 (-1)	399 (0)	0.143 (27%)
AgNP-HA700 (t = 8 days)	71 (-1)	399 (0)	0.132 (33%)
AgNP-HA700 (t = 10 days)	**71 (-1)**	**398 (-**1)	**0.097 (50%)**
AuNP (t = 0)	**57 (0)**	**535 (0)**	**0.567 (0)**
AuNP (t = 2 days)	59 (2)	537 (2)	0.402 (50%)
AuNP (t = 7 days)	58 (1)	537 (2)	0.324 (29%)
AuNP (t = 8 days)	57 (0)	537 (2)	0.291 (49%)
AuNP (t = 10 days)	**59 (2)**	**537 (2)**	**0.216 (62%)**

AuNP-HA200 (t = 0)	**82 (0)**	**561 (0)**	**0.554 (0)**
AuNP-HA200 (t = 2 days)	81 (-1)	560 (-1)	0.486 (12)
AuNP-HA200 (t = 7 days)	94 (12)	566 (5)	0.345 (38)
AuNP-HA200 (t = 8 days)	92 (10)	566 (5)	0.294 (47)
AuNP-HA200 (t = 10 days)	**107 (25)**	**566 (5)**	**0.231 (58)**
AuNP-HA700 (t = 0)	**84 (0)**	**548 (0)**	**0.394 (0)**
AuNP-HA700 (t = 2 days)	86 (2)	549 (1)	0.347 (12%)
AuNP-HA700 (t = 7 days)	87 (3)	548 (0)	0.296 (25%)
AuNP-HA700 (t = 8 days)	93 (9)	549 (1)	0.223 (43%)
AuNP-HA700 (t = 10 days)	**93 (9)**	**549** (1)	**0.132 (66%)**

Therefore, Ag nanoparticles are stabilized by the bound HA chains and show no sign of aggregation[298], while Au nanoparticles are less stable during ageing, as especially evidenced by the decrease in the absorption band at longer aging times. [299]

The experimental parameters displayed in Table 3.1.2 have been used to calculate the nanoparticle optical diameter (*d*, in nm) according to eq.s 3.1.3-3.1.4 for AgNP, where *a* and *b* are two constants:[215]

$$d = \left(1 - \frac{\lambda max}{a}\right)^{-1/b}$$ (8 nm <d <20 nm; a = 405, b =1.5) (3.1.3)

$$d = \left(\frac{\lambda max - a}{b}\right)^{-0.5}$$ (20 nm < d < 100 nm; a = 394, b =$9.58 \cdot 10^{-3}$) (3.1.4)

Similarly, eq. 3.1.5 was used for AuNP [216]:

$$d = \frac{\lambda\, max - 515.04}{0.3647} \qquad (3.1.5)$$

The optical nanoparticle diameter calculated as described above was used to determine the molar extinction coefficient at the wavelength of maximum absorbance of the plasmon band (ε_λ, in $M^{-1} \cdot cm^{-1}$).

For AgNP, one can use eq.s 3.1.6 and 3.1.7:[215]

$$\varepsilon = \varepsilon_0 + A^{Rd} \qquad (3.1.6)$$

where 8 nm <d <20 nm; $\boldsymbol{\varepsilon_0}$ = $1.23 \cdot 10^9$, A = $6.984 \cdot 10^8$ and R = 0.104;

$$\varepsilon = a + kd^{Rd} \qquad (3.1.7)$$

where 30 nm < *d* < 100 nm; a= $4.079\cdot10^{10}$, k=$2.017\cdot10^{9}$.

For AuNP, the corresponding expression is given in eq. 3.1.8 :[217]

$$\varepsilon_{gold} = Ad^{\gamma} \qquad (3.1.8)$$

where d ≤ 85 nm: *A*= $4.7\cdot10^{4}$; d > 85 nm: A=$1.6\cdot10^{8}$. concentration of the NP suspensions was calculated by assuming a spherical shape of the nanoparticle and a uniform face centred cubic (fcc) structure of the nanoclusters, with the length parameter of unit cell being respectively L=0.407 nm for AgNP and L=0.408 nm for AuNP [229], the corresponding unit cell volume (V_{cell} = L^3) values can be calculated as 0.0674 nm^3 for Ag and 0.0679 nm^3 for Au, respectively.

The optical diameter *d*, the molar extinction coefficient *ε* and the nanoparticle concentration values calculated by using the above described eqs. for the pellets of Ag and Au nanoparticles are listed in Table 3.1.3.

***Table** 3.1.3. Nanoparticle size, molar extinction coefficient and concentrations for AgNP and AuNP, at increasing ageing times (up to t=10 days) since the concentrated pellet preparation.*

Sample	d (nm)	ε (10^{8} $mol^{-1}\cdot L\cdot cm^{-1}$)	*c* (10^{-9} $mol\cdot L^{-1}$)	NP/mL [(a)]
AgNP (t = 0)	10	6.48	10.8	$2.09\cdot10^{8}$
AgNP (t = 2 days)	10	6.48	9.2	$1.77\cdot10^{8}$
AgNP (t = 7 days)	10	7.87	7.7	$1.13\cdot10^{8}$
AgNP (t = 8 days)	11	7.87	7.8	$1.13\cdot10^{8}$
AgNP (t = 10 days)	11	7.87	7.2	$1.04\cdot10^{8}$
AgNP-HA200 (t = 0)	17	24.9	13.2	$5.22\cdot10^{7}$
AgNP-HA200 (t = 2 days)	17	24.9	12.0	$4.75\cdot10^{7}$
AgNP-HA200 (t = 7 days)	17	24.9	9.6	$3.78\cdot10^{7}$
AgNP-HA200 (t = 8 days)	17	24.9	8.6	$3.41\cdot10^{7}$
AgNP-HA200 (t = 10 days)	17	24.9	6.5	$2.57\cdot10^{7}$
AgNP-HA700 (t = 0)	17	24.9	7.9	$3.11\cdot10^{7}$
AgNP-HA700 (t = 2 days)	17	24.9	6.6	$2.59\cdot10^{7}$
AgNP-HA700 (t = 7 days)	17	24.9	5.7	$2.26\cdot10^{7}$
AgNP-HA700 (t = 8 days)	17	24.9	5.3	$2.09\cdot10^{7}$
AgNP-HA700 (t = 10 days)	15	18.9	5.1	$2.94\cdot10^{7}$

AuNP (t = 0)	55	265	0.22	$2.64\cdot10^{4}$
AuNP (t = 2 days)	60	35.1	0.12	$1.03\cdot10^{4}$
AuNP (t = 7 days)	60	35.1	0.09	$8.27\cdot10^{3}$
AuNP (t = 8 days)	60	35.1	0.08	$7.42\cdot10^{3}$
AuNP (t = 10 days)	60	35.1	0.06	$5.52\cdot10^{3}$
AuNP-HA200 (t = 0)	126	1960	0.03	$2.76\cdot10^{2}$
AuNP-HA200 (t = 2 days)	126	1900	0.03	$2.68\cdot10^{2}$
AuNP-HA200 (t = 7 days)	140	2280	0.02	$1.08\cdot10^{2}$
AuNP-HA200 (t = 8 days)	140	2280	0.01	$9.25\cdot10^{1}$
AuNP-HA200 (t = 10 days)	140	2280	0.01	$7.25\cdot10^{1}$
AuNP-HA700 (t = 0)	90	1200	0.03	$8.67\cdot10^{2}$
AuNP-HA700 (t = 2 days)	93	1250	0.03	$6.70\cdot10^{2}$
AuNP-HA700 (t = 7 days)	90	1200	0.02	$6.52\cdot10^{2}$
AuNP-HA700 (t = 8 days)	93	1250	0.02	$4.30\cdot10^{2}$
AuNP-HA700 (t = 10 days)	93	1250	0.01	$2.55\cdot10^{2}$

[a] Since the volume of a NP, V_{NP}, is given by $V_{NP} = \frac{4}{3}\,\pi\left(\frac{d}{2}\right)^{3}$, the mole number of metal atoms for nanoparticle, n_{NP}, is given by $n_{NP} = 4\cdot\frac{V}{V_{cell}\cdot NA}$, where N_A is the Avogadro's constant ($6.02\cdot10^{23}$ atoms/mol) and 4 is the number of Ag or Au atoms that contains one-unit cell. The nanoparticle concentration (in NP/mL) is therefore obtained by using the molar concentration c and n_{NP}: *NP/mL*= $\frac{c}{n_{NP}}$

The nanoparticle diameter measured by DLS for as prepared AgNP and AuNP solutions is shown in Figure 3.1.3. Such a hydrodynamic size includes both the nanoparticle "core" size and the solvation shell around the metal core, and confirm the trend observed in the optical diameter determined by UV-vis, which depends on the plasmonic properties of the metal core and is affected by the dielectric medium where the NP is dispersed. In particular, for AgNP, the hydrodynamic diameter is 34(± 4) nm for bare nanoparticles and does not change much for hyaluronan-capped nanoparticles, being of 35(± 3) nm for HA200-conjugated and 44 (± 5) nm for HA700-conjugated nanoparticles, respectively. As to AuNP, the hydrodynamic diameter is 48 (±6) nm for bare nanoparticles, while the particle size roughly doubles by increasing up to 108 (± 17) nm for AuNP-HA200 and to 127(± 23) nm for AuNP-HA700, respectively.

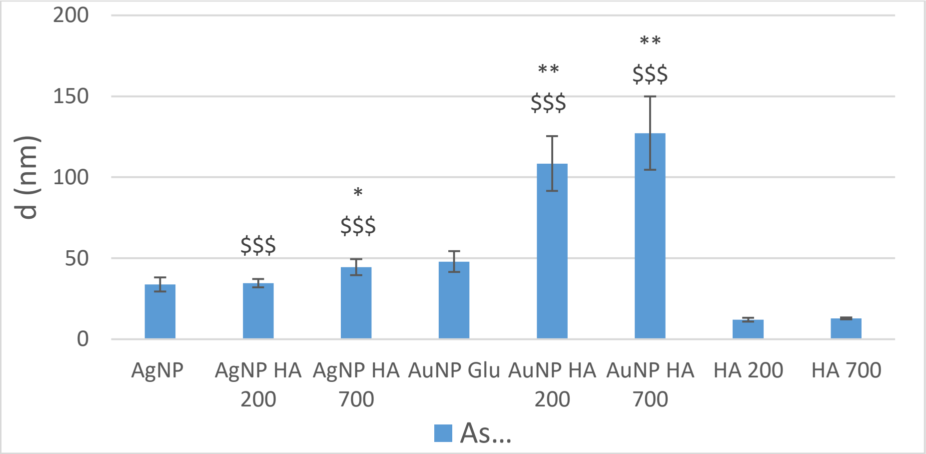

Figure 3.1.3. *Hydrodynamic size of the bare NPs (AgNP, AuNP) and the functionalized nanoparticles with HA (AgNP-HA200, AgNP-HA700, AuNP-HA200 and AuNP-HA700) measured by dynamic light scattering. (*) = p < 0.05 vs. bare AgNP or AuNP; (**) = p < 0.01 vs. bare AgNP or AuNP; ($$$) = p < 0.001 vs. the control HA 200 or HA 700 (one-way ANOVA).*

Figure 3.1.4 shows the hydrodynamic size for the pellets, which is, as expected, larger than the that measured for the as prepared dispersions, due to a partial aggregation of the nanoparticles upon the centrifugations and the rinsing. In addition, the hyaluronan-capped nanoparticles exhibit, in general, a larger size increase than the bare nanoparticles in the comparison to the same solutions before the centrifugation, Again, the size increase observed for Au-HA samples is higher than that found in Ag-HA samples. Specifically, in the case of AgNP, the hydrodynamic diameter is 79±14 nm for bare nanoparticles, while it is roughly two-times higher for hyaluronan-capped nanoparticles, with the measured values of 139±4 nm for AgNP-HA200 and 120±14 nm for AgNP-HA700, respectively. As to AuNP, the hydrodynamic diameter of 77± 4 nm for bare nanoparticles, while the particle size increases up to more than three times for AuNP-HA200 (i.e., 249 ± 15 nm) and four times for AuNP-HA700 (i.e., 322 ± 17 nm), respectively.

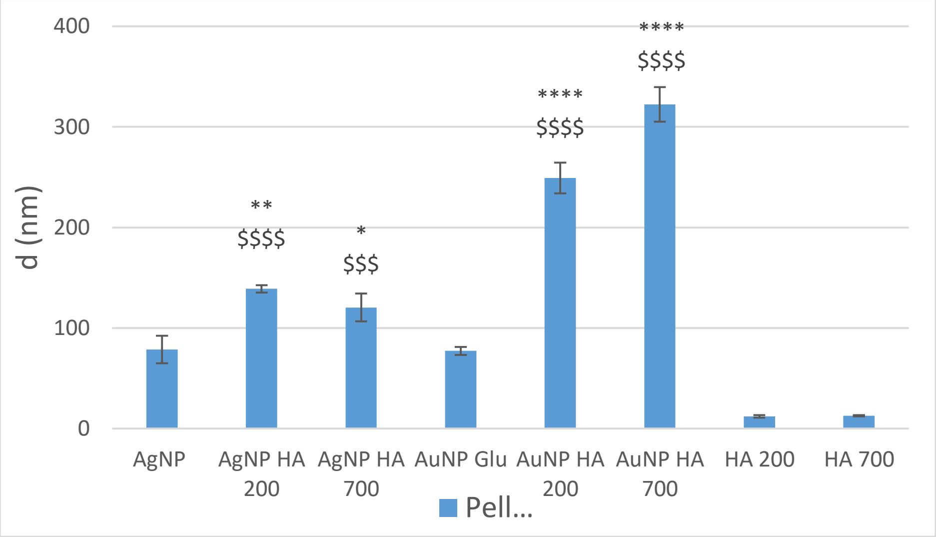

Figure 3.1.4. *Hydrodynamic size of the 'pellet 2' for NPs (AuNP, AgNP) and 'pellet 3' for NP-HA conjugated (AgNP-HA200, AgNP-HA700, AuNP-HA200 and AuNP-HA700) measured by dynamic light scattering. (**) = $p < 0.05$ *vs. bare AgNP or AuNP; (**) =* $p < 0.01$ *vs. bare AuNP or AgNP; ($$$) =* $p < 0.001$ *vs. the control HA 200 or HA 700 and ($$$$) =* $p < 0.0001$ *vs. the control HA 200 or HA 700 (one-way ANOVA).*

Firstly, the response of the different human tumour cell lines investigated, i.e., neuroblastoma (SH-SY5Y) and prostate (PC-3), to the hybrid NP-HA systems was investigated in terms of toxicity. Indeed, the toxic effect of nanoparticles is highly dependent on the organs, and more specifically, on the type of cell encountered. This is due to the variation in cell physiology, proliferation state (tumoral or resting cells), membrane characteristics and phagocyte characteristics among different cell types. In particular, cancer cells are generally more resistant towards nanoparticle-induced toxicity than normal cells, due to an increased rate of proliferation and metabolic activity.[300]

Cell viability experiments were carried out to evaluate the cellular response to the bare NPs and NP-HA conjugated systems. Specifically, the MTT assay was performed by incubating the cells for 24 hours at 37°C in a 5% CO_2 humidified atmosphere with the various samples (i.e., 'pellet 2' for AgNP and AuNP, 'pellet 3' for AgNP-HA200, AgNP-HA700, AuNP-HA200 and AuNP-HA700), diluted 10 times in the corresponding low-serum culture medium (see Materials and Methods). The final concentrations of the cell treatments are reported in Table 3.1.5.

Table 3.1.5. Concentration of 'pellet 2' for NP and 'pellet 3' for NP-HA conjugated used for MTT experiment in SH-SY5Y and PC-3 cell lines.

Sample	**[10^{-12} M]**	**NP/mL**
AgNP	720	$1.0 \cdot 10^{7}$
AgNP-HA200	650	$2.6 \cdot 10^{6}$
AgNP-HA700	510	$2.9 \cdot 10^{6}$
AuNP	6.2	$5.5 \cdot 10^{2}$
AuNP-HA200	1.0	$0.8 \cdot 10^{1}$
AuNP-HA700	1.1	$2.5 \cdot 10^{1}$

As expected, the hyaluronic acid samples for both MWs tested, do not show any cytotoxic effect (in terms of IC50) nor a statistically significant decrease in cell viability, in the two cell lines tested (Figures 3.1.8-3.1.9). In fact, hyaluronan is a primary component of the extra-cellular matrix of the mammalian connective tissues, and is naturally produced by the organism with the function of hydrating and protecting the tissues, therefore is not cytotoxic and has an excellent biocompatibility [301].

Figure 5 shows representative confocal microscopy micrographs (in blue, nuclear staining with Hoechst, in green the cytoskeleton actin staining with Actin Green, in red lysosomal staining with Lysotracker Red) for the different cell lines after 90 min of incubation with hyaluronic acid (0.1% w/v) at low molecular weight (Fig. 3.1.5b, HA200) or high molecular weight (Fig. 3.1.5c, HA700); the LSM micrographs of the negative controls of untreated cells (Fig. 3.1.5a, CTRL) are shown for reference.

A cell-specific response to the treatments with the hyaluronic acid was found. In particular, in neuroblastoma cells, where the interaction with the hyaluronic acid is not expected to be receptor-dependent, the uptake of the hyaluronan, for both the molecular weight used, is diffuse in the whole cytoplasm, as evidenced by the disappearance of the nuclear staining after the SH-SY5Y treatment with either HA 200 kDa or HA 700 kDa. In fact, it is likely that, upon a huge cellular internalisation of hyaluronic acid, the viscoelastic properties of the hydrogel can induce a ‘wrapping’ effect of the intracellular organelles, thus making less effective the dye staining. On the contrary, for prostate cells, which are expected to interact with HA through the CD-44 receptor, which is overexpressed in this cell line [302], a preferential localisation of the hyaluronan at the cell membrane is evidenced by the actin cytoskeleton staining as well as by the upholding of the intracellular organelle staining. Moreover, the specific interaction of the hyaluronan with the cell membrane is also supported by the different actin features displayed by PC-3 cells treated with the HA at the two different molecular weights.

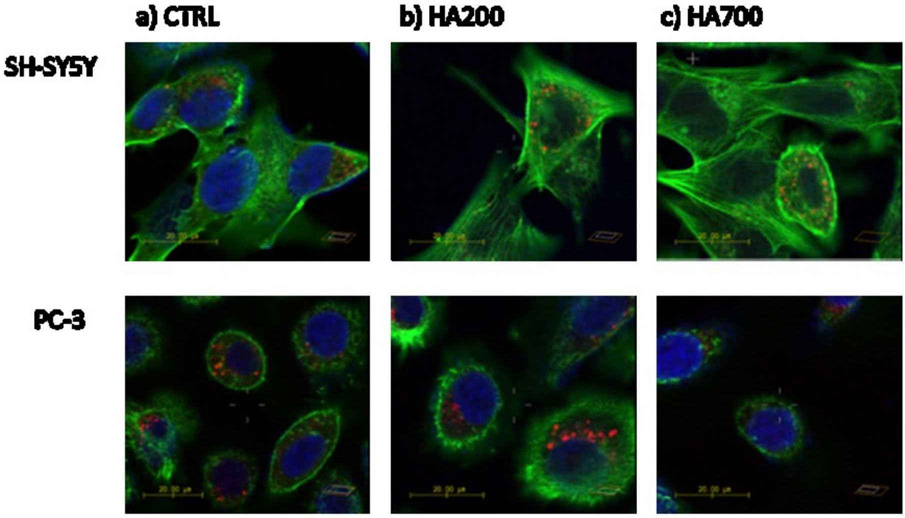

Figure 3.1.5. *LSM fluorescent micrographs of neuroblastoma (SH-SY5Y) and prostate (PC-3) tumour cells: in blue, the nuclear staining with Hoechst ($\lambda_{ex/em}$ = 405/425–450 nm); in green, the cytoskeleton actin staining with Actin Green ($\lambda_{ex/em}$ = 488/500–530 nm); in red, the lysosomal staining with Lysotracker Red ($\lambda_{ex/em}$ = 543/550–600 nm). Cellular treatments were carried out for 90 min with:* ***b)*** *HA 200 kDa (0.1 % w/v) and* ***c)*** *HA 700 kDa (0.1 % w/v); the negative control of untreated cells are shown in* ***a)****. Scale bar = 20 µm.*

In contrast to the cell treatments with the positive control of hyaluronic acid HA200 and Ha700 samples, cell specific responses were observed after the treatment with the other positive controls of bare NPs as well as with the hybrid NP-HA samples, as discussed in the following.

As to neuroblastoma, Figure 3.1.6 shows that the bare silver and gold nanoparticles induce a similar decrease in cell viability (about 40% less viable cells than the negative control, i.e., untreated cells, p<0.01 vs. CTRL, One-way Anova). The cell treatment with the bioconjugated AgNPs and AuNPs induces a higher toxicity in comparison with the bare NPs. It to note that both silver and gold nanoparticles after the functionalisation with either HA 200 kDa or 700 kDa induce a comparable decrease in cell viability (about 60% less viable cells than untreated cells, p<0.001 vs. CTRL, One-way Anova).

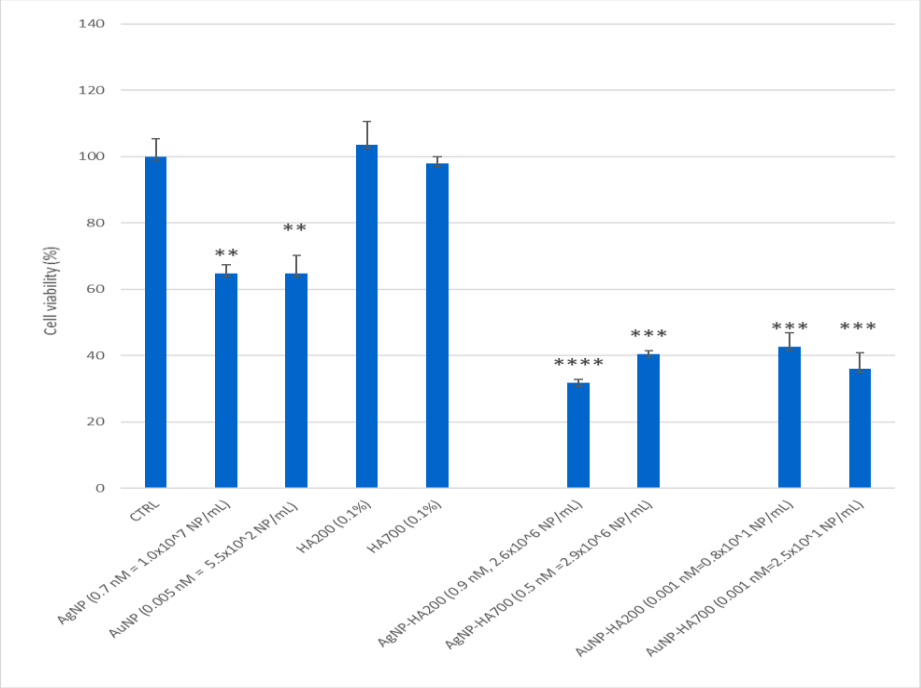

Figure 3.1.6: *Viability of neuroblastoma (SH-SY5Y) cell line after 24 h of treatment with AgNP 0.72 nM, 1.0·10*^{7} *NP/mL and AuNP 0.005 nM, 5.5·10*^{2} *NP/mL (10x 'pellet 2'), HA (200 kDa or 700 kDa, 10x 1% w/v), NP-HA conjugated (10x 'pellet 3'). (*) = p < 0.05, (****) = p < 0.0001 vs CTRL (one-way ANOVA).*

On the contrary, for prostate cells, which are expected to interact with HA through the CD-44 receptor, which is overexpressed in this cell line [302], a preferential localisation of the hyaluronan at the cell membrane is evidenced by the actin cytoskeleton staining as well as by the upholding of the intracellular organelle staining. Moreover, the specific interaction of the hyaluronan with the cell membrane is also supported by the different actin features displayed by PC-3 cells treated with the HA at the two different molecular weights.

The surface functionalization of NPs with HA, due to the presence of –COOH functional groups, increases the negative charge of NPs and, according to literature data, enhance their uptake.[303] Indeed polysaccharide conjugated NPs tend to be individually distributed and thus have freedom of access within the cell and a larger surface area available for interaction with cellular constituents. [304]

The confocal micrographs of SH-SY5Y cells stained at the nuclei (in blue), the cytoskeleton actin (in green) and the lysosomes (in red) after the treatments with bare silver and gold NPs and the corresponding HA200- and HA700-conjugated samples are shown in Figure 3.1.7.

It is evident that the bioconjugated AgNPs induce less lysosomal perturbation than the bare AgNPs, as displayed by the Lysotracker red emission, which is very high for the AgNP-treated cells in comparison to the untreated cells (see Fig. 3.1.5a). Moreover, in contrast to what found for the neuroblastoma cells treated with the HA200 and HA700 controls (see Fig. 3.1.5b-c) the nuclear staining is clearly visible in the cells treated with AgNP-HA200 (Fig. 3.1.7b) and AgNP-HA700 (Fig. 3.1.7c). This finding can be explained by: *(i)* the decreased viscoelastic character of the hybrid AgNP-HA systems than the control HA ones; and/or *(ii)* a less effective internalisation of HA conjugated to the silver nanoparticles, whose collapsed ensembles around the cell membrane are well visible as black aggregates in the optical bright field images (see white arrows in the Figure 3.1.5). As to the neuroblastoma cells treated with the bioconjugated AuNPs, no significant differences with respect to the treatment with bare AuNPs were detected (Fig. 3.1. 7d-f).

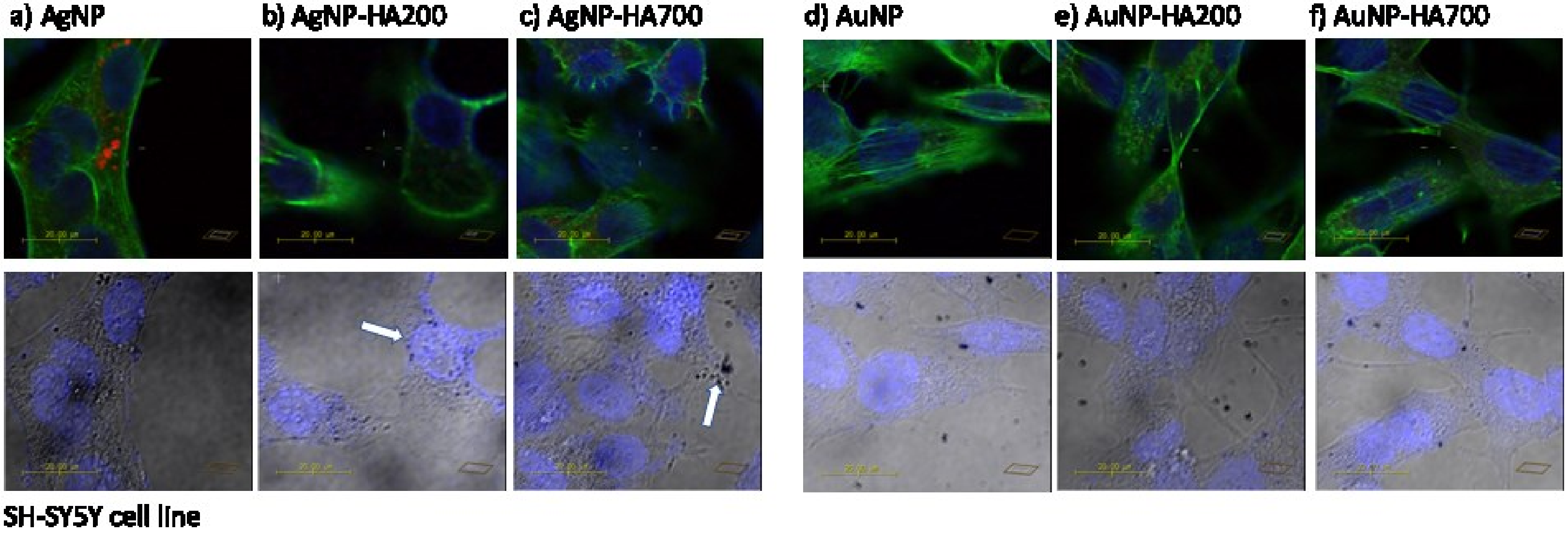

Figure 3.1.7: *LSM fluorescent micrographs of neuroblastoma (SH-SY5Y) tumour cells: in blue, the nuclear staining with Hoechst ($\lambda_{ex/em}$ = 405/425–450 nm); in green, the cytoskeleton actin staining with Actin Green ($\lambda_{ex/em}$ = 488/500–530 nm); in red, the lysosomal staining with Lysotracker Red ($\lambda_{ex/em}$ = 543/550–600 nm). Upper panels: merged confocal micrographs of nuclei + actin + lysosome; lower panels: merged confocal micrographs of nuclei + optical bright field micrographs. Cellular treatments were carried out for 90 min with:* ***a)*** *AgNP (0.72 nM = $1.0\cdot10^{7}$ NP/mL);* ***b)*** *AgNP-HA200 (0.65 nM= $2.6\cdot10^{6}$ NP/mL, 0.1% w/v HA);* ***c)*** *AgNP-HA700 (0.51 nM = $3.0\cdot10^{6}$ NP/mL, 0.1% w/v HA);* ***d****) AuNP (0.005 nM = $5.5\cdot10^{2}$ NP/mL);* ***e****) AuNP-HA200 (0.0010 nM= 7.2 NP/mL, 0.1% w/v HA);* ***f****) AuNP-HA700 (0.0011 nM = $2.5\cdot10^{1}$ NP/mL, 0.1% w/v HA). Scale bar = 20 µm.*

As to for PC-3 cells, the cell viability assay (Figure 3.1.8) demonstrated that bare AgNPs display a significant cytotoxicity with a 70% decrease in cell viability ($p<0.0001$ vs. CTRL, One-way Anova), while after 24 h of treatment with bare AuNPs the cell viability decreased of about 30 % ($p<0.0001$ vs. CTRL, One-way Anova).

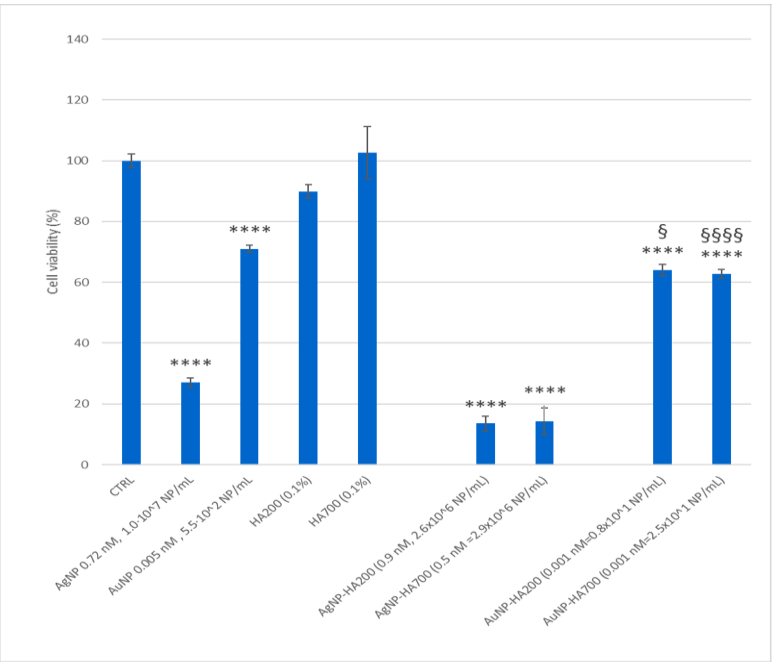

***Figure 3.1.8**: Viability of prostate cancer (PC-3) cell line after 24 h of treatment with AgNP 0.72 nM, $1.0 \cdot 10^7$ NP/mL and AuNP 0.005 nM, $5.5 \cdot 10^2$ NP/mL (10x ‘pellet 2’), HA (200 kDa or 700 kDa, 10x 1% w/v), NP-HA conjugated (10x ‘pellet 3’). (****) = $p < 0.0001$ vs CTRL; (§) = $p < 0.05$, (§§§§) = $p < 0.0001$ vs AuNP (one-way ANOVA).*

The PC-3 cells treatment with the bioconjugated NPs exhibit a nanoparticle-specific response. In fact, AgNP-HA samples are even more toxic than the bare silver nanoparticles (roughly 80% viability decrease; $p<0.0001$ vs. CTRL, One-way Anova), while cells incubated with AuNP-HA exhibit a slight decrease of viability (roughly 40% decrease vs. CTRL, $p<0.0001$; One-way Anova), which is significantly different than the result of treatment with the corresponding bare nanoparticles ($p<0.01$ vs. AuNP, One-way Anova). Interestingly, no significant differences could be noticed between 200 kDa and 700 kDa hyaluronic acid.

Since PC-3 cell line overexpresses the CD44 HA-receptor[302], these results suggest that the high toxicity of HA-conjugated AgNPs (final concentration of cell treatment of about 10^7 NP/mL) is likely related to the greater cellular uptake. Such an effect is less evident in the case of HA-conjugated AgNPs, used for the PC-3 cells treatment at the final concentration of about $5.5 \cdot 10^2$ NP/mL.

The confocal micrographs of PC-3 cells stained at the nuclei (in blue), the cytoskeleton actin (in green) and the lysosomes (in red) after the treatments with bare silver and gold NPs and the corresponding HA200- and HA700-conjugated samples are shown in Figure 3.1.9.

In the PC-3 prostate cell line, the bioconjugated NPs induce less lysosomal perturbation than the bare NPs, as displayed by the decreased emission of the Lysotracker probe in AgNP-HA (Figure 3.1.9 b-c) and AuNP-HA (Figure 3.1.9 e-f) treated cells in comparison to the corresponding bare nanoparticle of AgNP (Figure 3.1.9a) and AuNP (Figure 3.1.9d), respectively. As to the cytoskeleton actin, except the cells treated with AuNP-HA700 (Figure 3.1.9f), which display a pattern of green emission similar to that found for the corresponding treatment with HA700 (Figure 5c), all the treatments induce a thickening of the actin fibres especially visible at the cell membrane (Figure 3.1.9a-e).

Noteworthy, the Au nanoparticle aggregates are much larger in the PC-3 cells treated with AuNP-HA (see white arrows in Fig. 3.1.9e-f) than in those incubated with the bare AuNP (Fig. 3.1.9d), in contrast to what found in neuroblastoma cells, with comparable size and distribution of AuNP aggregates for SH-SY5Y cells treated with bare AuNPs (Fig. 3.1.7d) or AuNP-HA conjugates (Fig. 3.1.7e-f).

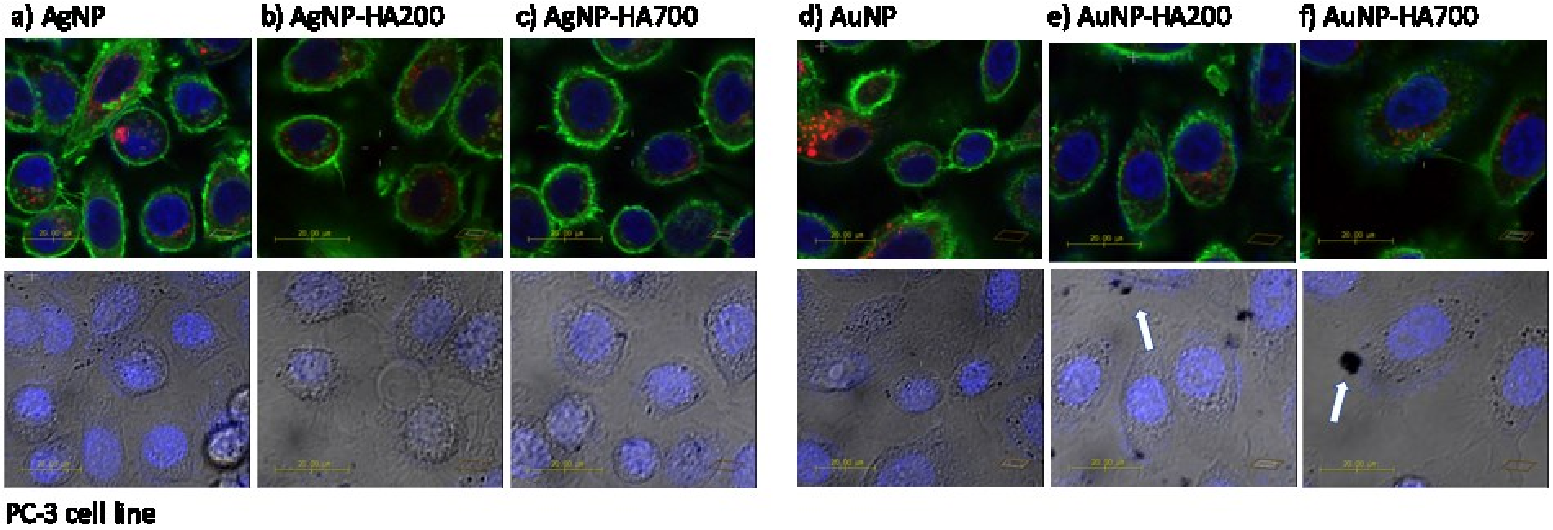

Figure 3.1.9: LSM fluorescent micrographs of prostate (PC-3) tumour cells: in blue, the nuclear staining with Hoechst ($\lambda_{ex/em}$ = 405/425–450 nm); in green, the cytoskeleton actin staining with Actin Green ($\lambda_{ex/em}$ = 488/500–530 nm); in red, the lysosomal staining with Lysotracker Red ($\lambda_{ex/em}$ = 543/550–600 nm). Upper panels: merged confocal micrographs of nuclei + actin + lysosome; lower panels: merged confocal micrographs of nuclei + optical bright field micrographs. Cellular treatments were carried out for 90 min with: **a)** AgNP (0.72 nM = $1.0 \cdot 10^7$ NP/mL); **b)** AgNP-HA200 (0.65 nM= $2.6 \cdot 10^6$ NP/mL, 0.1% w/v HA); **c)** AgNP-HA700 (0.51 nM = $3.0 \cdot 10^6$ NP/mL, 0.1% w/v HA); **d**) AuNP (0.005 nM = $5.5 \cdot 10^2$ NP/mL); **e**) AuNP-HA200 (0.0010 nM= 7.2 NP/mL, 0.1% w/v HA); **f**) AuNP-HA700 (0.0011 nM = $2.5 \cdot 10^1$ NP/mL, 0.1% w/v HA). Scale bar = 20 µm.

In summary, these results demonstrate a receptor specific response of the bioconjugated metal nanoparticles with different features depending on the type of NP, namely silver or gold, as well as on the molecular weight of the hyaluronic acid used for the nanoparticle functionalisation.

4. Conclusions

Metallic silver and gold nanoparticles were bioconjugated with pro-angiogenic 200 kDa hyaluronic acid or anti-angiogenic 700 kDa hyaluronic acid. Since the hyaluronic acid has a specific binding affinity against CD-44 receptor, which is overexpressed in some cancer cells, this study was aimed to setup a multifunctional theranostic platform with targeting capability towards cancer cells.

To test the targeting specificity of the newly fabricated systems, two tumour cell lines were used, namely SH-SY5Y neuroblastoma cells, which do not express CD-44, and PC-3 prostate cells, which overexpress CD-44 receptor, respectively.

As to neuroblastoma, the results of the cell viability assay demonstrated a similar increased cytoxicity by the bioconjugated AgNPs and AuNPs compared to the corresponding bare silver and gold nanoparticles, respectively. As to PC-3 cells, the bare AgNP showed a significant cytotoxicity compared to bare AuNPs. The treatment with the bioconjugated AgNP-HA were even more toxic than the bare silver nanoparticles, while cells incubated with AuNP-HA exhibited only a slight decrease of viability.

Morever, in neuroblastoma cells, where the interaction with the hyaluronic acid was not expected to be receptor-dependent, a diffuse uptake in the whole cytoplasm was achieved, for both the molecular weights of HA used, as evidenced by the disappearance of the nuclear staining. On the contrary, for prostate cells, expected to interact with HA through the CD-44 receptor, a preferential localisation of the hyaluronan at the cell membrane was evidenced by the actin cytoskeleton staining as well as the upholding of the intracellular organelles staining. These findings demonstrated the very promising potentialities for selective targeting and dose-dependent cytotoxicity in cancer therapy.

Section 3.2: A PLASMA CHEMISTRY-BASED METHOD FOR THE FABRICATION OF HYALURONAN-CONJUGATED METAL NANOPARTICLES WITH ANTI-INFLAMMATORY PROPERTIES

Abstract

Wound repair is a complex process that involves both processes of inflammation and angiogenesis, which are mutually dependent. During inflammatory reactions, immune cells synthesize and secrete pro-angiogenic factors that promote neovascularization, i.e. angiogenesis. Hyaluronan plays a significant role on the stimulus or suppression of angiogenesis, with different molecular sizes of HA exhibiting distinctly different- sometimes opposite -biological functions. Thus, for instance, for cancer treatment and prevention of keloid scar formation in wound repair, anti-angiogenic, high-molecular weigth (HMW) hyaluronan would be preferable to angiogenic, low-molecular weight (LMW) HA. However, the high viscosity and low stability against degradation of HMW HA often make difficult its handling and practical application. In this work, we conjugated a LMW HA (200 kDa) with an anti-angiogenic peptide sequence (GHHPHGK) and, to further increase the anti-angiogenic features, assembled hybrid hyaluronan/nanoparticle systems with silver of gold nanoparticles. The latter were fabricated by one-pot syntesis, with the simoultaneous reduction of a metal salt precursor, either via redox chemistry or by the use of microplasmas, and the bioconjugation of HA to the metal nanoparticle core. The biological effect of the HA@NP hybrids were investigated in terms of cell toxivity on endothelial cells as well as for the inhibitory activity on bacterial strains of a Gram positive and a Gram negative.

1. Introduction

Angiogenesis is the process in which the outgrowth of new blood vessels from existing ones occurs. It is a vital process because it allows forming tissues to receive oxygen and nutrients from the blood vessels.[305] The rapid development of blood capillaries that temporarily infilter injured tissues is also critical to their remodelling and repair, a phenomenon termed wound healing.[306]

Although the link between angiogenesis and inflammation has received much attention in recent years, there has long been evidence suggesting that these are two closely related processes. These include the appearance of newly formed blood vessels in granulation tissue, and the dual functionality of angiogenic factors, i.e., they exhibit both pro-inflammatory and pro-angiogenic effects. On the one side, inflammation and angiogenesis are capable of potentiating each other, on the othe side, these processes are distinct and separable.

Thus, angiogenesis is an important physiologic process that occurs in the body both under healthy (wound healing) and pathological conditions (inflammation).

The biologic roles, and cellular interactions of hyaluronic acid with cells, are highly dependent on the chain length of the HA polymer. In particular, HMW HA (>1000–5000 saccharide repeats) is space-filling, anti-angiogenic and it is an active modulator of proliferation and inflammation.[307] Specifically, native HMW HA serves to maintain a highly hydrated environment, regulate osmotic balance, acts as a shock-absorber and space-filler, and as a lubricant. Due to the numerous functional groups available for binding, and the highly anionic nature, HMW HA can sequester and release growth factors and other biologic signalling molecules leading to localize influence on cell behavior.[308] Moreover, HMW HA can also sheathe cells to prevent their interaction with other cells, and biologic signalling molecules with their cell-surface receptors.[309]

At concentration higher than 1 % (w/w), HMW HA is very viscous and difficult to handle. However, it exhibits a low stability in solution, due to the degradation of long chains polysaccharides by bacteria and the action of the pH and temperature.[233] On the other hand, LMW HA (<1000 repeats) exhibits low viscosity and a higher stability to the degradation in solution.[310-312] However, HA oligosaccharides promote tumour spreading by stimulating angiogenesis and creation of a microvascular network.[307, 313] Thus, LMW HA is inflammatory, immunostimulatory and angiogenic, by competitively binding the HA receptors on cell surfaces.

To address the fabrication of a hyaluronan-based nanomedicine for anti-angiogenic applcations, in this work we functionalised an angiogenic LMW HA scaffold with an antiangiogenic peptide sequence and with antiangiogenic metal nanoparticles.

The peptide sequence GHHPH derives from the histidine-rich region of Histidine-rich glycoprotein (HRGP). HRGP is an abundant 67 kDa plasma glycoprotein identified in many vertebrates and also in invertebrates. HRGP is synthesized in the liver, found in plasma and stored in the α-granules of thrombocytes[314]. Based on *in-vitro* studies, GHHPH has been reported to modulate angiogenesis,[315] to exhibit antibacterial properties[316] and to act as regulator of inflammation in the case of bacterial dermal infection.[317]

Noble metal nanoparticle such as AgNP and AuNP are known to exhibit anti-angiogenic activity and have a significant impact in various angiogenesis-dependent disorders such as rheumatoid arthritis, macular degeneration, diabetic retinopathy, and cancer.[318-321] In particular, AuNP bind growth factors such as VPF/VEGF165, bFGF and PlGF inhibit their activities[322] whereas AgNP inhibit vascular endothelial growth factor (VEGF) impeding the formation of new blood microvessels and can act as an anti-angiogenic molecule by targeting the activation of PI3K/Akt signalling pathways.[257, 323-327]

In this work, hyaluronic acid (200 kDa) was conjugated with GHHPHGK peptide sequence. Both HA and $HA_{GHHPHGK}$ were used for the one-step synthesis and bioconjugation of the gold and silver nanoparticles, carried out either by wet chemical or plasma-based reduction. The angiogenic and anti-inflammatory properties of the obtained hybrid HA@NP assemblies were tested respectively on human umbilical vein endothelial cells (HUVEC), in terms of cell viability, and on *S. aureus* ATCC 29213 and

E. coli ATCC 9637 bacterial strains, for determination of the minimum inhibitory concentration (MIC).

2. Materials and Methods

2.1. Chemicals

HA 200 kDa (HA 200) was provided by Fidia Farmaceutici spa (Italy); Sodium hydroxide (NaOH) was purchased by Honeywell Fluka (USA); Silver nitrate ($AgNO_3$) purity > 99%, sodium brohydride ($NaBH_4$) purity ≥ 99.0 %, D-(+)-glucose purity ≥ 99.5 %, Tetrachloroauric (III) acid trihydrate ($HAuCl_4 \cdot 3H_2O$) purity ≥ 99.9 %, tetrahydrofuran (THF) anhydrous, purity ≥ 99.9%, 1-Hydroxybenzotriazole (HOBt), N,N-Diisopropylethylamine (DIEA) Reagent Plus, ≥99%, N-(3-Dimethylaminopropyl)-N′-ethylcarbodiimide hydrochloride (EDC · HCl) purity ≥99.0%, Acetone purity ≥99.9%, phosphate buffer saline (PBS), deuterium oxide (D_2O) 99.9 % atom % D. Water was deionized (resistivity > 18.2 mΩ cm at 25 °C) and purified using a milli-Q unit (Milli-Q plus, Millipore, France). Glassware were first cleaned with aqua regia (HCl: HNO_3, 1:3 volume ratio) and then rinsed with water before starting.

Medium 200 supplemented with LSGS, 3-(4,5-dimethylthiazol-2-yl)-2,5-diphenyltetrazolium bromide (MTT reagent), dimethyl sulfoxide (DMSO) purity ≥99.7%, Tris(hydroxymethyl) aminomethane hydrochloride (TRIS-HCl) purity ≥99.7%, calcium chloride ($CaCl_2$) purity ≥97.0%, sodium sulphate ($NaSO_4$) purity ≥99.0 % were purchased from Sigma-Aldrich (USA). Brain Heart Infusion broth (BHI) and Mueller Hinton (MH) broth and agar were purchased by Oxoid (Italy); methanol was purchased by Honeywell, USA.

2.2. Synthesis of hyaluronic acid-GHHPHGK conjugate

0.372 g of HA200 were suspended in 15 mL of THF, under stirring at 4°C. To the previous suspension were added: 0.150 mg of HOOBt previously dissolved in 15 mL of THF: H_2O (1:1), 0.0566 g of DIEA dissolved in 7.5 mL of THF: H_2O (1:1), 0.070 g of GHHPHGK-NH_2 dissolved in 700 µL of H_2O. The reaction mixture was maintained under stirring at 4°C for 30 minutes. Then, 0.0165 g of EDC · HCl were dissolved in 1.4 mL of water and added to the reaction mixture. After 24 hours, the product was precipitate adding 300 mL of Acetone. The precipitate was dissolved in the minimum volume of water (65 mL) and dialysed against water by a dialysis tube (12-14 kDa cut-off); then the dialysed was lyophilised (Labconco, Freeze dry system, USA).

2.3. $HA_{GHHPHGK}$ derivate characterization: Nuclear Magnetic Resonance

1H NMR spectra were recorded at 500 MHz on a Varian Unity Inova spectrometer (Varian, USA). The experiments were performed in D_2O at 27 °C and the chemical shifts are reported as δ (ppm), referenced to the resonance of residual HOD. Unequivocal assignments of 1H resonances were supported by mono- and bi- dimensional experiments (gCOSY and gHSQC). 1H -NMR (D_2O, 500 MHz, ppm): 8.68 (s, 3H, H-2 of the imidazole ring), 7.41, 7.35 and 7.31 (s, 3 H totally, H-5 of the imidazole ring), 5.03 (br s, CH of H), 4.6-4.5 (br m, H-1 of glucuronic acid and H-1 of N-acetylglucosamine), 4.31 (br s, CH of K), 4.01 (br s, CH of P), 3.9-3.2 (br m, H-2, H-3, H-4 and H-5 of glucuronic acid; H-2, H-3,H-4, H-5, H-6 of N-acetylglucosammine, $\underline{CH_2}$ of G, $\underline{CH_2}$ 5 a and b of P, $\underline{CH_2}$ of H), 3.13 and 3.03 (br m, ε $\underline{CH_2}$ of K), 2. 36 (br m, CHa-3 of P), 2.11-1.95 (br m, CHa-4 of P and CH_3 of N-acetylglucosamine), 1.9-1.7 (br m, CHb-3, CHb-4 of P and β $\underline{CH_2}$ of K), 1.49 (br m, δ $\underline{CH_2}$ of K), 1.10 (br m, γ $\underline{CH_2}$ of K).

2.4. HA@Ag and HA@Au: wet chemical synthesis

Silver nanoparticles (AgNP) in aqueous solution were prepared (Equation 3.2.1) by adding to a solution 0.2 % (w/v %) of HA200/$HA200_{GHHPHGK}$ under magnetic stirring in an ice bath, firstly a solution of $AgNO_3$ 0.5 mM ($AgNO_3$ final concentration 0.03 mM) and then, was added drop wise over 5 minutes, a freshly prepared aqueous $NaBH_4$ solution 100 mM ($NABH_4$ final concentration 0.6 mM). After 105 minutes, under stirring, the reaction was completed and the solution colour from colourless became yellow.

$$Ag^+ + [BH_4]^- + 3H_2O \xrightarrow{HA\ (0°C)} Ag^0 + H_3BO_3 + 3.5\ H_2, \qquad (3.2.1)$$

The “bare” AgNP(C) (without the hyaluronic acid) were synthetized following the method of Mavani et al.[125] Briefly, to a solution of $NaBH_4$ 2 mM, under stirring and in an ice bath, a solution of $AgNO_3$ 1 mM was added, in a very low drop wise. The reaction was maintained in ice bath and under stirring for 45 minutes and in the end the initially colourless solution became yellow.

The AuNP and HA@Au were synthetized adding to an aqueous $HAuCl_4$ solution 0.5 mM in HA200/HA200$_{GHHPHGK}$ 0.2% (or in water to obtain AuNP), NaOH 7 mM and Glucose 5 Mm; the reaction was occurred in 1 minute when the yellow solution became purple-red. The reaction mixture was conducted under stirring and at controlled temperature of 25°C using Eppendorf ThermoMixer (Equation 3.2.2).

$$2Au^{3+} + 3C_6H_{12}O_6 + 6OH^- \xrightarrow{T=25°C} 3C_6H_{12}O_7 + 3H_2O + 2Au^0 \qquad (3.2.2)$$

2.5. HA@Ag and HA@Au: plasma reduction

HA@Ag(p) synthesis was performed using atmospheric-pressure microplasma. The synthesis was carried out by using atmospheric-pressure microplasma: the discharge current of 3 mA was applied to a solution of $AgNO_3$ 1 mM and HA200 or 200$_{GHHPHGK}$ 0.2 % (% w/w) for 15 minutes; during the plasma ignition the solution was not stirred and changed colour from transparent to yellow-brown. In the same conditions (3 Ma, 15 minutes), AgNP(P) reference was synthetized by applying microplasma to a solution 1 mM of $AgNO_3$ and tri-sodium citrate 5 mM. During the synthesis the solution was maintained at a temperature < 5 °C using an ice bath (Scheme 3.2.1.a). No stirring was applied at the liquid surface in a flow of 25 sccm argon (Ar) from a pressurized stainless-steel capillary tube (inner diameter = 0.6 mm) whose tip was positioned approximately 2 mm above the surface. A platinum (Pt) foil immersed in the solution served as counter electrode. The microplasma was ignited and sustained by a ballasted direct-current power supply with the capillary electrically biased at negative high voltage and the Pt foil electrically grounded to promote cathodic reduction reactions at the plasma-liquid interface.

The synthesis of HA@Au was carried out by using atmospheric-pressure microplasma: NaOH 7 mM was added to a solution of $HAuCl_4$ 0.5 mM in HA200/200$_{GHHPHGK}$ 0.2 % to which the discharge current 5 mA (with the value of resistance 140 kΩ) was applied, without stirring, for 15 minutes changing colour from yellow to red-purple (Scheme 3.2.1.b); during the synthesis the solution was maintained at a temperature < 5 °C using an ice bath.

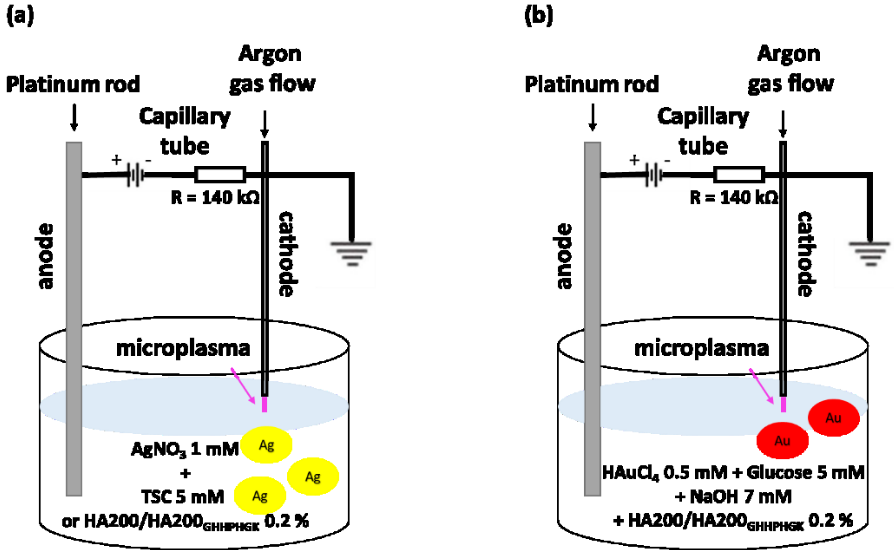

Scheme 3.2.1. *Scheme of the microplasma system for the synthesis of (a) silver nanoparticles and (b) gold nanoparticles.*

2.6. Preparation of concentrate and washed nanoparticles pellet

The as prepared HA@NP solutions obtained through synthesis were concentrated and washed with milliQ water twice by centrifugation at 10000 rpm for about 4 minutes at 15 °C (Eppendorf Centrifuge 5417R, FA453011 Rotor, Italy), using 0.5 mL Amicon Ultra centrifugal filters (Merk Millipore, USA) with a molecular weight cut-off 30 kDa. The as prepared reference AuNP and AgNP were centrifuged and washed in Eppendorf at 8000 rpm for 15 minutes for the AuNP and at 13000 rpm for 20 minutes for AgNP. The characterization of the resulting pellet was carried out by UV-visible spectroscopy and dynamic light scattering analyser (DLS, HORIBA LB-550, USA).

2.7. UV-Visible and Dynamic light scattering nanoparticles characterization

The UV-Vis spectra were obtained by using Lambda2S spectrophotometer (Perkin Elmer, USA) at 25°C; 3 mL quartz cuvette with a 1 cm path length or into 300 µL quartz cuvette with 0.1 cm path length were used for the sample analysis (by UV-visible and DLS mesurements)

In order to investigate the NP hydrodynamic size, DLS measurements were carried out at 25°C by using the dynamic light scattering particle size distribution analyzer (DLS, HORIBA LB-550, USA) with a light source 650 nm (laser diode, 5mW and a photo multiplier tube detector).

2.8. Cellular assay

Cell culture

Human umbilical vein endothelial cells (HUVEC) were cultivated in Medium200 supplemented with LSGS (fetal bovine serum, 2% v/v, hydrocortisone 1 µg mL^{-1} ,human epidermal growth factor, 10 ng mL^{-1}, basic fibroblast growth factor, 3 ng mL^{-1}, heparin, 10 µg mL^{-1}), in tissue-culture treated Corning flasks (Sigma-Aldrich, St. Louis, MO), in humidified atmosphere (5% CO_2) at 37°C (Heraeus Hera Cell 150C incubator).

Cytotoxic assay

For the cellular treatments, cells were seeded at a density of $1 \cdot 10^4$ cells/well in Medium200 supplemented with LSGS on 96 wells cell culture plates (Cellstar, Sigma Aldrich, USA). In order to treat the cells with the

NP, the pellets were diluted directly in the Medium200. The evaluation of the biological effect of studied compounds on HUVEC cells viability was performed after 24 hours of incubation. Cells were quantified by the reaction with MTT reagent (0.5 mg mL^{-1}). After 90 minutes, the reaction was stopped by DMSO addition and absorbance was measured at 570 nm (Varioskan® Flash Spectral Scanning Multimode Readers, Thermo Scientific, USA). Results were expressed as % of viable cells referred to the concentration of each compound.

2.9. Bacterial assays

Strains and culture conditions

The strains tested in this study were *Escherichia coli* ATCC 9637 and *Staphylococcus aureus* ATCC 29213, belonging to the collection of Bacteriological Laboratory of Fidia Farmaceutici S.p.A. (Noto, Italy). Frozen stocks of each strain were retrieved from -80°C freezer and plated on MH agar plates. After 24h of incubation at 37°C in aerobic conditions (Memmert incubator, GmbH + Co. KG, Äußere Rittersbacher Straße), a single colony of each strain was picked to inoculate 10.0 mL of MH broth and incubated overnight (16-18 h). The overnight broth cultures were then used for the assay.

Agar diffusion assay

The putative inhibition activity of the NP was investigated determining the zone of inhibition by the agar diffusion assay modifying the method described by CLSI M7-A7 for bacteria.[328] Briefly, 200 µL of each NP were deposited in 6.0 mm wells previously punched in MH agar where 100 µL of tested bacterial suspension were spread at the concentration of about $1.0 \cdot 10^6$ CFU/mL, determined spectrophotometrically (OD_{630}, using a spectrophotometer Synergy HT, Bioteck, USA). [328, 329] After 24 h of incubation at 37°C under aerobic conditions, the inhibitory effect was detected by an inhibition zone around the wells. The inhibition zone were highlighted by spraying the MH plates with a water-based 3-(4,5-dimethylthiazol-2-yl)-2,5-diphenyl tetrazolium bromide (MTT) solution which provides the grown colonies with a violet coloration. The chloramphenicol (30 µg mL^{-1}) was used as reference antimicrobial agent. The results were the mean of three individual experiments.

Broth microdilution assay

The broth microdilution assay was used to define the MIC (Minimum Inhibitory Concentration) for each tested NP against *Escherichia coli* ATCC 9637 and *Staphylococcus aureus* ATCC 29213.[328] The MIC is defined as the lowest concentration of substance that inhibits the growth of a microorganism as detected by the naked eye, according to CLSI M27-A3[328] it was determined using 96-well plates.

For the assay individual bacterial colonies, pre-cultured overnight on MH agar (Oxoid, Italy), were checked for purity and suspended in 5.0 mL of sterile NaCl 0.85% w/v solution, until they reached a density corresponding to McFarland 1 (3.0×10^8 CFU/mL) with an equivalent OD_{630} of 0.16 – 0.2 (Bioteck Synergy HT, USA). The saline bacterial suspension was then diluted in MH broth to obtain a final concentration in each well of about 5.0×10^5 CFU/mL.[328] The positive control was MH broth inoculated with the tested strain; the negative control was sterile MH broth. The 96-well plates were incubated as described by CLSI M100-S23.[328] The absence of growth was determined spectrophotometrically (OD_{630} Bioteck Synergy HT, USA) and confirmed by spreading on MH agar the bacterial suspension. The experiments were carried out twice in duplicate.[328]

3. Results and discussions

3.1. Hyaluronic acid-GHHPHGK conjugate characterization

The 1H-NMR spectrum (Figure 3.2.1) of the conjugate shows all the expected signals from both the protons of the peptide and from those of the hyaluronic acid units. Evidence of the formation of the amide bond between carboxylic group of hyaluronic acid residue and the amino group of side chain of lysine was provided by a significant upfield shift ($\Delta\delta = -0.10$ ppm) of ε-methylene protons ($\delta = 3.13$ ppm) of the K-NH_2 moiety, as compared to the corresponding resonance of the non-conjugated peptide (δ = 3.03 ppm). For the complete assignment of the all protons resonances see Materials and Methods on Section 2.3.

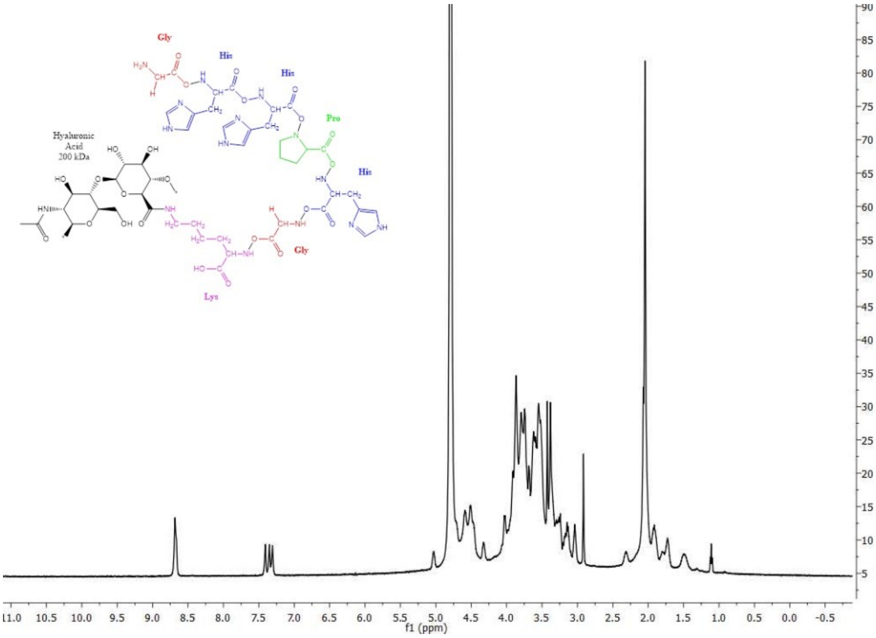

Figure 3.2.1. *The 1H-NMR spectrum of the hyaluronic acid-GHHPHGK conjugate.*

The quantity of GHHPHGK peptide present in the conjugate is determined from the ratio between the integration value of the signal at 2.05 ppm (relating to the acetyl groups of HA) and the integration value of the signal at 1.49 ppm (relating to δ CH_2 of K), or one of the H-2 or H-5 signals of the imidazole ring (at 8.69 and 7.41-7.31 ppm, respectively). In both case the results of integrated ratio is ~15%.

3.2. Fabrication and characterization of hyaluronic acid-coated nanoparticles with wet chemical and microplasma reduction.

The UV-visible spectra of the NP and HA@NP hybrids synthetized by chemical or plasma reduction show different features of the surface plasmon resonance peaks (Fig. 3.2.2).

In the case of silver nanoparticles (Fig. 3.2.2a), both hybrid HA@Ag(C) sample shows a decrease of about 42 % in the absorbance compared to the bare, borohydride-capped AgNP(C). Similarly, also for HA@Ag(P) the ipochromic shift is about 33 % with respect to the bare, citrate-capped AgNP(P). In general, the nanoparticles prepared via plasma were more polydispersed and red-shifted (i.e., larger in size due to an increase of the nanoparticle optical diameter by the formation of the HA shell around the metallic core[220, 221]) in comparison to the corresponding ones prepared by chemical reduction. In fact, the FHWM of the plasmon peaks of AgNP(C) and HA@Ag(C) ranged between 63 nm and 72 nm, while for AgNP(P) and HA@Ag(P) ranged between 87 nm and 99 nm (Table 3.2.1).

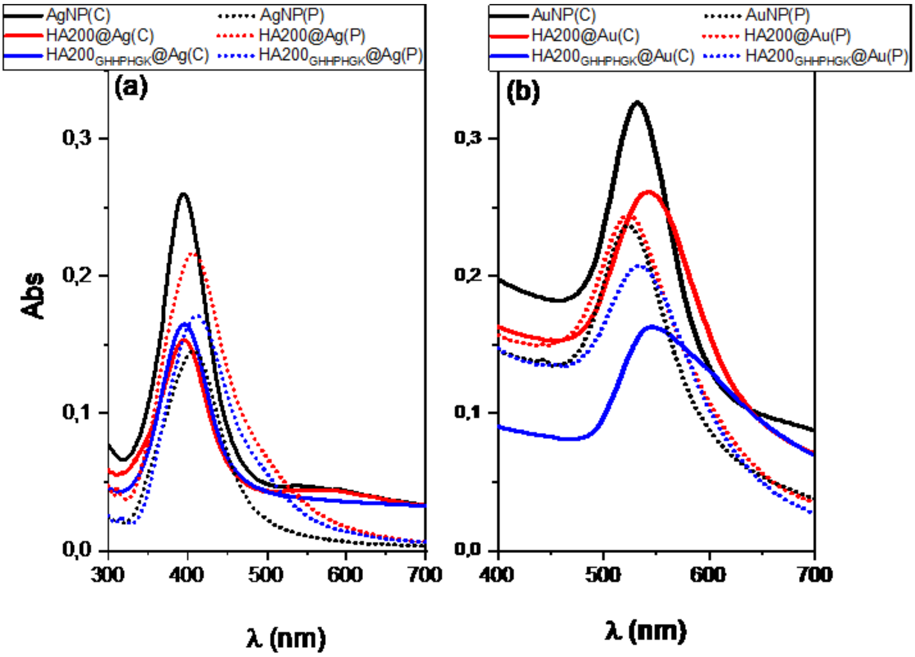

Figure 3.2.2. *UV-visible spectra of the (a) AgNP(C) (black solid line), HA200@Ag(C) (red solid line), HA200$_{GHHPHGK}$@AgNP(C) (blue solid line) synthetized by wet chemical synthesis AgNP(P) (black dash line), HA200@Ag(P) (red dash line), HA200$_{GHHPHGK}$@AgNP(P) (blue dash line) synthetized by microplasma. (b) AuNP(C) (black solid line), HA200@Au(C) (red solid line), HA200$_{GHHPHGK}$@Au(C) (blue solid line) synthetized by wet chemical synthesis and AuNP(P) (black dash line), HA200@Au(P) (red dash line), HA200$_{GHHPHGK}$@Au(P) (blue dash line) synthetized by microplasma.*

More in detail, the red shift was more evident in the case of HA200$_{GHHPHGK}$@Ag ($\Delta\lambda$ = 2.2 nm and 3.6 nm respectively for chemical and microplasma syntheses, see Table 3.2.1) than for HA200@Ag ($\Delta\lambda$ = 1.8 nm and 1.2 nm for chemical and microplasma syntheses, respectively). This effect is likely due to the extra interactions between the histidine groups of the peptide and the Ag^+ ions during the seed formation and growth process, leading to the formation of a thicker shell for the peptide-conjugated HA than for HA.[229] To note, this effect is especially evident for the silver nanoparticles fabricated by plasma than the corresponding obtained by the chemical reduction (see the Δd_0 values in table 3.2.1).

Table 3.2.1. *UV-visible parameters of NP and HA@NP fabricated by chemical (C) or plasma (P) reduction methods for the wavelength at the maximum of plasmon absorption (*λ_{max}, Abs_{max}*) and the full width at half maximum (FWHM). Calculated optical size (*d_0*) and nanoparticles concentration (molar and NP/mL).*

	λ_{max} (nm)	**Abs_{max}**	**FWHM** (nm)	**d_0** (nm)	**Δd_0[(a)] %**	**NP concentration (10^{-9} M)**	**NP/mL**
AgNP(C)	395.3	0.26	66	12	-	1.584	$1.7 \cdot 10^{10}$
AgNP(P)	407.5	0.14	87	33	-	0.073	$3.7 \cdot 10^{7}$
HA200@Ag(C)	397.1	0.15	63	14	14	1.083	$7.6 \cdot 10^{9}$
HA200@Ag(P)	408.7	0.22	89	35	6	0.093	$4.0 \cdot 10^{7}$
HA200$_{GHHPHGK}$@Ag(C)	397.5	0.16	72	14	14	0.930	$5.9 \cdot 10^{8}$
HA200$_{GHHPHGK}$@Ag(P)	411.1	0.17	99	38	13	0.057	$1.8 \cdot 10^{7}$
AuNP(C)	535	0.33	53	55	-	0.031	$2.4 \cdot 10^{3}$
AuNP(P)	523	0.24	51	22	-	0.828	$1.3 \cdot 10^{9}$
HA200@Au(C)	543	0.26	70	76	28	0.028	$6.5 \cdot 10^{2}$
HA200@Au(P)	524	0.25	58	24	8	0.577	$6.2 \cdot 10^{8}$
HA200$_{GHHPHGK}$@AuNP(C)	546	0.16	101	84	35	0.010	$3.4 \cdot 10^{2}$
HA200$_{GHHPHGK}$@AuNP(P)	534	0.21	59	52	58	0.088	$1.2 \cdot 10^{7}$

(a) The optical size increase of HA@NP compared to the corresponding bare NP, calculated as follows: $\Delta d_0 = d_0(HA@NP) - d_0(\text{bare NP})$.

Similar to what found for silver, also for the gold nanoparticles fabricated with the two methods exhibit a red-shift of plasmon peak for the hybrid HA@Au samples in comparison to AuNP (Figure 3.2.2b). As discussed above, such shifts are indicative of the increase in the nanoparticle optical diameter (Table 3.2.1), favoured by the interaction of the 'hard' ligand species in the HA chain with the metal surface.[220, 221] Similar to what found for the silver nanoparticles, the larger red-shifts observed for the peptide-conjugated HA can be related to additional interactions between the three histidine groups on the side chains of the peptide with the metal ions during the seed and growth process.

To note, two different trends in terms of size range and polydispersity for the nanoparticles fabricated by the chemical reduction or the plasma method, respectively. In general, the former show a larger size (around 55 nm for bare AuNP(C), and about 80 nm for both HA-capped NPs, respectively) in comparison to the corresponding silver NPs synthesised by the chemical reduction method (typical size range of 10-14 nm). Moreover, the broad plasmon band for $HA200_{GHHPHGK}$@Au(C) evidences the presence of several populations of size distribution (see the high value of FWHM parameter in Table 3.2.1). On the contrary, AuNP(P) and HA@Au(P) exhibit smaller size in comparison to the corresponding AgNP(P) and HA@Ag(P), while for $HA_{GHHPHGK}$@Au(P) the plasmon band points to the formation of a monodisperse solution of larger nanoparticles (52 nm vs. 38 nm, see Table 3.2.1).

A possible explanation on the difference found between gold and silver nanoparticles in the $HA200_{GHHPHGK}$@NP hybrids can be related to the different charge of the respective metal precursor salts, i.e., monovalent silver or trivalent gold, respectively. The metal ion-peptide interaction, mostly driven by the charge transfer effects between the imidazole ring in the three histidine groups of the peptide sequence and the metal cations, is expected higher for Au^{3+} than for Ag^{+} .[330]

For the purification of HA@NP hybrids, especially to remove any possible unreacted reagents, the as prepared systems were centrifuged and rinsed with Millipore water and the pellet collected. For example, in the case of AgNP, the unreacted Ag^{+} in solution can lead to cell toxicity and a further antibacterial effect; in the case of the AuNP the unreacted Au^{3+} can lead to a further antimicrobial activity.[331]

In Figure 3.2.3, the UV-visible spectra of bare AgNP(C), AgNP(P), AuNP(C) and AuNP(P) pellets obtained upon centrifugation and rinsing show opposite trends for the samples synthesised via plasma with respect to those synthesised by chemical reduction, with red-shifts in both AgNP(C) and AgNP(P), and blue-shifts in both AuNP(C) and AuNP(P), , respectively.

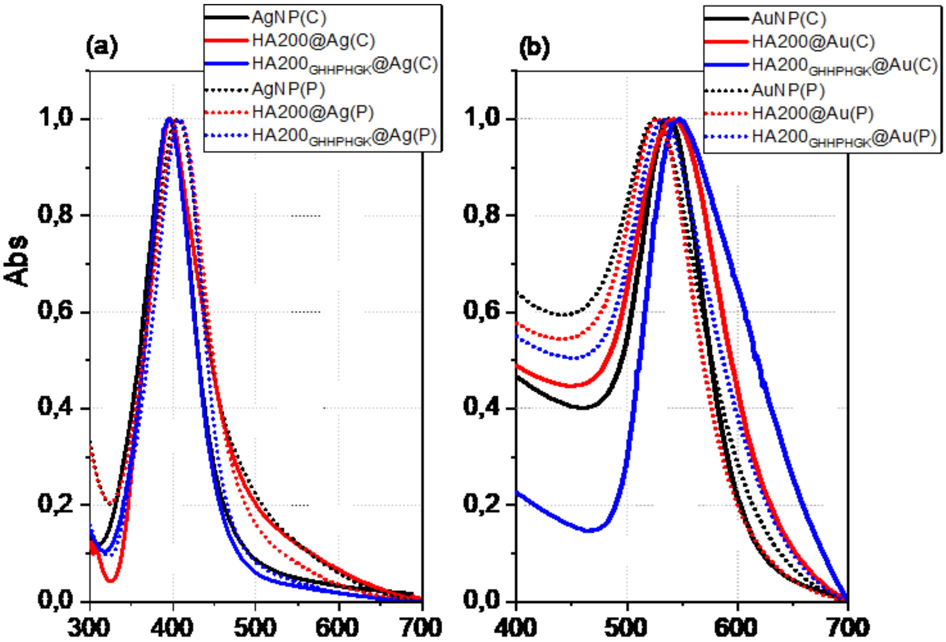

Figure 3.2.3. *UV-visible spectra of (a) pellet AgNP(C) (black solid line), pellet HA200@Ag(C) (red solid line), pellet HA200$_{GHHPHGK}$@Ag(C) (blue solid line), AgNP(P) (black dash line), pellet HA200@Ag(P) (red dash line), pellet HA200$_{GHHPHGK}$@Ag(P) (blue dash line). UV-visible spectra of (b) pellet AuNP(C) (black solid line), pellet HA200@Au(C) (red solid line), pellet HA200$_{GHHPHGK}$@Au(C) (blue solid line), AuNP(P) (black dash line), pellet HA200@Au(P) (red dash line), pellet HA200$_{GHHPHGK}$@AuNP(P) (blue dash line). Normalized curves from absorbance 0 to 1.*

These findings point to the different thickesses, obtained by the two different syntetic approaches (plasma or chemical reduction), of the hyaluronan shell irreversibly bound around the metal core of the nanoparticles. In particular, for the silver-based nanoparticles, the synthesis via plasma resulted in larger nanoparticles than the corresponding ones prepared by chemical reduction. The opposite trend was instead found for the gold-based nanoparticles.

The optical diameter and the concentration, calculated on the basis of the analyses of the UV-visible spectra[215-217, 229, 230, 332], are reported in Table 3.2.2.

Table 3.2.2. *Experimental parameters of wavelength at the maximum plasmon asdsorption (λ_{max}) and full width at half maximum (FWHM), and calculated nanoparticle optical size (d_o) and concentration for the the pellet samples resuspended in water after the purification step.*

	λ_{max} (nm)	**FWHM (nm)**	**Δ(FWHM)[(a)] (nm)**	**d_0 (nm)**	**NP concentration (10^{-9} M)**	**NP/mL**
AgNP(C)	395	68	2	12	7.25	$8.1 \cdot 10^{10}$
AgNP(P)	406	89	2	31	0.582	$3.8 \cdot 10^{8}$
HA200@Ag(C)	396	62	-1	13	5.92	$5.4 \cdot 10^{10}$
HA200@Ag(P)	407	87	-2	32	0.551	$3.1 \cdot 10^{8}$
$HA200_{GHHPHGK}$@Ag(C)	397	69	-3	14	5.03	$3.6 \cdot 10^{10}$
$HA200_{GHHPHGK}$@Ag(P)	411	98	-1	38	0.309	$1.0 \cdot 10^{8}$
AuNP(C)	539	87	34	66	0.284	$2.0 \cdot 10^{4}$
AuNP(P)	524	52	1	24	4.63	$6.2 \cdot 10^{9}$
HA200@Au(C)	542	112	42	73	0.166	$8.3 \cdot 10^{3}$
HA200@Au(P)	525	56	-2	27	3.91	$3.6 \cdot 10^{9}$
$HA200_{GHHPHGK}$@Au(C)	546	116	15	84	0.128	$4.2 \cdot 10^{3}$
$HA200_{GHHPHGK}$@AuNP(P)	534	65	6	53	0.41	$5.1 \cdot 10^{7}$

(a) Δ(FWHM) is the variation of the FWHM of the pellet compared to that of as prepared suspentions, i.e., $\Delta(FWHM) = FWHM_{pellet} - FWHM_{as\ prepared}$.

The comparison between the optical size and the hydrodynamic diameter for the nanoparticles fabricated by plasma or chemical reduction is shown in Figure Fig. 3.2.5b.

For both synthetic approaches, the hydrodynamic diameter (d_h) is higher than the oprtical size (d_o), except in the case of glucose-capped AuNP(C) and HA@AuNP(C), where d_o and d_h are quite similar or the gap ($\Delta d = d_h - d_o$) is small. This finding suggests that the glucose used as reducing agent for the synthesis of the 'bare' gold nanoparticles, in the redox process of the wet chemistry approach likely contributes to form a dense and 'rigid' shell around the nanoparticle, which roughly corresponds to the hydration shell around the nanoparticle monitored by DLS. [231, 333]

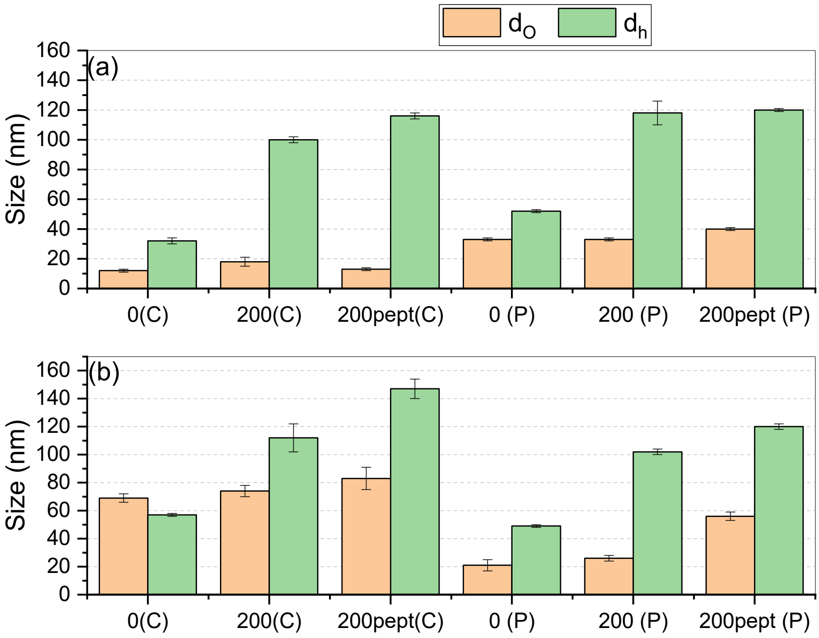

Figure 3.2.4. *Comparison between optical diameter and hydrodynamic diameter of silver- (a) and gold- (b) based nanoparticle pellets fabricated via chemical reduction (C) or the plasma method (P). For each triplet, from the left to the right are displayed the values of bare NPs (0), HA-capped NPs (200) and HA200$_{GHHPHGK}$-capped NPs (200pept), respectively.*

3.3. Cell viability assay

The cytotoxicity of AgNP and AuNP coated with HA200 and HA200$_{GHHPHGK}$ obtained by wet chemical or microplasma syntheses was evaluated by MTT assay on HUVEC cell line. Two fixed hyaluronan concentrations (i.e., 0.1 % and 0.05% w/v) were used, to have a comparison on the different effects on the cell viability by the functionalisation with the metal nanoparticles (Figure 3.2.5).

To note, NP(C) and HA@NP(C) showed, in general, a decrease in cell viability not found in NP(P) and HA@NP(P), respectively. A slightly higher toxicity was detected in silver-based systems (with a negative peak of 30%

decrease in the viable cells for treatments with 0.1% HA200GHHPHGK@AgNP(C) with respect to control untreated cells, statistical significance p<0.0001; One-way Anova) than in gold-based system, according to literature. [334-337]

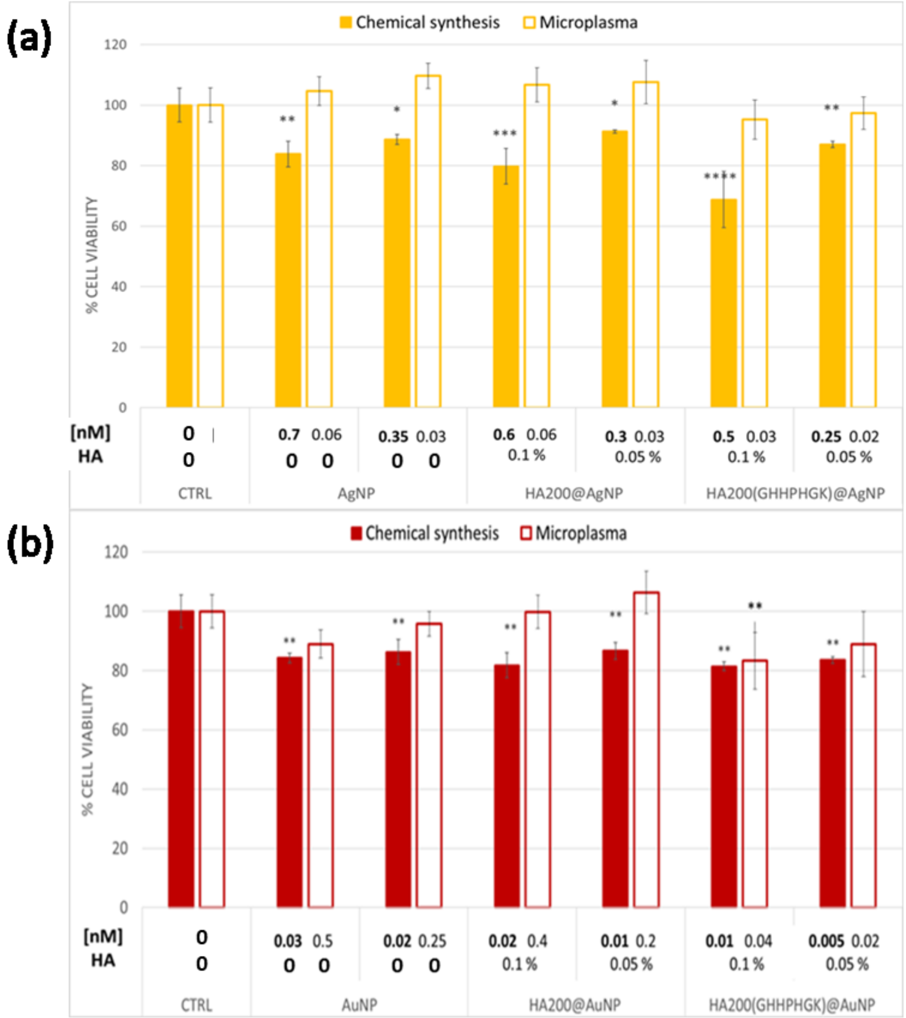

Figure 3.2.5. *Dose-response experiment for HUVEC cell line. (a) Cells were incubated for 24h with AgNP(C), HA200@Ag(C), HA200$_{GHHPHGK}$@A(C)g, AgNP(P), HA200@Ag(P), HA200$_{GHHPHGK}$@Ag(P). Results are presented as mean ± SD of triplicate experiments and normalized to the values for control untreated cells. *p≤0.05, **p≤0.01, *** p≤0.001, **** p≤0.0001 statistical significance with respect to the control (one-way analysis of variance). (b) Dose-response experiment for HUVEC cell line. Cells were incubated for 24h with AuNP(C), HA200@Au(C), HA200$_{GHHPHGK}$@AuNP(C), AuNP(P), HA200@Au(P), HA200$_{GHHPHGK}$@AuNP(P). Results are presented as mean ± SD of triplicate experiments*

*and normalized to the values for control untreated cells. *p≤0.05, **p≤0.01, statistical significance with respect to the control (one-way analysis of variance).*

Very interestingly, in the case of silver-based systems (Fig. 3.2.5a) the lower toxicity of samples synthesised by plasma can be related to the significantly lower nanoparticle concentration (about one order of magnitude, i.e, treatment concentrations of about 10^{-1} nM for Ag(C) and HA@Ag(C) vs. 10^{-2} nM for Ag(P) and HA@Ag(P)). However, in the case of gold-based samples, the concentration trend is exactly the opposite, i.e., higher in the Au(P) and HA@Au(P) (about 10^{-1}-10^{-2} nM) than in Au(C) and HA@Au(C) (about 10^{-2}-10^{-3} nM), respectively. Thus, the cell toxicity cannot be explained by the nanoparticle concentration but it is more likely related to another physicochemical properties that is the size.

In fact, according to the results discussed above (Table 3.2.2 and Figure 3.2.4), the size range for systems fabricated via chemical reduction is of the order of 12-14 nm (i.e. 'small' size) and 55-84 nm (i.e., 'large' size) for silver- and gold-based samples, respectively. On the other hand, the samples synthesised via plasma, exhibit a 'medium' size range of 33-38 and 22-52 nm for silver- and gold-based samples, respectively. Since the nanoparticle size is one of the crucial parameters that tune their cell toxicity,[103] one can hypothesize that HA-capped nanoparticles with a medium size range obtained by plasma synthesis, at the used experimental conditions, allowed for a minimal cell perturbation in terms of toxicity, which was not the case for both the small and the large HA-capped nanoparticles synthesised by chemical reduction.

3.4. Bacterial assay

The antibacterial activity of the AuNP and AgNP against planktonic-organised and biofilm organised bacteria have largely reported in literature[338-341] and various putative mechanisms of action have been hypothesised [340] (see Chapter 1 above). Antimicrobial activities of nanoparticles differ according to the metal type, synthesis methods, the different capping agents, and different tested strains, according to results reported in literature.[340, 342, 343] This study was aimed to discriminate the different response of a Gram positive (*Escherichia coli*) and a Gram negative (*Staphylococcus aureus*) in terms of inhibitory effects by the NP obtained by different synthesis technique and after the interaction with the HA200 and $HA_{GHHPHGK}$.

The photographs of *Escherichia coli* ATCC 9637 (a) and *Staphylococcus aureus* ATCC 29213 (b) bacterial strains treated for the agar diffusion assay with AgNP(C)/HA@Ag(C) and AgNP(P)/HA@Ag(P) samples are shown in Figures 3.2.6 and 3.2.7, respectively.

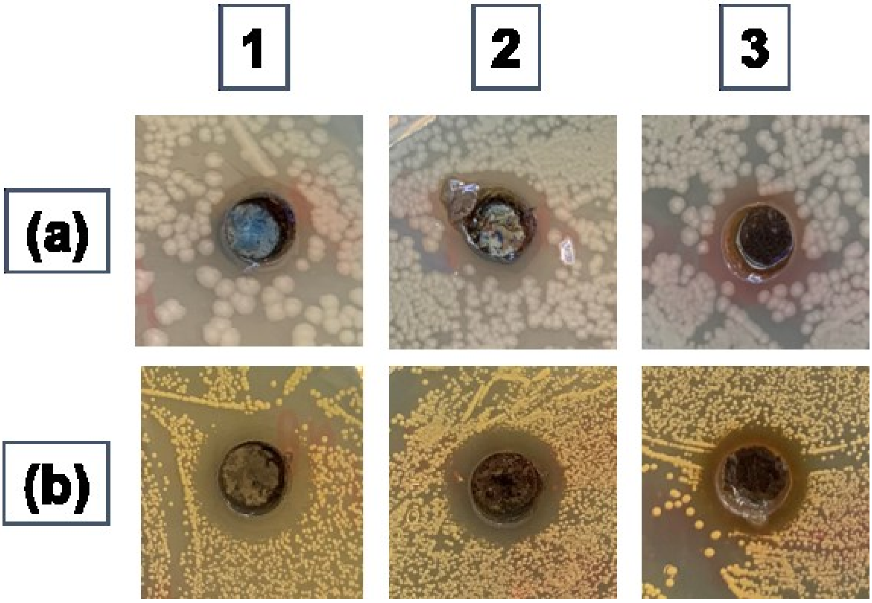

Figure 3.2.6. *Clear zones of inhibition demonstrated by silver nanoparticles synthesised by wet chemical reduction, using agar diffusion assay.* ***(a)*** *Plate of MH spread with Escherichia coli ATCC 9637: (1) AgNP(C), (2) HA200@Ag(C), (3) $HA200_{GHHPHGK}$@Ag(C),* ***(b)*** *Plate of MH spread with Staphylococcus aureus ATCC 29213: (1) HA200@Ag(C), (2) AgNP(C), (3) $HA200_{GHHPHGK}$@Ag(C).*

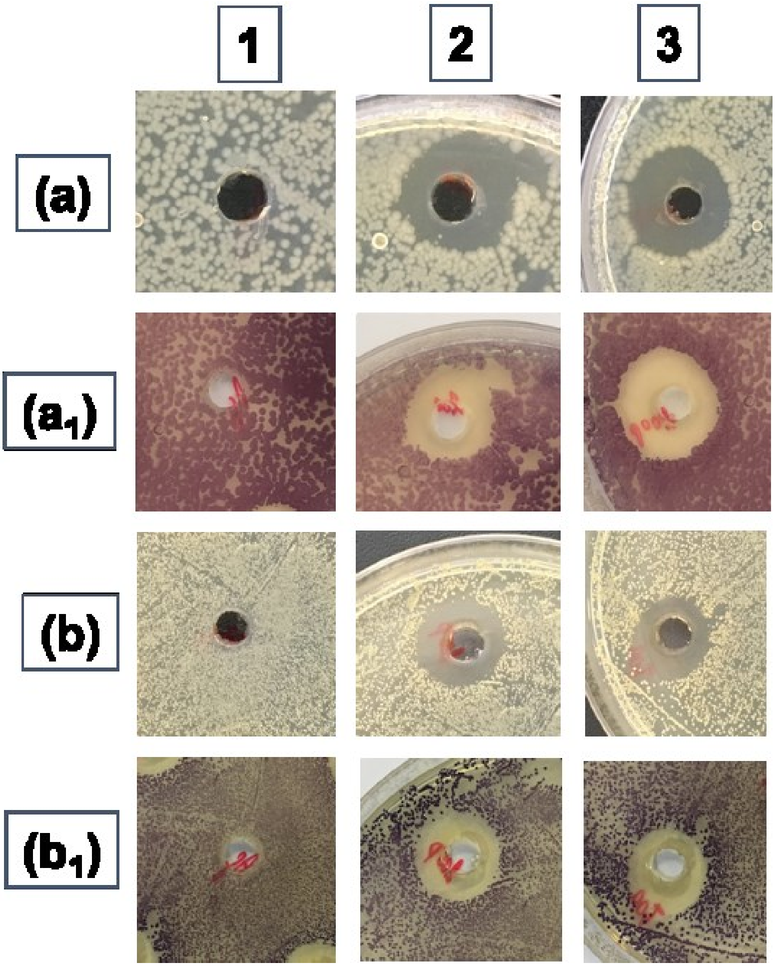

Figure 3.2.7. *Clear zones of inhibition demonstrated by plasma synthetized silver nanoparticles, using agar diffusion assay. (a) Plate of MH spread with Escherichia coli ATCC 9637; (b) Plate of MH spread with Staphylococcus aureus ATCC 29213; (1) AgNP(P), (2) HA200@Ag(P), (3) HA200*$_{GHHPHGK}$*@Ag(P); (a1) plate (a) after MTT reduction; (b1) plate (b) after MTT reduction.*

From a qualitative point of view, results point to a bacterial specificity in the inhibition by contact measured by the agar diffusion assay for the systems synthesised by chemical reduction. The photographs showed a poorly defined area of inhibition for *Escherichia coli* (Fig. 3.2.6a) and instead a clear area of inhibition for *Staphylococcus aureus* (Fig. 3.2.6b). In the case of the samples prepared via plasma reduction, both the Gram potitive (Fig. 3.2.7a) and the Gram negative (Fig. 3.2.7b) showed a clear zone of inhibition, visibly thicker for the bacteria treated with HA200$_{GHHPHGK}$@Ag(P) than for those treated with *HA200@Ag(P).* On the contrary, the treatment with the bare, citrate-capped AgNP(P) did not induce any inhibition zone.

Table 3.2.3 summarises the results obtained by the analysis of the photographic recording of the agar diffusion plate assay.

Table 3.2.3. *Inhibitory activity of silver nanoparticles sinthesised by wet chemical and microplasma methods against Escherichia coli ATCC 9637 and Staphylococcus aureus ATCC 29213 determined using agar diffusion assay in comparison with chloramphenicol (CHL).*

	Zone of inhibition (mm)			
	nM	ng/mL	*Escherichia coli* ATCC 9637	*Staphylococcus aureus* ATCC 29213
CHL		$30\cdot10^{-3}$	21.0	25.5
AgNP(C)	37	42	8.0	11.0
AgNP(P)	23	1.3	-	-
HA200@Ag(C)	56	52	11.0	10.0
HA200@Ag(P)	22	1.1	15.0	13.0
HA200$_{GHHPHGK}$@Ag(C)	82	66	9.0	9.0
HA200$_{GHHPHGK}$ Ag(P)	14	0.7	18.0	15.0

Note: *the concentration was expressed as nM and ng/mL. Interpretative criteria: very strong = diameter of inhibition zone ≥ 18.0 mm; strong = diameter of inhibition zone (18.0, 13.0] mm; good = diameter of inhibition zone (13.0, 11.0] mm; weak = diameter of inhibition zone (11.0, 9.0] mm; very weak = diameter of inhibition zone (9.0, 8.0) mm; no activity = diameter of inhibition zone < 8.0 mm.

The HA200$_{GHHPHGK}$@Ag(P) showed a very strong (ZOI = 18.0 mm) inhibitory activity against Gram-negative E. coli ATCC 9637 and a strong (ZOI = 15.0 mm) inhibitory activity against Gram-positive S. aureus ATCC 29213. When the HA200$_{GHHPHGK}$@Ag(C) were obtained by wet chemical method showed a weak (ZOI = 9.0 mm) inhibitory activity against *E. coli* ATCC 9637 and S. aureus ATCC 29213.

The HA200@Ag(P) synthetized by microplasma method showed a strong (ZOI = 15.0 mm) inhibitory activity against E. coli ATCC 9637 and a good (ZOI = 13.0 mm) inhibitory activity against S. aureus ATCC 29213. When the HA200@Ag were obtained by wet chemical method showed a good (ZOI = 11.0 mm) inhibitory activity was showed against E. coli ATCC

9637 and a weak (ZOI = 10.0 mm) inhibitory activity against S. aureus ATCC 29213.

Antimicrobial activity of HA200@Ag(P) and $HA200_{GHHPHGK}$@Ag(P) against tested strains was higher than “bare” AgNP(P). Moreover, the presence of the peptide increases the antimicrobial activity against *E. coli* ATCC 9637 and *S. aureus* ATCC 29213 of NP with respect HA200@Ag(P).

The antimicrobial activity of AgNP(C) was higher than HA200@Ag(C) and $HA200_{GHHPHGK}$@Ag(C). In general, it is possible to notice that HA200@Ag(P) and $HA200_{GHHPHGK}$@Ag(P) were the most active against both *E. coli* ATCC 9637 and *S. aureus* ATCC 29213, it could be due to the optimised plasma synthesis method and to the antimicrobial action of the peptide against both Gram-positive and Gam-negative bacteria.[344]

The absence of inhibition zone diameter for gold nanoparticles synthesised by wet chemical and plasma reduction (data not shown) and plasma synthesised silver nanoparticles (without HA) could be due to possible physicochemical interactions with agar medium.

Several investigations report for AuNP and AgNP MIC value range through a wide extend range of variation and it is difficult to compare the results and to draw general consideration.[340, 345-347] Moreover, lacks standard protocols to evaluate antimicrobial activity of the NP and different methods currently used by researchers.[346] In the present study, the antimicrobial activity of NP was investigated also using broth microdilution assay and the concentration of NP was reported as nanomolar (nM) and µg/mL which is the standard unit for the MIC measurements.[328, 348]

Using broth microdilution assay, all AgNP(C) and AuNP(C) showed inhibitory activity against both tested strains, at a concentration (µg/mL) much lower than chloramphenicol (CHL) ones used as control (Table 3.2.4).

Table 3.2.4. *Inhibitory activity of synthetized silver and gold nanoparticles synthesised by wet chemical and microplasma methods against Escherichia coli ATCC 9637 and Staphylococcus aureus ATCC 29213 using broth dilution assay in comparison with chloramphenicol (CHL).*

	Minimal inhibitory concentration (MIC)			
	Escherichia coli **ATCC 9637**		***Staphylococcus aureus*** **ATCC 29213**	
	nM	ng/mL	nM	ng/mL
Ag NP(C)[1]	2.3	2.6	9.3	10.5
Ag NP(P)[2]	5.8	0.3	-	-
HA200 Ag NP(C)[1]	3.5	3.3	14.0	13.0
HA200 Ag NP(P)[2]	2.8	0.1	5.5	0.3
HA200$_{\text{GHHPHGK}}$ Ag NP(C)[1]	9.0	4.2	20.5	16.6
HA200$_{\text{GHHPHGK}}$ Ag NP(P)[2]	0.9	0.3	1.8	0.06
Au NP(C)[1]	0.6	14.5	0.6	14.5
HA200 Au NP(C)[1]	0.6	0.01	0.6	0.01
HA200$_{\text{GHHPHGK}}$ Au NP(C)[1]	0.2	0.006	0.2	0.006
CHL	25 x 10^3	8.0 x 10^3	25 x 10^3	8.0 x 10^3

Notes: [1] the nanoparticles were tested at the following concentration ranges: AgNP(C) from 9.3 nM (= 10.5 ng/mL) to 1.2 nM (= 1.3 ng/mL); HA200@Ag(C) from 14 nM (= 13.0·ng/mL) to 1.8 nM (= 1.6 ng/mL); HA200$_{\text{GHHPHGK}}$@Ag(C) from 21 nM (= 16.6·g/mL) to 2.6 nM (= 2.1·ng/mL); AuNP(C) from 0.6 nM (= 0.02 ng/mL) to 0.07 (= 0.002 ng/mL); HA200@Au(C) from 0.6 nM (= 0.01 ng/mL) to 0.07 nM (= 0.002 ng/mL); HA200$_{\text{GHHPHGK}}$@Au(C) from 0.2 (= 0.006 µg/mL) to 0.03 nM (= 0.001 µg/mL);

[2] The nanoparticles were tested at the following concentration ranges: AgNP(P) from 5.8 nM (= 0.3 ng/mL) to 0.7 nM (= 0.04 ng/mL); HA200@Ag(P) from 5.5 nM (= 0.3 ng/mL) to 0.7 nM (= 0.03 ng/mL); HA200$_{\text{GHHPHGK}}$@Ag(P) from 3.6 nM (= 0.01 ng/mL) to 0.5 nM (= 0.01 ng/mL); AuNP(P) from 30 nM (= 0.7 ng/mL) to 3.7 nM (= 0.09 ng/mL); HA200@Au(P) from 20 nM (= 0.5 ng/mL) to 2.4 nM (= 0.006 µg/mL); HA200$_{\text{GHHPHGK}}$@Au(P) from 2.0 nM (= 0.05 ng/mL) to 0.3 nM (= 0.001 ng/mL; chloramphenicol was tested at the concentration range from 1.2 x 10^5 to 5 x 10^2 ng/mL.

AuNP(C)/AuNP(P), HA200@Au(C)/HA200@Au(P), HA200GHHPHGK@Au(C) and HA200$_{\text{GHHPHGK}}$@Au(P) did not show difference in MIC value between *Escherichia coli* ATCC 9637 and *Staphylococcus aureus* ATCC 29213, with a concentration ranging from 0.24 to 0.58 nM.

In particular, the highest inhibitory activity was showed by HA200$_{\text{GHHPHGK@}}$AuNP(C), with a MIC value of 0.24 nM. The AuNP(C), not coated with hyaluronic acid, and HA200@Au(C), coated with hyaluronic acid at lowest tested molecular weight, showed the lowest inhibitory activity between AuNP(C) (MIC values of 0.58 and 0.55 nM, respectively), against both *E. coli* ATCC 9637 and *S. aureus* ATCC 29213.

The AgNP(C) showed MIC values higher than AuNP(C), ranging from 2.31 to 9 nM. The inhibitory activity was different between the two tested strains. The highest inhibitory activity was showed by AgNP(C) against *E. coli* ATCC 9637 which a MIC value of of 2.31 nM. The HA200@Ag(C) excited a 1.5-fold inhibitory activity, lower than that of AgNP alone, with a MIC value of 3.5 nM for *E. coli* ATCC 9637. The HA200$_{\mathrm{GHHPHGK}}$@Ag showed a lethal concentration of 9 nM against *E. coli* ATCC 9637. All tested silver nanoparticles showed a 4-fold lower inhibitory activity against the Gram-positive strain *S. aureus* ATCC 29213.

All plasma synthetized silver nanoparticles showed a lower inhibitory activity against *E. coli* ATCC 9637 and *S. aureus* ATCC 29213, except AgNP(P) which did not inhibit the growth of Gram-positive tested strain (Table 3.2.4). For plasma synthetized silver nanoparticles, MIC values ranging from 0.90 to 5.82 nM, much lower than chloramphenicol (CHL), used as control.

The highest inhibitory activity was showed by HA200 $_{\mathrm{GHHPHGK}}$@AgNP(P) with a MIC value of 0.90 nM. The HA200@Ag(P) showed an inhibitory activity lower than that of HA200 $_{\mathrm{GHHPHGK}}$@Ag(P) with a MIC values of 2.75 nM. The lowest inhibitory activity, between plasma synthetized silver nanoparticles was observed for AgNP(P) against *E. coli* ATCC 9637 (5.82 nM).

The inhibitory activity of HA200@Ag(P), HA200 $_{\mathrm{GHHPHGK}}$@Ag(P), against *S. aureus* ATCC 29213 was 2-fold lower than that observed against *E. coli* ATCC 9637.

In agreement with several studies which reported that *S. aureus* was more resistant against AgNP than Gram-negative *E. coli,* probably due to differences in membrane structure and in cell wall composition which could influence bacterial accessibility to NP.[79, 343, 346] The results of this study showed MIC values lower than that often reported in the literature.[340, 342, 343, 345-347]

Plasma synthetized gold nanoparticles did not show inhibitory activity except AuNP(P) that showed a MIC value of 29.80 nM. Moreover, the

$HA200_{GHHPHGK}$@Au(P) at the highest obtained concentration (78 nM) showed a percentage of 64%, determined as $[(CFU_{not\ treated} - CFU_{treated})/CFU_{not\ treated}] \times 100$, against *E. coli* ATCC 9637.

Nanoparticles obtained from gold exhibited a higher inhibitory activity with respect to that one obtained from silver.

AuNP fabricated by wet chemical reduction exhibit a higher antibacterial activity compared with the silver nanoparticles fabricated both by plasma and chemical methods, which is probably why the mechanism through which NPs cause bacterial death is dependent on the components and structure of the bacterial cell. Probably, for these strains, the non-oxidative AuNP mechanism is more efficient than the oxidative mechanism (with ROS production) of the AgNP leading to an increase in the antibacterial activity. The differences on the antibacterial activity could be due to different NP size, in fact, AuNP(C) exhibited a bigger optical diameter than AgNP(P) (d_0 raged between 66-84 nm and 31-35 nm for the AuNP(C) and AgNP(P), respectively).[349]

4. Conclusions

In this work, hyaluronic acid-wrapped AuNP and AgNP were fabricated by two comparative approaches that used green processes of wet chemical reduction and plasma chemistry. Low molecular weight (200 kDa), pro-angiogenic hyaluronic acid was conjugated with an anti-angiogenic/anti-inflammatory peptide (GHHPHGK sequence) to scrutinise, if any, the modulation of angiogenic and inflammatory activities of the hybrid HA@NP systems.

The optical characterisation by UV-visible spectroscopy evidenced the formation of larger nanoparticles (bigger optical diameter) stabilised by the hyaluronan shell coating and this effect was more evident for AuNP than AgNP. In particular, HA200@Au(C) and $HA200_{GHHPHGK}$@Au(C) synthesised by chemical reduction (respectively 76 nm and 84 nm in optical size) and the plasma synthetised HA200@Au(P) and

HA200$_{GHHPHGK}$@Au(P) (24 nm and 52 nm, respectively) exhibited a general increase in size compared to the bare AuNP (55 nm) and AuNP(P) (22 nm), especially for the GHHPHGK-HA conjugate.

The cell viability assay on a HUVEC cell line showed a significant toxicity only for AgNP(C) and HA@Ag(C) systems, with a maximum decrease in cell viability (about 30% compared to control untreated cells) for the treatment with HA200$_{GHHPHGK}$@Ag(C). The cells treatment with AgNP(P), AuNP(C) or AuNP(P), both bare and HA-coated nanoparticles, did not show a significant toxicity.

Except for plasma-synthesised bare AuNP(P) and AgNP(P), all the tested NPs showed a great antibacterial effect on skin patogens Gram-negative *E. coli* ATCC 9637 and Gram-positive *S. aureus* ATCC 29213. In particular, AgNP(C) exhibited a similar antibacterial effect against *E. coli* ATCC 9637 and *S. aureus* ATCC 29213, as confirmed by the analyses of the zone of inhibition (ZOI) in agar diffusion assays and minimal inhibitory concentration (MIC) in broth dilution tests. All the gold-based system did not show inhibition by contact in the agar diffusion test at the used experimental conditions. However, in the broth dilution method, the highest antibacterial activity was actually detected for HA200$_{GHHPHGK}$@Au(C), with much lower MIC value (0.2 nM) than the other cases, both Au-based and Ag-based. A possible explanation of these findings can be related to the strong charge transfer effects between the histidine groups in the peptide sequence and the gold metal ion precursors during the synthesis, which resulted in a thick shell of the peptide-conjugated HA around the metal core (so, a relatively high number of peptide molecules). Moreover, in the hybrid HA@Au, a more oriented arrangement of the peptide towards the metal surface system compared to the analogous HA@Ag, support the idea that such and arrangement allows for the protection of the peptide molecules against early degradation, during their interaction with the bacteria and, therefore, a more efficient anti-angiogenic and anti-inflammatory activity. According to this picture, the second most efficient system for the antibacterial activity was found to be HA200$_{GHHPHGK}$@Ag(P) (MIC value of

0.9 nM and ZOI of 18 mm), where a thinner (and probably less ordered) shell of peptide-conjugated HA was efficiently wrapped around the nanoparticles.

CHAPTER 4

HYALURONAN-DECORATED GOLD AND SILVER NANOPARTICLES AT THE INTERFACE WITH THE CELLS MEMBRANE

MOTIVATION OF THE STUDY

Inorganic nanoparticles (NPs) exhibit relevant physical properties for application in biomedicine and specifically for both diagnosis and therapy (i.e. theranostic) of severe pathologies, such as cancer and wound healing treatments. The inorganic NP core is often not stable in aqueous suspension and can induce cytotoxic effects. For this reason, over the years, several coating strategies were suggested to improve the NP stability in aqueous solutions as well as the NP biocompatibility. Among the various components which can be used for NP coatings there are synthetic and natural polymers such as hyaluronic acid. The synthesis of the polymer-capped nanoparticles improve their suitable properties, decreasing the side effects such as cytotoxicity and bio-accumulation.

A relevant point for biomedical applications is the penetration of nanoparticles (NPs) through the cell and biological barriers. Important biological barriers are the cell membranes, which are dynamic, fluid structures essential to the life of a cell, they are formed by amphipathic lipids, which consist of hydrophobic and hydrophilic portions. In order to scrutinize the interaction and the activity of the NP and HA@NP, obtained by chemical and plasma methods, with model membrane in real-time, quart crystal microbalance with dissipation monitoring was used; additionally, the uptake and distribution study of these systems on human umbilical vein endothelial cell line was studied by LSM technique.

HYALURONAN-DECORATED GOLD AND SILVER NANOPARTICLES AT THE INTERFACE WITH THE CELL MEMBRANE

Abstract

The rapid development of nanomaterials has led to an increase in the number variety of engineered nanoparticles in the environment. Nanoparticles (NPs) are present in the environment because of their nanoscale size.Given their increasing use in sunscreens, cosmetics and other personal products and their use in the nanomedicine such as in the wound healing field, they may enter the bloodstream by permeation through skin. Given this degree of exposure, it is important to understand the implications human health. It can be possible studying the interaction of the NP such as noble metal NP with model membrane and the interaction with the true cell cytoskeleton of endothelial cells.

In this work we investigate the interactions between AgNP and AuNP, coated with hyaluronic acid at three different molecular weight (200, 700 and 1200 kDa) and synthetized by wet chemical and microplasma methods, and the bilayer both synthetic by real-time quartz crystal microbalance with dissipation monitoring (QCM-D) technique and real by laser confocal scanning microscopy (LCSM) to investigate the interaction with the cell cytoskeleton of the Human Umbilical Vein Endothelial Cells (HUVEC).

1. Introduction

Metal nanoparticles are widely studied in different fields of nanomedicine; application of nanotechnology in medicine currently is being developed and it involves employing nanoparticles to deliver drugs, in the diagnostic field, in the wound care and in the antibacterial treatments. [350, 351]

Noble metal nanoparticles, in particular AuNP and AgNP, have elicited a lot of interest as model theranostic platforms owing to their apparently low toxicity, ease of synthesis and versatility in functionalization with various moieties (including antibodies, peptides and DNA/RNA) to get specific cell target.[103]

Thanks to the increasing importance of gold and silver nanoparticles, new synthesis strategies were developed in order to obtain biocompatible NPs using green and easier methods without organic and toxic reagents on mild reaction conditions. [352]

Tailoring wet chemical synthesis and microplasma synthesis allows to obtain polymer-coating nanoparticles;[353] the NPs wrapping with biopolymers such as hyaluronic acid allows to prolong the in vivo circulation and to specific delivery of the hybrid systems thanks to the targeting of specific receptors on the cell membrane, such as CD44 overexpressed in carcinogenic (prostatic cancer cell line, PC-3)[354] and human primary cell lines (such as endothelial cells, HUVEC) [355]. Moreover, for silver nanoparticles the interaction with the membrane is well known and it is involved in the toxicity and antibacterial activity, in particular AgNPs interact with the bacterial membrane and are able to penetrate inside the cell. Transmission electron microscopy data shows that AgNPs adhere and penetrate into *E. coli* cells and also are able to induce the formation of pits in the cell membrane.[356, 357] AgNPs have been observed within *E. coli* cells albeit at sizes much smaller than the original particles; moreover, Ag NPs with oxidized surfaces induce the formation of ‘‘huge holes’’ in *E. coli* surfaces; after the interaction, large portions of the cellular content seemed to be ‘‘eaten away’’.[357] According to AuNP studies about cell membranes conducted by Cho et al. we can notice that the uptake of AuNP by SK-BR-3 cells was dependent on the surface charge, where positively charged AuNPs present a higher uptake rate compared to the neutral or negatively charged AuNPs, additionally this interaction does not involve toxicity via membrane destabilisation.[358]

Thus, one way to really understand the biological properties of the hybrid-NPs systems as well as their fate and their behaviour once they get in contact with biological media, is to study the interaction between hybrids systems and the model or real cell membranes. Biomimetic membrane models, such as supported lipid bilayer, are interesting tools to approach and understand NPs–cell membrane interactions. The use of these models permits, first of all, to control physical and chemical parameters and to rapidly compare membrane types and the influence of different media conditions. The interactions between NPs and cell membranes can be qualified and quantified using analytical and modelling methods.[359]

In this contest, there is an increasing interest in using quartz crystal microbalance with dissipation monitoring (QCM-D) to investigate the interaction of nanoparticles (NPs) with model surfaces. The high sensitivity, ease of use and the ability to monitor interactions in real-time has made it a popular technique for colloid chemists, biologists, bioengineers, and biophysicists. QCM-D has been recently used to probe the interaction of NPs with supported lipid bilayers (SLBs) as model cell membranes. The interaction of NPs with SLBs is highly influenced by the quality of the lipid bilayers. Unlike many surface sensitive techniques, by using QCM-D, the quality of SLBs can be assessed in real-time, hence QCM-D studies on SLB-NPs interactions are less prone to the artefacts which arise from not well formed bilayers. The ease of use and commercial availability of a wide range of sensor surfaces also have made QCM-D a versatile tool for studying NP interactions with lipid bilayers.[360]

It is equally important to study the interaction of the hybrid-NPs systems and real cell membrane in order to investigate not only the interactions with phospholipid bilayer but also the induced response of the cellular receptors. For this kind of investigations, Laser Scanning microscopy is a useful technique because it allows to perform real-time imaging with a relative simple preparation of the sample. Additionally, this technique allows to perform uptake studies and to analyse the distribution of the hybrid-nanosystems on the organelles and cell compart as well as to scrutinize the cytosol modification after NPs uptake.[361]

In this work, we scrutinize the interaction between a model membrane POPC-SLB and AuNP and AgNP, hybrid-systems HA@Ag and HA@Au obtained by wet chemical and plasma synthesis, by QCM-D measurements and the interaction with real cell membrane, treating

HUVEC cell line with the previous sample, obtaining information about the activity, uptake and distribution of the systems inside the cells after internalization.

2. Materials and methods

2.1. Chemicals

Sodium hydroxide (NaOH) was purchased by Honeywell Fluka (USA); Silver nitrate ($AgNO_3$) purity > 99%, sodium brohydride ($NaBH_4$) purity ≥ 99.0 %, D-(+)-glucose purity ≥ 99.5 %, Tetrachloroauric (III) acid trihydrate ($HAuCl_4 \cdot 3H_2O$) purity ≥ 99.9 %

HA 200 kDa (HA 200), HA 700 kDa (HA 700) and HA 1200 kDa (HA 1200) were provided by Fidia Farmaceutici spa (Italy); phosphate buffer saline (PBS). Chloroform ($CHCl_3$) was purchased by Merk, Ammonia solution 25 % (% w/w) was purchased by Merk, Hydrogen peroxide (H_2O_2) 30 % (% w/w) was purchased by Sigma Aldrich, 1-palmitoyl-2-oleoyl-sn-glycero-3-phosphocholine (POPC) purchased from Avanti Polar Lipids (USA). Water was deionized (resistivity > 18.2 mΩ cm at 25 °C) and purified using a milli-Q unit (Milli-Q plus, Millipore, France). Glassware were first cleaned with aqua regia (HCl: HNO_3, 1:3 volume ratio) and then rinsed with water before starting. Medium200 supplemented with LSGS was purchased from Sigma-Aldrich (USA).

2.2. Synthesis of Hyaluronic acid-coated nanoparticles

2.2.1. Wet-chemistry reduction method.

The aqueous solution of $AgNO_3$ was reduced with $NaBH_4$ in the presence of HA. Briefly, a solution of $AgNO_3$ 0.5 mM was added to a solution 0.2 % (w/v) of HA200 or HA700 or HA1200 under magnetic stirring in an ice bath. Then, a freshly prepared aqueous $NaBH_4$ solution 100 mM was added dropwise over 5 minutes. The initially colourless solution became yellow and was stirred in ice bath for 105 minutes (Fig. 2.1a). The synthesis of bare, borohydride-capped AgNP(C) was carried out using the method of Mavani et al. [125]

For the synthesis of HA-coated AuNP(C) to an aqueous $HAuCl_4$ solution 0.5 mM were added NaOH 7 mM and glucose 5 mM. The reaction mixture was maintained under stirring and at controlled temperature of 25°C using Eppendorf ThermoMixer. The HA-capped gold nanoparticles were formed approximately in 1 minute. As to the bare, glucose-capped AuNP, the same reaction was conducted in water instead of HA 0.2% aqueous solution.

For both HA@Ag and HA@Au hybrids, the as prepared colloidal dispersions were concentrated by two repeated centrifugation steps (4 minutes; 9391 xg; 15 °C) in a Eppendorf Centrifuge (5417R, FA453011 Rotor, Italy), with washing with milliQ water in between the two centrifugations. 0.5 mL Amicon Ultra centrifugal filters (Merk Millipore, USA) were used, with a molecular weight cut-off of 30 kDa. As to the reference bare AuNP and AgNP samples, the pellets were obtained by double centrifugation and washing in Eppendorf at 6010xg for 15 minutes for AuNP and at 11766xg for 20 minutes for AgNP, respectively.

2.2.2. *Plasma Synthesis of Hyaluronic acid coated Silver Nanoparticles (HA@Ag)*

HA@Ag(P) synthesis was performed using atmospheric-pressure microplasma. The synthesis was carried out as follows: the discharge current was applied to a solution of $AgNO_3$ 1 mM and HA 0.2 % to obtain HA@Ag or TSC 5 mM to obtain the reference AgNP(P). The atmospheric-pressure microplasma was initiated at the liquid surface in a flow of 25 sccm argon (Ar) from a pressurized stainless-steel capillary tube (inner diameter = 0.6 mm) whose tip was positioned approximately 2 mm above the surface. A platinum (Pt) foil immersed in the solution served as counter electrode. The microplasma was ignited and sustained by a ballasted direct-current power supply with the capillary electrically biased at negative high voltage and the Pt foil electrically grounded to promote cathodic reduction reactions at the plasma-liquid interface. In the microplasma system, the discharge current was 3 mA (with the value of resistance 140 kΩ) and it was applied to the $HA@Ag^+$ solution for 15 minutes changing colour from transparent to yellow-brown. No stirring was applied. The temperature of the solution was maintained during the experiment < 5 °C using an ice bath and it was monitored by an infrared thermal camera.

HA@Au(P) synthesis was performed using atmospheric-pressure microplasma. The synthesis was carried out adding NaOH 7 mM to a $HAuCl_4$ solution 0.5 mM (in water for the reference or in HA 0.2 % to obtain coated NP). In the microplasma system, the discharge current was 5 mA (with the value of resistance 140 kΩ) and it was applied to the HA-Au^{3+} solution for 15 minutes changing colour from yellow to red-purple. No stirring was applied. The temperature of the solution was maintained < 5 °C during the experiment using an ice bath to avoid the increase of the NP size[214]; the temperature was measured by an infrared thermal camera.

The reference glucose capped-AuNP were synthetized by mycoplasma adding 5 mM of glucose solution to a solution of $HAuCl_4$ 0.5 mM. The applied discharge current was 5 mA (with the value of resistance 140 kΩ) for 15 minutes; the solution changed colour from yellow to red-purple.

For both HA@Ag(P) and HA@Au(P) hybrids, the as prepared colloidal dispersions were concentrated by two repeated centrifugation steps (4 minutes; 9391 xg; 15 °C) in a Eppendorf Centrifuge (5417R, FA453011 Rotor, Italy), with washing with milliQ water in between the two centrifugations. 0.5 mL Amicon Ultra centrifugal filters (Merk Millipore, USA) were used, with a molecular weight cut-off of 30 kDa. As to the reference bare AuNP(P) and AgNP(P) samples, the pellets were obtained by double centrifugation and washing in Eppendorf at 6010xg for 15 minutes for AuNP(P) and at 11766xg for 20 minutes for AgNP(P), respectively.

2.3. Preparation of small unilamellar vesicles (SUVs) dispersions

Small unilamellar vesicles (SUVs) were prepared from chloroform solutions of POPC (5 mg/mL). PBS solution 10 mM was prepared using tablets (0.01 M phosphate buffer containing 3 mM KCl and 0.14 M NaCl, pH 7.4). The buffer was filtered with the syringe filter (0.22µm, GE

Healthcare, USA) and degassed for 30 minutes under ultrasonic bath (Labsonic 2, FALC Instruments, Italy). A chloroform solution of POPC (5 mg/mL) and Rhod-DHPE (1 wt %) was taken in a round-bottom flask, and, after evaporating the solvent under argon flow, the dried lipid film formed on the wall of the flask was emulsified in PBS (to obtain SUV) and vortexed. The lipid dispersions were, therefore, extruded 13 times through a 100 nm polycarbonate membrane, followed by other 13 times through a 30 nm membrane (Avanti Polar Lipids).

Vesicles prepared in this way typically measured 30 nm, as determined by DLS analyser (HORIBA LB-550, USA). The refrigerated vesicle solutions were stored under N_2 and used within two weeks, according to an established protocol.[362] Before the use, the size of SUVs was checked by DLS measurements.

2.4. *Quartz crystal microbalance with dissipation (QCM-D) monitoring*

The measurements were performed on the Q-Sense E1 (Biolin) instrument operating with a constant flow of 100 µL/min, at a temperature of 25 °C. The sensor crystals were cleaned by immersion overnight in a sodium dodecyl sulphate solution (0.4% w/v in H2O-MilliQ), followed by copious MilliQ-H_2O washing, then N_2 blow drying and UV-ozone treatment for the removal of surface organic contamination (two steps of 15’ each with water rinsing in between and at the end). The tweezers were cleaned with a piranha basic solution (NH_3 : H_2O_2 : H_2O volume ratio = 4: 1: 1), followed by copious rinsing with MilliQ-H_2O. For the QCM-D runs, NP-HA and NP pellet samples were dissolved in 10 mM PBS buffer to the final concentration of 0.1% w/v in HA and 0.7 nM and 0.06 nM for AgNP and AgNP(P) ,respectively; 0.05 nM or 0.5 nM for AuNP and AuNP(P), respectively.

All solutions were outgassed for 30 minutes under ultrasonic bath (Labsonic 2, FALC Instruments, Italy) and were analysed at 100 µL/minutes starting in PBS 10 mM. For the physicochemical characterization the vesicles, diluted to a final concentration of 0.1 mg mL^{-1}, were adsorbed on the silica surfaces and then were rinsed with PBS buffer 10 mM.

2.5. *Cell cultures and maintenance*

Human umbilical vein endothelial cell line was cultured in plastic flasks in Medium200 supplemented LSGS (fetal bovine serum, 2% v/v, hydrocortisone 1 µg mL^{-1} ,human epidermal growth factor, 10 ng mL^{-1}, basic fibroblast growth factor, 3 ng mL^{-1}, heparin, 10 µg mL^{-1}), in tissue-culture treated 25 cm^2 Corning flasks (Sigma-Aldrich, St. Louis, MO), in humidified atmosphere (5% CO_2) at 37°C (Heraeus Hera Cell 150C incubator). For the cellular treatments, the day before the experiment cells were seeded in full medium on TPP® tissue culture plates (Sigma-Aldrich, St. Louis, MO). The HA-conjugated silver and gold nanoparticle samples were concentrated 5 times up to the final HA concentration of 1% w/v or, in the case of the bare AgNP and AuNP reference samples, up to the maximum washing by centrifugation steps to avoid aggregation (typically ‘pellet 2’ samples), and added to the cells in culture medium at the desired final concentration for incubation times of 90 min for the confocal microscopy experiments.

2.6. *Confocal microscopy analysis*

For LSM live cell imaging analysis, cells were seeded at a density of 2.5 · 10^4 cells/well in 12 mm glass bottom dishes (Willco Wells, Amsterdam). The day after cells were washed with no-supplemented Medium200, and treated with HA-conjugated NP and bare NP samples for 90 min. During the last 20 min of the total treatment time, the cells were stained with LysoTracker Red (150 nM) (LysoTracker™ Red DND-99, TermoFisher), a deep red-fluorescent dye for labelling and tracking acidic lysosome organelles in live cells and Hoechst33342 (1 µg/mL) (Hoechst 33342 Solution, ThermoFisher) for fixed and live cell fluorescent staining of DNA and nuclei in cellular imaging technique. Cells were rinsed with fresh PBS and cellular fixation was performed with high purity paraformaldehyde (4% w/v) in PBS. For the straining of cytoskeleton actin, cells were permeabilized with 0.02% w/v Triton X-100 in the presence of 10% bovine serum albumin (BSA) and treated with a high-affinity F-actin probe, conjugated with green-fluorescent Alexa Fluor® 488 dye (ActinGreen™ 488 ReadyProbes® Reagent, TermoFisher).

LSM imaging was performed with an Olympus FV1000 confocal laser scanning microscope (Olympus, Shinjuku, Japan), equipped with diode UV (405 nm, 50 mW), multiline Argon (457, 488, 515 nm, total 30 mW), HeNe(G) (543 nm, 1 mW) and HeNe(R) (633 nm, 1 mW) lasers. An oil immersion objective (60xO PLAPO) and spectral filtering systems were used. The detector gain was fixed at a constant value and images were collected, in sequential mode randomly all through the area of the well. The image analysis was carried out using Huygens Essential software (by Scientific Volume Imaging B.V., The Netherlands). The statistical analysis was performed with ImageJ software and one-way ANOVA test.

3. Results and Discussions

3.1. HA@NP pellet characteristics

In this work, from stabilized AuNP and AgNP synthetized by wet chemical method and by microplasma[105] nanoparticles pellets were obtained and the most important characteristics of the samples were showed in table 4.1. In table 4.1 was reported the comparison of the optical diameter (d_0), the hydrodynamic diameter (d_h) and the concentration (molar and in NP/mL) between the pellet suspension obtained from the as prepared suspension synthetized by wet chemical synthesis and plasma synthesis.

Table 4.1. *UV-visible parameters and characterization of the pellet-NP obtained by wet chemistry and plasma reduction.*

	MW (kDa)	**d_0 nm**	**d_h nm**	**nM**	**NP/mL**
AgNP	0 (C)	12	32	5.64	$6.33 \cdot 10^7$
	200 (C)	13	100	5.92	$5.23 \cdot 10^7$
	700 (C)	25	199	1	$1.24 \cdot 10^6$
	1200 (C)	20	220	1.66	$4.03 \cdot 10^6$
	0 (P)	31	52	0.58	$3.76 \cdot 10^8$
	200 (P)	32	118	0.55	$3.07 \cdot 10^8$
	700 (P)	33	214	0.4	$2.00 \cdot 10^8$
	1200 (P)	32	245	0.5	$2.69 \cdot 10^8$
AuNP	0 (C)	66	57	0.28	$1.96 \cdot 10^4$
	200 (C)	73	112	0.17	$8.30 \cdot 10^3$
	700 (C)	123	208	0.04	$3.66 \cdot 10^2$

1200 (C)	134	234	0.05	$3.87 \cdot 10^{2}$
0 (P)	24	49	4.62	$6.09 \cdot 10^{10}$
200 (P)	27	102	3.91	$3.51 \cdot 10^{10}$
700 (P)	35	195	1.63	$6.97 \cdot 10^{9}$
1200 (P)	30	222	2.85	$1.94 \cdot 10^{10}$

Note: C= wet chemical synthesis; P=plasma synthesis.

Starting with the concentrations indicated in Table 4.1, the QCMD and LSM experiments were carried out.

3.2. Interaction of the hybrid hyaluronan-conjugated nanoparticles with model cell membranes: a QCM-D study

QCM-D experiments were performed to investigate the interaction of the hyaluronan-functionalized nanoparticles plasma and chemical method synthetized, in comparison with the bare NP, with model cell membranes made of supported lipid bilayers.

The dissipation parameter gives meaningful information about the viscoelastic properties of the film adsorbed, which are useful to characterize the interaction of SLBs with different molecules and nanosystems. The QCM-D response observed after the addition of vesicles onto the silica-coated QCM-D sensor shows the expected two-phase behaviour for POPC SUVs adsorbing onto hydrophilic substrate[363], i.e.: (i) firstly, the adsorption of intact vesicles onto the silica surface until a critical coverage is reached (corresponding to the minimum in frequency shift and the maximum in dissipation shift); (ii) secondly, the spontaneous vesicles rupture/fusion resulting into the formation of a homogeneous SLB (typical shift values in frequency and dissipation respectively of $\Delta f \sim -26$ Hz and $\Delta D < 0.5 \cdot 10^{-6}$, as reported in the literature.[364]

The experiments were performed starting the measurement in PBS (10 mM) for 5 minutes, then the addition of SUV 0.1 mg mL^{-1} during 7 min and 3 min of buffer rinsing. After the SLB formation and the buffer rinsing the sample (HA-conjugated NPs or positive controls of bare NPs and HA) was injected into the measurement cell for 10 min and the final rinsing was carried out PBS for 5 min. The experiment was conducted at the flow rate of 100 µL/min.

Figure 4.1 showed the QCM-D curves of frequency shifts and dissipation shifts corresponding to the fifth overtones to investigate the interaction the SLB and the HA and HA@NP systems.

For all cases, the first part of the experiment (i.e., vesicle adsorption) displayed in Figure 4.1, points to the successful formation of a SLB following the rupture and fusion of the SUV adsorbed at the sensor surface. Introduction of HA and HA@NP systems produced a negligible change in f, indicating no change in mass.

To notice, in Fig. 4.1a and Table 4.2, compared to the HA200 ($\Delta D = 0.71 \times 10^6$) the HA200@Ag(C) and HA200@Ag(P) showed high shifts of the dissipation of 1.3×10^6 and 3.1×10^6, respectively; smaller shifts were observed for HA200@Au(C) and HA200@Au(P) of 1.1×10^6 and 0.9×10^6 respectively. In Fig. 4.1b and Table 4.2, compared to the HA700 ($\Delta D = 0.36 \times 10^6$) the HA700@Ag(C) and HA700@Ag(P) showed shifts of the dissipation of 0.74×10^6 and 1.9×10^6, respectively; higher shifts were observed for HA700@Au(C) and HA700@Au(P) of 0.6×10^6 and 1.2×10^6, respectively. In Fig. 4.1c and Table 4.2, compared to the HA1200 ($\Delta D = 0.74 \times 10^6$) the HA1200@AgNP(C) and HA1200@AgNP(P) showed shifts of the dissipation of 1.9×10^6 and ~0, respectively; for HA1200@AuNP(C) and HA1200@AuNP(P) were observed shifts of 2.2×10^6 and -0.9×10^6, respectively. In Fig. 4.1d Table 4.2, it possible to notice the ΔD of the bare nanoparticles and the dissipation shifts were negative for AgNP(C), AgNP(P) and AuNP(C) (of -0.3×10^6, -0.1×10^6, -0.2×10^6) and ~0 for AuNP(P).

Table 4.2. *ΔD obtained by the QCM-D curves about the interaction of the pellet-NP obtained by wet chemistry and plasma reduction and the SLB.*

	MW (kDa)	**$\Delta D \cdot 10^6$**		**MW (kDa)**	**$\Delta D \cdot 10^6$**
AgNP	0 (C)	-0.3	AuNP	0 (C)	-0.2
AgNP	0 (P)	-0.1	AuNP	0 (P)	-
	HA200	0.71		HA200	0.71
AgNP	200 (C)	1.3	AuNP	200 (C)	1.1
AgNP	200 (P)	3.1	AuNP	200 (P)	0.9

	HA700	0.36		HA700	0.36
AgNP	700 (C)	0.74	AuNP	700 (C)	0.6
AgNP	700 (P)	1.9	AuNP	700 (P)	1.2
	HA1200	0.74		HA1200	0.74
AgNP	1200 (C)	1.2	AuNP	1200 (C)	2.2
AgNP	1200 (P)	-	AuNP	1200 (P)	-0.9

Note: C= wet chemical synthesis; P=plasma synthesis.

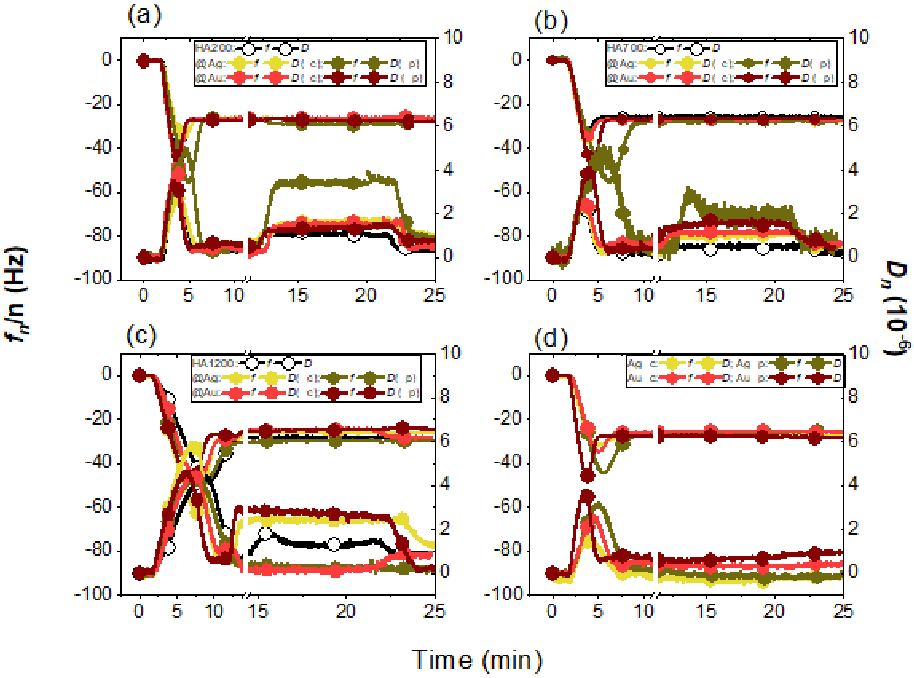

Figure 4.1. *QCM-D curves of frequency shifts (left hand side axes) and dissipation shifts (right hand side axes) corresponding to the fifth overtones for POPC vesicles (0.1 mg· mL^{-1}) adsorption on SiO$_2$ QCM-D sensors and, after, the addition of:* ***a)*** *HA200, HA200@Ag(C), HA200@Au(C), HA200@Ag(P), HA200@Au(P);* ***b)*** *HA700, HA700@Ag(C), HA700@Au(C), HA700@Ag(P), HA700@Au(P);* ***c)*** *HA1200, HA200@Ag(C), HA1200@Au(C), HA1200@Ag(P), HA1200@Au(P);* ***d)*** *AgNP(C), AuNP(C), AgNP(P), AuNP(P).*

In the case of AgNP and HA@Ag systems, to the sample addition follows the rinsing step in which the dissipation do not came back to the initial value indicating irreversible interactions; the opposite consideration could be observed in the case of AuNP and HA@Au.

To study the properties of hyaluronic acid or HA-hybrid systems attachment to cell membranes, SLBs were formed on silica surface and the interaction were studied in real-time by QCMD technique.[365]

Several studies were conducted to investigate the interaction between HA and SLBs to understand the biological activity and modulation of the biopolymer and to obtain new drug delivery systems such as the enhanced topical delivery of hyaluronic acid encapsulated in liposomes.[366] HA is a non-Newtonian fluid with viscoelastic properties and its interaction with SLB leads to the increase of the dissipation value[367] for HA200, HA700 and HA1200 (ΔD of 7×10^5, 4×10^5, 7×10^5, respectively) meaning the formation of softer layer after HA addition.[365]

To notice, upon addition of the HA-conjugated NP hybrid systems to the pre-formed SLBs, the QCM-D curves of dissipation and frequency shifts reflect the influence of both hyaluronan and the NP components in the interaction with the supported lipid bilayers (Fig. 4.1a-c) and in particular the hybrid systems showed an increase in the dissipation variation: HA200@Ag(C) and HA200@Ag(P) showed high shifts of the dissipation of 1.3×10^6 and 3.1×10^6, respectively; smaller shifts were observed for HA200@Au(C) and HA200@Au(P) of 1.1×10^6 and 0.9×10^6 respectively. Compared to the HA700 ($\Delta D = 0.36 \times 10^6$) the HA700@Ag(C) and HA700@AgNP(P) showed shifts of the dissipation of 0.74×10^6 and 1.9×10^6, respectively; higher shifts were observed for HA700@Au(C) and HA700@Au(P) of 0.6×10^6 and 1.2×10^6, respectively and the same effect was observable for HA1200@Ag(C) and HA1200@Au(C) with ΔD values of 1.9×10^6 and 2.2×10^6, respectively; these increases in the ΔD could be due to the increase in the SLB fluidity and viscoelasticity after the perturbation of the phospholipids bilayer by the hybrid systems.[368] These findings point to a stronger viscoelastic character of the interface established between the SLB and the hybrid HA@Ag and HA@Au systems with the 200 kDa (chemical and plasma) and 1,200 kDa(chemical)-molecular weight hyaluronan in comparison with the 700 kDa (chemical and plasma)-molecular weight one.

The HA1200@Ag(P) and HA1200@Au(P) showed a different response regarding the ΔD, in fact, it was possible to observe a negligible variation of the dissipation for HA1200@Ag meaning no interaction with the SLB and -0.9 x 10^6 for HA1200@Au (Fig. 4.1c). Similarly, by addition to the SLBs of bare AgNP and AuNP (Fig. 4.1d) solutions, a significant decrease in the dissipation was detected, which was higher for silver ($\Delta D \sim -0.3 \cdot 10^6$) than for gold ($\Delta D \sim -0.2 \cdot 10^6$) nanoparticles. This effect is well known in the literature, the nanoparticles affect the lipid conformation and the resulting membrane stresses are relieved by the rigidity of the membrane and by the leakage of some lipid molecules from the bilayer. Only a small amount of lipid is removed consistent with the small amount of NP adsorption, and the lipid removal occurs leading to small pores or other forms of membrane defects that are not significant enough to perturb membrane stability.[368, 369]

Moreover, after the rinsing, the HA@Ag curves did not recover to the initial values but a residual increased dissipation was found for both, thus, confirming an irreversible interaction mostly related to an actual adsorption, as observed for the bare AgNP. On the contrary, as observed for the bare AuNP and the control HA samples, the hybrid HA@Au systems showed a reversible interaction and the curve shifts were mostly related to solvent exchange in the measurement chamber as well as to the change of density and viscoelasticity at the interface with the artificial cell membranes.

Figure 4.2 shows the dissipation versus frequency shifts in characteristic D/f plots. This graph allows to drop the time as explicit variable; in turn, it allows to interpret the temporal homogeneity of the investigated attachment process due to fast kinetics for sparse data points and slow attachment kinetics, reaching the steady state, for overlapping dense points.[370]

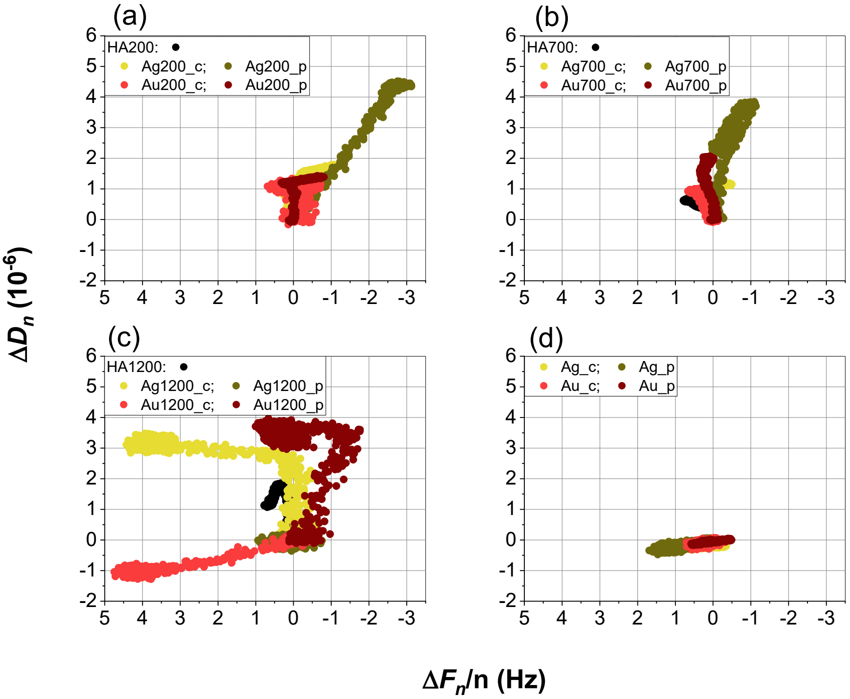

Figure 4.2. *D–f plots for adsorption on SLB of the* ***a)*** *HA200, HA200@Ag(C), HA200@Au(C), HA200@Ag(P), HA200@Au(P);* ***b)*** *HA700, HA700@Ag(C), HA700@Au(C), HA700@Ag(P), HA700@Au(P);* ***c)*** *HA1200, HA200@Ag(C), HA1200@Au(C), HA1200@Ag(P), HA1200@Au(P);* ***d)*** *AgNP(C), AuNP(C), AgNP(P), AuNP(P).*

In the QCM-D measurements the viscous and elastic contributions of a soft-wet biointerface were taken into account by the simultaneous detection of change in frequency Δf and dissipation ΔD. The signal from rigid adlayers was only weakly damped (small ΔD/Δf ratio). Conversely, soft adlayers had a large dissipation factor (high ΔD/Δf).[371]

It is interesting to note, as be expected, the HA200, HA700, HA1200 showed in the D-f plots graphs (Fig. 4.2a-c) a high slope that meant a high viscoelastic character of the adlayer.[371] It was possible to observe the same effect for the HA200@Ag and HA200@Au (both plasma and chemical synthetized), for the HA700@Ag and HA700@Au (both plasma and chemical synthetized) and for the HA1200@Ag and HA1200@Au (Fig.

4.2a-c). It was possible to notice that soft adlayers had a large dissipation factor (high ΔD/Δf).[372]

Conversely, the D-f plots of the HA1200@Ag(P), HA1200@Au(P) and the bare AgNP(C), AgNP(P), AuNP(C), AuNP(P) (Fig. 2c-d) showed weakly damped (small ΔD/Δf ratio) trend that was signal from rigid layer.[104]

The Figure 4.3 showed the LSM fluorescent micrographs of human umbilical vein cells (HUVEC) after incubation with AgNP and AuNP alone and in association with HA200, HA700 and HA1200 and the corresponding references.

Gold and silver nanoparticles were reported to induce strong modifications depending on the size and concentration.[373]

After incubation with AgNP(C) (Fig. 4.3b) it was possible to observe a different morphology of the actin staining, and in particular the cells lost their elongated form and took the spherical form.

The treatment of HUVEC cells with HA did not induce relevant changes in comparison with the control (Fig. 4.3d, Fig. 4.3g, Fig. 4.3l).

The incubation with the HA@AgNP(C) systems (Fig. 4.3e, Fig. 4.3h, Fig. 4.3m) showed the protective role of the HA from the AgNP toxicity, in fact it was possible to observe that the morphology of the cells was maintained compared to the control and the actin staining shows regular membrane fibres. Interestingly, the intensity of the lysosome staining in the presence of HA@AgNP(C) decreased probably due to the quenching effect of these systems.

Compared to the AgNP(C), AuNP(C) did not show any influence on the cell morphology, cells look like the same shell of the control. Important to known the intensity after the lysosome fluorescence increased in the presence of HA200@Au(C) and HA700@Au(C), compared to the control. The incubation with HA1200@Au(C) the lysosome staining was less evidence probably due to the different properties and viscosity of the HA1200.

Accordingly with the MTT assay (Chapter 5, results and discussions) the gold and silver nanoparticles synthetized by microplasma method are less toxic compared to the wet chemical reduction synthesised ones; that led to small modification morphology in the LSM fluorescent micrographs of human umbilical vein cells (HUVEC) after incubation with AgNP(P) and AuNP(P) alone and in association with HA200, HA700 and HA1200 and the corresponding references showed in Figure 4.4.

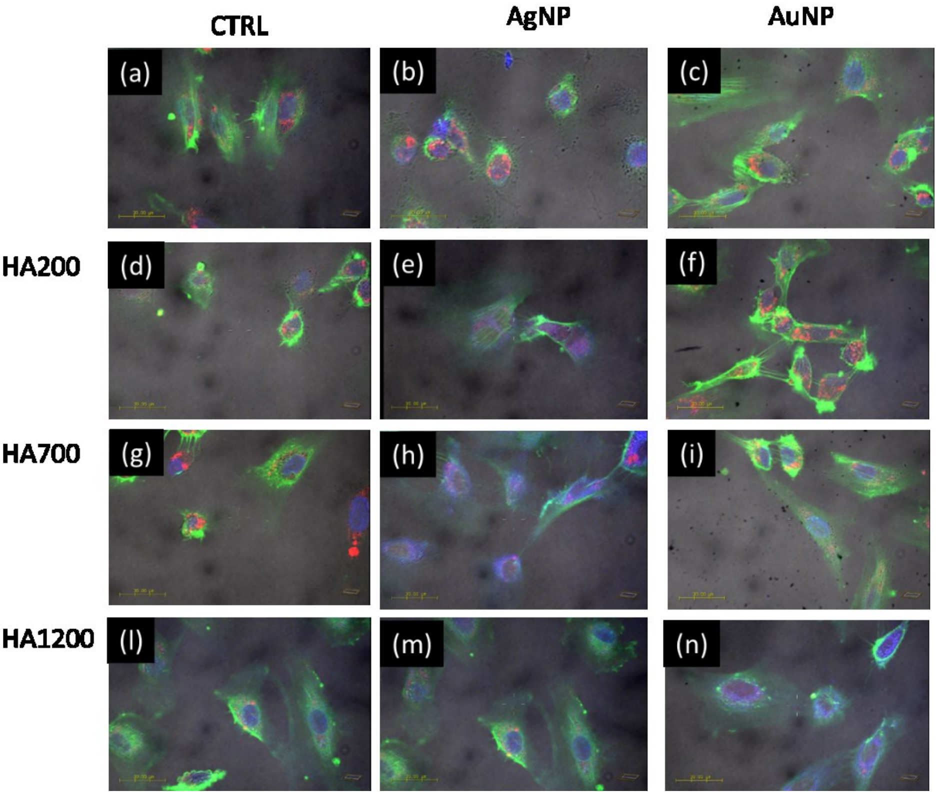

Figure 4.3. *LSM fluorescent micrographs of human umbilical vein cells (HUVEC): in blue, the nuclear staining with Hoechst ($\lambda_{ex/em}$ = 405/425–450 nm); in green, the cytoskeleton actin staining with Actin Green ($\lambda_{ex/em}$ = 488/500–530 nm); in red, the lysosomal staining with Lysotracker Red ($\lambda_{ex/em}$ = 543/550–600 nm). Panels merged confocal micrographs of nuclei + actin + lysosome+ optical bright field micrographs. Cellular treatments were carried out for 90 min with:* ***a)*** *15 µL water;* ***b)*** *AgNP(C) (0.6 nM = 6.3 x 10^6 NP/mL) ;* ***c)*** *AuNP(C) (0.28 nM = 2.0·10^3 NP/mL);* ***d)*** *HA200, 0.1% w/v;* ***e)*** *HA200@Ag(C) (0.6 nM= 5 x 10^6 NP/mL, 0.1% w/v HA);* ***f)*** *HA200@Au(C) (0.17 nM = 8·10^2 NP/mL, 0.1% w/v HA),* ***g)*** *HA700, 0.1% w/v;* ***h)*** *HA700@Ag(C) (0.1 nM= 1 x 10^2 NP/mL, 0.1% w/v HA);* ***i)*** *HA700@Au(C) (0.004 nM = 3·10^1 NP/mL, 0.1% w/v HA),* ***l)*** *HA1200 , 0.1%*

*w/v; **m)** HA1200@Ag(C) (0.2 nM= 4 x 10^5 NP/mL, 0.1% w/v HA); **n**) HA1200@AuNP(C) (0.005 nM = 4·10^1 NP/mL, 0.1% w/v HA). Scale bar = 30 µm.*

The actin staining in the control (Fig. 4.3a and 4.4a) shows regular membrane fibres and some globular aggregates, while lysosomal staining exhibit the characteristic punctual distribution.[373]

To notice, after incubation with AgNP(P) and HA200@Ag(P), (Fig. 4.4b) a different morphology of the actin staining, and in particular the cells lost their elongated form and looked like round shape; there was not change in the lysosome staining.

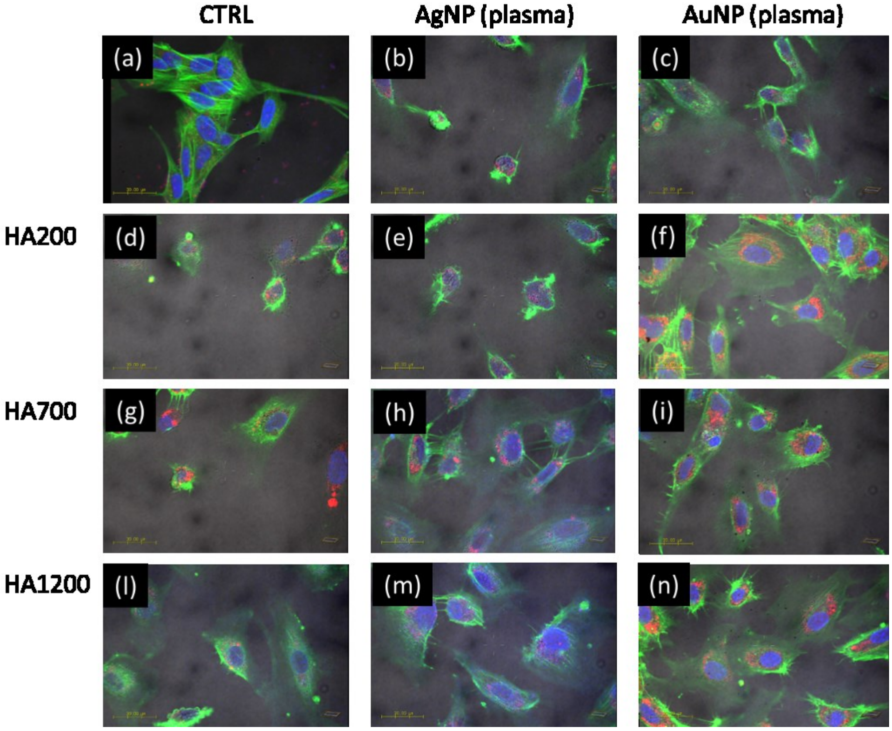

Figure 4.4. *LSM fluorescent micrographs of human umbilical vein cells (HUVEC): in blue, the nuclear staining with Hoechst ($\lambda_{ex/em}$ = 405/425–450 nm); in green, the cytoskeleton actin staining with Actin Green ($\lambda_{ex/em}$ = 488/500–530 nm); in red, the lysosomal staining with Lysotracker Red ($\lambda_{ex/em}$ = 543/550–600 nm). Panels merged confocal micrographs of nuclei + actin + lysosome+ optical bright field micrographs. Cellular treatments were carried out for 90 min with: **a)** HUVEC control 15 µL of sterilized water; **b)** AgNP(P) (0.06 nM = 3.8·10^7 NP/mL; **c)** AuNP(P) (0.51 nM = 6.2·10^8 NP/mL); **d**) HA200 , 0.1% w/v; **e**) HA200@AgNP (0.6 nM= 3.1 ·10^7 NP/mL, 0.1% w/v HA); **f**)*

HA200@AuNP (0.4 nM = $3.6\cdot10^8$ NP/mL, 0.1% w/v HA), ***g)*** *HA700 , 0.1% w/v;* ***h)*** *HA700@AgNP (0.04 $\cdot10^7$ nM= 2 NP/mL, 0.1% w/v HA);* ***i)*** *HA700@AuNP (0.2 nM = $7\cdot10^9$ NP/mL, 0.1% w/v HA),* ***l)*** *HA1200 , 0.1% w/v;* ***m)*** *HA1200@AgNP (0.05 nM= 2.7 $\cdot10^8$ NP/mL, 0.1% w/v HA);* ***n)*** *HA1200@AuNP (0.3 nM = $1.9\cdot10^9$ NP/mL, 0.1% w/v HA). Scale bar = 30 µm.*

The treatment of HUVEC cells with HA does not induce relevant changes in comparison with the control (Fig. 4.4d, Fig. 4.4g, Fig. 4.4l).

After the incubation with the AgNP(P) in the presence of HA systems (Fig. 4.4e, Fig. 4.4h, Fig. 4.4m), it is possible to notice the protective role of the HA against the toxic activity of the AgNP(P); in fact, after AgNP(P) treatment the morphology and cells viability of the cells was maintained compared to the control and the actin staining shows regular membrane fibres.

Compared to the control, the incubation of the bare NP(P) (Fig. 4.4b and Fig. 4.4c) influence the structure of the actin; the images show the presence of small actin globular aggregates. The same condition do not affect significantly the lysosome staining.

The incubation of the cells with HA@Au(P) (Fig. 4.4f, Fig. 4.4i, Fig. 4.4n) led to the reassembly of the actin that choose the high florescence because the aggregate of the actin were formed. Lysosomes in the presence of HA@Au(P) increased the fluorescence staining compared to the HA and AuNP(P) alone.

With HA@Au (both obtained by chemical and plasma synthesis) a change of the staining colours is observable with a more effective actin activation (corresponding to the increase in intensity of green emission) and even more elongated and denser fibres in comparison to controls. However, the actin activation can be distinguished, especially associated with the dotted spots colocalizing with aggregates of lysosomes.

AuNP are partially internalized and detectable in optical bright field by the dark spots that correspond to colloidal aggregates,[374] that induce lysosomal swelling as observed for AuNP and HA@AuNP synthesised by wet chemical and microplasma reduction.[375]

4. Conclusions

In this work were scrutinized the interaction of the AgNP and AuNP synthesized with and without HA at three molecular weights (200, 700 and 1200 kDa) by wet chemical and plasma methods with model (SLB by real-time QCM-D technique) and real cellular membrane (by LSM microscopy). The QCMD measurements evidences that after the SLB formation the introduction of HA and HA@NP systems produced a negligible change in f, indicating no change in mass. The variation of the dissipation meant a real-time interaction with the studied systems and the perturbation of the fluidity of the formed bilayer.

The interaction with HUVEC cells treated with NP and HA@NP synthesized by wet chemical and plasma methods was evaluated by LSM images. The treatment of HUVEC cells with HA did not induce relevant changes in comparison with the control. When the cells were incubated with the HA@Ag(P) and HA@Ag(C) in the presence of HA systems it was possible to notice the protective role of the HA from the AgNP toxicity and the morphology and cells viability was maintained compared to the control and the actin staining showed regular membrane fibres. Compared to the control, the incubation of the NP(P) alone influenced the structure of the actin that showed the presence of small actin globular aggregates; the same condition did not affect significantly the lysosome staining. The incubation of the cells with HA@AuNP(C) led to the reassembly of the actin and to an increase in the fluorescence. Lysosomes in the presence of HA@Au(C) increased the fluorescence staining compared to the HA and AuNP(C) alone because colloidal aggregates AuNP were partially internalized.

CHAPTER 5

A HYBRID MULTIFUNCTIONAL PLATFORM OF INORGANIC NANOPARTICLES CONJUGATED WITH HYALURONIC ACID FOR ANGIOGENIC AND ANTIBACTERIAL PROPERTIES

MOTIVATION OF THE STUDY

The wide application of the noble nanoparticles in nanomedicine field drives researchers to develop green, easy and biocompatible syntheses.

Plasmas at atmospheric pressure method and in particular microplasma allows to sythetize noble metallic NPs (Ag, Au) in a simple, fast and versatile way without the using of any reducing agents. The mild reaction conditions allow to use of biological capping agents and to develop the synthesis in water.

In this study, silver and gold nanoparticles are generated by the reduction of silver and gold salt in a hyaluronic acid aqueous solution (at three different molecular weights 200 kDa, 700 kDa and 1200 kDa) by microplasma to synthesize HA@NP(P) nanohybrid systems. The NP and HA@NP systems obtained by microplasma methods were characterised and compared to the same hybrids-NPs obtained by wet chemical method. In particular, was compared the cytotoxicity of the plasma and chemical NPs by MTT assay on the HUVEC cell line. Furthermore, how these HA@NP(P) influence the wound healing process in comparison with the chemical synthetized nanohybrid systems was examined by microbiological studies on pathogenic bacteria strains of *E. Coli* and *S. Aureus*, to study their antibacterial effects on the wound healing process.

A HYBRID MULTIFUNCTIONAL PLATFORM OF INORGANIC NANOPARTICLES CONJUGATED WITH HYALURONIC ACID FOR ANGIOGENIC AND ANTIBACTERIAL PROPERTIES

Abstract

Plasmas at atmospheric pressure method is a simple, fast, and versatile tool for the synthesis of noble metallic NPs (Ag, Au). Thanks to the nanoparticles optical and biological properties, they are widely used in new nanoscaled technologies including medicine, physic, optic and electronic field. To date, many synthesis methods were developed to produce particles and control their size, shape and aggregation such as chemical synthesis, sonochemistry, ultraviolet-visible (UV-vis) irradiation, flame pyrolysis and laser ablation. In particular, gold and silver nanoparticles exhibit different biological activity as angiogenic regulator and antibacterial activity, respectively. In the synthesis, the use of natural polymers as NPs stabilizer and capping agent such as hyaluronic acid allow to form new nanohybridsystems with different or enhanced biological activity.

In this study, silver and gold nanoparticles are generated by the reduction of silver and gold salt in an hyaluronic acid 200 kDa, 700 kDa and 1200 kDa aqueous solution by microplasma in order to synthetize HA@NP(P) nanohybrid systems. The NP and HA@NP systems were characterized by UV-visible spectroscopy, in order to study the plasmonic properties of hyaluronic acid hybrids with metallic nanoparticles, and their stability during the aging time. Dynamic light scattering (DLS) was carried out to characterise the NP hydrodynamic size. The cytotoxicity of the plasma systems in comparison with the chemical synthetized HA@NP was evaluated by MTT assay on the HUVEC cell line. Furthermore, the way in which these HA@NP(P) influence the wound healing process in comparison with the chemical synthetized nanohybrid systems was examined by microbiological studies on pathogenic bacteria strains of *E. coli* and *S. aureus*, in order to study their antibacterial effects on the wound healing process.

1. Introduction

Noble metals (Ag/Au) nanoparticles have been studies due to their tunable properties (size, morphology, shape, etc) and potential applications in many sectors of science and technology such as electronics[376, 377], solar cells[378, 379], and bio applications such as biophysical studies[280], biological sensing[380], imaging[380], medical diagnostics,[381] cancer therapy,[382] gene therapy,[383] medicines,[384] optics, [385] as well as in catalysis.[385]

In order to synthetize metal nanoparticles, different synthesis approaches were developed such as chemical methods based on the chemical reduction of the metal salts, electrochemical pathways or the controlled decomposition of metastable organometallic compounds;[91, 92, 94-96] biological methods which utilize extracts (microorganisms, proteins, amino acids, polysaccharides, and vitamins) from bio-organisms as reductant, capping agents or both;[101] physical methods including plasma reduction, thermal reduction, photochemical reduction, radiolysis, laser ablation and microwave treatment.[97, 98]

As a special category of plasma being confined within submillimeter scale in at least one dimension, microplasma has attracted tremendous interests for nanofabrication due to their unique characteristics;[99] in fact, microplasma allows to obtain NPs by direct reduction of the metal salts in solution at atmospheric pressure.[100]

The synthesis of AuNP and AgNP by microplasma allows to obtain spherical NPs in the presence of small molecules such as fructose[386] or citrate[387] or polymers as capping agents. In the work of De Vos et al.[105] presents a comparative study of the reduction of aqueous silver (Ag) and gold (Au) salts to colloidal Ag and Au nanoparticles, respectively, by a gaseous, cathodic, atmospheric-pressure microplasma electrode using polyvinylalcohol (PVA) as capping agent obtaining monodisperse NP with high yield.

In this work we used the hyaluronic acid, a natural polymer, at three different molecular weights (200 kDa, 700 kDa and 1200 kDa) as stabilizing and capping agents in the microplasma synthesis of gold and silver nanoparticles. HA exhibits different biological activities depending on the molecular weights, sometimes in conflict with each other. High molecular weight HA species with > 600 kDa are space-filling, anti-angiogenic and immunosuppressive; they are involved in ovulation, embryogenesis, wound repair and tissue regeneration.[388] Instead, HA fragments of lower molecular weight are inflammatory (<1000 repeats), immunostimulatory and pro-angiogenic, and under certain conditions, low molecular weight HA species (20–200 kDa) work as an endogenous "danger signals", while even smaller fragments can ameliorate these effects.[389]

The bare and HA capped synthetized NP were characterised by UV-vis and DLS measurements and their stability during the aging time and after the electrolyte addition was investigated. Moreover, the comparison of the biological responses between AuNP and AgNP with and without HA200, HA700 and HA1200 synthetized by wet chemical and microplasma method was investigated and in particular was evaluated the cytotoxicity of the two sets of nanosystems (chemical and plasma) on the HUVEC cell line and their antibacterial activity and response on pathogenic bacteria, S. aureus ATCC 29213 and E. coli ATCC 9637 by broth microdilution assay and agar diffusion assay.

2. Materials and methods

2.1. Chemicals

HA 200 kDa (HA 200), HA 700 kDa (HA 700) and HA 1200 kDa (HA 1200) were provided by Fidia Farmaceutici spa (Italy); Sodium hydroxide (NaOH) was purchased by Honeywell Fluka (USA); Silver nitrate ($AgNO_3$) purity > 99%, D-(+)-Glucose purity ≥ 99.5 %, Tetrachloroauric (III) acid trihydrate ($HAuCl_4 \cdot 3H_2O$) purity ≥ 99.9 %, sodium chloride (NaCl) ACS reagents purity ≥ 99 %, sodium nitrate ($NaNO_3$) purity ≥ 99 %. Water was deionized (resistivity > 18.2 mΩ cm at 25 °C) and purified using a milli-Q unit (Milli-Q plus, Millipore, France). Glassware were first cleaned with aqua regia (HCl: HNO_3, 1:3 volume ratio) and then rinsed with water before starting.

Medium 200 supplemented with LSGS, 3-(4,5-dimethylthiazol-2-yl)-2,5-diphenyltetrazolium bromide (MTT reagent), dimethyl sulfoxide (DMSO) purity ≥99.7%, Tris(hydroxymethyl) aminomethane hydrochloride (TRIS-HCl) purity ≥99.7%, calcium chloride ($CaCl_2$) purity ≥97.0%, sodium sulphate ($NaSO_4$) purity ≥99.0 % were purchased from Sigma-Aldrich (USA). Brain Heart Infusion broth (BHI) and Mueller Hinton (MH) broth and agar were purchased by Oxoid (Italy); methanol were purchased by Honeywell, USA.

2.2. Plasma Synthesis of Hyaluronic acid coated Silver Nanoparticles (HA@Ag)

HA@Ag(P) synthesis was performed using atmospheric-pressure microplasma. The synthesis was carried out as follows $AgNO_3$ solution 1 mM was mixed with HA solution with a final concentration of 0.2 % or a tri-sodium citrate 5 mM to obtain the reference AgNP(P). The atmospheric-pressure microplasma was initiated at the liquid surface in a flow of 25 sccm argon (Ar) from a pressurized stainless-steel capillary tube (inner diameter = 0.6 mm) whose tip was positioned approximately 2 mm above the surface. A platinum (Pt) foil immersed in the solution served as counter electrode. The microplasma was ignited and sustained by a ballasted direct-current power supply with the capillary electrically biased at negative high voltage and the Pt foil electrically grounded to promote cathodic reduction reactions at the plasma-liquid interface. In the microplasma system, the discharge current was 3 mA (with the value of resistance 140 kΩ) and it was applied to the HA@Ag^+ solution for 15 minutes changing colour from transparent to yellow-brown (Equation 5.1). No stirring was applied (Figure 5.1). The temperature of the solution was maintained during the experiment < 5 °C using an ice bath and it was monitored by an infrared thermal camera.

$$Ag^+_{(aq)} + 1e^- \rightarrow Ag_{(s)} \qquad E° = 0.7996 \text{ V versus SHE} \qquad (5.1)$$

Figure 5.1. *Synthesis of the HA@Ag(P) and the experimental apparatus ($AgNO_3$ 1mM, HA 0.2 mg mL^{-1}).*

2.3. Plasma Synthesis of Hyaluronic acid coated Gold Nanoparticles (HA@Au)

HA@Au(P) synthesis was performed using atmospheric-pressure microplasma. The synthesis was carried out adding NaOH 7 mM to a $HAuCl_4$ solution 0.5 mM (in water for the reference or in HA 0.2 % to obtain coated NP). In the microplasma system, the discharge current was 5 mA (with the value of resistance 140 kΩ) and it was applied to the HA-Au^{3+} solution for 15 minutes changing colour from yellow to red-purple (Equation 2). No stirring was applied (Figure 5.2). The temperature of the solution was maintained < 5 °C during the experiment using an ice bath to avoid the increase of the NP size[214]; the temperature was measured by an infrared thermal camera.

$$[AuCl_4]^-_{(aq)} + 3e^- \rightarrow Au_{(s)} + 4Cl^-_{(aq)} \quad E°=1.002 \text{ V versus SHE} \tag{5.2}$$

Figure 5.2. *Synthesis of the HA@Au(P) and the experimental apparatus ($HAuCl_4$ 0.5 mM, HA 0.2 mg mL^{-1}, NaOH 7 mM).*

The reference AuNP (glucose capped) were synthetized by mycoplasma adding 5 mM of glucose solution to a solution of $HAuCl_4$ 0.5 mM. The applied discharge current was 5 mA (with the value of resistance 140 kΩ) for 15 minutes; the solution changed colour from yellow to red-purple.

2.4. Preparation of concentrate and washed nanoparticles pellet

After the synthesis, the as prepared HA@NP(P) solutions were concentrated and washed with milliQ water for two times by centrifugation at 9391 xg for about 4 minutes at 15 °C (Eppendorf Centrifuge 5417R, FA453011 Rotor, Italy), using 0.5 mL Amicon Ultra centrifugal filters (Merk Millipore, USA) with a molecular weight cut-off 30 kDa. The reference pellets of the AuNP and AgNP were obtained by double centrifugation and washing in Eppendorf at 6010 xg for 15 minutes for the AuNP and at 11766 xg for 20 minutes for AgNP. The resulting pellet was characterized by UV-visible spectroscopy and dynamic light scattering analyzer (DLS, HORIBA LB-550, USA).

2.5. UV-Visible characterization of the nanoparticles

UV-Vis spectra were recorded at 25°C using Lambda2S spectrophotometer (Perkin Elmer, USA). The measurements were performed into a 3 mL quartz cuvette with a 1 cm path length or into 300 µL quartz cuvette with 0.1 cm path length. After each synthesis and pellet preparation, UV-Vis spectrum was recorded in order to check the NP spectrum in terms of absorbance and maximum wavelength.

The optical parameters of the wavelength at the maximum of plasmon absorbance ($\lambda_{\mathrm{m}ax}$) and the corresponding Abs values were used to calculate the optical diameter (d_O, in nm) and the molar extinction coefficient (ε, in L mol^{-1} cm^{-1}), according to eq.s (5.4)-(5.6) for AgNP[215] and eqs. (5.7) and (5.8) for AuNP [216, 217]:

$$d_O = \left(\frac{1-\lambda_{\mathrm{m}ax}}{a}\right)^{-\frac{1}{b}} \qquad \text{for } 8< d <20 \text{ nm} \qquad (5.4)$$

$$d_O = \left(\frac{\lambda_{max} - a}{b}\right)^{0.5} \quad \text{for } 20 < d < 100 \text{ nm} \tag{5.5}$$

$$\varepsilon = \varepsilon^0 + Ae^{Rd} \quad \text{for } 8 < d < 30 \text{ nm} \tag{5.6}$$

$$\varepsilon = a + kd \quad \text{for } 30 < d < 100 \text{ nm} \tag{5.7}$$

where a and b are constants (a=405 and b=1.5 in eq.4; a=397 and b=9.58· 10^{-3} in eq. 5.5) as well as A and R (A=6.984 · 10^{8}; R=0.104) and a and k (a =-4.709 · 10^{10}; k=2.017 · 10^{9} in the Eq. 5.7) .

$$d_O = \frac{\lambda_{max} - 515.04}{0.3647} \tag{5.8}$$

$$\varepsilon = Bd^{\gamma} \tag{5.9}$$

where B and γ are two constants (B = 4.7 · 10^4 and γ=3.30 for $d_O \leq$ 85 nm; B = 1.6 · 10^8; γ=1.47 for d_O > 85 nm).

2.6. Dynamic light scattering characterization

DLS measurement were obtained at 25°C using dynamic light scattering particle size distribution analyzer (DLS, HORIBA LB-550, USA) with a light source 650 nm (laser diode, 5mW and a photo multiplier tube detector). The measurements were performed into a 3 mL quartz cuvette with a 1 cm path length. After each synthesis and pellet preparation, DLS measurements were carried out in order to investigate the NP hydrodynamic size.

2.7. Flocculation experiment

Gradual addition of NaCl concentrated solution (5 M) was added to the NP pellet suspensions. Sequential additions (50, 100, 200, 300, 400, 500 and 600 mM) of NaCl were carried out until complete NP aggregation was reached. Before and after every addition, UV-visible spectra of the samples were recorded using Lambda2S spectrophotometer (Perkin Elmer, USA).

2.8. ATR-FTIR spectra

The silicon wafers are cut in a surface of 0.8 cm x 1 cm and washed with methanol and iso-octane. 100 µL of sample (HA, NP or HA@NP) was putted on the cleaned silicon surface and left to dry at room temperature. The ATR-FTIR spectra was recorded using Spectrum Two™ FTIR Spectrometer (Perkin Elmer, USA).

2.9. Atomic force microscopy

Ten microliters of the NP washed pellet was put on freshly cleaved muscovite mica (Ted Pella, Inc.) and incubated at room temperature for 5 minutes. After that, the mica surface was washed with 1 mL of ultrapure water, dried under a gentle nitrogen stream, and immediately imaged. Scans were recorded using a Cypher atomic force microscopy (AFM) instrument (Asylum Research, Oxford Instruments, Santa Barbara, CA), operating in tapping-mode and furnished with a scanner at an XY scan range of 30/40lm (closed/open loop). Tetrahedral tips, made of silicon and mounted on rectangular 30lm long cantilevers, were purchased from Olympus (AT240TS, Oxford Instruments). The probes had nominal spring constants of 2N/m and driving frequencies of 70kHz. Images and sizes of particles were measured using a free tool in the MFP-3DTM offline section analysis software.

2.10. Cellular assay

Cell culture

Human umbilical vein endothelial cells (HUVEC) were cultivated in Medium200 supplemented LSGS (fetal bovine serum, 2% v/v, hydrocortisone 1 µg mL^{-1}, human epidermal growth factor, 10 ng mL^{-1}, basic fibroblast growth factor, 3 ng mL^{-1}, heparin, 10 µg mL^{-1}). The cells were grown in tissue-culture treated Corning flasks (Sigma-Aldrich, St. Louis, MO) in humidified atmosphere (5% CO_2) at 37°C (Heraeus Hera Cell 150C incubator).

Cytotoxic assay

For the cellular treatments, cells were seeded at a density of $1 \cdot 10^4$ cells/well in Medium200 supplemented with LSGS on 96 wells cell culture plates (Cellstar, Sigma Aldrich, USA). In order to treat the cells with the NP, the pellets were diluted directly in the Medium200. The evaluation of the biological effect of studied compounds on HUVEC cells viability was performed after 24 hours of incubation. Cells were quantified by the reaction with MTT reagent (0.5 mg mL^{-1}). After 90 minutes, the reaction was stopped by DMSO addition and absorbance was measured at 570 nm (Varioskan® Flash Spectral Scanning Multimode Readers, Thermo Scientific, USA). Results were expressed as % of viable cells referred to the concentration of each compound.

2.10. Bacterial strains and culture conditions

The strains tested in this study were *Escherichia coli* ATCC 9637 and *Staphylococcus aureus* ATCC 29213, belonging to the collection of Bacteriological Laboratory of Fidia Farmaceutici S.p.A. (Noto, Italy). The media were: Brain Heart Infusion broth (BHI - Oxoid, Italy) and Mueller Hinton (MH - Oxoid, Italy) broth and agar. The incubation was performed for 18-24 h at 37°C in aerobic conditions (memmert incubator, GmbH + Co. KG, Äußere Rittersbacher Straße). For the assays, the strain from stock (stored at -80°C in BHI broth with 20.0%v/v glycerol) was plated on MH agar plates; after 24h of incubation a single colony of each strain was picked to inoculate 10.0 mL of MH broth and incubated overnight (16-18 h). The overnight broth cultures were used for the assays.[390, 391]

Broth microdilution assay

The broth microdilution assay was performed inoculating *Escherichia coli* ATCC 9637 and *Staphylococcus aureus* ATCC 29213 in serial two fold dilutions of tested nanoparticles, modifying the methods described by CLSI M7-A7 for bacteria.[328, 391, 392]

The NP were dispensed in a 96-well plate performing serial dilutions in MH broth (Oxoid, Italy). For the inoculum, individual colonies or overnight broth culture were checked for purity and the densities adjusted to McFarland 1 (3.1×10^8 CFU/mL) with an equivalent OD_{630} of 0.16 – 0.2 (Bioteck Synergy ht). The bacterial suspension was then diluted 1:500 in MH broth (Oxoid, Italy) to obtain a final concentration of about 3.1×10^5 CFU/mL in each well. [328, 392]

MH broth (Oxoid, Italy) inoculated with the tested strain was used as a positive control and sterile MH broth (Oxoid, Italy) was used as negative control. The 96-well plates were incubated at 37°C for 24 h in aerobic conditions, according to CLSI M100-S23 .[348]

The Minimum Inhibitory Concentration (MIC) was the lowest concentration of nanoparticles that completely inhibited visible bacterial growth in the well, according to CLSI M27-A3.[393] The absence of growth was confirmed measuring spectrophotometrically (OD_{630} Bioteck Synergy ht) and spreading on MH agar (Oxoid, Italy) 100 µL from each well in which the bacterial growth appeared inhibited. The experiments were carried out two times in duplicate.

Agar diffusion assay

The agar well diffusion assay was performed modifying the method described by CLSI M7-A7.[328] Briefly, 200 µL of each nanoparticle suspension were deposited in 6.0 mm wells previously punched in MH agar. For the inoculum, the bacterial suspension were prepared using sterile saline solution (NaCl 0.85% w/v, Sigma Aldrich, Italy), until a turbidity corresponding to 3.1×10^5 CFU/mL, determined spectrophotometrically (OD_{630}, using a spectrophotometer Bioteck Synergy ht) as described by CLSI M7-A7 and 100 µL were spread on MH agar surface to confirm the initial vital bacterial concentration.[390, 392] The inhibitory effect was detected by an inhibition zone around the wells containing the tested nanoparticle suspension after 24 h of incubation at 37°C under aerobic conditions.[390, 392] The inhibition zone were highlighted spraying the MH plates with a water-based 3-(4,5-dimethylthiazol-2-yl)-2,5-diphenyl tetrazolium bromide (MTT) solution which gives the grown colonies a violet colouration. The chloramphenicol (30 µg/mL) was used as reference antimicrobial agent. The results were the mean of three individual experiments.

2.11. Determination of enzymatic collagenase activity after treatment with silver and gold nanoparticles

During the first phase of wound hearing the body works to attain haemostasis and collagen has key role. Moreover, during the inflammatory phase collagen adsorbs wounds exudate promoting re-epithelialization and wound repair. During the repair phase the collagen serves as biodegradable substance for cellular migration and capillary growth necessary for the repair process.[394]

The effects of tested nanoparticles on collagenase enzymatic activity was determined spectrophotometrically quantifying the fragment produced by the enzymatic reaction against external standard.[395-397] The enzymatic activity of collagenase was detected spectrophotometrically (absorbance of fragment at 320 nm), measuring the production of the fragment glicil-L-prolil-D-arginine (yellow) produced from the synthetic substrate PZ-L-prolil-L-leucyl-glicil-L-prolil-D-arginine (PZ = 4-phenylazobenzyloxycarbonyl), after extraction with a solution of ethyl acetate acidified with citric acid. For the assay, a collagenase solution (ranging from 0.35 to 1.2 nkatal/ml) was prepared using a buffer solution of 25 mM TRIS-HCl, 10mM $CaCl_2$ (pH 7.1 adjusted using HCl). The enzymatic reaction between collagenase and 1.23 mM substrate solution (PZ-L-prolil-L-leucyl-glicil-L-prolil-D-arginine dissolved in methanol using 10µl/mg of substrate) was carried out for 15 min at 37° C in a water bath and the two fragments PZ-L-prolil-L-leucine and glicil-L-prolil-D-arginine were obtained. The glicil-L-prolil-D-arginine (yellow) fragment was extracted using ethyl acetate solvent in presence of citric acid. The organic solution was dehydrated using Na_2OS_4 anhydrous and the absorbance was determined spectrophotometrically (at 320 nm, using a UV-1200 spectrometer). The substrate solution mixed with buffer solution was used as blank.

The enzymatic activity was quantified as Eq 5.10:

$$Activity\ [nkat/mL] = \frac{Sample\ Abs_{320} \times Standard\ Conc.[\mu moles/mL]}{Sample\ Abs_{320}} \times \frac{50 \times 1000}{900} \times df \qquad (5.10)$$

where: standard concentration was 0.02 μmoles/mL, 50 was the dilution factor of sample, 1000 was the conversion factor from μmoles to *n*moles, 900 were the seconds in 15 minutes, df was the dilution factor of collagenase to obtain a solution with a final activity ranging from 0.35 to 1.2 nkat/mL.

The results are expressed as a relative percentage of collagenase activity ($\%A$) calculated as Eq 5.11:

$$\%A = \frac{\text{Activity of treated sample}}{\text{Activity of not treated sample}} \times 10 \qquad (5.11)$$

3. Results and discussions

3.1. Nanoparticles synthesis and characterization

In this work, stabilized AuNP and AgNP by using HA at different molecular weight (HA200/HA700/HA1200) were synthetized by microplasma; the microplasma technology allows the direct reduction of the Ag^+ and Au^{3+} ions at the gas-liquid interface without the use of any reducing agent.[105] Colloidal dispersions of spherical metal nanoparticles and of the corresponding pellets were successfully synthetized and the most important characteristics of the samples were showed in table 5.1. In Table 5.1 was reported the comparison of the λ_{max} of the NP pellet plasmonic peaks, the optical diameter (d_0), the hydrodynamic diameter (d_h) and the concentration (molar and in NP/mL) between the pellet suspension obtained from the as prepared suspension synthetized by wet chemical synthesis and plasma synthesis.

Table 5.1. *UV-visible parameters and characterization of the pellet-NP obtained by wet chemistry and plasma reduction.*

	λ_{max} (nm)	**d_0 (nm)**	**d_h (nm)**	**nM**	**NP/mL**
AgNP(C)	395	12	32	5.6	$6.3 \cdot 10^7$
AgNP (P)	406	31	52	0.6	$3.8 \cdot 10^8$
AgNP HA200(C)	396	13	100	5.9	$5.2 \cdot 10^7$
AgNP HA200(P)	407	32	118	0.6	$3.1 \cdot 10^8$
AgNP HA700(C)	403	25	199	1	$1.2 \cdot 10^6$
AgNP HA700(P)	408	33	214	0.4	$2.0 \cdot 10^8$
AgNP HA1200(C)	401	20	220	1.7	$4.0 \cdot 10^6$
AgNP HA1200(P)	407	32	245	0.5	$2.7 \cdot 10^8$
AuNP(C)	535	66	57	0.3	$2.0 \cdot 10^4$
AuNP(P)	524	24	49	4.2	$6.1 \cdot 10^{10}$
AgNP HA200(C)	542	73	112	0.2	$8.3 \cdot 10^3$
AgNP HA200(P)	525	27	102	3.9	$3.5 \cdot 10^{10}$
AgNP HA700(C)	559	123	208	0.04	$3.7 \cdot 10^2$
AgNP HA700(P)	528	35	195	1.6	$7.0 \cdot 10^9$
AgNP HA1200(C)	565	134	234	0.1	$3.9 \cdot 10^2$
AgNP HA1200(P)	526	30	222	2.9	$1.9 \cdot 10^{10}$

Notes: C= wet chemical synthesis; P=plasma synthesis.

To notice that the pellets exhibited the expected plasmon peaks centred at λ_{max} = 395-403 nm (range of wavelength for the maximum absorbance) for spherical AgNP(C) having 10-30 nm diameter and λ_{max} = 406-408 nm for AgNP(P) having 30-40 nm diameter. Another observation was the red-shift of the λ_{max} in the presence of the HA compared to the bare NP (citrate-capped AgNP and glucose-capped AuNP): for the AgNP(C) is observable a $\Delta\lambda_{max}$ = 8 nm in the case of HA700@Ag(C) and of AgNP(P) and a $\Delta\lambda_{max}$ = 2 nm in the case of HA700@Ag(P); for the AuNP(C) is observable a high $\Delta\lambda_{max}$ = 30 nm in the case of HA1200@Au(C) and for AuNP(P) a smaller $\Delta\lambda_{max}$ =4 nm in the case of HA700@Au(P).

Starting from λ_{max} it was possible to calculate the optical diameter of the all synthetized nanoparticles using the Equation 2.4, 2.5 and 2.8 (see the Chapter 2, Section 2.5, materials and methods). It is possible to observe that the d_0 of the AgNP synthesised by wet chemical reduction, ranged from 12 nm for AgNP(C) to 25 nm for HA700@AgNP(C), were smaller than the optical diameters of the AgNP(P) d_0 ranged from 31 for AgNP(P) to 33 nm for HA700@AgNP(P). On the contrary, the d_0 of the AuNP synthesised by wet chemical reduction is ranged from 66 nm to 134 nm for AuNP(C) and HA700@AuNP(C) respectively, were bigger than the optical diameters of the AuNP(P) d_0 ranged from 24 to 35 nm for AuNP(P) and HA700@AuNP(P).

Comparing d_0 and d_h of the AuNP(C) and AgNP(C) showed in Table 5.1, it is possible to evidences a larger difference between the hydrodynamic size and the optical size in the case of HA@Ag(C), HA@Ag(P) and HA@AuNP(P) (with a percent of variation of 87%, 85% and 82%, respectively), instead smaller difference was observed in the case of HA@Au(C) (43%).

The concentration of silver nanoparticles pellet are ranged between 0.40 nM ($2.00 \cdot 10^8$ NP/mL) and 0.58 nM ($3.76 \cdot 10^8$ NP/mL) for the HA700@Ag(P) and AgNP(P), respectively and from 1.00 nM ($1.24 \cdot 10^6$ NP/mL) to 6 nM ($6.33 \cdot 10^7$ NP/mL) for HA700@Ag(P) and AgNP(P), respectively; the pellet concentration of gold nanoparticles are ranged between 0.04 ($3.66 \cdot 10^2$ NP/mL) and 0.28 nM ($1.96 \cdot 10^4$ NP/mL) for HA700@Au(C) and AuNP, respectively and between 1.64 nM ($6.97 \cdot 10^9$ NP/mL) for the HA700@Au(P) and 4.62 nM ($6.09 \cdot 10^{10}$ NP/mL) for the AuNP(P).

In Table 5.1, it is possible to observe that, compared with the "bare" NP, with the increase in the HA molecular weight it is observable a red-shift of the λ_{max} relative to the increasing in NP optical diameter due to the wrapping of the NP by the HA chain.[220, 221, 398, 399]

In Table 5.1, it is possible to observe the increasing in the d_0 for the HA@NP(P) compared to the NP(P).[400] Shimmin et al. widely discussed about this effect and demonstrated that in the presence of polymers, the NP stabilizing process occurs and the hydrodynamic size increase that leads to the formation of bigger nanoparticles; the polymer molecules which interact with the nanoparticle surfaces with a sufficiently dense coating provide a steric barrier against aggregation. [220, 231]

Taken together, these results can be indicative of an actual coating of the metal nanoparticle by HA, with the resulting increase in the nanoparticle optical and hydrodynamic diameter due to the coating of the metal core by the hyaluronan polymer chains.[220, 221]

A further characterization of the hybrid systems was obtained by using the AFM technique in order to scrutinize the difference in morphology of the metal-HA nanoparticles.

The figure 5.3 shows the phase, amplitude and height AFM images of the HA200, HA200@Ag(C), HA200@Au(C), HA200@Ag(P) and HA200Au(P)

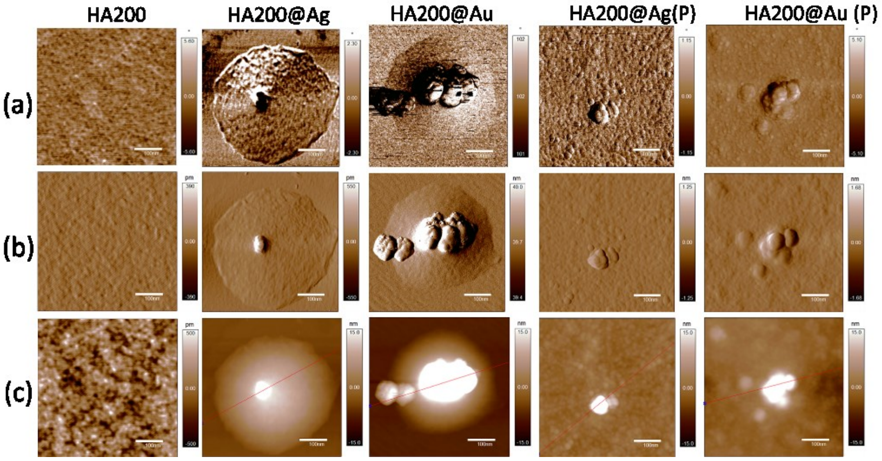

Figure 5.3. *AFM images of HA200, HA200@Ag(C), HA200@Au(C), HA200@Ag(P) and HA200@Au(P) from the pellet suspension; (a) phase, (b) amplitude and (c) height images.*

In Figure 5.3, the AFM images of the HA200 shows a layer of HA macromolecules < 0.5 nm thick, indicating aggregation forces between chains as well as rather strong hydrophilic interactions between mica and HA. This kind of structure is reported in literature[401] and it is typical of the low molecular weight HA which tended to form a network lying on the substrate, when deposited from aqueous solution. The apparent stiffness of HA molecules in these latter images should not reflect rigidity of single HA chains, but rather suggest that during slow dehydration HA molecules stick together and to the mica.

HA200@Ag(C) and HA200@Au(C) images (Figure 5.3) show the typical structure of the polymer-coated NP and as suggested by the work of Almalik et al.,[402] it is possible to observe the presence of an HA monolayer around the core of aggregated particles. In particular the HA200@Au(C) seems to an NP aggregate compared to the HA200@Ag(C). The dimensions obtained by high section were 25 nm and 60 nm for HA200@Ag(C) and HA200@Au(C), respectively and were 27 nm and 30 nm for HA200@Ag(C) and HA200@Au(P), respectively (Figure 5.4). The HA200@Ag(P) and HA200@Au(P) are show different features compared to the correspondent wet chemical reduction synthesised ones and exhibited different microscopic characteristics that were typical of globular hybrid-polymers metal nanoparticles systems.[403]

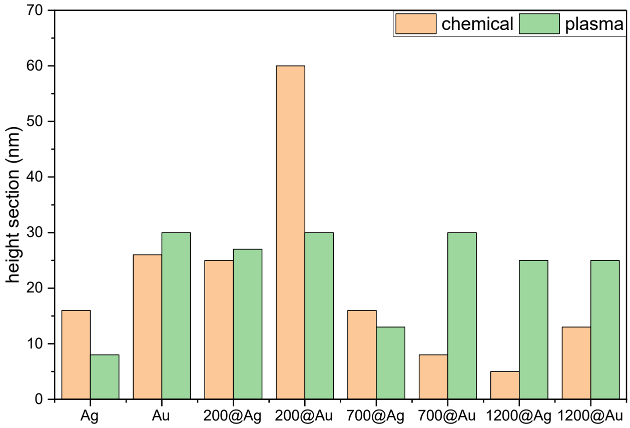

Figure 5.4. *Height section of the plasma and wet chemical synthetized nanoparticles*

Figure 5.5 showed the phase, amplitude and height AFM images of the HA700, HA700@Ag(C), HA700@Au(C), HA700@Ag(P) and HA700Au(P).

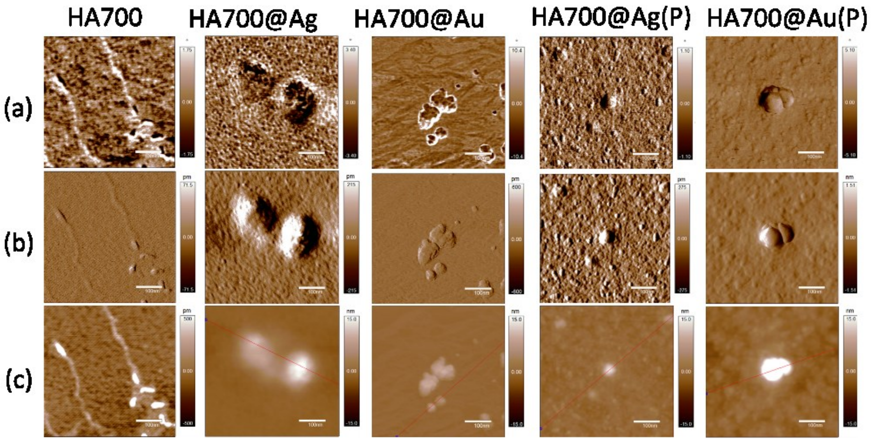

Figure 5.5. *AFM images of HA700, HA700@Ag(C), HA700@Au(C), HA700@Ag(P) and HA700Au(P) from the pellet suspension; (a) phase, (b) amplitude and (c) height images.*

The AFM images of the HA700 (Figure 5.5) shows a different assembly compared to the HA200 (Figure 5.3). As reported by Cowman et al.,[404] HA700 appeared in an extended structural forms as a result of intramolecular association. Wide loops and sharp hairpin-like turns were formed by antiparallel association of chain segments into stabilizing structures. The HA200@Ag(C), HA700@Au(C) and HA700@Au(P) show a spherical and poly-globular structure due to the wrapping of the NP by HA; the HA700@Ag(P) AFM image presented two single nanoparticles as a wrapped and spherical structure. The structure in figure 5.5 are typical of the polymer-coated metal nanoparticle systems as reported by Wang et al.[405] were dextran is used as a protecting agent as well as a reduction agent for the synthesis of metal nanoparticles. The coating of dextran to the nanoparticle surface ensures a high level of biocompatibility, enabling the as-produced particles to be used directly for biological applications without further surface functionalization. The 3D AFM image shows the well dispersed spherical nanoparticles surrounded by dextran molecules. The synthesized nanoparticles are coordinated with hydroxyl group of dextran molecules which in turn prevents their large-scale aggregation.[406]

The dimensions obtained by high section were 15 nm and 8 nm for HA700@Ag(C) and HA700@Au(C), respectively and were 12 nm and 30 nm for HA700@Ag(P) and HA700@Au(P), respectively (Figure 5.4).

In figure 5.6 showed the phase, amplitude and height AFM images of the HA1200, HA1200@Ag(C), HA1200@Au(C), HA1200@Ag(P) and HA1200Au(P).

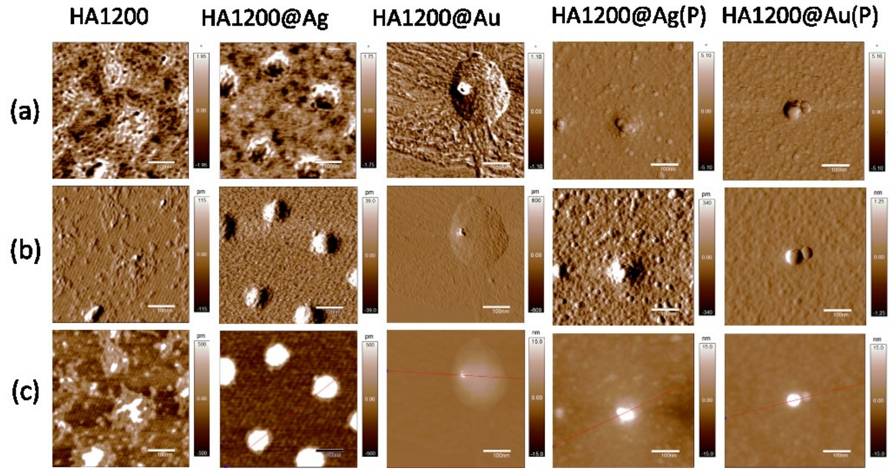

Figure 5.6. *AFM images of HA1200, HA1200@Ag(C), HA1200@Au(C), HA1200@Ag(P) and HA700Au(P) from the pellet suspension; (a) phase, (b) amplitude and (c) height images.*

The HA1200 AFM images shows the formation of amorphous and globular structures and that indicated that hydrophobic interactions between chains may exert a pivotal role in aqueous solution.[401]

While the HA1200@Ag(C) exhibited a spherical structure with a height section of ~ 5 nm, the HA1200@Ag(P) exhibited a poly-globular structure with a height section of ~ 25 nm. The HA1200@Au(C) exhibited a structure very similar to HA200@Ag(C) and HA200@Au(C) (figure 5.3) with a height section of 14 nm, the HA1200@Ag(P) exhibited a poly-globular structure with a height section of ~ 25 nm (figure 5.4).

In Figure 5.7 showed the phase, amplitude and height AFM images of the AgNP(C), AuNP(C), AgNP(P), AuNP(P).

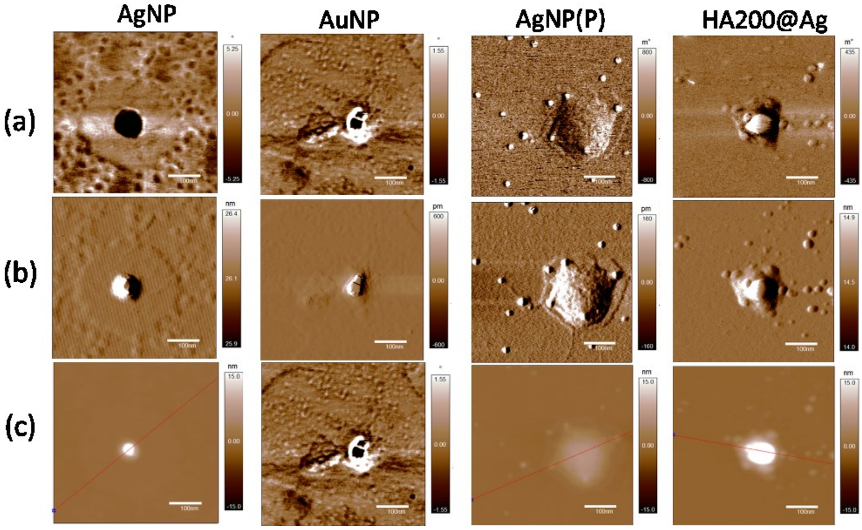

Figure 5.7. *AFM images of* AgNP, AuNP, AgNP(P), AuNP(P) *from the pellet suspension; (a) phase, (b) amplitude and (c) height images.*

All the NPs showed a spherical morphology as reported in literature[201, 387, 407] with a height section of 16 nm for AgNP(C) and 25 nm for AuNP(C); the plasma synthetized NP exhibited height section of ~ 25 nm for AgNP(P) and 8 nm for AuNP(P) (Figure 5.4).

To have further evidences of the interactions between NPs synthetized by microplasma and HA, IR spectra of the hybrids systems were carried out Figure 5.8.

The Figure 5.8 shows the characteristic IR spectra of the hyaluronic acid at three different molecular weight (HA200, HA700 and HA1200) with and without AuNP(P) and AgNP(P); it is possible to observe the characteristic peaks at about 3400-3200 cm^{-1} for the OH and NH stretching, at 2950-2850 cm^{-1} for the C–H$_2$ symmetrical stretching, at about 1600-1500 cm^{-1} can be attributed to C=O stretching and N–H bending, at about 1480-1350 cm^{-1} for the C–H$_2$ bending peak and at 1140-985 cm^{-1} for the C–O-C stretching of the proteoglycan sugar ring.[242]

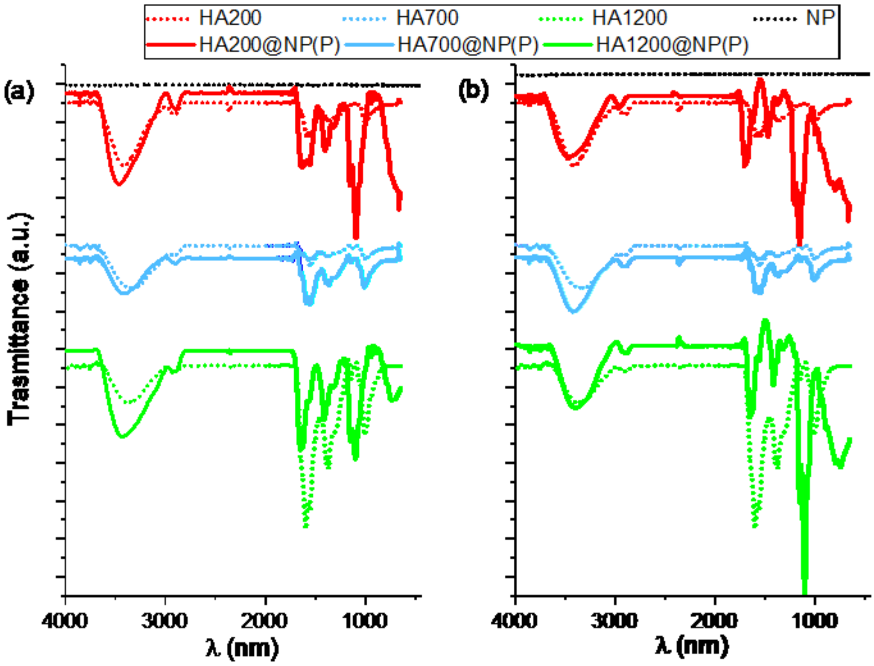

Figure 5.8. *IR/ATR spectra of the (a) AgNP(P) (black solid line), HA200@Ag(P) (red solid line), HA700@Ag(P) (blue sold line), HA1200@Ag(P) (green solid line), HA 200 (red dot line), HA700 (blue dot line), HA1200 (green dot line) and (b) AuNP(P) (black solid line), HA200@Au(P) (red solid line), HA700@Au(P) (blue sold line), HA1200@Au(P) (green solid line), HA 200 (red dot line), HA700 (blue dot line), HA1200 (green dot line)*

It is possible to observe (Figure 5.8 and Table 5.2) that the –OH stretching at about 3350-3400 cm^{-1} in the ATR-FTIR spectra of HA at three molecular weight exhibits a blue shift in the ATR-FTIR spectra of HA@NP. It suggests that the interaction between the hydroxyl groups of the HA and the NP occurs in solution; moreover, the signal of the -C=0 stretching and –NH bending 1600-1500 cm^{-1} of the HA@NP exhibit un blue shift compared to the same HA signals and it suggest that these signals attend in the NP suspension stabilizing process.[243-245]

Table 5.2. *Peak position (cm^{-1}) of the characteristic transmittance spectra of the hyaluronic acid.*

	-OH/-NH stetch.	**-CH$_2$ stretch.**	**-C=0 stretch. –NH bend.**	**-CH$_2$ bend.**	**C-O-C stretch.**
HA200	3414	2895	1556	1372	1011
HA700	3355	2888	1558	1368	1011
HA1200	3379	2888	1601	1396	1012
AgNP(P)	-	-	-	-	-
HA200@Ag(P)	3460	3289	1604	1405	1095
HA700@Ag(P)	3413	2890	1558	1369	1013
HA1200@Ag(P)	3423	2926	1652	1412	1099
AuNP(P)	-	-	-	-	-
HA200@Au(P)	3459	2943	1696	1467	1156
HA700@Au(P)	3413	2894	1566	1367	1008
HA1200@Au(P)	3397	2891	1650	1395	1099

The stability of the NPs during 15 days of aging time was investigate. Figure 5.8 shows the variation of the λ_{Max} as a function of the aging time (0, 3, 6, 9, 12, 15 days) of the AgNP, AuNP, AgNP(P) and AuNP(P) plasmonic peaks; in particular the full symbols represent the nanoparticles synthesised by wet chemical reduction and the open symbols the microplasma synthetized ones; the orange colour represents the AgNP and the wine represents the AuNP.

Figure 5.8 shows that AgNP and AuNP both wet chemical and plasma synthesized exhibit two different aging trends: AgNP aging (with and without HA) shows λ_{max} red-shift of the plasmonic peaks (in all cases the $\Delta\lambda_{max}< 1$ nm) due to the formation of bigger aggregate compared with the as prepared suspension.[235] Instead, for the AuNP(P) it is possible to observe that the $\Delta\lambda_{max}$ decrease and $\Delta\lambda_{max} < 1$ nm in all cases except for the HA1200@Au(P) and HA200@AuNP with $\Delta\lambda_{max} = 2.7$ and $\Delta\lambda_{max} = 1.3$ nm, respectively at 15 days of aging time. The AuNP suspension initially contains aggregates of various sizes at the initial growth stages. It might be possible that, at this stage, the nuclei particles have multiple sizes. UV-visible absorption spectra after 15 days of aging illustrate a $\Delta\lambda_{max} < 0$ that is a clear indication of the existence of the small and stable NP in colloidal form.[236] It is probable that the big and not stable NP present in the suspension at the time 0 stick on the inner walls of the vial; together with this effect the NP nucleation take place leading to further formation of smaller NP.

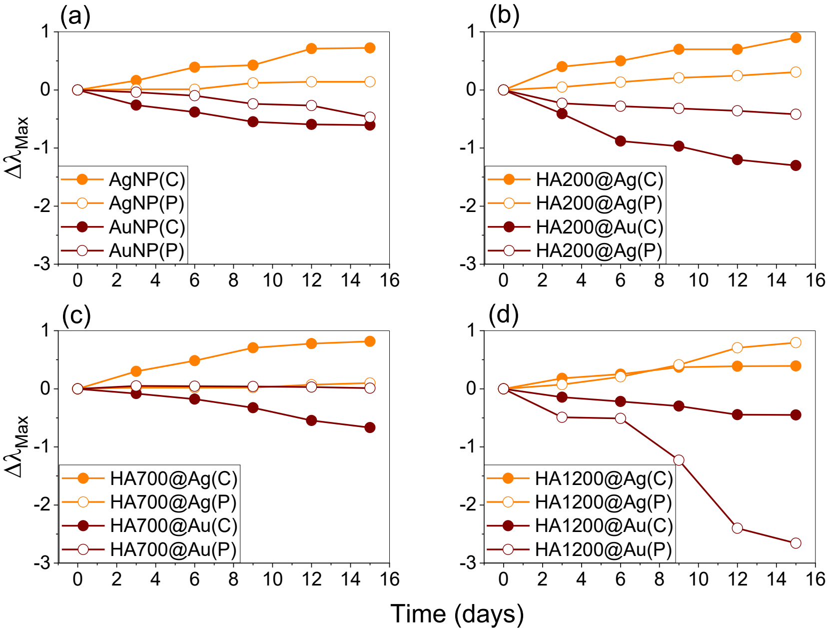

Figure 5.8. *(a) $\Delta\lambda_{max}$, of bare NPs and (b) $\Delta\lambda_{max}$ HA200@NP, (c) $\Delta\lambda_{max}$ HA700@NP, (d) $\Delta\lambda_{max}$ HA1200@NP as a function of the aging time (0, 3, 6, 9, 12, 15 days).*

These observations on the AuNP(P) aging were verified by TEM measurements. The TEM images (Figure 5.9) show a decrease in size of the HA200@Ag(P) after three days of aging time. Moreover, as shown in the size distribution (Figure 5.10), the HA200@Ag(P) aged (compared to the HA200@Ag(P) as prepared) have a tight range of the NP size. In fact, in Figure 5.10 it is possible to notice that the size of the as prepared HA200@Ag(P) is ranged between 20-30 nm with a percentage of about

45%, on the other hand three days after the nanoparticles are mainly ranged between 0 and 10 nm with more than 80% of NP percentage and only the 20% of NPs in a range size of 10 and 20 nm.

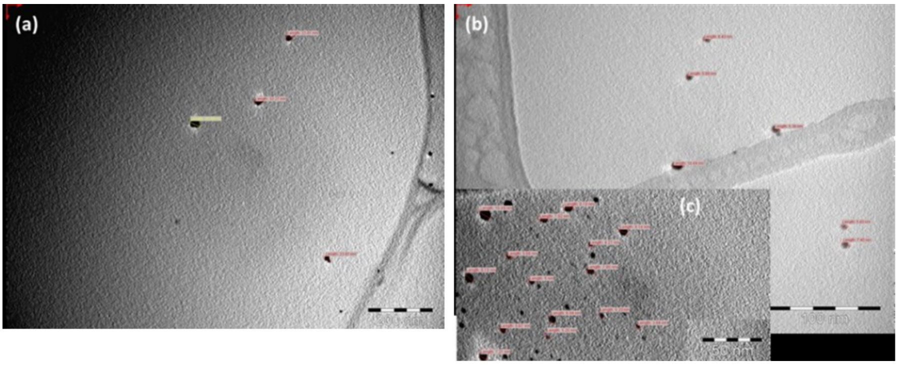

Figure 5.9. *TEM image of systems: (a) HA200@Au(P) as prepared and (b) and (c) Hy200@Au(P) 3 days aged;*

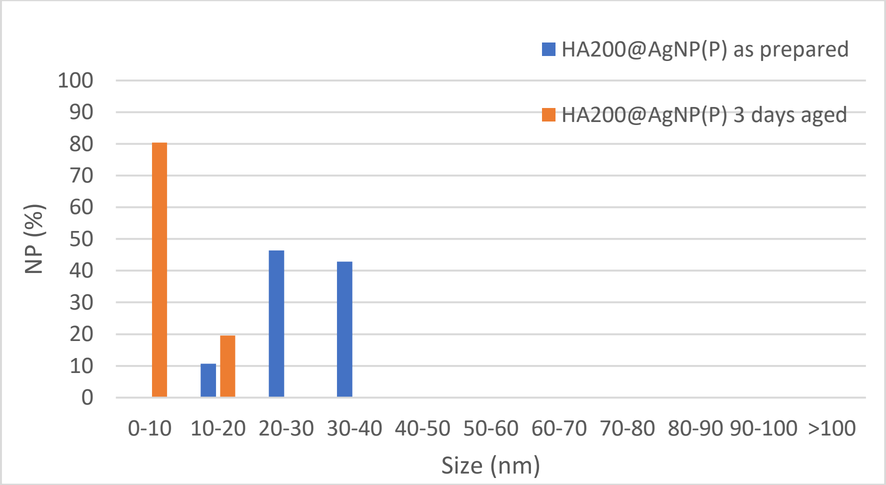

Figure 5.10. *Size distribution and percentage of nanoparticles of the systems: blue Hy200@Au(P) as prepared (i= 5mA, t=15min, $HAuCl_4$ 0.5 mM), N (number of particles)= 52, (d)orange HA200@Au(P) 3 days aged (i=5mA, t=15min, $HAuCl_4$ 0.5 mM), N= 54.*

A similar effect is confirmed by TEM images of the HA700@Au(P) (Figure 5.11.a and Figure 5.11.b); the NP size distribution changes after three days of aging (Figure 5.12) shows a tight range of size (between 10 and 40 nm) compared to the wide size range of the NPs as prepared (between 0 and 60 nm); these changes in the size distribution are confirmed by the decrease of FWHM during the aging time.

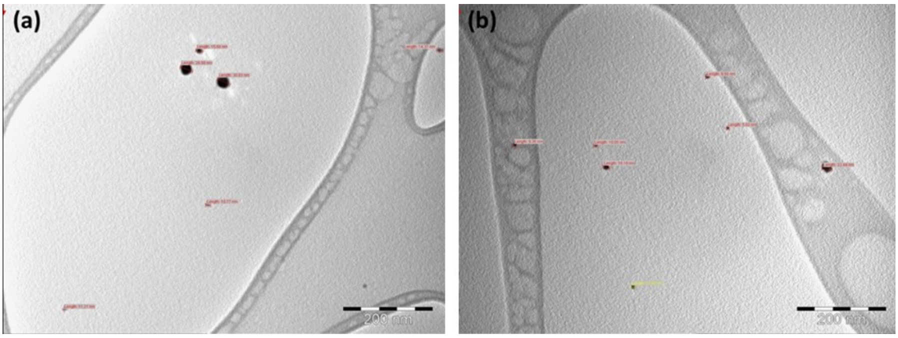

Figure 5.11. TEM image of systems: (a) HA700@Au(P) as prepared and (b) HA700@Au(P) 3 days aged.

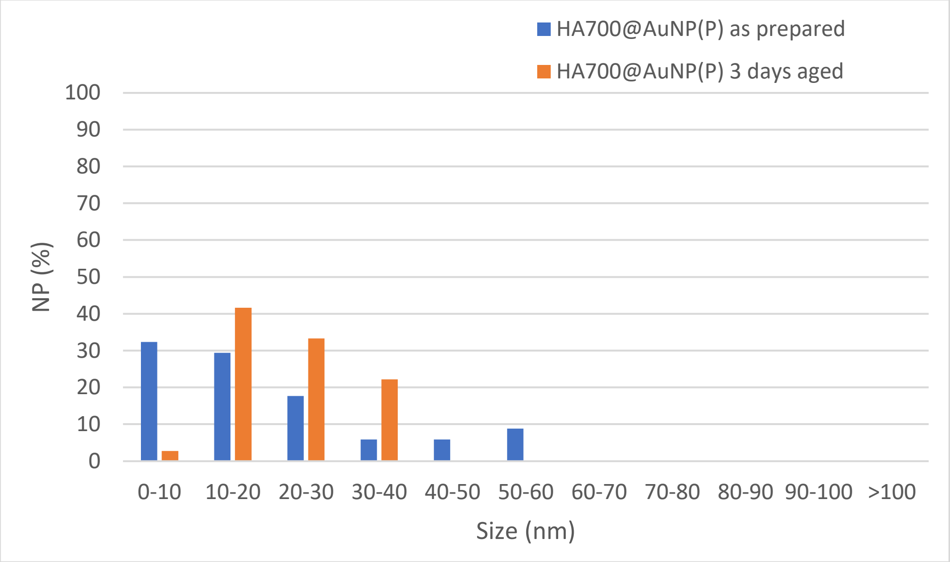

Figure 5.12. Size distribution and percentage of nanoparticles of the systems: (c)blue HA700@Au(P) as prepared (i= 5mA, t=15min, $HAuCl_4$ 0.5 mM), N (number of particles)= 51, (d) orange HA700@Au(P) 3 days aged (i=5mA, t=15min, HAuCl4 0.5 mM), N= 50.

Moreover, this effect can be explained in terms of different effects of the HA on the NP size evolution, namely a digestive ripening effect for gold,[237] by which the size of the NP decreased prompted by the interaction with the hyaluronan chains, and an Ostwald type growth for silver,[238] likely due to a lower level of interaction between the polysaccharide chains and the metal atoms.

Figure 5.13 shows the capacity of the hyaluronic acid to stabilize the NP suspension and avoid flocculation after addition of the aggregation

NaCl concentration; this concentration differed for AgNP(P) and AuNP(P). The charged shell of the NP allows to maintain the NP in suspension thanks to their electrostatic repulsions. The flocculation process occurs when the addition of an electrolyte to the suspension lead to the neutralization of the superficial NP charge forming big aggregate.[239]

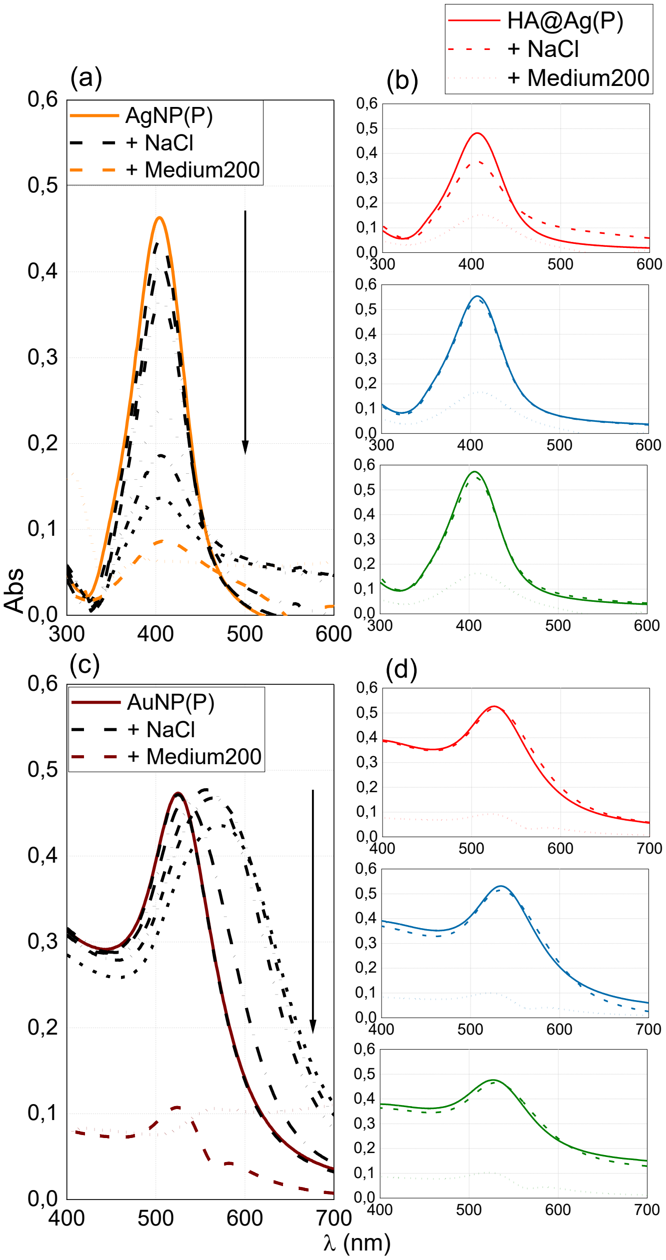

Figure 5.13. *UV-visible spectra of (a) bare AgNP(P) (0.58 nM = 3.76 x 10^8 NP/mL) before (solid line) and after (dashed lines) the gradual addition of a concentrated NaCl aqueous solution in the concentration range from 50 mM to 0.6 M. (b) HA-coated nanoparticles before (solid line) and after (dashed lines) the direct addition of: 0.6 M NaCl*

to HA200@Ag(P) (red curves, 0.55 nM = 3.07 · 10^8 NP/mL), HA700@Ag(P) (blue curves, 0.40 nM = 2.00 · 10^8 NP/mL) and HA1200@Ag(P) (green curves, 0.50 nM = 2.69 · 10^8 NP/mL). (c) Bare AuNP(P) (4.62 nM = 6.09 x 10^{10} NP/mL) before (solid line) and after (dashed lines) the gradual addition of a concentrated NaCl aqueous solution in the concentration range from 50 mM to 0.5 M. (d) HA-coated nanoparticles before (solid line) and after (dashed lines) the direct addition of: 0.6 M NaCl to HA200@Au(P) (red curves, 3.91 nM = 3.51 · 10^{10} NP/mL), HA700@Au(P) (blue curves, 1.63 nM = 6.97 · 10^9 NP/mL) and HA1200@Au(P) (green curves, 2.85 nM = 1.94 · 10^{10} NP/mL).

The Fig. 5.13a shows the gradual addition of a NaCl solution, ranging from 50 mM to 600 mM, to the AgNP(P) suspension 0.62 nM (5.81 · 10^8 NP/mL); it is possible to observe a modification of the plasmonic peak shape and its gradual decrease in the absorbance due to the aggregation of the AgNP suspension. The complete flocculation was observed for the 600 mM NaCl addition. The direct addition of NaCl 600mM to the HA@Ag(P) (Fig. 5.13b) did not lead to the complete aggregation of the suspension, in fact the plasmonic peak features was maintained but it is possible to observe a small decrease in the absorbance of 3.5 % and 5% for the HA700@Ag(P) and HA1200@Ag(P), respectively. In the case of HA200@Ag(P) the decrease of the absorbance is about of 23 % and it is possible to observe an increase of the 21 % of the FWHM after electrolyte addition. It could be due to the better stabilization of the NPs by the higher MW HA compared to the HA 200 kDa.[220, 408] In all cases the HA exhibits the protective action against aggregation after NaCl addition.[240]

The resuspension of the silver nanoparticles in Medium200 leads to the partial aggregation of the NP due to the interaction with the proteins of the fetal bovine serum, of the human epidermal and basic fibroblast growth factor and other molecules present in the cell medium.[409]

The Fig. 5.13c shows the gradual addition of a NaCl solution, ranging from 50 mM to 500 mM, to the AuNP(P) suspension 1.34 nM (8.88 · 10^9 NP/mL); it is possible to observe a modification of the plasmonic peak shape and its gradual decrease in the absorbance due to the aggregation of the AuNP(P) suspension. The complete flocculation was observed for the 500 mM NaCl addition. The direct addition of NaCl 500mM to the

HA@Au(P) (Fig. 5.13d) did not lead to the complete aggregation of the suspension, in fact the plasmonic peak features was maintained but it is possible to observe a small decrease in the absorbance of 1 % for the HA200@Au and about 3% for HA700@Au and HA1200@Au. It could be due to the HA protective action against aggregation after NaCl addition.[241] The resuspension of the gold nanoparticles in Medium200 leads to the complete aggregation of the NP due to the interaction with the proteins of the fetal bovine serum, of the human epidermal and basic fibroblast growth factor and other molecules present in the cell medium. The aggregation of gold nanoparticles after the interaction with proteins is an important process exploited in nanomedicire to develop highly specific immunoassay system for antibodies. The assay is based on the aggregation of gold nanoparticles that are coated with protein antigens in the presence of their corresponding antibodies. The aggregation of the gold nanoparticles results in an absorption change at 620 nm that is monitored using an absorption plate reader.[410]

3.2. Cellular assay

In this work, the cytotoxicity of the plasma synthetized AgNP(P) and AuNP(P) with and without HA at three different molecular weight was compared with chemical synthetized NP. HUVEC cell line was used to scrutinize the possible biological application of these systems, starting from the washed and concentrated pellets. In Figure 5.14a, it is possible to notice that AgNP(C) and HA@Ag(C) exhibit higher cytotoxicity compared to the same systems obtained by plasma methods. In fact, according to the literature,[334-337] AgNP(C) exhibits a significant cytotoxicity with a cell viability of about 65%; instead the cell viability of the AgNP(P) is still not significant.

This is an interesting result because of pectin-capped AgNP(P) show a strong cytotoxicity against cancer cells such as human melanoma cells at concentration of about 10 μg/mL.[411] In the primary cell culture such as mouse fibroblast and liver cells the AgNP synthetized by microplasma, as revealed by XTT assay, exhibit an IC50 of 61 μg/mL and 449 μg/mL, respectively.[412] The chemical synthetized AgNP does not exhibits cytotoxicity on HUVEC line at concentration less than 10 µg/mL.[413] This effect could mean a higher resistance of the primary cell line to the AgNP cytotoxicity.

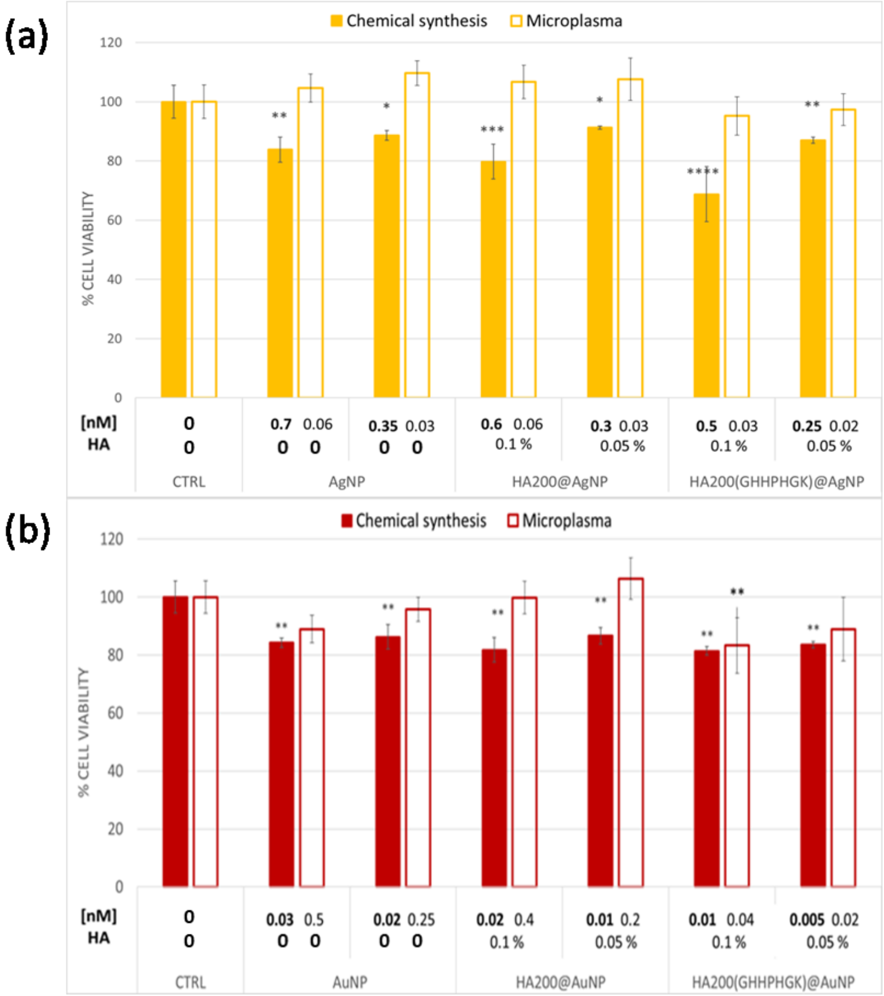

Figure 5.14. *Dose response experiment for HUVEC cell line. Cells were incubated for 24h with (a) AgNP(P), HA200@Ag(P), HA700@Ag(P), HA1200@Ag(P), AgNP(C), HA200@Ag(C), HA700@Ag(C), HA2100@Ag(C) and (b) 24h with AuNP(P), HA200@Au(P), HA700@Au(P), HA1200@Au(P), AuNP(C), HA200@Au(C), HA700@Au(C), HA2100@Au(C). Results are presented as mean ± SD of triplicate experiments and normalized to the values for control untreated cells. *p≤0.05, **p≤0.01, *** p≤0.001, **** p≤0.0001 statistical significance with respect to the control (one-way analysis of variance).*

Figure 5.14b demonstrates a significant cytotoxic response of AuNP© and HA@Au(C) compared to the control (*$p \leq 0.05$, **$p \leq 0.01$, one-way analysis of variance) with a cell viability more than 80%; instead the AuNP(P) and HA@Au(P) that do not provoke cytotoxicity compared to the control. This effect confirms that chemical and plasma synthetized AuNP do not demonstrate a strong cytotoxicity and do not affect significantly the growth and the viability of the primary cell line.[414, 415]

3.3. Bacterial assays

Broth microdilution assay

Broth microdilution and agar diffusion are the most commonly used methods to determine the minimal inhibitory MIC of antimicrobial agents and other substance that could kill or inhibit the growth of bacteria. In order to investigate the antibacterial capability of tested NP both methods are used in this study.[416]

Using broth microdilution assay, all AgNP and AuNP synthesised by wet chemical reduction showed inhibitory activity against both tested strains, at a concentration (µg/mL) much lower than chloramphenicol (CHL) used as control (Table 5.3).

Table 5.3. *Inhibitory activity of silver and gold nanoparticles synthesised by wet chemical and plasma reduction against Escherichia coli ATCC 9637 and Staphylococcus aureus ATCC 29213 using broth dilution assay in comparison with chloramphenicol (CHL).*

	Minimal inhibitory concentration (MIC)			
	Escherichia coli **ATCC 9637**		***Staphylococcus aureus*** **ATCC 29213**	
	nM	ng/mL	nM	ng/mL
AgNP(C)[1]	2.3	2.62	9.3	10.5
AgNP(P)[2]	5.8	0.3	-	-
HA200@Ag(C)[1]	3.5	3.26	14	13.0
HA200@Ag(P)[2]	2.8	0.1	5.5	0.3
HA700@Ag(C)[1]	5.5	3.86	22	15.4
HA700@Ag(P)[2]	2.5	0.1	5.1	0.2
HA1200@Ag(C)[1]	7.4	4.30	14.8	86
HA1200@Ag(P)[2]	2.5	0.1	5.0	0.2
AuNP(C)[1]	0.6	14.5	0.6	14.5
HA200@Au(C)[1]	0.6	0.01	0.6	0.01

HA700@Au(C)[1]	0.4	0.01	0.4	0.01
HA1200@Au(C)[1]	-	-	-	-
CHL	25 x 10^3	8.0 x 10^3	25 x 10^3	8.0 x 10^3

Notes: [1] the nanoparticles were tested at the following concentration ranges: AgNP(C) from 9.3 nM (= 10.5 ng/mL) to 1.2 nM (= 1.31·ng/mL); HA200@Ag(C) from 14 nM (= 13 ng/mL) to 1.75 nM (= 1.6 ng/mL); HA700@Ag(C) from 22 nM (= 1.54 ng/mL) to 2.8 nM (= 1.93·ng/mL); HA1200@Ag(C) from 15 nM (= 8.60 ng/mL) to 1.8 nM (= 1.07·ng/mL); AuNP(C) from 0.6 nM (= 0.02 ng/mL) to 0.07 (= 0.002 ng/mL); HA200@Au(C) from 0.6 nM (= 0.01 ng/mL) to 0.07 nM (= 0.002 ng/mL); HA700@Au(C) from 0.4 nM (= 0.01 ng/mL) to 0.05 nM (= 0.001 ng/mL); HA1200@Au(C) from 0.2 nM (= 0.005 ng/mL) to 0.03 nM (= 0.001 µg/mL.

[2] The nanoparticles were tested at the following concentration ranges: AgNP(P) from 5.8 nM (= 0.3 ng/mL) to 0.7 nM (= 0.04 µg/mL); HA200@Ag(P) from 5.5 nM (= 0.3 ng/mL) to 0.7 nM (= 0.03 ng/mL); HA700@Ag(P) from 5.1 nM (= 0.2 ng/mL) to 0.6 nM (= 0.003 ng/mL); HA1200@Ag(P) from 5.0 nM (= 0.2 ng/mL) to 0.6 nM (= 0.003 ng/mL); AuNP(P) from 29.8 nM (= 0.7 ng/mL) to 3.7 nM (= 0.01 ng/mL); HA200@Au(P) from 19.5 nM (= 0.5 ng/mL) to 2.4 nM (= 0.06g/mL); HA700@Au(P) from 8.2 nM (= 0.2 ng/mL) to 1.02 nM (= 0.03 ng/mL); HA1200@Au(P) from 14.2 nM (= 0.5 ng/mL) to 1.8 nM (= 0.04 ng/mL); chloramphenicol was tested at the concentration range from 1.24 x 10^5 to 5 x 10^2 µg/mL.

All AuNP(C) showed the same MIC value against both tested strains, *Escherichia coli* ATCC 9637 and *Staphylococcus aureus* ATCC 29213, with a concentration ranging from 0.42 to 0.58 nM. In particular, the highest inhibitory activity was showed by HA700@Au(C), with a MIC value of 0.42nM.

The AuNP(C), not coated with HA, and HA200@Au(C) at lowest tested molecular weight, showed the lowest inhibitory activity with MIC values of 0.58 and 0.55 nM, respectively, against both *E. coli* ATCC 9637 and *S. aureus* ATCC 29213. Our results obtained using AuNP(C) was different from the most popular results reported in literature which exhibit a more pronounced activity against Gram-negative bacteria than Gram-positive ones. [79, 343, 346, 417]

The AgNP(C) showed MIC values higher than AuNP(C), ranging from 2.31 to 7.38 nM. This results were confirmed by literature.[342, 347] The inhibitory activity change with molecular weight of coating hyaluronic acid and was different between the two tested strains, for each nanoparticle suspension. The highest inhibitory activity was showed by AgNP(C) against *E. coli* ATCC 9637 which a MIC value of 2.31 nM. The HA200@Ag(C) excited a 1.5-fold inhibitory activity, lower than that of AgNP(C) alone, with a MIC value of 3.5 nM for *E. coli* ATCC 9637. The

HA700@Ag(C) showed a lethal concentration of 5.50 nM against *E. coli* ATCC 9637. The lowest inhibitory activity was showed by HA1200@Ag(C), with a lethal concentration of 7.38 nM. All tested AgNP showed a lower inhibitory activity against the Gram-positive strain *S. aureus* ATCC 29213. This results could be associated with the cell wall structure that has less peptidoglycan content in Gram-negative bacteria as compare to Gram-positive bacterial cell wall.[417] In particular, the inhibitory activity was 4-fold lower for AgNP(C), HA200@Ag(C) and HA700@Ag(C) and 2-fold lower for HA1200@Ag(C).

All plasma synthetized AgNP showed inhibitory activity against *E. coli* ATCC 9637 and *S. aureus* ATCC 29213, except AgNP(P) which did not inhibit the growth of Gram-positive tested strain (Table 5.3). The AgNP(P) showed MIC values ranging from 0.90 to 5.82 nM, much lower than that chloramphenicol (CHL) ones, used as control. In particular, the inhibitory activity of HA200@Ag(P), HA700@Ag(P), HA1200@Ag(P) against *S. aureus* ATCC 29213 was 2-fold lower than that observed against *E. coli* ATCC 9637. This results confirmed a more pronounced activity against Gram-negative bacteria than Gram-positive ones. [79, 343, 346, 417]

The HA1200@Ag(P), HA700@Ag(P) and HA200@Ag(P) showed a good inhibitory activity with a MIC values of 2.47 nM, 2.54nM and 2.75nM, respectively. The lowest inhibitory activity, was observed for AgNP(P) against *E. coli* ATCC 9637 (MIC value of 5.82 nM). This results could be due to the absence of the HA that promote the internalization of the nanosystems through the cell wall.[417]

The AuNP(P) showed a MIC value of 29.80 nM against *E. coli* ATCC 9637 but HA@Au(P) did not showed inhibitory activity against both tested strains.

It is important to consider that a recent study reported a possible resistance of AgNP E. coli 013, *P. aeruginosa* CCM 3955 and *E. coli* CCM 3954 after repeated exposure to AgNP. This resistance seems to be only phenotypic and due to the production of adhesive flagellum protein flagellin which lead to the aggregation of NP.[418]

Agar diffusion assay

Using agar diffusion assay, all AgNP synthetized by wet chemical method (Figure 5.16) and all HA@Ag(P) (Figure 5.17) showed inhibitory activity against tested strains.

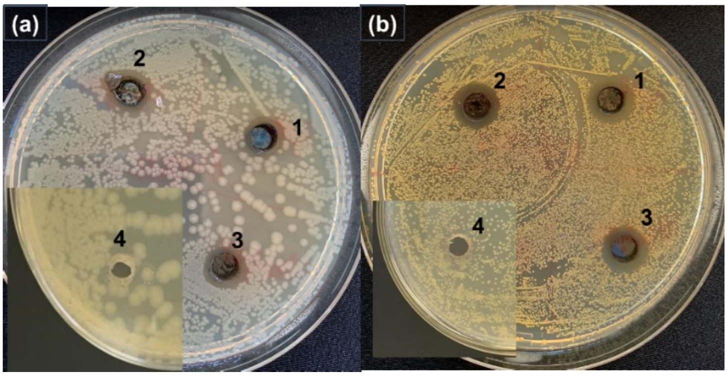

Figure 5.16. *Clear zones of inhibition demonstrated by silver nanoparticles synthesised by wet chemical reduction, using agar diffusion assay. (a) Plate of MH spread with Escherichia coli ATCC 9637: (1) AgNP(C), (2) HA200@Ag(C), (3) HA700@Ag(C), (4) HA1200@Ag(C); (b) Plate of MH spread with Staphylococcus aureus ATCC 29213: (1) AgNP(C), (2) HA200@Ag(C), (3) HA700@Ag(C), (4) HA1200@Ag(C).*

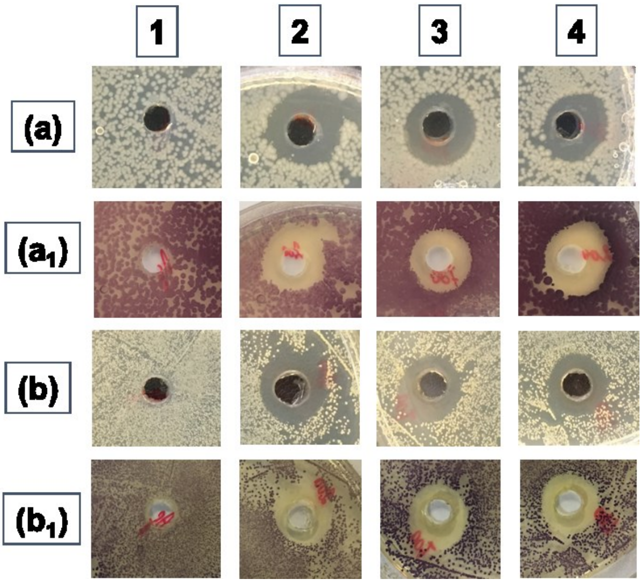

Figure 5.17*. Inhibitory activity of plasma synthetized silver nanoparticles, using agar diffusion assay. (a) Plate of MH spread with Escherichia coli ATCC 9637; (b) Plate of MH*

spread with Staphylococcus aureus ATCC 29213; (1) AgNP(P), (2) HA200@Ag(P); (3) HA700@Ag(P), (4) HA1200@Ag(P); (a$_1$) plate (a) after MTT reduction; (b$_1$) plate (b) after MTT reduction.

The HA200@Ag(P) showed a strong (ZOI = 15.0 mm) inhibitory activity against *E. coli* ATCC 9637 and a good (ZOI = 13.0 mm) inhibitory activity against *S. aureus* ATCC 29213. The HA1200@Ag(P) showed a strong (ZOI = 14.0 mm) inhibitory activity against *E. coli* ATCC 9637 and a good (ZOI = 13.0 mm) inhibitory activity against *S. aureus* ATCC 29213. On the contrary, the HA700@Ag(P) showed a strong (ZOI = 14.0 mm) inhibitory activity against *S. aureus* ATCC 29213 and a good (ZOI = 13.0 mm) inhibitory activity against *E. coli* ATCC 9637. This results could be due to a different effect of the HA at 700 kDa in the interaction with cell wall, compared to the other molecular weight (Table 5.4).

Table 5.4. *Inhibitory activity silver nanoparticles synthesised by chemical and plasma reduction against Escherichia coli ATCC 9637 and Staphylococcus aureus ATCC 29213 determined using agar diffusion assay in comparison with chloramphenicol (CHL).*

	Zone of inhibition (mm)			
	nM	**ng/mL**	***Escherichia coli*** **ATCC 9637**	***Staphylococcus aureus*** **ATCC 29213**
CHL		$30 \cdot 10^{-3}$	21.0	23.5
AgNP	37	42	8.0	11.0
AgNP(P)	23	1.3	-	-
HA200@Ag	56	52	11.0	10.0
HA200@Ag(P)	22	1.1	15.0	13.0
HA700@Ag	82	66	10.0	11.0
HA700@Ag(P)	20	6.2	13.0	14.0
HA1200@Ag	23	1.3	7.0	-
HA1200@Ag(P)	20	3.4	14.0	13

Notes: *the concentration was expressed as nM and µg/mL. Interpretative criteria: *very strong* = diameter of inhibition zone ≥ 18.0 mm; *strong* = diameter of inhibition zone (18.0, 13.0] mm; *good* = diameter of inhibition zone (13.0, 11.0] mm; *weak* = diameter of inhibition zone (11.0, 9.0] mm; *very weak* = diameter of inhibition zone 9.0, 8.0 mm; *no activity* = diameter of inhibition zone < 8.0 mm.

The HA200@Ag(C) (Table 5.4) showed a good (ZOI = 11.0 mm) inhibitory activity against *E. coli* ATCC 9637 and it was possible to notice the same effect of HA700@Ag(C) against *S. aureus* ATCC 29213. The HA700@Ag showed a weak inhibitory activity against *E. coli* ATCC 9637 with a ZOI of 10.0 mm. HA1200@Ag(C) (Table 5.4) showed a weak (ZOI = 7.0 mm) inhibitory activity against *E. coli* ATCC 9637 and no inhibitory activity against *S. aureus* ATCC 29213. These results showed different effects related to HA molecular weight and tested Gram-positive and Gram-negative strain.[419, 420]

The absence of inhibition zone diameter for gold nanoparticles synthesised by wet chemical and microplasma reduction and plasma synthetized silver nanoparticles could be due to possible chemical-physical interactions with agar medium.

3.4. Determination of enzymatic collagenase activity after treatment with silver and gold nanoparticles

The collagenase[421] is useful in enzymatic wound debridement. The results present in the literature promise that the collagenase and its degradation products may regulate bound inflammation and thus wound repair.

The Figure 5.18 shows the relative percentage of collagenase activity (%A) after treatment with nanoparticles synthesised by wet chemical reduction. The collagenase activity decreased after treatment with all tested nanoparticles, except plasma synthetized Ag NP.[422]

The AuNP(C), HA200@Au(C) and HA200@Au(P), HA700@Au(P), HA1200@Au(P) and HA700@Ag(P) brought a statistically significant decreased (*P<0.05*) of collagenase activity. The HA700@Au(C) and HA1200@Au(C) synthesised by wet chemical reduction and plasma synthetized AuNP(P), HA200@Au(P) brought to a statistically significant decreased (*P<0.01*) of collagenase activity. These effects could be due to chemical interaction between tested NP and collagenase which lead to inhibition of the activity.[422]

The AgNP(C)/AgNP(P), HA1200@Ag(P) and HA700@Au(C), HA1200@Au(C), HA200@Ag(C) determined a decrease of collagenase activity not statistical significant. These results are promised for application in debridement in chronic wounds and burns together with collagenase that help to achieve efficient angiogenesis epithelialization and efficient heling.[422, 423]

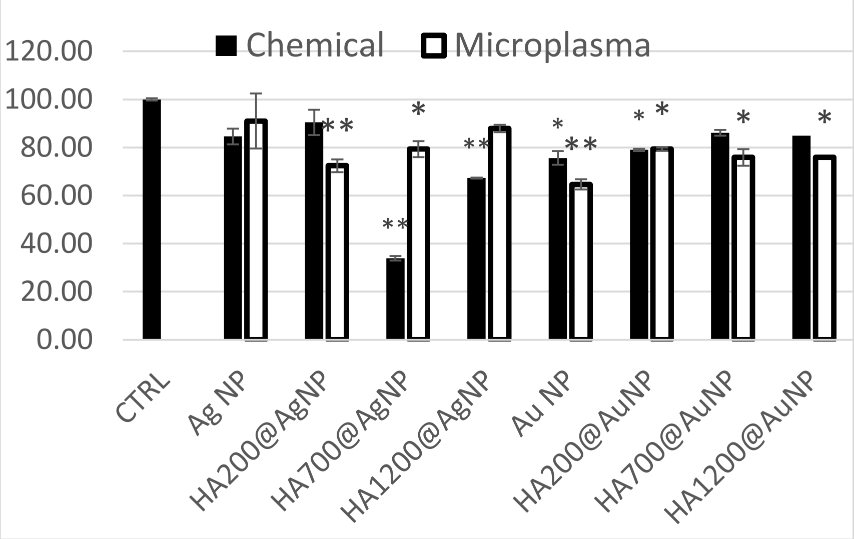

Figure 5.18. *Percentage of collagenase activity after treatment with nanoparticles synthesised by chemical (black solid bars) and plasma (empty bars) method compared with control. The significant differences of the collagenase activity compared to the control are indicated by asterisks: *statistically significant (P<0.05); **statistically significant (P<0.01).*

Conclusions

In this work, silver and gold nanoparticles are successfully synthesized by the reduction of silver and gold salts in a hyaluronic acid 200 kDa, 700 kDa and 1200 kDa aqueous solution by microplasma. Compared to the wet chemical synthesis, the optical characterisation by UV-visible evidenced significant differences in the plasmon peak in comparison with the spectra of bare NPs in terms of red-shift and peak broadening. Moreover, the molecular weight of the HA resulted to have a role in the dimensions of the hybrid nanoparticles, as evidenced by DLS measurements. The stability upon ageing showed different aging trends for gold and silver nanoparticles confirmed by TEM images. In fact, while in the fresh HA a linear correlation was observed between the HA MW and the intrinsic viscosity of the polymer, more complex curve fit functions were found for the aged samples. As to the HA-capped NPs the study of the aging effect demonstrated a NP size evolution indicative of an Ostwald type growth for silver and a digestive ripening effect for gold, respectively.

Comparing d_0 and d_h of the AuNP and AgNP, it was possible to evidence a larger difference between the hydrodynamic size and the optical size in the case of HA@AgNP(C), HA@Ag(P) and HA@Au(P), whereas smaller difference was observed in the case of HA@Au(C).

The AFM images showed different morphology for the HA@Ag and HA@Au synthetized by wet chemical a plasma methods, and in particular wet chemical synthetized NP showed the soft HA shell, in the case of the HA@NP(P) AFM images showed a spherical and poly-globular structure due to the wrapping of the NP by HA.

The cell viability assay showed significant toxicity of the AgNP and HA@Ag systems and in particular HA1200@Ag exhibited toxicity of ~ 30% on the HUVEC cell line. The AgNP(P) systems, AuNP and AuNP(P) with and without HA did not show high toxicity (< 20%) on the HUVEC cell line. Except for plasma synthesized AuNP, tested NP showed a great antibacterial effect on pathological skin bacteria, Gram-negative *E. coli*

ATCC 9637 and Gram-positive *S. aureus* ATCC 29213. In particular, AuNP(C) (with and without HA) synthesised by wet chemical reduction showed an excellent inhibitory activity (MIC values ranging between 0.58 nM and 0.42 nM) against all tested strains and the highest inhibitory activity was showed by HA700@Au(C), with a MIC value of 0.42 nM. The AgNP(C) showed higher MIC values than AuNP ranging from 2.31 nM to 7.38 nM (HA200@Ag exhibit a high inhibitory activity, with a MIC value of 3.50 nM). It is possible to notice that for the AuNP(C) and AgNP(C) in the presence of HA1200 there was not inhibitory activity or was very low (MIC 7.38 nM). Another important observation was that plasma synthesised AgNP exhibited a higher inhibitory effect than chemically syhtesised ones, with MIC values ranging between 2.42 nM and 5.82 nM. The MIC results were confirmend by the ZOI values that was larger for the plasma synthesised AgNP (ranging from 13 mm to 15 mm) compared to the chemically ones (ranging from 8 mm to 11 mm). Moreover, although AuNP(C) exhibited very low MIC, they did not inhibit the tested strains on agar, thus, it was not possible to display ZOIs for these samples. No bacterial inhibition of the plasma sythetised AuNP was confirmed not only by absence of MIC values but also by the absence of the ZOIs. The collagenase activity after incubation with all the tested nanoparticles was evaluated. While bare AgNP(C) did not inhibit significantly the collagenase activity (> 80 %); in the presence of HA the AgNP(C) inhibited singnificantly the collagenase activity and in particular with HA700@AgNP(C) and HA1200@AgNP(C) the collagenase activity was of < 40 % and <70 %, respectively. Whereas, HA@Ag(P) showed a less inhibition of the enzyme activity which was ranged between 70 % and 90 %. Moreover, AuNP synthesised by wet chemical and plasma reduction inhibited the collagenase activity weakly (about 80%).

CHAPTER 6

CONCLUSION AND OUTLOOK

Thesis work conclusions

In this industrial PhD thesis hybrid systems hyaluronic acid-coated AuNP and AgNP were successfully synthesized by wet chemical synthesis and/or microplasma reduction, by one pot reaction. The characterization of these systems evidenced the effective wrapping of the metal core by a shell of hyaluronic acid. To scrutinise a wide interval of response in terms of physicochemical properties (including viscosity, thus the thickness of the polymer shell, and the stability against aging or ionic strength, the polydispersity) as well as of biological activity (such as pro- or anti-angiogenic), three ranges of hyaluronan molecular size, namely low MW (200 kDa), medium MW (700 kDa) and high MW (1,200 kDa) were used.

In Chapter 2 hyaluronic acid-capped gold and silver spherical nanoparticles were synthetized by using a reproducible green wet chemical method based on the reduction of the metal salt by sodium borohydride (for AgNP) or glucose (in basic environment, for AuNP). After the synthesis, the NP were characterised by UV-visible spectroscopy evidenzing hypochromic shift, red-shift and peak broadening when the synthesis was conducted in the presence of HA due to the increase in the NP optical diameter and the wrapping of the nanoparticles stabilised by the hyaluronan shell coating. The correlation between the NP size (both hydrodynamic and optical diameter) and the HA molecular weight was confirmed in the purified NP pellet suspensions. The aging effect demonstrated a NP size evolution indicative of an Ostwald type growth for silver and a digestive ripening effect for gold, respectively. These findings pointed to a multifaceted role of the hyaluronan used in the synthesis, as solvent, capping and co-reducing agent

In Chapter 3 was evaluated the theranostic and angiogenic regulator activity of the hybrids synthesised via chemical reduction, namely HA@Ag(C) and HA@Au(C) (section 3.1), in the comparison with those fabricated by microplasma synthesis (HA@Ag(P) and HA@Au(P), section 3.2). In section 3.1, metallic silver (AgNP) and gold (AuNP) nanoparticles were synthesised in the presence of hyaluronic acid at low (200 kDa) or high (700 kDa). The as prepared resulting nanohybrids were characterised by UV-visble spectroscopy and by DLS to study the optical properties, the size and the stability from aggregation during ageing. The biological activity of the newly synthesised HA-conjugated NPs as teheranostic platforms towards cancer cells was investigated by cell viability assays and confocal microscopy on two cancer cell lines SHSY2Y and PC-3. HA-AgNPs and HA-AuNPs induced a higher toxicity in comparison with the bare NPs SHSY2Y cell line that did not express the CD44 receptor, the treatment of the PC-3 cell line with HA-AgNP were even more toxic than the bare AgNP while cells incubated with AuNP-HA exhibited a slight decrease in viability. The presence of the HA in the nanohybrids led to different localization of the HA@NP inside the cells; in PC-3 cell line HA@NP induced less lysosomal perturbation than the bare NP whereas in the SHSY2Y the nuclear staining is clearly visible As far as it concerns the cytoskeleton actin (except the cells treated with AuNP-HA700) all the treatments induced a thickening of the actin fibres especially visible at the cell membrane. In the Section 3.2, hyaluronic acid-capped gold and silver spherical nanoparticles and their analogous with hyaluronic acid conjugate with the anti-angiogenic peptide GHHPHGK were synthetized by using a green wet chemical and the physical plasma method. The optical characterisation by UV-visible evidenced significant differences in the plasmon peak in comparison with the spectra of bare NPs in terms of red-shift and peak broadening, thus pointing to the formation of larger nanoparticles stabilised by the hyaluronan shell coating as evinced by DLS measurements. The cell viability assay showed significant toxicity of the AgNP(C) and in particular $HA200_{GHHPHGK}$@Ag(C) exhibited the highest toxicity on the HUVEC cell line. The AgNP(P), AuNP(P) systems with and without HA200/$HA200_{GHHPHGK}$ did not show significant toxicity on the HUVEC cell line. Except for plasma synthesised AuNPs, all tested NP showed a great antibacterial effect on skin patogens Gram-negative E. coli ATCC 9637 and Gram-positive S. aureus ATCC 29213 determined using agar diffusion assay and broth dilution methods. In particular, AgNP(C)/HA@Ag(C) and AgNP(P)/HA@Ag(P) exhibited an antibacterial effect against E. coli ATCC 9637 and S. aureus ATCC 29213 but also

AuNP(C) nanohybrids showed an excellent antibacterial effect against the tested strains with MICs lower than silver nanoparticles.

In Chapter 4 were studied the interaction between the NPs synthesised by wet chemical and plasma reduction and HA@NP with model cell membranes of supported lipid bilayers (SLBs) and actual cellular membranes of endhothelial cells (HUVEC line) by the acoustic sensing technique of quarzt crystal microbalance with dissipation monitoring (QCM-D) and the laser scanning confocal microscopy (LSM). The addition of HA and HA@NP systems to pre-formed SLB did not evicence a mass uptake (i.e., change in frequency) but only viscoelastic changes (related to shifts in dissipation) pointing to the fluidity perturbation of artificial cell membranes. The cell treatment by HA@Ag(P) and HA@Ag(C) did not evidence relevant changes in terms of cytoskeleton actin and lysosome staining in comparison with the control untreated cells, thus demonstrating a ‘protective’ role of the HA shell around the metallic core of the nanoparticle. The cell treatment by bare Au(P) and Au(C), as well as HA@Au(P) and HA@Au(C) showed the presence of small actin globular aggregates compared to the fibrillar structure observed in the control untreated cells. Moreover, the coating by hyaluronic acid of the gold nanoparticles was especially effective to enhance their uptake, as evidenced by lysosome engrossment in the cells treated by HA@Au(P) and HA@Au(C) samples, respectively.

In Chapter 5, silver and gold nanoparticles were successfully synthesized by the reduction of silver and gold salts in a hyaluronic acid 200 kDa, 700 kDa and 1,200 kDa aqueous solution by microplasma and were largely characterised (UV-visible spectroscopy, DLS and TEM). The plasma synthesised NP and HA@NP were compared to chemically synthesised ones in terms of plasmon peak features and it was possible to observe a red shift and brodering of the peaks in the presence of the HA during the synthesis. The stability upon ageing showed different aging trends for gold and silver nanoparticles confirmed by TEM images. As to the HA-capped NPs the study of the aging effect demonstrated a NP size evolution indicative of an Ostwald type growth for silver and a digestive ripening effect for gold, respectively. The AFM images showed that NP synthesised by wet chemical reduction exhibited the soft HA shell, whereas, the AFM images of HA@NP(P) showed a spherical and polyglobular structure due to the wrapping of the NP by HA. The cell viability assay showed significant toxicity of the AgNP(C) and HA@AgNP(C) systems (HA1200@Ag(C) cell viability of ~ 70%) on the HUVEC cell line. A lower toxicity was observed in the cases of AuNP(C) and AuNP(P) (cell viability > 80%) on the HUVEC cell line. Except for plasma synthesized AuNP, tested NP showed a great antibacterial effect on pathological skin bacteria, Gram-negative *E. coli* ATCC 9637 and Gram-positive *S. aureus* ATCC 29213. In particular, AuNP(C) (with and without HA) showed an excellent inhibitory activity (MIC values ranging between 0.58 nM and 0.42 nM) against all tested strains. Moreover, AgNP(P) exhibited a higher inhibitory effect than AgNP(C), with MIC values ranging between 2.42 nM and 5.82 nM. The MIC results were confirmed by the ZOI values for the AgNP but although AuNP(C) exhibited very low MIC, they did not inhibit the tested strains on agar. The collagenase activity after incubation with all the tested nanoparticles was significantly inhibited by HA@Ag(C) high HA molecular weights, whereas, HA@Ag(P) and AuNP(C) exhibited a weakly inhibition on the collagenase activity.

Outlook.

Future perspectives involve a new strategy of HA peptide synthesis and the chemical and plasma synthesis of new HA-peptide@NP conjugates, considering pro- and anti-angiogenic peptide and their physicochemical characterization.

The HA@NP will be tested on the HUVEC by wound healing scratch assay to scrutinize the angiogenic properties of the tested samples and the migration of the endothelial cell after HA_{pept}@NP incubation.

Moreover, the antibacterial activity of the tested nanosystems will be tested on a broad range of pathogenic bacteria strains (such as *pseudomonas aeruginosa* and beta-hemolytic *streptococci*) which affect skin wounds.

Additionally, will be studied the capability of the plasma (Plasma RF torch and DBD) to activate the silicon surface and other silicon-like surfaces to enhance the wettability and the adhesion properties of HA200, HA700, HA1200 and HA_{pept} with and without gold and silver nanoparticles and to find the better pre- and post- plasma treatment to develop wound dressings for the treatment of chronic wounds.

References

1. Chakrabarti, S.; Chattopadhyay, P.; Islam, J.; Ray, S.; Raju, P. S.; Mazumder, B., Aspects of Nanomaterials in Wound Healing. *Current Drug Delivery* **2018,** *16* (1), 26-41.
2. Nethi, S. K.; Das, S.; Patra, C. R.; Mukherjee, S., Recent advances in inorganic nanomaterials for wound-healing applications. *Biomaterials Science* **2019,** *7* (7), 2652-2674.
3. Han, G.; Ceilley, R., Chronic Wound Healing: A Review of Current Management and Treatments. *Advances in Therapy* **2017,** *34* (3), 599-610.
4. Jones, R. E.; Foster, D. S.; Longaker, M. T., Management of Chronic Wounds—2018. *Jama* **2018,** *320* (14).
5. Jackson, W. M.; Nesti, L. J.; Tuan, R. S., Concise Review: Clinical Translation of Wound Healing Therapies Based on Mesenchymal Stem Cells. *STEM CELLS Translational Medicine* **2012,** *1* (1), 44-50.
6. Pragnell, J.; Neilson, J., The social and psychological impact of hard-to-heal wounds. *British journal of nursing (Mark Allen Publishing)* **2010,** *19* (19), 1248-52.
7. Price, R. D.; Myers, S.; Leigh, I. M.; Navsaria, H. A., The Role of Hyaluronic Acid in Wound Healing. *American Journal of Clinical Dermatology* **2005,** *6* (6), 393-402.
8. Upton, D.; Penn, F., The Psychological Consequences of Wounds - a Vicious Circle that Should not be Overlooked. *Wounds UK* **2011,** *7*, 136-138.
9. Shaw, T. J.; Martin, P., Wound repair at a glance. *Journal of Cell Science* **2009,** *122* (18), 3209-3213.
10. Gonzalez, A. C. d. O.; Costa, T. F.; Andrade, Z. d. A.; Medrado, A. R. A. P., Wound healing - A literature review. *Anais Brasileiros de Dermatologia* **2016,** *91* (5), 614-620.
11. Eming, S. A.; Krieg, T.; Davidson, J. M., Inflammation in Wound Repair: Molecular and Cellular Mechanisms. *Journal of Investigative Dermatology* **2007,** *127* (3), 514-525.
12. Carmeliet, P., Angiogenesis in health and disease. *Nature Medicine* **2003,** *9* (6), 653-660.
13. Armulik, A.; Genové, G.; Betsholtz, C., Pericytes: Developmental, Physiological, and Pathological Perspectives, Problems, and Promises. *Developmental Cell* **2011,** *21* (2), 193-215.

14. Alon, R.; Nourshargh, S., Learning in motion: pericytes instruct migrating innate leukocytes. *Nature Immunology* **2013,** *14* (1), 14-15.

15. Medrado, A.; Costa, T.; Prado, T.; Reis, S.; Andrade, Z., Phenotype characterization of pericytes during tissue repair following low-level laser therapy. *Photodermatology, Photoimmunology & Photomedicine* **2010,** *26* (4), 192-197.

16. Tonnesen, M. G.; Feng, X.; Clark, R. A. F., Angiogenesis in Wound Healing. *Journal of Investigative Dermatology Symposium Proceedings* **2000,** *5* (1), 40-46.

17. Takakura, N., Role of hematopoietic lineage cells as accessory components in blood vessel formation. *Cancer Science* **2006,** *97* (7), 568-574.

18. Medrado, A. R. A. P.; Pugliese, L. S.; Reis, S. R. A.; Andrade, Z. A., Influence of low level laser therapy on wound healing and its biological action upon myofibroblasts. *Lasers in surgery and medicine* **2003,** *32* (3), 239-244.

19. Crocker, D. J.; Murad, T. M.; Geer, J. C., Role of the pericyte in wound healing. *Experimental and Molecular Pathology* **1970,** *13* (1), 51-65.

20. Intergovernmental Panel on Climate, C., Summary for Policymakers. In *Climate Change 2013 - The Physical Science Basis*, 2014; pp 1-30.

21. Choi, S. S.; Diehl, A. M., Epithelial-to-mesenchymal transitions in the liver. *Hepatology* **2009,** *50* (6), 2007-2013.

22. Eming, S. A.; Martin, P.; Tomic-Canic, M., Wound repair and regeneration: Mechanisms, signaling, and translation. *Science Translational Medicine* **2014,** *6* (265), 265sr6-265sr6.

23. Gazzabin, L.; Serantoni, S.; Palumbo, F. P.; Giordan, N., Hyaluronic acid and metallic silver treatment of chronic wounds: healing rate and bacterial load control. *Journal of Wound Care* **2019,** *28* (7), 482-490.

24. Nussbaum, S. R.; Carter, M. J.; Fife, C. E.; DaVanzo, J.; Haught, R.; Nusgart, M.; Cartwright, D., An Economic Evaluation of the Impact, Cost, and Medicare Policy Implications of Chronic Nonhealing Wounds. *Value in Health* **2018,** *21* (1), 27-32.

25. Järbrink, K.; Ni, G.; Sönnergren, H.; Schmidtchen, A.; Pang, C.; Bajpai, R.; Car, J., The humanistic and economic burden of chronic wounds: a protocol for a systematic review. *Systematic Reviews* **2017,** *6* (1).

26. Guo, S.; DiPietro, L. A., Factors Affecting Wound Healing. *Journal of Dental Research* **2010,** *89* (3), 219-229.

27. Rodriguez, P. G.; Felix, F. N.; Woodley, D. T.; Shim, E. K., The Role of Oxygen in Wound Healing: A Review of the Literature. *Dermatologic Surgery* **2008,** *34* (9), 1159-1169.

28. Swift, M. E.; Kleinman, H. K.; DiPietro, L. A., Impaired wound repair and delayed angiogenesis in aged mice. *Laboratory investigation; a journal of technical methods and pathology* **1999,** *79* (12), 1479-87.

29. Swift, M. E.; Burns, A. L.; Gray, K. L.; DiPietro, L. A., Age-related alterations in the inflammatory response to dermal injury. *The Journal of investigative dermatology* **2001,** *117* (5), 1027-35.

30. Meyer, L. J. M.; Stern, R., Age-Dependent Changes of Hyaluronan in Human Skin. *Journal of Investigative Dermatology* **1994,** *102* (3), 385-389.

31. Gilliver, S. C.; Ashworth, J. J.; Ashcroft, G. S., The hormonal regulation of cutaneous wound healing. *Clin Dermatol* **2007,** *25* (1), 56-62.

32. Kiecolt-Glaser, J. K.; Marucha, P. T.; Malarkey, W. B.; Mercado, A. M.; Glaser, R., Slowing of wound healing by psychological stress. *Lancet (London, England)* **1995,** *346* (8984), 1194-6.

33. Marucha, P. T.; Kiecolt-Glaser, J. K.; Favagehi, M., Mucosal wound healing is impaired by examination stress. *Psychosomatic medicine* **1998,** *60* (3), 362-5.

34. Brem, H.; Tomic-Canic, M., Cellular and molecular basis of wound healing in diabetes. *The Journal of clinical investigation* **2007,** *117* (5), 1219-22.

35. Franz, M. G.; Steed, D. L.; Robson, M. C., Optimizing healing of the acute wound by minimizing complications. *Current problems in surgery* **2007,** *44* (11), 691-763.

36. Wilson, J. A.; Clark, J. J., Obesity: impediment to postsurgical wound healing. *Advances in skin & wound care* **2004,** *17* (8), 426-35.

37. Szabo, G.; Mandrekar, P., A recent perspective on alcohol, immunity, and host defense. *Alcoholism, clinical and experimental research* **2009,** *33* (2), 220-32.

38. Ahn, C.; Mulligan, P.; Salcido, R. S., Smoking-the bane of wound healing: biomedical interventions and social influences. *Advances in skin & wound care* **2008,** *21* (5), 227-36; quiz 237-8.

39. Arnold, M.; Barbul, A., Nutrition and wound healing. *Plastic and reconstructive surgery* **2006,** *117* (7 Suppl), 42s-58s.

40. Toole, B. P., Hyaluronan: from extracellular glue to pericellular cue. *Nature Reviews Cancer* **2004,** *4* (7), 528-539.

41. Chen, W. Y. J.; Abatangelo, G., Functions of hyaluronan in wound repair. *Wound Repair and Regeneration* **2002,** *7* (2), 79-89.

42. Stern, R.; Asari, A.; Sugahara, K., Hyaluronan fragments: An information-rich system. *European Journal of Cell Biology* **2006,** *85* (8), 699-715.

43. Stern, R.; Maibach, H. I., Hyaluronan in skin: aspects of aging and its pharmacologic modulation. *Clinics in Dermatology* **2008,** *26* (2), 106-122.

44. Moseley, R.; Walker, M.; Waddington, R. J.; Chen, W. Y. J., Comparison of the antioxidant properties of wound dressing materials–carboxymethylcellulose, hyaluronan benzyl ester and hyaluronan, towards polymorphonuclear leukocyte-derived reactive oxygen species. *Biomaterials* **2003,** *24* (9), 1549-1557.

45. Oksala, O.; Salo, T.; Tammi, R.; Häkkinen, L.; Jalkanen, M.; Inki, P.; Larjava, H., Expression of proteoglycans and hyaluronan during wound healing. *Journal of Histochemistry & Cytochemistry* **2017,** *43* (2), 125-135.

46. Gerdin, B.; Hällgren, R., Dynamic role of hyaluronan (HYA) in connective tissue activation and inflammation. *Journal of Internal Medicine* **1997,** *242* (1), 49-55.

47. Hart, J., Inflammation 2: its role in the healing of chronic wounds. *Journal of Wound Care* **2002,** *11* (7), 245-249.

48. Wisniewski, H. G.; Vilcek, J., TSG-6: an IL-1/TNF-inducible protein with anti-inflammatory activity. *Cytokine & growth factor reviews* **1997,** *8* (2), 143-56.

49. Frenkel, J. S., The role of hyaluronan in wound healing. *International Wound Journal* **2014,** *11* (2), 159-163.

50. Turley, E. A.; Noble, P. W.; Bourguignon, L. Y. W., Signaling Properties of Hyaluronan Receptors. *Journal of Biological Chemistry* **2002,** *277* (7), 4589-4592.

51. Borgognoni, L., *Low molecular weight hyaluronic acid induces angiogenesis and modulation of the cellular infiltrate in primary and secondary healing wounds*. 1996; Vol. 6, p 127-131.

52. Singer, A. J.; Epstein, F. H.; Clark, R. A. F., Cutaneous Wound Healing. *New England Journal of Medicine* **1999,** *341* (10), 738-746.

53. Manju, S.; Sreenivasan, K., Conjugation of curcumin onto hyaluronic acid enhances its aqueous solubility and stability. *Journal of Colloid and Interface Science* **2011,** *359* (1), 318-325.

54. Zhang, X.; Zhou, P.; Zhao, Y.; Wang, M.; Wei, S., Peptide-conjugated hyaluronic acid surface for the culture of human induced pluripotent stem cells under defined conditions. *Carbohydrate Polymers* **2016,** *136*, 1061-1064.

55. Akbik, D.; Ghadiri, M.; Chrzanowski, W.; Rohanizadeh, R., Curcumin as a wound healing agent. *Life Sciences* **2014,** *116* (1), 1-7.

56. Thangapazham, R. L.; Sharad, S.; Maheshwari, R. K., Skin regenerative potentials of curcumin. *BioFactors* **2013,** *39* (1), 141-149.

57. Teow, S.-Y.; Liew, K.; Ali, S. A.; Khoo, A. S.-B.; Peh, S.-C., Antibacterial Action of Curcumin against Staphylococcus aureus: A Brief Review. *Journal of Tropical Medicine* **2016,** *2016*, 1-10.

58. Sharma, M.; Sahu, K.; Singh, S. P.; Jain, B., Wound healing activity of curcumin conjugated to hyaluronic acid: in vitro and in vivo evaluation. *Artificial Cells, Nanomedicine, and Biotechnology* **2017,** *46* (5), 1009-1017.

59. Babizhayev, M. A.; Yermakova, V. N.; Sakina, N. L.; Evstigneeva, R. P.; Rozhkova, E. A.; Zheltukhina, G. A., Nα-Acetylcarnosine is a prodrug of L-carnosine in ophthalmic application as antioxidant. *Clinica Chimica Acta* **1996,** *254* (1), 1-21.

60. Guiotto, A.; Calderan, A.; Ruzza, P.; Borin, G., Carnosine and Carnosine-Related Antioxidants: A Review. *Current Medicinal Chemistry* **2005,** *12* (20), 2293-2315.

61. Sebastiano Sciuto, V. G., Enrico Rizzarelli, Francesco Bellia, Valeria Lanza, Susanna Vaccaro, Luciano Messina, Derivatives obtained from Hyaluronic acid and carnosine. 2015.

62. Kalashnikova, I.; Das, S.; Seal, S., Nanomaterials for wound healing: scope and advancement. *Nanomedicine : nanotechnology, biology, and medicine* **2015,** *10* (16), 2593-2612.

63. Buzea, C.; Pacheco, I. I.; Robbie, K., Nanomaterials and nanoparticles: Sources and toxicity. *Biointerphases* **2007,** *2* (4), MR17-MR71.

64. Tocco, I.; Zavan, B.; Bassetto, F.; Vindigni, V., Nanotechnology-Based Therapies for Skin Wound Regeneration. *Journal of Nanomaterials* **2012,** *2012*, 1-11.

65. Lara, H. H.; Garza-Trevino, E. N.; Ixtepan-Turrent, L.; Singh, D. K., Silver nanoparticles are broad-spectrum bactericidal and virucidal compounds. *J Nanobiotechnology* **2011,** *9*, 30.

66. Dykman, L.; Khlebtsov, N., Gold nanoparticles in biomedical applications: recent advances and perspectives. *Chemical Society Reviews* **2012,** *41* (6), 2256-2282.

67. Das, S.; Baker, A. B., Biomaterials and Nanotherapeutics for Enhancing Skin Wound Healing. *Frontiers in Bioengineering and Biotechnology* **2016,** *4*.

68. Oyarzun-Ampuero, F.; Vidal, A.; Concha, M.; Morales, J.; Orellana, S.; Moreno-Villoslada, I., Nanoparticles for the Treatment of Wounds. *Current Pharmaceutical Design* **2015,** *21* (29), 4329-4341.

69. Le Ouay, B.; Stellacci, F., Antibacterial activity of silver nanoparticles: A surface science insight. *Nano Today* **2015,** *10* (3), 339-354.

70. Lok, C.-N.; Zou, T.; Zhang, J.-J.; Lin, I. W.-S.; Che, C.-M., Controlled-Release Systems for Metal-Based Nanomedicine: Encapsulated/Self-Assembled Nanoparticles of Anticancer Gold(III)/Platinum(II) Complexes and Antimicrobial Silver Nanoparticles. *Advanced Materials* **2014,** *26* (31), 5550-5557.

71. Parnsamut, C.; Brimson, S., Effects of silver nanoparticles and gold nanoparticles on IL-2, IL-6, and TNF-α production via MAPK pathway in leukemic cell lines. *Genetics and Molecular Research* **2015,** *14* (2), 3650-3668.

72. Asharani, P.; Sethu, S.; Lim, H. K.; Balaji, G.; Valiyaveettil, S.; Hande, M. P., Differential regulation of intracellular factors mediating cell cycle, DNA repair and inflammation following exposure to silver nanoparticles in human cells. *Genome integrity* **2012,** *3* (1), 2.

73. Chen, S. A.; Chen, H. M.; Yao, Y. D.; Hung, C. F.; Tu, C. S.; Liang, Y. J., Topical treatment with anti-oxidants and Au nanoparticles promote healing of diabetic wound through receptor for advance glycation end-products. *European journal of pharmaceutical sciences : official journal of the European Federation for Pharmaceutical Sciences* **2012,** *47* (5), 875-83.

74. Gupta, M.; Agrawal, U.; Vyas, S. P., Nanocarrier-based topical drug delivery for the treatment of skin diseases. *Expert Opinion on Drug Delivery* **2012,** *9* (7), 783-804.

75. Rai, M.; Yadav, A.; Gade, A., Silver nanoparticles as a new generation of antimicrobials. *Biotechnology Advances* **2009,** *27* (1), 76-83.

76. Chopra, I., The increasing use of silver-based products as antimicrobial agents: a useful development or a cause for concern? *Journal of Antimicrobial Chemotherapy* **2007,** *59* (4), 587-590.

77. Boote, B. W.; Byun, H.; Kim, J.-H., Silver–Gold Bimetallic Nanoparticles and Their Applications as Optical Materials. *Journal of Nanoscience and Nanotechnology* **2014,** *14* (2), 1563-1577.

78. Chaloupka, K.; Malam, Y.; Seifalian, A. M., Nanosilver as a new generation of nanoproduct in biomedical applications. *Trends in Biotechnology* **2010,** *28* (11), 580-588.
79. Kim, J. S.; Kuk, E.; Yu, K. N.; Kim, J.-H.; Park, S. J.; Lee, H. J.; Kim, S. H.; Park, Y. K.; Park, Y. H.; Hwang, C.-Y.; Kim, Y.-K.; Lee, Y.-S.; Jeong, D. H.; Cho, M.-H., Antimicrobial effects of silver nanoparticles. *Nanomedicine: Nanotechnology, Biology and Medicine* **2007,** *3* (1), 95-101.
80. Ruparelia, J. P.; Chatterjee, A. K.; Duttagupta, S. P.; Mukherji, S., Strain specificity in antimicrobial activity of silver and copper nanoparticles. *Acta Biomaterialia* **2008,** *4* (3), 707-716.
81. Tian, J.; Wong, K. K. Y.; Ho, C.-M.; Lok, C.-N.; Yu, W.-Y.; Che, C.-M.; Chiu, J.-F.; Tam, P. K. H., Topical Delivery of Silver Nanoparticles Promotes Wound Healing. *ChemMedChem* **2007,** *2* (1), 129-136.
82. Adhya, A.; Bain, J.; Dutta, G.; Hazra, A.; Majumdar, B.; Ray, O.; Ray, S.; Adhikari, S., Healing of burn wounds by topical treatment: A randomized controlled comparison between silver sulfadiazine and nano-crystalline silver. *Journal of Basic and Clinical Pharmacy* **2015,** *6* (1).
83. Mijnendonckx, K.; Leys, N.; Mahillon, J.; Silver, S.; Van Houdt, R., Antimicrobial silver: uses, toxicity and potential for resistance. *BioMetals* **2013,** *26* (4), 609-621.
84. Mohammed, A. E., Green synthesis, antimicrobial and cytotoxic effects of silver nanoparticles mediated by Eucalyptus camaldulensis leaf extract. *Asian Pacific Journal of Tropical Biomedicine* **2015,** *5* (5), 382-386.
85. Ley, H. H. a. Y., Asiah and Munajat, Yusof Surface plasmon resonance sensor of silver film based on Kretchmann configuration *Jurnal Teknologi* **2015,** *76 (13)*, 95-99.
86. Bhattacharya, R.; Mukherjee, P., Biological properties of "naked" metal nanoparticles☆. *Advanced Drug Delivery Reviews* **2008,** *60* (11), 1289-1306.
87. Pivodová, V.; Franková, J.; Galandáková, A.; Ulrichová, J., In Vitro AuNPs' Cytotoxicity and Their Effect on Wound Healing. *Nanobiomedicine* **2015,** *2*.
88. Yakimovich, N. O.; Ezhevskii, A. A.; Guseinov, D. V.; Smirnova, L. A.; Gracheva, T. A.; Klychkov, K. S., Antioxidant properties of gold nanoparticles studied by ESR spectroscopy. *Russian Chemical Bulletin* **2009,** *57* (3), 520-523.
89. Lau, P.; Bidin, N.; Islam, S.; Shukri, W.; Zakaria, N.; Musa, N.; Krishnan, G., Influence of gold nanoparticles on wound healing treatment

in rat model: Photobiomodulation therapy. *Lasers in surgery and medicine* **2017,** *49* (4), 380-386.

90. Leu, J. G.; Chen, S. A.; Chen, H. M.; Wu, W. M.; Hung, C. F.; Yao, Y. D.; Tu, C. S.; Liang, Y. J., The effects of gold nanoparticles in wound healing with antioxidant epigallocatechin gallate and alpha-lipoic acid. *Nanomedicine : nanotechnology, biology, and medicine* **2012,** *8* (5), 767-75.

91. Sriram, M.; Zong, K.; Vivekchand, S. R. C.; Gooding, J. J., Single nanoparticle plasmonic sensors. *Sensors (Basel)* **2015,** *15* (10), 25774-25792.

92. Turkevich, J.; Stevenson, P. C.; Hillier, J., A study of the nucleation and growth processes in the synthesis of colloidal gold. *Discussions of the Faraday Society* **1951,** *11* (0), 55-75.

93. Wiley, B.; Sun, Y.; Mayers, B.; Xia, Y., Shape-Controlled Synthesis of Metal Nanostructures: The Case of Silver. *Chemistry - A European Journal* **2005,** *11* (2), 454-463.

94. Frens, G., Controlled Nucleation for the Regulation of the Particle Size in Monodisperse Gold Suspensions. *Nature Physical Science* **1973,** *241* (105), 20-22.

95. Kimling, J.; Maier, M.; Okenve, B.; Kotaidis, V.; Ballot, H.; Plech, A., Turkevich Method for Gold Nanoparticle Synthesis Revisited. *The Journal of Physical Chemistry B* **2006,** *110* (32), 15700-15707.

96. Pillai, Z. S.; Kamat, P. V., What Factors Control the Size and Shape of Silver Nanoparticles in the Citrate Ion Reduction Method? *The Journal of Physical Chemistry B* **2004,** *108* (3), 945-951.

97. Cushing, B. L.; Kolesnichenko, V. L.; O'Connor, C. J., Recent Advances in the Liquid-Phase Syntheses of Inorganic Nanoparticles. *Chemical Reviews* **2004,** *104* (9), 3893-3946.

98. Safavi, A.; Tohidi, M., Microwave-assisted synthesis of gold, silver, platinum and palladium nanostructures and their use in electrocatalytic applications. *J Nanosci Nanotechnol* **2014,** *14* (9), 7189-98.

99. Belmonte, T.; Arnoult, G.; Henrion, G.; Gries, T., Nanoscience with non-equilibrium plasmas at atmospheric pressure. *Journal of Physics D: Applied Physics* **2011,** *44* (36), 363001.

100. Lin, L.; Starostin, S. A.; Li, S.; Hessel, V., Synthesis of metallic nanoparticles by microplasma. *Physical Sciences Reviews* **2018,** *3* (10).

101. Korbekandi, H.; Iravani, S.; Abbasi, S., Production of nanoparticles using organisms. *Critical reviews in biotechnology* **2009,** *29* (4), 279-306.

102. Pietro, P. D.; Strano, G.; Zuccarello, L.; Satriano, C., Gold and Silver Nanoparticles for Applications in Theranostics. *Curr Top Med Chem* **2016,** *16* (27), 3069-3102.

103. Di Pietro, P.; Strano, G.; Zuccarello, L.; Satriano, C., Gold and Silver Nanoparticles for Applications in Theranostics. *Current Topics in Medicinal Chemistry* **2016,** *16* (27), 3069-3102.

104. Forte, G.; Travaglia, A.; Magrì, A.; Satriano, C.; La Mendola, D., Adsorption of NGF and BDNF derived peptides on gold surfaces. *Phys. Chem. Chem. Phys.* **2014,** *16* (4), 1536-1544.

105. De Vos, C.; Baneton, J.; Witzke, M.; Dille, J.; Godet, S.; Gordon, M. J.; Sankaran, R. M.; Reniers, F., A comparative study of the reduction of silver and gold salts in water by a cathodic microplasma electrode. *Journal of Physics D: Applied Physics* **2017,** *50* (10).

106. Sau, T. K.; Rogach, A. L.; Jäckel, F.; Klar, T. A.; Feldmann, J., Properties and Applications of Colloidal Nonspherical Noble Metal Nanoparticles. *Advanced Materials* **2010,** *22* (16), 1805-1825.

107. Faraday, M., X. The Bakerian Lecture. —Experimental relations of gold (and other metals) to light. *Philosophical Transactions of the Royal Society of London* **1857,** *147*, 145-181.

108. Turkevich, J.; Stevenson, P. C.; Hillier, J., A study of the nucleation and growth processes in the synthesis of colloidal gold. *Discussions of the Faraday Society* **1951,** *11*.

109. Kapoor, S.; Lawless, D.; Kennepohl, P.; Meisel, D.; Serpone, N., Reduction and Aggregation of Silver Ions in Aqueous Gelatin Solutions. *Langmuir* **1994,** *10* (9), 3018-3022.

110. LaMer, V. K.; Dinegar, R. H., Theory, Production and Mechanism of Formation of Monodispersed Hydrosols. *Journal of the American Chemical Society* **1950,** *72* (11), 4847-4854.

111. Polte, J.; Tuaev, X.; Wuithschick, M.; Fischer, A.; Thuenemann, A. F.; Rademann, K.; Kraehnert, R.; Emmerling, F., Formation Mechanism of Colloidal Silver Nanoparticles: Analogies and Differences to the Growth of Gold Nanoparticles. *ACS Nano* **2012,** *6* (7), 5791-5802.

112. Pong, B.-K.; Elim, H. I.; Chong, J.-X.; Ji, W.; Trout, B. L.; Lee, J.-Y., New Insights on the Nanoparticle Growth Mechanism in the Citrate Reduction of Gold(III) Salt: Formation of the Au Nanowire Intermediate and Its Nonlinear Optical Properties. *The Journal of Physical Chemistry C* **2007,** *111* (17), 6281-6287.

113. Mazzonello, A.; Valdramidis, V.; Farrugia, C.; Grima, J.; Gatt, R., *Synthesis and characterization of silver nanoparticles*. 2017; Vol. 7, p 41.

114. Perepichka, I. I.; Mezour, M. A.; Perepichka, D. F.; Lennox, R. B., High thermal stability of block copolymer-capped Au and Cu nanoparticles. *Chem. Commun.* **2014,** *50* (80), 11919-11921.

115. Pal, N. K.; Kryschi, C., A facile one-pot synthesis of blue and red luminescent thiol stabilized gold nanoclusters: a thorough optical and microscopy study. *Physical Chemistry Chemical Physics* **2015,** *17* (33), 21423-21431.

116. Shem, P. M.; Sardar, R.; Shumaker-Parry, J. S., Soft ligand stabilized gold nanoparticles: Incorporation of bipyridyls and two-dimensional assembly. *Journal of Colloid and Interface Science* **2014,** *426*, 107-116.

117. Dorjnamjin, D.; Ariunaa, M.; Shim, Y., Synthesis of Silver Nanoparticles Using Hydroxyl Functionalized Ionic Liquids and Their Antimicrobial Activity. *International Journal of Molecular Sciences* **2008,** *9* (5), 807-820.

118. Bönnemann, H.; Braun, G.; Brijoux, W.; Brinkmann, R.; Tilling, A. S.; Seevogel, K.; Siepen, K., Nanoscale colloidal metals and alloys stabilized by solvents and surfactants Preparation and use as catalyst precursors. *Journal of Organometallic Chemistry* **1996,** *520* (1-2), 143-162.

119. Sperling, R. A.; Parak, W. J., Surface modification, functionalization and bioconjugation of colloidal inorganic nanoparticles. *Philosophical Transactions of the Royal Society A: Mathematical, Physical and Engineering Sciences* **2010,** *368* (1915), 1333-1383.

120. Lowry, K. M.; Beavers, E. M., Thermal stability of sodium hyaluronate in aqueous solution. *Journal of Biomedical Materials Research* **1994,** *28* (10), 1239-1244.

121. Mishra, Y. K.; Suvarna, S.; Das, U.; Kc, S.; Mishra, S.; Sudarshan, M.; Saha, K. D.; Dey, S.; Chakraborty, A.; Narayana, Y., Synthesis of a novel glucose capped gold nanoparticle as a better theranostic candidate. *Plos One* **2017,** *12* (6).

122. Creighton, J. A.; Blatchford, C. G.; Albrecht, M. G., Plasma resonance enhancement of Raman scattering by pyridine adsorbed on silver or gold sol particles of size comparable to the excitation wavelength. *Journal of the Chemical Society, Faraday Transactions 2: Molecular and Chemical Physics* **1979,** *75* (0), 790-798.

123. Sriram, M.; Zong, K.; Vivekchand, S.; Gooding, J., Single Nanoparticle Plasmonic Sensors. *Sensors* **2015,** *15* (10), 25774-25792.

124. Oliveira, M. M.; Ugarte, D.; Zanchet, D.; Zarbin, A. J. G., Influence of synthetic parameters on the size, structure, and stability of

dodecanethiol-stabilized silver nanoparticles. *Journal of Colloid and Interface Science* **2005,** *292* (2), 429-435.

125. Mavani, K.; Shah, M., *Synthesis of Silver Nanoparticles by using Sodium Borohydride as a Reducing Agent*. 2013.

126. Song, K. C.; Lee, S. M.; Park, T. S.; Lee, B. S., Preparation of colloidal silver nanoparticles by chemical reduction method. *Korean Journal of Chemical Engineering* **2009,** *26* (1), 153-155.

127. Sato-Berrú, R.; Redón, R.; Vázquez-Olmos, A.; Saniger, J. M., Silver nanoparticles synthesized by direct photoreduction of metal salts. Application in surface-enhanced Raman spectroscopy. *Journal of Raman Spectroscopy* **2009,** *40* (4), 376-380.

128. Soroushian, B.; Lampre, I.; Belloni, J.; Mostafavi, M., Radiolysis of silver ion solutions in ethylene glycol: solvated electron and radical scavenging yields. *Radiation Physics and Chemistry* **2005,** *72* (2-3), 111-118.

129. Neri, F.; Compagnini, G.; Gucciardi, P.; D'Andrea, C.; Fazio, B.; G. Donato, M.; Fazio, E.; Satriano, C.; Messina, E.; D'Urso, L., *Tuning the structural and optical properties of gold/silver nanoalloys prepared by laser ablation in liquids for ultra-sensitive spectroscopy and optical trapping*. 2011; Vol. 89.

130. Tonks, L.; Langmuir, I., Oscillations in Ionized Gases. *Physical Review* **1929,** *33* (2), 195-210.

131. Pankaj, S. K.; Thomas, S., Cold Plasma Applications in Food Packaging. In *Cold Plasma in Food and Agriculture*, 2016; pp 293-307.

132. Grill, A., *Cold Plasma Generation*. 2009; p 24-45.

133. Keidar M, B., *Plasma Engineering*. 2013.

134. Mariotti, D.; Sankaran, R. M., Microplasmas for nanomaterials synthesis. *Journal of Physics D: Applied Physics* **2010,** *43* (32).

135. Rumbach, P.; Griggs, N.; Sankaran, R. M.; Go, D. B., Visualization of Electrolytic Reactions at a Plasma-Liquid Interface. *IEEE Transactions on Plasma Science* **2014,** *42* (10), 2610-2611.

136. Richmonds, C.; Mohan Sankaran, R., *Plasma-liquid electrochemistry: Rapid synthesis of colloidal metal nanoparticles by microplasma reduction of aqueous cations*. 2008; Vol. 93, p 131501-131501.

137. Fridman, G.; Friedman, G.; Gutsol, A.; Shekhter, A. B.; Vasilets, V. N.; Fridman, A., Applied Plasma Medicine. *Plasma Processes and Polymers* **2008,** *5* (6), 503-533.

138. Mariotti, D.; Mohan Sankaran, R., *Microplasmas for nanomaterials synthesis*. 2010; Vol. 43, p 241-323001.

139. Yuri P. Raizer, J. E. A., Gas Discharge Physics. *Springer-Verlag Berlin Heidelberg* **1991**, XI, 449.

140. Becker, K. H.; Schoenbach, K. H.; Eden, J. G., Microplasmas and applications. *Journal of Physics D: Applied Physics* **2006,** *39* (3), R55-R70.

141. Mariotti, D.; Sankaran, R. M., Perspectives on atmospheric-pressure plasmas for nanofabrication. *Journal of Physics D: Applied Physics* **2011,** *44* (17).

142. Owens, D. K.; Wendt, R. C., Estimation of the surface free energy of polymers. *Journal of Applied Polymer Science* **1969,** *13* (8), 1741-1747.

143. Liu, X.; Atwater, M.; Wang, J.; Huo, Q., Extinction coefficient of gold nanoparticles with different sizes and different capping ligands. *Colloids and Surfaces B: Biointerfaces* **2007,** *58* (1), 3-7.

144. Huang, X.; Li, Y.; Zhong, X., Effect of experimental conditions on size control of Au nanoparticles synthesized by atmospheric microplasma electrochemistry. *Nanoscale Research Letters* **2014,** *9* (1).

145. Korbekandi, H.; Iravani, S.; Abbasi, S., Production of nanoparticles using organisms. *Critical Reviews in Biotechnology* **2009,** *29* (4), 279-306.

146. Reddy, A. S.; Chen, C. Y.; Chen, C. C.; Jean, J. S.; Chen, H. R.; Tseng, M. J.; Fan, C. W.; Wang, J. C., Biological synthesis of gold and silver nanoparticles mediated by the bacteria Bacillus subtilis. *Journal of nanoscience and nanotechnology* **2010,** *10* (10), 6567-74.

147. Garcia, M. A., Surface plasmons in metallic nanoparticles: fundamentals and applications. . *Journal of Physics D: Applied Physics, IOP Publishing* **2011,** *44* (28).

148. Skoog, D. A., Holler, F. J., & Crouch, S. R. , *Principles of instrumental analysis*. 6th ed. ed.; 2007.

149. Hammond, J.; Bhalla, N.; Rafiee, S.; Estrela, P., Localized Surface Plasmon Resonance as a Biosensing Platform for Developing Countries. *Biosensors* **2014,** *4*, 172-188.

150. Duque, J. S.; Blandón, J. S.; Riascos, H., Localized Plasmon resonance in metal nanoparticles using Mie theory. *Journal of Physics: Conference Series* **2017,** *850*.

151. Fu, Q.; Sun, W., Mie theory for light scattering by a spherical particle in an absorbing medium. *Applied Optics* **2001,** *40* (9).

152. Jain, P. K.; Lee, K. S.; El-Sayed, I. H.; El-Sayed, M. A., Calculated Absorption and Scattering Properties of Gold Nanoparticles of Different Size, Shape, and Composition: Applications in Biological Imaging and

Biomedicine. *The Journal of Physical Chemistry B* **2006,** *110* (14), 7238-7248.

153. Rastar, A.; Yazdanshenas, M. E.; Rashidi, A.; Bidoki, S. M., Theoretical Review of Optical Properties of Nanoparticles. *Journal of Engineered Fibers and Fabrics* **2018,** *8* (2).

154. Ramalingam, P.; Reddy, Y.; Kumar, K.; Chandu, B.; Rajendran, K., Evaluation of metformin hydrochloride in Wistar rats by FTIR-ATR spectroscopy: A convenient tool in the clinical study of diabetes. *Journal of Natural Science, Biology and Medicine* **2014,** *5* (2).

155. Ausili, A.; Sánchez, M.; Gómez-Fernández, J., Attenuated total reflectance infrared spectroscopy: A powerful method for the simultaneous study of structure and spatial orientation of lipids and membrane proteins. *Biomedical Spectroscopy and Imaging* **2015,** *4*, 159-70.

156. Liu, J.; Saw, R. E.; Kiang, Y. H., Calculation of Effective Penetration Depth in X-Ray Diffraction for Pharmaceutical Solids. *Journal of Pharmaceutical Sciences* **2010,** *99* (9), 3807-3814.

157. Choi, S.; Choi, W.; Kim, S.; Lee, S.-Y.; Noh, I.; Kim, C.-W., Purification and biocompatibility of fermented hyaluronic acid for its applications to biomaterials. *Biomater Res* **2014,** *18*, 6-6.

158. Binnig, G.; Quate, C. F.; Gerber, C., Atomic force microscope. *Physical review letters* **1986,** *56* (9), 930-933.

159. Giessibl, F. J., Advances in atomic force microscopy. *Reviews of Modern Physics* **2003,** *75* (3), 949-983.

160. Lopes, G.; Cotta, E.; Da Fonseca Filho, H., Differential Equations Applied to Atomic Force Microscopy: A Strategy to Classical Mechanics Teaching in Undergraduation. *British Journal of Education, Society & Behavioural Science* **2016,** *14*, 1-9.

161. Kimura, K.; Kobayashi, K.; Yamada, H.; Horiuchi, T.; Ishida, K.; Matsushige, K., Orientation control of ferroelectric polymer molecules using contact-mode AFM. *European Polymer Journal* **2004,** *40* (5), 933-938.

162. Sugimura, H.; Nakagiri, N., AFM lithography in constant current mode. *Nanotechnology* **1997,** *8* (3A), A15-A18.

163. Fan, D.; Sakai, Y.; Chelikowsky, J. R., Discrimination of Bond Order in Organic Molecules Using Noncontact Atomic Force Microscopy. *Nano Letters* **2019**.

164. Zhang, M.; Liu, M.; Prest, H.; Fischer, S., Nanoparticles secreted from ivy rootlets for surface climbing. *Nano Lett* **2008,** *8* (5), 1277-80.

165. Fan, Z.; Sun, L.; Huang, Y.; Wang, Y.; Zhang, M., Bioinspired fluorescent dipeptide nanoparticles for targeted cancer cell imaging and real-time monitoring of drug release. *Nature nanotechnology* **2016,** *11* (4), 388-94.

166. Lee, H.; Lee, B. P.; Messersmith, P. B., A reversible wet/dry adhesive inspired by mussels and geckos. *Nature* **2007,** *448*, 338.

167. Alsteens, D.; Müller, D. J.; Dufrêne, Y. F., Multiparametric Atomic Force Microscopy Imaging of Biomolecular and Cellular Systems. *Accounts of Chemical Research* **2017,** *50* (4), 924-931.

168. Alsteens, D.; Newton, R.; Schubert, R.; Martinez-Martin, D.; Delguste, M.; Roska, B.; Müller, D. J., Nanomechanical mapping of first binding steps of a virus to animal cells. *Nature nanotechnology* **2016,** *12*, 177.

169. Pfreundschuh, M.; Harder, D.; Ucurum, Z.; Fotiadis, D.; Müller, D. J., Detecting Ligand-Binding Events and Free Energy Landscape while Imaging Membrane Receptors at Subnanometer Resolution. *Nano Letters* **2017,** *17* (5), 3261-3269.

170. Alsteens, D.; Gaub, H. E.; Newton, R.; Pfreundschuh, M.; Gerber, C.; Müller, D. J., Atomic force microscopy-based characterization and design of biointerfaces. *Nature Reviews Materials* **2017,** *2*, 17008.

171. Li, M.; Xi, N.; Wang, Y.; Liu, L., Nanoscale Multiparametric Imaging of Peptide-Assembled Nanofibrillar Hydrogels by Atomic Force Microscopy. *IEEE Transactions on Nanotechnology* **2019,** *18*, 315-328.

172. Ukkund, S. J.; Bhat, A. H.; Khan, J.; Hakeem, N. A.; Puthiyillam, P.; Ashraf, M.; Udupa, A., Experimental investigation on synthesis, characterization and antibacterial properties of silver nanoparticles from Cinnamon zeylanicum extract. 2019.

173. Rao, A.; Schoenenberger, M.; Gnecco, E.; Glatzel, T.; Meyer, E.; Brändlin, D.; Scandella, L., Characterization of nanoparticles using Atomic Force Microscopy. *Journal of Physics: Conference Series* **2007,** *61*, 971.

174. Gołek, F.; Mazur, P.; Ryszka, Z.; Zuber, S., AFM image artifacts. *Applied Surface Science* **2014,** *304*, 11-19.

175. Egor, U.; Kromka, A.; Kozak, H.; Reme, Z.; Rezek, B., Artifacts in Atomic Force Microscopy of Biological Samples. 2012.

176. Udpa, L.; Ayres, V. M.; Yuan, F.; Qian, C.; Kumar, S. A., Deconvolution of atomic force microscopy data for cellular and molecular imaging. *IEEE Signal Processing Magazine* **2006,** *23* (3), 73-83.

177. Neumeier, J. Photophysics of Graphene Quantum Dots. 2015.

178. Neustadt, D. H., Intra-articular injections for osteoarthritis of the knee. *Cleveland Clinic Journal of Medicine* **2006,** *73* (10), 897-898.
179. García-Abuín, A.; Gómez-Díaz, D.; Navaza, J. M.; Regueiro, L.; Vidal-Tato, I., Viscosimetric behaviour of hyaluronic acid in different aqueous solutions. *Carbohydrate Polymers* **2011,** *85* (3), 500-505.
180. Awad, H. A.; Bonnevie, E. D.; Galesso, D.; Secchieri, C.; Cohen, I.; Bonassar, L. J., Elastoviscous Transitions of Articular Cartilage Reveal a Mechanism of Synergy between Lubricin and Hyaluronic Acid. *Plos One* **2015,** *10* (11).
181. Francesco Della Valle, A. R., Silvana Lorenzi 1990. Hyaluronic acid fractions having pharmaceutical activity, methods for preparation thereof, and pharmaceutical compositions containing the same
182. Sauerbrey, G., Verwendung von Schwingquarzen zur Wägung dünner Schichten und zur Mikrowägung. *Zeitschrift für Physik* **1959,** *155* (2), 206-222.
183. Grasso, G.; Satriano, C.; Milardi, D., A neglected modulator of insulin-degrading enzyme activity and conformation: The pH. *Biophysical Chemistry* **2015,** *203-204*, 33-40.
184. Doliška, A.; Ribitsch, V.; Stana Kleinschek, K.; Strnad, S., Viscoelastic properties of fibrinogen adsorbed onto poly(ethylene terephthalate) surfaces by QCM-D. *Carbohydrate Polymers* **2013,** *93* (1), 246-255.
185. Ahumada, L.; González, M.; Sandoval, O.; Olmedo, J., Evaluation of Hyaluronic Acid Dilutions at Different Concentrations Using a Quartz Crystal Resonator (QCR) for the Potential Diagnosis of Arthritic Diseases. *Sensors* **2016,** *16* (11).
186. MINSKY, M. Microscopy apparatus 1957.
187. Zenkevich, É.; Martin, J.; Von Borczyskowski, C.; A Ageeva, T.; Titov, V.; Knyukshto, V., Laser Confocal and Spatially-Resolved Fluorescence Spectroscopy of Porphyrin Distribution on Plasma Deposited Polymer Films. *Macroheterocycles* **2008,** *1*.
188. Zhang, L. W.; Monteiro-Riviere, N. A., Use of confocal microscopy for nanoparticle drug delivery through skin. *Journal of biomedical optics* **2013,** *18* (6), 061214.
189. Zou, Y.; Celli, A.; Zhu, H.; Elmahdy, A.; Cao, Y.; Hui, X.; Maibach, H., Confocal laser scanning microscopy to estimate nanoparticles’ human skin penetration in vitro. *International Journal of Nanomedicine* **2017,** *Volume 12*, 8035-8041.

190. Shim, J.; Seok Kang, H.; Park, W. S.; Han, S. H.; Kim, J.; Chang, I. S., Transdermal delivery of mixnoxidil with block copolymer nanoparticles. *Journal of controlled release : official journal of the Controlled Release Society* **2004,** *97* (3), 477-84.

191. Klingberg, H.; B. Oddershede, L.; Loeschner, K.; Larsen, E. H.; Loft, S.; Møller, P., Uptake of gold nanoparticles in primary human endothelial cells. *Toxicology Research* **2015,** *4* (3), 655-666.

192. Li, F.; Shi, Y.; Liang, J.; Zhao, L., Curcumin-loaded chitosan nanoparticles promote diabetic wound healing via attenuating inflammation in a diabetic rat model. *Journal of Biomaterials Applications* **2019**, 0885328219860929.

193. Torrano, A. A.; Bräuchle, C., Precise quantification of silica and ceria nanoparticle uptake revealed by 3D fluorescence microscopy. *Beilstein Journal of Nanotechnology* **2014,** *5*, 1616-1624.

194. Chen, F.; Johnston, R., Plasmonic Properties of Silver Nanoparticles on Two Substrates. *Plasmonics* **2009,** *4*, 147-152.

195. El-Nour, K. M. A.; Eftaiha, A. a.; Al-Warthan, A.; Ammar, R. A. J. A. j. o. c., Synthesis and applications of silver nanoparticles. **2010,** *3* (3), 135-140.

196. Prabhu, S. P., Eldho K Silver nanoparticles: mechanism of antimicrobial action, synthesis, medical applications, and toxicity effects. *International nano letters* **2012,** *2* (1), 32.

197. Sperling, R. A.; Gil, P. R.; Zhang, F.; Zanella, M.; Parak, W., Biological applications of gold nanoparticles. *J Chemical Society Reviews* **2008,** *37* (9), 1896-1908.

198. Wu, Y.; Ali, M. R.; Chen, K.; Fang, N.; El-Sayed, M. A., Gold nanoparticles in biological optical imaging. *J Nano Today* **2019**.

199. Cong, W.; Xudong, G.; Zhongqin, C.; Yue, C.; Haixia, C., Preparation, Characterization and Application of Polysaccharide-Based Metallic Nanoparticles: A Review. *Polymers* **2017,** *9* (12).

200. Abdel-Mohsen, A. M.; Hrdina, R.; Burgert, L.; Krylová, G.; Abdel-Rahman, R. M.; Krejčová, A.; Steinhart, M.; Beneš, L., Green synthesis of hyaluronan fibers with silver nanoparticles. *Carbohydrate Polymers* **2012,** *89* (2), 411-422.

201. Suvarna, S.; Das, U.; Kc, S.; Mishra, S.; Sudarshan, M.; Saha, K. D.; Dey, S.; Chakraborty, A.; Narayana, Y., Synthesis of a novel glucose capped gold nanoparticle as a better theranostic candidate. *PLOS ONE* **2017,** *12* (6), e0178202.

202. Engelbrekt, C.; Sørensen, K. H.; Zhang, J.; Welinder, A. C.; Jensen, P. S.; Ulstrup, J., Green synthesis of gold nanoparticles with starch–glucose and application in bioelectrochemistry. *Journal of Materials Chemistry* **2009,** *19* (42), 7839-7847.

203. Castro-Guerrero, C. F.; Morales-Cepeda, A. B.; Hernández-Vega, L. K.; Díaz-Guillén, M. R., Fructose-mediated gold nanoparticles synthesis. *Cogent Chemistry* **2018,** *4* (1), 1447262.

204. Jung, J.; Raghavendra, G. M.; Kim, D.; Seo, J., One-step synthesis of starch-silver nanoparticle solution and its application to antibacterial paper coating. *Int J Biol Macromol* **2018,** *107* (Pt B), 2285-2290.

205. Agudelo, W.; Montoya, Y.; Bustamante, J., Using a non-reducing sugar in the green synthesis of gold and silver nanoparticles by the chemical reduction method. *Dyna (Medellin, Colombia)* **2018,** *85*, 69-78.

206. Meshram, S.; R. Bonde, S.; Gupta, I.; Gade, A.; Rai, M., Green synthesis of silver nanoparticles using white sugar. *Nanobiotechnology, IET* **2013,** *7*, 28-32.

207. Cárdenas-Triviño, G.; Ruiz-Parra, M.; Vergara-González, L.; Ojeda-Oyarzún, J.; Solorzano, G., Synthesis and Bactericidal Properties of Hyaluronic Acid Doped with Metal Nanoparticles. *Journal of Nanomaterials* **2017,** *2017*, 1-9.

208. Rayahin, J. E.; Buhrman, J. S.; Zhang, Y.; Koh, T. J.; Gemeinhart, R. A., High and Low Molecular Weight Hyaluronic Acid Differentially Influence Macrophage Activation. *ACS Biomater Sci Eng* **2015,** *1* (7), 481-493.

209. Choi, J.-Y.; Park, C. H.; Lee, J., Effect of Polymer Molecular Weight on Nanocomminution of Poorly Soluble Drug. *Drug Delivery* **2008,** *15* (5), 347-353.

210. Kim; Choi; Choi; Park; Ryu, Hyaluronic Acid-Coated Nanomedicine for Targeted Cancer Therapy. *Pharmaceutics* **2019,** *11* (7).

211. Liang, J.; Zeng, F.; Zhang, M.; Pan, Z.; Chen, Y.; Zeng, Y.; Xu, Y.; Xu, Q.; Huang, Y., Green synthesis of hyaluronic acid-based silver nanoparticles and their enhanced delivery to CD44+ cancer cells. *RSC Advances* **2015,** *5* (54), 43733-43740.

212. Zhang, X.; Yao, M.; Chen, M.; Li, L.; Dong, C.; Hou, Y.; Zhao, H.; Jia, B.; Wang, F., Hyaluronic Acid-Coated Silver Nanoparticles As a Nanoplatform for in Vivo Imaging Applications. *ACS Applied Materials & Interfaces* **2016,** *8*.

213. Vincenza Corsa, A. N., Sonia Bisicchia Process for the production of hyaluronic acid in Escherichia coli or Bacillus megaterium. 2015.

214. De Penning, R.; Tran, M.; Padalkar, S.; Turner, M., *Effect of citrate ratio and temperature on gold nanoparticle size and morphology*. IOP Publishing Ltd: 2016; Vol. 3.

215. Paramelle, D.; Sadovoy, A.; Gorelik, S.; Free, P.; Hobley, J.; Fernig, D. G., A rapid method to estimate the concentration of citrate capped silver nanoparticles from UV-visible light spectra. *The Analyst* **2014,** *139* (19).

216. He, Y. Q.; Liu, S. P.; Kong, L.; Liu, Z. F., A study on the sizes and concentrations of gold nanoparticles by spectra of absorption, resonance Rayleigh scattering and resonance non-linear scattering. *Spectrochimica Acta Part A: Molecular and Biomolecular Spectroscopy* **2005,** *61* (13-14), 2861-2866.

217. Navarro, J. R. G.; Werts, M. H. V., Resonant light scattering spectroscopy of gold, silver and gold–silver alloy nanoparticles and optical detection in microfluidic channels. *The Analyst* **2013,** *138* (2), 583-592.

218. López-Lorente, Á. I.; Valcárcel, M.; Mizaikoff, B., Continuous flow synthesis and characterization of tailor-made bare gold nanoparticles for use in SERS. *Microchimica Acta* **2014,** *181* (9-10), 1101-1108.

219. Oliveira, J. P.; Prado, A. R.; Keijok, W. J.; Ribeiro, M. R. N.; Pontes, M. J.; Nogueira, B. V.; Guimarães, M. C. C., A helpful method for controlled synthesis of monodisperse gold nanoparticles through response surface modeling. *Arabian Journal of Chemistry* **2017**.

220. Shimmin, R. G.; Schoch, A. B.; Braun, P. V., Polymer Size and Concentration Effects on the Size of Gold Nanoparticles Capped by Polymeric Thiols. *Langmuir* **2004,** *20* (13), 5613-5620.

221. Chudobova, D.; Nejdl, L.; Gumulec, J.; Krystofova, O.; Rodrigo, M.; Kynicky, J.; Ruttkay-Nedecky, B.; Kopel, P.; Babula, P.; Adam, V.; Kizek, R., Complexes of Silver(I) Ions and Silver Phosphate Nanoparticles with Hyaluronic Acid and/or Chitosan as Promising Antimicrobial Agents for Vascular Grafts. *International Journal of Molecular Sciences* **2013,** *14* (7), 13592-13614.

222. Kemp, M. M.; Kumar, A.; Clement, D.; Ajayan, P.; Mousa, S.; Linhardt, R. J., Hyaluronan- and heparin-reduced silver nanoparticles with antimicrobial properties. *Nanomedicine : nanotechnology, biology, and medicine* **2009,** *4* (4), 421-429.

223. Hien, N. Q.; Van Phu, D.; Duy, N. N.; Quoc, L. A., Radiation synthesis and characterization of hyaluronan capped gold nanoparticles. *Carbohydrate Polymers* **2012,** *89* (2), 537-541.

224. Chandra, A.; Singh, M., Biosynthesis of amino acid functionalized silver nanoparticles for potential catalytic and oxygen sensing applications. *Inorganic Chemistry Frontiers* **2018,** *5* (1), 233-257.

225. Tue Anh, N.; Phu, D.; Duy, N.; Du, B.; Hien, N., Synthesis of alginate stabilized gold nanoparticles by γ-irradiation with controllable size using different Au3+ concentration and seed particles enlargement. *Radiation Physics and Chemistry* **2010,** *79*, 405-408.

226. Huang, L.; Maolin, Z.; Peng, J.; Xu, L.; Li, J.; Wei, G., Synthesis, size control and fluorescence studies of gold nanoparticles in carboxymethylated chitosan aqueous solutions. *Journal of colloid and interface science* **2008,** *316*, 398-404.

227. Yang, S.; Wang, Y.; Wang, Q.; Zhang, R.; Ding, B., UV irradiation induced formation of Au nanoparticles at room temperature: The case of pH values. *Colloids and Surfaces A-physicochemical and Engineering Aspects - COLLOID SURFACE A* **2007,** *301*, 174-183.

228. Dobias, J.; Bernier-Latmani, R., Silver Release from Silver Nanoparticles in Natural Waters. *Environmental Science & Technology* **2013,** *47* (9), 4140-4146.

229. Di Pietro, P.; Zaccaro, L.; Comegna, D.; Del Gatto, A.; Saviano, M.; Snyders, R.; Cossement, D.; Satriano, C.; Rizzarelli, E., Silver nanoparticles functionalized with a fluorescent cyclic RGD peptide: a versatile integrin targeting platform for cells and bacteria. *RSC Advances* **2016,** *6* (113), 112381-112392.

230. Uddin, J., Terahertz multispectral imaging for the analysis of gold nanoparticles' size and the number of unit cells in comparison with other techniques. *International Journal of Biosensors & Bioelectronics* **2018,** *4* (3).

231. Almalik, A.; Benabdelkamel, H.; Masood, A.; Alanazi, I. O.; Alradwan, I.; Majrashi, M. A.; Alfadda, A. A.; Alghamdi, W. M.; Alrabiah, H.; Tirelli, N.; Alhasan, A. H., Hyaluronic Acid Coated Chitosan Nanoparticles Reduced the Immunogenicity of the Formed Protein Corona. *Scientific Reports* **2017,** *7* (1).

232. Daniel, S. C. G. K.; Banu, B. N.; Harshiny, M.; Nehru, K.; Ganesh, P. S.; Kumaran, S.; Sivakumar, M., Ipomea carnea-based silver nanoparticle synthesis for antibacterial activity against selected human pathogens. *Journal of Experimental Nanoscience* **2014,** *9* (2), 197-209.

233. Chen, H.; Qin, J.; Hu, Y., Efficient Degradation of High-Molecular-Weight Hyaluronic Acid by a Combination of Ultrasound, Hydrogen Peroxide, and Copper Ion. *Molecules* **2019,** *24* (3).

234. Tokita, Y.; Okamoto, A., Hydrolytic degradation of hyaluronic acid. *Polymer Degradation and Stability* **1995,** *48* (2), 269-273.

235. Zamanhuri, N. A.; Alrozi, R.; Osman, M., *Biosynthesis of silver nanoparticles using pink guava waste extract (PGWE)*. 2012; p 98-102.

236. Tyagi, H.; Kushwaha, A.; Kumar, A.; Aslam, M., A Facile pH Controlled Citrate-Based Reduction Method for Gold Nanoparticle Synthesis at Room Temperature. *Nanoscale Research Letters* **2016,** *11* (1).

237. Uppal, M. A.; Kafizas, A.; Lim, T. H.; Parkin, I. P., The extended time evolution size decrease of gold nanoparticles formed by the Turkevich method. *New Journal of Chemistry* **2010,** *34* (7), 1401-1407.

238. Thanh, N. T. K.; Maclean, N.; Mahiddine, S., Mechanisms of Nucleation and Growth of Nanoparticles in Solution. *Chemical Reviews* **2014,** *114* (15), 7610-7630.

239. Lawler, D. F.; Mikelonis, A. M.; Kim, I.; Lau, B. L. T.; Youn, S., Silver nanoparticle removal from drinking water: flocculation/sedimentation or filtration? *Water Science and Technology: Water Supply* **2013,** *13* (5), 1181-1187.

240. Lin, S.; Cheng, Y.; Liu, J.; Wiesner, M. R., Polymeric Coatings on Silver Nanoparticles Hinder Autoaggregation but Enhance Attachment to Uncoated Surfaces. *Langmuir* **2012,** *28* (9), 4178-4186.

241. Gangula, A.; Chelli, J.; Bukka, S.; Poonthiyil, V.; Podila, R.; Kannan, R.; Rao, A. M., Thione–gold nanoparticles interactions: Vroman-like effect, self-assembly and sensing. *Journal of Materials Chemistry* **2012,** *22* (43).

242. Fischer, R. L.; McCoy, M. G.; Grant, S. A., Electrospinning collagen and hyaluronic acid nanofiber meshes. *Journal of Materials Science: Materials in Medicine* **2012,** *23* (7), 1645-1654.

243. Cheng, Z.; Zhang, F.; Liu, W.; Cui, L.; Kang, L., A novel preparation for a PVA/l-histidine/AgNPs membrane and its antibacterial property. *RSC Advances* **2015,** *5* (67), 54182-54187.

244. Salih, E.; M. Reicha, F.; El-Sherbiny, I., Electrochemical Synthesis of New Silver-Chitosan/Polyvinyl Alcohol Hybrid Nanoparticles and Evaluation of Their Antibacterial Activities. *Journal of Nanoscience and Technology* **2016**.

245. Pimpang, P.; Choopun, S., Monodispersity and Stability of Gold Nanoparticles Stabilized by Using Polyvinyl Alcohol. *Chiang Mai Journal of Science* **2011,** *38*, 31-31.

246. Bharali, D. J.; Mousa, S. A., Emerging nanomedicines for early cancer detection and improved treatment: Current perspective and future promise. *Pharmacology & Therapeutics* **2010,** *128* (2), 324-335.

247. Sahoo, A. K.; Banerjee, S.; Ghosh, S. S.; Chattopadhyay, A., Simultaneous RGB Emitting Au Nanoclusters in Chitosan Nanoparticles for Anticancer Gene Theranostics. *ACS Applied Materials & Interfaces* **2013,** *6* (1), 712-724.

248. Yezhelyev, M. V.; Gao, X.; Xing, Y.; Al-Hajj, A.; Nie, S.; O'Regan, R. M., Emerging use of nanoparticles in diagnosis and treatment of breast cancer. *The Lancet Oncology* **2006,** *7* (8), 657-667.

249. Thota, S.; Crans, D. C., *Metal Nanoparticles*. 2018.

250. Ventola, C. L., The nanomedicine revolution: part 1: emerging concepts. *P T* **2012,** *37* (9), 512-25.

251. Moore, K. A.; Pate, K. M.; Soto-Ortega, D. D.; Lohse, S.; van der Munnik, N.; Lim, M.; Jackson, K. S.; Lyles, V. D.; Jones, L.; Glassgow, N.; Napumecheno, V. M.; Mobley, S.; Uline, M. J.; Mahtab, R.; Murphy, C. J.; Moss, M. A., Influence of gold nanoparticle surface chemistry and diameter upon Alzheimer’s disease amyloid-β protein aggregation. *Journal of Biological Engineering* **2017,** *11* (1).

252. Lee, K.-S.; El-Sayed, M. A., Gold and Silver Nanoparticles in Sensing and Imaging: Sensitivity of Plasmon Response to Size, Shape, and Metal Composition. *The Journal of Physical Chemistry B* **2006,** *110* (39), 19220-19225.

253. Zeng, S.; Yong, K.-T.; Roy, I.; Dinh, X.-Q.; Yu, X.; Luan, F., A Review on Functionalized Gold Nanoparticles for Biosensing Applications. *Plasmonics* **2011,** *6* (3), 491-506.

254. Loo, C.; Lowery, A.; Halas, N.; West, J.; Drezek, R., Immunotargeted Nanoshells for Integrated Cancer Imaging and Therapy. *Nano Letters* **2005,** *5* (4), 709-711.

255. Buttacavoli, M.; Albanese, N. N.; Di Cara, G.; Alduina, R.; Faleri, C.; Gallo, M.; Pizzolanti, G.; Gallo, G.; Feo, S.; Baldi, F.; Cancemi, P., Anticancer activity of biogenerated silver nanoparticles: an integrated proteomic investigation. *Oncotarget* **2018,** *9* (11).

256. Lin, J.; Huang, Z.; Wu, H.; Zhou, W.; Jin, P.; Wei, P.; Zhang, Y.; Zheng, F.; Zhang, J.; Xu, J.; Hu, Y.; Wang, Y.; Li, Y.; Gu, N.; Wen, L., Inhibition of autophagy enhances the anticancer activity of silver nanoparticles. *Autophagy* **2014,** *10* (11), 2006-2020.

257. Gurunathan, S.; Lee, K.-J.; Kalishwaralal, K.; Sheikpranbabu, S.; Vaidyanathan, R.; Eom, S. H., Antiangiogenic properties of silver nanoparticles. *Biomaterials* **2009,** *30* (31), 6341-6350.

258. Sangiliyandi, G., Antitumor activity of silver nanoparticles in Dalton’s lymphoma ascites tumor model. *International Journal of Nanomedicine* **2010**.

259. Horikoshi, S.; Serpone, N., *Microwaves in Nanoparticle Synthesis*. 2013.

260. Maillard, J.-Y.; Hartemann, P., Silver as an antimicrobial: Facts and gaps in knowledge. *Critical reviews in microbiology* **2012,** *39*.

261. Seil, J. T.; Webster, T. J., Antimicrobial applications of nanotechnology: methods and literature. *Int J Nanomedicine* **2012,** *7*, 2767-81.

262. Chatterjee, D. K.; Diagaradjane, P.; Krishnan, S., Nanoparticle-mediated hyperthermia in cancer therapy. *Therapeutic Delivery* **2011,** *2* (8), 1001-1014.

263. Maillard, J.-Y.; Hartemann, P., Silver as an antimicrobial: facts and gaps in knowledge. *Critical Reviews in Microbiology* **2012,** *39* (4), 373-383.

264. Sajja, H. K.; East, M. P.; Mao, H.; Wang, Y. A.; Nie, S.; Yang, L., Development of multifunctional nanoparticles for targeted drug delivery and noninvasive imaging of therapeutic effect. *Curr Drug Discov Technol* **2009,** *6* (1), 43-51.

265. Franci, G.; Falanga, A.; Galdiero, S.; Palomba, L.; Rai, M.; Morelli, G.; Galdiero, M., Silver Nanoparticles as Potential Antibacterial Agents. *Molecules* **2015,** *20* (5), 8856-8874.

266. Presti, D.; Scott, J. E., Hyaluronan-mediated protective effect against cell damage caused by enzymatically produced hydroxyl (OH·) radicals is dependent on hyaluronan molecular mass. *Cell Biochemistry and Function* **1994,** *12* (4), 281-288.

267. Fukuda, K.; Takayama, M.; Ueno, M.; Oh, M.; Asada, S.; Kumano, F.; Tanaka, S., Hyaluronic acid inhibits interleukin-1-induced superoxide anion in bovine chondrocytes. *Inflammation Research* **1997,** *46* (3), 114-117.

268. Cortivo, R.; Brun, P.; Cardarelli, L.; O'Regan, M.; Radice, M.; Abatangelo, G., Antioxidant effects of hyaluronan and its α-methyl-prednisolone derivative in chondrocyteand cartilage cultures. *Seminars in Arthritis and Rheumatism* **1996,** *26* (1), 492-501.

269. Zhu, Z.; Wang, Y.-M.; Yang, J.; Luo, X.-S., Hyaluronic acid: a versatile biomaterial in tissue engineering. *Plastic and Aesthetic Research* **2017,** *4* (12).

270. Chen, W. Y. J., Functions of Hyaluronan in Wound Repair. In *Hyaluronan*, 2002; pp 147-156.

271. Mattheolabakis, G.; Milane, L.; Singh, A.; Amiji, M. M., Hyaluronic acid targeting of CD44 for cancer therapy: from receptor biology to nanomedicine. *Journal of Drug Targeting* **2015,** *23* (7-8), 605-618.

272. Jordan, A. R.; Racine, R. R.; Hennig, M. J. P.; Lokeshwar, V. B., The Role of CD44 in Disease Pathophysiology and Targeted Treatment. *Frontiers in Immunology* **2015,** *6*.

273. Necas, J.; Bartosikova, L.; Brauner, P.; Kolar, J., Hyaluronic acid (hyaluronan): a review. *Veterinární Medicína* **2008,** *53* (No. 8), 397-411.

274. Eliaz, R. E.; Szoka, F. C., Jr., Liposome-encapsulated doxorubicin targeted to CD44: a strategy to kill CD44-overexpressing tumor cells. *Cancer Res* **2001,** *61* (6), 2592-601.

275. Arpicco, S.; De Rosa, G.; Fattal, E., Lipid-Based Nanovectors for Targeting of CD44-Overexpressing Tumor Cells. *Journal of Drug Delivery* **2013,** *2013*, 1-8.

276. Ganesh, S.; Iyer, A. K.; Morrissey, D. V.; Amiji, M. M., Hyaluronic acid based self-assembling nanosystems for CD44 target mediated siRNA delivery to solid tumors. *Biomaterials* **2013,** *34* (13), 3489-3502.

277. Turley, E. A.; Belch, A. J.; Poppema, S.; Pilarski, L. M., Expression and function of a receptor for hyaluronan-mediated motility on normal and malignant B lymphocytes. *Blood* **1993,** *81* (2), 446-53.

278. Aruffo, A.; Stamenkovic, I.; Melnick, M.; Underhill, C. B.; Seed, B., CD44 is the principal cell surface receptor for hyaluronate. *Cell* **1990,** *61* (7), 1303-1313.

279. Marhaba, R.; Zöller, M., CD44 in Cancer Progression: Adhesion, Migration and Growth Regulation. *Journal of Molecular Histology* **2003,** *35* (3), 211-231.

280. Agnantis, N. J.; Goussia, A. C.; Batistatou, A.; Stefanou, D., Tumor markers in cancer patients. an update of their prognostic significance. Part II. *In Vivo* **2004,** *18* (4), 481-8.

281. Nagano, O.; Saya, H., Mechanism and biological significance of CD44 cleavage. *Cancer Science* **2004,** *95* (12), 930-935.

282. Ropponen, K.; Tammi, M.; Parkkinen, J.; Eskelinen, M.; Tammi, R.; Lipponen, P.; Agren, U.; Alhava, E.; Kosma, V. M., Tumor cell-

associated hyaluronan as an unfavorable prognostic factor in colorectal cancer. *Cancer Res* **1998,** *58* (2), 342-7.

283. Auvinen, P.; Tammi, R.; Parkkinen, J.; Tammi, M.; Ågren, U.; Johansson, R.; Hirvikoski, P.; Eskelinen, M.; Kosma, V.-M., Hyaluronan in Peritumoral Stroma and Malignant Cells Associates with Breast Cancer Spreading and Predicts Survival. *The American Journal of Pathology* **2000,** *156* (2), 529-536.

284. Itano, N.; Atsumi, F.; Sawai, T.; Yamada, Y.; Miyaishi, O.; Senga, T.; Hamaguchi, M.; Kimata, K., Abnormal accumulation of hyaluronan matrix diminishes contact inhibition of cell growth and promotes cell migration. *Proceedings of the National Academy of Sciences* **2002,** *99* (6), 3609-3614.

285. Toole, B. P., Hyaluronan promotes the malignant phenotype. *Glycobiology* **2002,** *12* (3), 37R-42R.

286. Sugahara, K. N.; Murai, T.; Nishinakamura, H.; Kawashima, H.; Saya, H.; Miyasaka, M., Hyaluronan Oligosaccharides Induce CD44 Cleavage and Promote Cell Migration in CD44-expressing Tumor Cells. *Journal of Biological Chemistry* **2003,** *278* (34), 32259-32265.

287. Laurent, T. C.; Fraser, J. R., Hyaluronan. *FASEB J* **1992,** *6* (7), 2397-404.

288. Papakonstantinou, E.; Roth, M.; Karakiulakis, G., Hyaluronic acid: A key molecule in skin aging. *Dermato-Endocrinology* **2014,** *4* (3), 253-258.

289. Lokeshwar, V. B.; Obek, C.; Soloway, M. S.; Block, N. L., Tumor-associated hyaluronic acid: a new sensitive and specific urine marker for bladder cancer. *Cancer Res* **1997,** *57* (4), 773-7.

290. Zeng, C.; Toole, B. P.; Kinney, S. D.; Kuo, J. W.; Stamenkovic, I., Inhibition of tumor growth in vivo by hyaluronan oligomers. *Int J Cancer* **1998,** *77* (3), 396-401.

291. Ghatak, S.; Misra, S.; Toole, B. P., Hyaluronan Oligosaccharides Inhibit Anchorage-independent Growth of Tumor Cells by Suppressing the Phosphoinositide 3-Kinase/Akt Cell Survival Pathway. *Journal of Biological Chemistry* **2002,** *277* (41), 38013-38020.

292. Misra, S.; Ghatak, S.; Zoltan-Jones, A.; Toole, B. P., Regulation of Multidrug Resistance in Cancer Cells by Hyaluronan. *Journal of Biological Chemistry* **2003,** *278* (28), 25285-25288.

293. Fakhari, A.; Berkland, C., Applications and emerging trends of hyaluronic acid in tissue engineering, as a dermal filler and in osteoarthritis treatment. *Acta Biomaterialia* **2013,** *9* (7), 7081-7092.

294. Jung, J.; Park, S.; Hong, S.; Ha, M. W.; Park, H.-g.; Park, Y.; Lee, H.-J.; Park, Y., Synthesis of gold nanoparticles with glycosides: synthetic trends based on the structures of glycones and aglycones. *Carbohydrate Research* **2014,** *386*, 57-61.

295. Zhang, X.; Yao, M.; Chen, M.; Li, L.; Dong, C.; Hou, Y.; Zhao, H.; Jia, B.; Wang, F., Hyaluronic Acid-Coated Silver Nanoparticles As a Nanoplatform for in Vivo Imaging Applications. *ACS Applied Materials & Interfaces* **2016,** *8* (39), 25650-25653.

296. Garcia, M. A., Surface plasmons in metallic nanoparticles: fundamentals and applications. *Journal of Physics D: Applied Physics* **2011,** *44* (28).

297. Uppal, M. A.; Kafizas, A.; Lim, T. H.; Parkin, I. P., The extended time evolution size decrease of gold nanoparticles formed by the Turkevich method. *New Journal of Chemistry* **2010,** *34* (7).

298. Šimáková, P.; Gautier, J.; Procházka, M.; Hervé-Aubert, K.; Chourpa, I., Polyethylene-glycol-Stabilized Ag Nanoparticles for Surface-Enhanced Raman Scattering Spectroscopy: Ag Surface Accessibility Studied Using Metalation of Free-Base Porphyrins. *The Journal of Physical Chemistry C* **2014,** *118* (14), 7690-7697.

299. Zamanhuri, N. A.; Alrozi, R.; Osman, M. S., Biosynthesis of silver nanoparticles using pink guava waste extract (PGWE). In *2012 IEEE Business, Engineering & Industrial Applications Colloquium (BEIAC)*, 2012; pp 98-102.

300. Kong, B.; Seog, J. H.; Graham, L. M.; Lee, S. B., Experimental considerations on the cytotoxicity of nanoparticles. *Nanomedicine* **2011,** *6* (5), 929-941.

301. Ghosh, K., Biocompatibility of hyaluronic acid: From cell recognition to therapeutic applications. In *Natural-Based Polymers for Biomedical Applications*, 2008; pp 716-737.

302. Chen, C.; Zhao, S.; Karnad, A.; Freeman, J. W., The biology and role of CD44 in cancer progression: therapeutic implications. *Journal of Hematology & Oncology* **2018,** *11* (1).

303. Foroozandeh, P.; Aziz, A. A., Insight into Cellular Uptake and Intracellular Trafficking of Nanoparticles. *Nanoscale Research Letters* **2018,** *13* (1).

304. Ong, C.; Lim, J. Z. Z.; Ng, C. T.; Li, J. J.; Yung, L. Y. L.; Bay, B. H., Silver Nanoparticles in Cancer: Therapeutic Efficacy and Toxicity. *Current Medicinal Chemistry* **2013,** *20* (6), 772-781.

305. De Palma, M.; Biziato, D.; Petrova, T. V., Microenvironmental regulation of tumour angiogenesis. *Nature Reviews Cancer* **2017,** *17*, 457.
306. Arnold, F.; West, D. C., Angiogenesis in wound healing. *Pharmacology & therapeutics* **1991,** *52* (3), 407-22.
307. Pardue, E. L.; Ibrahim, S.; Ramamurthi, A., Role of hyaluronan in angiogenesis and its utility to angiogenic tissue engineering. *Organogenesis* **2008,** *4* (4), 203-214.
308. Lai, P. H.; Chang, Y.; Chen, S. C.; Wang, C. C.; Liang, H. C.; Chang, W. C.; Sung, H. W., Acellular biological tissues containing inherent glycosaminoglycans for loading basic fibroblast growth factor promote angiogenesis and tissue regeneration. *Tissue engineering* **2006,** *12* (9), 2499-508.
309. West, D. C.; Kumar, S., The effect of hyaluronate and its oligosaccharides on endothelial cell proliferation and monolayer integrity. *Experimental cell research* **1989,** *183* (1), 179-96.
310. Huang; Huang; Lew; Fan; Chang; Huang, Gamma-Irradiation-Prepared Low Molecular Weight Hyaluronic Acid Promotes Skin Wound Healing. *Polymers* **2019,** *11* (7).
311. Maharjan, A. S.; Pilling, D.; Gomer, R. H., High and Low Molecular Weight Hyaluronic Acid Differentially Regulate Human Fibrocyte Differentiation. *PLOS ONE* **2011,** *6* (10), e26078.
312. Kim, J.; Park, Y.; Tae, G.; Lee, K. B.; Hwang, C. M.; Hwang, S. J.; Kim, I. S.; Noh, I.; Sun, K., Characterization of low-molecular-weight hyaluronic acid-based hydrogel and differential stem cell responses in the hydrogel microenvironments. *Journal of Biomedical Materials Research Part A* **2009,** *88A* (4), 967-975.
313. Koyama, H.; Hibi, T.; Isogai, Z.; Yoneda, M.; Fujimori, M.; Amano, J.; Kawakubo, M.; Kannagi, R.; Kimata, K.; Taniguchi, S.; Itano, N., Hyperproduction of hyaluronan in neu-induced mammary tumor accelerates angiogenesis through stromal cell recruitment: possible involvement of versican/PG-M. *The American journal of pathology* **2007,** *170* (3), 1086-99.
314. Wakabayashi, S., New Insights into the Functions of Histidine-Rich Glycoprotein. 2013; pp 467-493.
315. Magrì, A.; Grasso, G.; Corti, F.; Finetti, F.; Greco, V.; Santoro, A. M.; Sciuto, S.; La Mendola, D.; Morbidelli, L.; Rizzarelli, E., Peptides derived from the histidine–proline rich glycoprotein bind copper ions and exhibit anti-angiogenic properties. *Dalton Transactions* **2018,** *47* (28), 9492-9503.

316. Rydengård, V.; Olsson, A.-K.; Mörgelin, M.; Schmidtchen, A., Histidine-rich glycoprotein exerts antibacterial activity. *FEBS Journal* **2007,** *274* (2), 377-389.

317. Shannon, O.; Rydengard, V.; Schmidtchen, A.; Morgelin, M.; Alm, P.; Sorensen, O. E.; Bjorck, L., Histidine-rich glycoprotein promotes bacterial entrapment in clots and decreases mortality in a mouse model of sepsis. *Blood* **2010,** *116* (13), 2365-2372.

318. Mukherjee, P.; Bhattacharya, R.; Wang, P.; Wang, L.; Basu, S.; Nagy, J. A.; Atala, A.; Mukhopadhyay, D.; Soker, S., Antiangiogenic properties of gold nanoparticles. *Clinical cancer research : an official journal of the American Association for Cancer Research* **2005,** *11* (9), 3530-4.

319. Arvizo, R. R.; Rana, S.; Miranda, O. R.; Bhattacharya, R.; Rotello, V. M.; Mukherjee, P., Mechanism of anti-angiogenic property of gold nanoparticles: role of nanoparticle size and surface charge. *Nanomedicine : nanotechnology, biology, and medicine* **2011,** *7* (5), 580-587.

320. Roh, Y.-J.; Rho, C. R.; Cho, W.-K.; Kang, S., The Antiangiogenic Effects of Gold Nanoparticles on Experimental Choroidal Neovascularization in Mice. *Investigative Ophthalmology & Visual Science* **2016,** *57* (15), 6561-6567.

321. Bartczak, D.; Muskens, O. L.; Nitti, S.; Millar, T. M.; Kanaras, A. G., Nanoparticles for inhibition of in vitro tumour angiogenesis: synergistic actions of ligand function and laser irradiation. *Biomaterials Science* **2015,** *3* (5), 733-741.

322. Darweesh, R. S.; Ayoub, N. M.; Nazzal, S., <p>Gold nanoparticles and angiogenesis: molecular mechanisms and biomedical applications</p>. *International Journal of Nanomedicine* **2019,** *Volume 14*, 7643-7663.

323. Saeed, B. A.; Lim, V.; Yusof, N. A.; Khor, K. Z.; Rahman, H. S.; Abdul Samad, N., Antiangiogenic properties of nanoparticles: a systematic review. *International journal of nanomedicine* **2019,** *14*, 5135-5146.

324. Gurunathan, S.; Lee, K.-J.; Kalishwaralal, K.; Sheikpranbabu, S.; Vaidyanathan, R.; Eom, S., Antiangiogenic properties of silver nanoparticles. *Biomaterials* **2009,** *30*, 6341-50.

325. Kemp, M.; Kumar, A.; Mousa, S.; Dyskin, E.; Yalcin, M.; Ajayan, P.; Linhardt, R.; Mousa, S., Gold and Silver Nanoparticles Conjugated with Heparin Derivative Possess Anti-Angiogenesis Properties. *Nanotechnology* **2009,** *20*, 455104.

326. Mukherjee, S.; Patra, C. R., Therapeutic application of anti-angiogenic nanomaterials in cancers. *Nanoscale* **2016,** *8* (25), 12444-12470.

327. Baharara, J.; Namvar, F.; Mousavi, M.; Ramezani, T.; Mohamad, R., Anti-Angiogenesis Effect of Biogenic Silver Nanoparticles Synthesized Using Saliva officinalis on Chick Chorioalantoic Membrane (CAM). *Molecules* **2014,** *19* (9), 13498-13508.

328. M7-A7, METHODS FOR DILUTION ANTIMICROBIAL SUSCEPTIBILITY TESTS FOR BACTERIA THAT GROW AEROBICALLY. *Clinical Laboratory Standards Institute* **2006**.

329. C, A. B. A. H., ANTIBACTERIALACTIVITY OF SILVER NANOPARTICLES CONJUGATED WITH ANTIBIOTICS. *BIONANO FRONTIER* **2014,** *7* (2).

330. Maruyama, T.; Matsushita, H.; Shimada, Y.; Kamata, I.; Hanaki, M.; Sonokawa, S.; Kamiya, N.; Goto, M., Proteins and protein-rich biomass as environmentally friendly adsorbents selective for precious metal ions. *Environ Sci Technol* **2007,** *41* (4), 1359-64.

331. Jo, M.-R.; Bae, S.-H.; Go, M.-R.; Kim, H.-J.; Hwang, Y.-G.; Choi, S.-J., Toxicity and Biokinetics of Colloidal Gold Nanoparticles. *Nanomaterials* **2015,** *5* (2), 835-850.

332. Beer, Bestimmung der Absorption des rothen Lichts in farbigen Flüssigkeiten. *Annalen der Physik und Chemie* **1852,** *162* (5), 78-88.

333. Cheng, M. J.; Prabakaran, P.; Kumar, R.; Sridhar, S.; Ebong, E. E., Synthesis of Functionalized 10-nm Polymer-coated Gold Particles for Endothelium Targeting and Drug Delivery. *J Vis Exp* **2018,** (131), 56760.

334. Guo, H.; Zhang, J.; Boudreau, M.; Meng, J.; Yin, J.-j.; Liu, J.; Xu, H., Intravenous administration of silver nanoparticles causes organ toxicity through intracellular ROS-related loss of inter-endothelial junction. *Particle and Fibre Toxicology* **2016,** *13* (1).

335. Porenczuk, A.; Grzeczkowicz, A.; Maciejewska, I.; Gołaś, M.; Piskorska, K.; Kolenda, A.; Gozdowski, D.; Kopeć-Swoboda, E.; Granicka, L.; Olczak-Kowalczyk, D. J. A. i. c.; University, e. m. o. o. W. M., An initial evaluation of cytotoxicity, genotoxicity and antibacterial effectiveness of a disinfection liquid containing silver nanoparticles alone and combined with a glass-ionomer cement and dentin bonding systems. **2019,** *28* (1), 75-83.

336. Suresh, C.; Gayathri, R.; Priya, V. V. J. D. I. T., In vitro cytotoxicity studies of silver nanoparticles with activated folic acid on cancer cell lines. **2019,** *12* (4).

337. Tang, J.; Lu, X.; Chen, B.; Cai, E.; Liu, W.; Jiang, J.; Chen, F.; Shan, X.; Zhang, H. J. T. J. o. t. s., Mechanisms of silver nanoparticles-induced cytotoxicity and apoptosis in rat tracheal epithelial cells. **2019,** *44* (3), 155-165.

338. Patil, M. P.; Kim, G.-D., Eco-friendly approach for nanoparticles synthesis and mechanism behind antibacterial activity of silver and anticancer activity of gold nanoparticles. *Applied Microbiology and Biotechnology* **2016,** *101* (1), 79-92.

339. Podsiadlo, P.; Sinani, V. A.; Bahng, J. H.; Kam, N. W.; Lee, J.; Kotov, N. A., Gold nanoparticles enhance the anti-leukemia action of a 6-mercaptopurine chemotherapeutic agent. *Langmuir* **2008,** *24* (2), 568-74.

340. Burdușel, A.-C.; Gherasim, O.; Grumezescu, A. M.; Mogoantă, L.; Ficai, A.; Andronescu, E., Biomedical Applications of Silver Nanoparticles: An Up-to-Date Overview. *Nanomaterials* **2018,** *8* (9).

341. Ghanavati Behbahan, F.; Salari, M.; Mousavi, S. R.; Rezaei, R., Antimicrobial activities of Gold nanoparticles against Salmonella typhimurium. *Advanced Herbal Medicine* **2017,** *3* (1), 26-30.

342. Zawrah, M.; Abd El-Moez, S., Antimicrobial Activities of Gold Nanoparticles against Major Foodborne Pathogens. *Life Science Journal* **2011,** *8*.

343. Yuan, Y.-G.; Peng, Q.-L.; Gurunathan, S., Effects of Silver Nanoparticles on Multiple Drug-Resistant Strains of Staphylococcus aureus and Pseudomonas aeruginosa from Mastitis-Infected Goats: An Alternative Approach for Antimicrobial Therapy. *International Journal of Molecular Sciences* **2017,** *18*, 569.

344. Rydengard, V.; Olsson, A. K.; Morgelin, M.; Schmidtchen, A., Histidine-rich glycoprotein exerts antibacterial activity. *The FEBS journal* **2007,** *274* (2), 377-89.

345. Lima, E.; Guerra, R.; Lara, V.; Guzmán, A., Gold nanoparticles as efficient antimicrobial agents for Escherichia coli and Salmonella typhi. *Chemistry Central Journal* **2013,** *7* (1).

346. Zarei, M.; Jamnejad, A.; Khajehali, E., Antibacterial effect of silver nanoparticles against four foodborne pathogens. *Jundishapur J Microbiol* **2014,** *7* (1), e8720-e8720.

347. Kundu, S., Gold Nanoparticles: Their Application as i Antimicrobial Agents and Vehicles of Gene Delivery. *Advances in Biotechnology & Microbiology* **2017,** *5*.

348. M100-S23, Performance Standards for Antimicrobial Susceptibility Testing; Twenty-Third Informational Supplement. *Clinical and Laboratory Standards Institute* **2013,** *10* (1).

349. Wang, L.; Hu, C.; Shao, L., The antimicrobial activity of nanoparticles: present situation and prospects for the future. *International journal of nanomedicine* **2017,** *12*, 1227-1249.

350. Malysheva, A.; Lombi, E.; Voelcker, N. H., Bridging the divide between human and environmental nanotoxicology. *Nature Nanotechnology* **2015,** *10*, 835.

351. Sajid, M.; Ilyas, M.; Basheer, C.; Tariq, M.; Daud, M.; Baig, N.; Shehzad, F., Impact of nanoparticles on human and environment: review of toxicity factors, exposures, control strategies, and future prospects. *Environmental science and pollution research international* **2015,** *22* (6), 4122-43.

352. Bakand, S.; Hayes, A.; Dechsakulthorn, F., Nanoparticles: a review of particle toxicology following inhalation exposure. *Inhalation toxicology* **2012,** *24* (2), 125-35.

353. Gottschalk, F.; Nowack, B., The release of engineered nanomaterials to the environment. *Journal of environmental monitoring : JEM* **2011,** *13* (5), 1145-55.

354. Senbanjo, L. T.; AlJohani, H.; Majumdar, S.; Chellaiah, M. A., Characterization of CD44 intracellular domain interaction with RUNX2 in PC3 human prostate cancer cells. *Cell Communication and Signaling* **2019,** *17* (1), 80.

355. A Blaheta, R.; Powerski, M.; Hudak, L.; Juengel, E.; Jonas, D.; von Knethen, A.; Willhelm Doerr, H.; Cinatl, J., Tumor-Endothelium Cross Talk Blocks Recruitment of Neutrophils to Endothelial Cells: A Novel Mechanism of Endothelial Cell Anergy 1. *Neoplasia (New York, N.Y.)* **2009,** *11*, 1054-63.

356. Raffi, M.; Hussain, F.; Bhatti, T.; Akhter, J.; Hameed, A.; Hassan, M., Antibacterial Characterization of Silver Nanoparticles against E. Coli ATCC-15224. *JOURNAL OF MATERIALS SCIENCE & TECHNOLOGY* **2007,** *24*, 192-196.

357. Smetana, A. B.; Klabunde, K. J.; Marchin, G. R.; Sorensen, C. M., Biocidal Activity of Nanocrystalline Silver Powders and Particles. *Langmuir* **2008,** *24* (14), 7457-7464.

358. Cho, E. C.; Zhang, Q.; Xia, Y., The effect of sedimentation and diffusion on cellular uptake of gold nanoparticles. *Nature nanotechnology* **2011,** *6* (6), 385-391.

359. Rascol, E.; Devoisselle, J.-M.; Chopineau, J., The relevance of membrane models to understand nanoparticles–cell membrane interactions. *Nanoscale* **2016,** *8* (9), 4780-4798.

360. Yousefi, N.; Tufenkji, N., Probing the Interaction between Nanoparticles and Lipid Membranes by Quartz Crystal Microbalance with Dissipation Monitoring. *Frontiers in Chemistry* **2016,** *4*.

361. Hofmann, D.; Mailänder, V., Pharmacology of nanocarriers on the microscale: importance of uptake mechanisms and intracellular trafficking for efficient drug delivery. *Nanomedicine : nanotechnology, biology, and medicine* **2013,** *8* (3), 321-323.

362. Satriano, C.; Svedhem, S.; Kasemo, B., Well-defined lipid interfaces for protein adsorption studies. *Physical chemistry chemical physics : PCCP* **2012,** *14* (48), 16695-8.

363. Satriano, C.; Edvardsson, M.; Ohlsson, G.; Wang, G.; Svedhem, S.; Kasemo, B., Plasma Oxidized Polyhydroxymethylsiloxane—A New Smooth Surface for Supported Lipid Bilayer Formation. *Langmuir* **2010,** *26* (8), 5715-5725.

364. Keller, C. A.; Kasemo, B., Surface Specific Kinetics of Lipid Vesicle Adsorption Measured with a Quartz Crystal Microbalance. *Biophysical Journal* **1998,** *75* (3), 1397-1402.

365. Oh, S.; Wilcox, M.; Pearson, J. P.; Borrós, S., Optimal design for studying mucoadhesive polymers interaction with gastric mucin using a quartz crystal microbalance with dissipation (QCM-D): Comparison of two different mucin origins. *European Journal of Pharmaceutics and Biopharmaceutics* **2015,** *96*, 477-483.

366. L. Vázquez-González, M.; Calpena, A.; Domènech, Ò.; Teresa Montero, M.; Borrell, J., Enhanced topical delivery of hyaluronic acid encapsulated in liposomes: A surface-dependent phenomenon. *Colloids and Surfaces B: Biointerfaces* **2015,** *134*.

367. Ahumada, L. A. C.; González, M. X. R.; Sandoval, O. L. H.; Olmedo, J. J. S., Evaluation of Hyaluronic Acid Dilutions at Different Concentrations Using a Quartz Crystal Resonator (QCR) for the Potential Diagnosis of Arthritic Diseases. *Sensors (Basel)* **2016,** *16* (11), 1959.

368. Bailey, C. M.; Kamaloo, E.; Waterman, K. L.; Wang, K. F.; Nagarajan, R.; Camesano, T. A., Size dependence of gold nanoparticle interactions with a supported lipid bilayer: A QCM-D study. *Biophysical Chemistry* **2015,** *203-204*, 51-61.

369. Kamaloo, E.; Bailey, C.; Camesano, T. A., Effect of Concentration on the Interactions of Gold Nanoparticles with Model Cell Membranes: A

QCM-D Study. In *Nanotechnology to Aid Chemical and Biological Defense*, 2015; pp 67-76.

370. Assero, G.; Satriano, C.; Lupo, G.; Anfuso, C. D.; Marletta, G.; Alberghina, M., Pericyte adhesion and growth onto polyhydroxymethylsiloxane surfaces nanostructured by plasma treatment and ion irradiation. *Microvascular Research* **2004,** *68* (3), 209-220.

371. Voinova, M. V.; Rodahl, M.; Jonson, M.; Kasemo, B., Viscoelastic Acoustic Response of Layered Polymer Films at Fluid-Solid Interfaces: Continuum Mechanics Approach. *Physica Scripta* **1999,** *59* (5), 391-396.

372. Tonda-Turo, C.; Carmagnola, I.; Ciardelli, G., Quartz Crystal Microbalance With Dissipation Monitoring: A Powerful Method to Predict the in vivo Behavior of Bioengineered Surfaces. *Frontiers in bioengineering and biotechnology* **2018,** *6*, 158-158.

373. Cucci, L. M.; Munzone, A.; Naletova, I.; Magrì, A.; La Mendola, D.; Satriano, C., Gold nanoparticles functionalized with angiogenin-mimicking peptides modulate cell membrane interactions. *Biointerphases* **2018,** *13* (3).

374. Satriano, C.; Munzone, A.; Cucci, L. M.; Giacomelli, C.; Trincavelli, M. L.; Martini, C.; Rizzarelli, E.; La Mendola, D., Angiogenin-mimetic peptide functionalised gold nanoparticles for cancer therapy applications. *Microchemical Journal* **2018,** *136*, 157-163.

375. Ma, X.; Hartmann, R.; Jimenez de Aberasturi, D.; Yang, F.; Soenen, S. J. H.; Manshian, B. B.; Franz, J.; Valdeperez, D.; Pelaz, B.; Feliu, N.; Hampp, N.; Riethmuller, C.; Vieker, H.; Frese, N.; Golzhauser, A.; Simonich, M.; Tanguay, R. L.; Liang, X. J.; Parak, W. J., Colloidal Gold Nanoparticles Induce Changes in Cellular and Subcellular Morphology. *ACS Nano* **2017,** *11* (8), 7807-7820.

376. Li, Y.; Wu, Y.; Ong, B. S., Facile Synthesis of Silver Nanoparticles Useful for Fabrication of High-Conductivity Elements for Printed Electronics. *Journal of the American Chemical Society* **2005,** *127* (10), 3266-3267.

377. Gao, B.; Osorio, E. A.; Babaei Gaven, K.; van der Zant, H. S. J., Three-terminal electric transport measurements on gold nano-particles combined withex situTEM inspection. *Nanotechnology* **2009,** *20* (41), 415207.

378. Tan, H.; Santbergen, R.; Smets, A. H. M.; Zeman, M., Plasmonic Light Trapping in Thin-film Silicon Solar Cells with Improved Self-Assembled Silver Nanoparticles. *Nano Letters* **2012,** *12* (8), 4070-4076.

379. Sönnichsen, C.; Reinhard, B. M.; Liphardt, J.; Alivisatos, A. P., A molecular ruler based on plasmon coupling of single gold and silver nanoparticles. *Nature Biotechnology* **2005,** *23* (6), 741-745.

380. Li, M.; Yang, D.-P.; Wang, X.; Lu, J.; Cui, D., Mixed protein-templated luminescent metal clusters (Au and Pt) for H2O2 sensing. *Nanoscale Research Letters* **2013,** *8* (1), 182.

381. Rosi, N. L.; Mirkin, C. A., Nanostructures in Biodiagnostics. *Chemical Reviews* **2005,** *105* (4), 1547-1562.

382. El-Sayed, I. H.; Huang, X.; El-Sayed, M. A., Selective laser photo-thermal therapy of epithelial carcinoma using anti-EGFR antibody conjugated gold nanoparticles. *Cancer Letters* **2006,** *239* (1), 129-135.

383. Arvizo, R. R.; Bhattacharyya, S.; Kudgus, R. A.; Giri, K.; Bhattacharya, R.; Mukherjee, P., Intrinsic therapeutic applications of noble metal nanoparticles: past, present and future. *Chemical Society Reviews* **2012,** *41* (7), 2943-2970.

384. Navarro, J. R. G.; Manchon, D.; Lerouge, F.; Cottancin, E.; Lermé, J.; Bonnet, C.; Chaput, F.; Mosset, A.; Pellarin, M.; Parola, S., Synthesis, electron tomography and single-particle optical response of twisted gold nano-bipyramids. *Nanotechnology* **2012,** *23* (14), 145707.

385. Petkova, G. A.; Záruba, K.; Žvátora, P.; Král, V., Gold and silver nanoparticles for biomolecule immobilization and enzymatic catalysis. *Nanoscale Research Letters* **2012,** *7* (1), 287.

386. Yasin, H. M.; Waqqar, A.; Awais, A.; Bhatti, A. S.; Rehman, N., Micro-plasma assisted synthesis of multifunctional D-fructose coated silver nanoparticles. *Materials Research Express* **2019**.

387. Wang, R.; Zuo, S.; Wu, D.; Zhang, J.; Zhu, W.; Becker, K.; Fang, J., Microplasma-Assisted Synthesis of Colloidal Gold Nanoparticles and Their Use in the Detection of Cardiac Troponin I (cTn-I). *Plasma Processes and Polymers* **2015,** *12*, 380.

388. Tian, X.; Azpurua, J.; Hine, C.; Vaidya, A.; Myakishev-Rempel, M.; Ablaeva, J.; Mao, Z.; Nevo, E.; Gorbunova, V.; Seluanov, A., High-molecular-mass hyaluronan mediates the cancer resistance of the naked mole rat. *Nature* **2013,** *499* (7458), 346-349.

389. Stern, R., Devising a pathway for hyaluronan catabolism: are we there yet? *Glycobiology* **2003,** *13* (12), 105R-115.

390. Inturri, R.; Stivala, A.; Furneri, P. M.; Blandino, G., Growth and adhesion to HT-29 cells inhibition of Gram-negatives by Bifidobacterium longum BB536 e Lactobacillus rhamnosus HN001 alone and in

combination. *European review for medical and pharmacological sciences* **2016,** *20* (23), 4943-4949.
391. Toscano, M.; De Grandi, R.; Stronati, L.; De Vecchi, E.; Drago, L., Effect of Lactobacillus rhamnosus HN001 and Bifidobacterium longum BB536 on the healthy gut microbiota composition at phyla and species level: A preliminary study. *World J Gastroenterol* **2017,** *23* (15), 2696-2704.
392. Inturri R, T. L., Li Volti G, Oliveri S, Blandino G, In vitro inhibitory activity of Bifidobacterium longum BB536 and Lactobacillus rhamnosus HN001 alone or in combination against bacterial and Candida spp. reference strains and clinical isolates. *Accepted by Heliyon* **2019**.
393. M27-A3, Reference method for broth dilution antifungal susceptibily testing of yeasts. *Clinical and Laboratory Standards Institute* **2008,** *28*.
394. Wu, S.; Applewhite, A. J.; Niezgoda, J.; Snyder, R.; Shah, J.; Cullen, B.; Schultz, G.; Harrison, J.; Hill, R.; Howell, M.; Speyrer, M.; Utra, H.; de Leon, J.; Lee, W.; Treadwell, T., Oxidized Regenerated Cellulose/Collagen Dressings: Review of Evidence and Recommendations. *Adv Skin Wound Care* **2017,** *30* (11S Suppl 1), S1-S18.
395. Di Pasquale, R.; Vaccaro, S.; Caputo, M.; Cuppari, C.; Caruso, S.; Catania, A.; Messina, L., Collagenase-assisted wound bed preparation: An in vitro comparison between
Vibrio alginolyticus
and
Clostridium histolyticum
collagenases on substrate specificity. *International Wound Journal* **2019**.
396. Vaccaro, S.; Caputo, M.; Cuppari, C.; Gennari, G. New Process For The Production And Purification Of The Collagenase Enzyme From Vibrio Alginolyticus. EP 2839000 B1, 2013/04/17, 2016.
397. Wuensch, E.; Heidrich, H. G., [ON THE QUANTITATIVE DETERMINATION OF COLLAGENASE]. *Hoppe-Seyler's Zeitschrift fur physiologische Chemie* **1963,** *333*, 149-51.
398. Zhang, X.; Yao, M.; Chen, M.; Li, L.; Dong, C.; Hou, Y.; Zhao, H.; Jia, B.; Wang, F., *Hyaluronic Acid-Coated Silver Nanoparticles As a Nanoplatform for in Vivo Imaging Applications*. 2016; Vol. 8.
399. Mandal, T. K.; Fleming, M. S.; Walt, D. R., Preparation of Polymer Coated Gold Nanoparticles by Surface-Confined Living Radical Polymerization at Ambient Temperature. *Nano Letters* **2002,** *2* (1), 3-7.

400. Ouellette, M.; Masse, F.; Lefebvre-Demers, M.; Maestracci, Q.; Grenier, P.; Millar, R.; Bertrand, N.; Prieto, M.; Boisselier, É., Insights into gold nanoparticles as a mucoadhesive system. *Scientific reports* **2018,** *8* (1), 14357.
401. Jacoboni, I.; Valdre, U.; Mori, G.; Quaglino, D., Jr.; Pasquali-Ronchetti, I., Hyaluronic acid by atomic force microscopy. *Journal of structural biology* **1999,** *126* (1), 52-8.
402. Almalik, A.; Donno, R.; Cadman, C. J.; Cellesi, F.; Day, P. J.; Tirelli, N., Hyaluronic acid-coated chitosan nanoparticles: Molecular weight-dependent effects on morphology and hyaluronic acid presentation. *Journal of Controlled Release* **2013,** *172* (3), 1142-1150.
403. Potara, M.; Baia, M.; Farcau, C.; Astilean, S., Chitosan-coated anisotropic silver nanoparticles as a SAB - Surface-enhanced Raman spectroscopy (SERS) is a technique that has become widely used for identifying and providing structural information about molecular species in low concentration. There is an ongoing interest in finding optimum particle size, shape and spatial distribution for optimizing the SERS substrates and pushing the sensitivity toward the single-molecule detection limit. This work reports the design of a novel, biocompatible SERS substrate based on small clusters of anisotropic silver nanoparticles embedded in a film of chitosan biopolymer. The SERS efficiency of the biocompatible film is assessed by employing Raman imaging and spectroscopy of adenine, a significant biological molecule. By combining atomic force microscopy with SERS imaging we find that the chitosan matrix enables the formation of small clusters of silver nanoparticles, with junctions and gaps that greatly enhance the Raman intensities of the adsorbed molecules. The study demonstrates that chitosan-coated anisotropic silver nanoparticle clusters are sensitive enough to be implemented as effective plasmonic substrates for SERS detection of nonresonant analytes at the single-molecule level. ERS substrate for single-molecule detection. *Nanotechnology* **2012,** *23* (5), 055501.
404. Cowman, M. K.; Li, M.; Balazs, E. A., Tapping Mode Atomic Force Microscopy of Hyaluronan: Extended and Intramolecularly Interacting Chains. *Biophysical Journal* **1998,** *75* (4), 2030-2037.
405. Cong Wang, X. G., Zhongqin Chen, Yue Chen and Haixia Chen, Preparation, Characterization and Application of Polysaccharide-Based Metallic Nanoparticles: A Review. *Polymers* **2017,** *9* (12).

406. Shanan, Z.; Murbat, H.; j. Alzaidy, A., Synthesis gold nanoparticles using microplasma discharge and study their structural properties. *Advances in Natural and Applied Sciences* **2017,** *11*, 613-622.

407. Thong, Y. L.; Chin, O. H.; Ong, B. H.; Huang, N. M., Synthesis of silver nanoparticles prepared in aqueous solutions using helium dc microplasma jet. *Japanese Journal of Applied Physics* **2015,** *55* (1S), 01AE19.

408. Bae, E.; Park, H.-J.; Park, J.; Yoon, J.; Kim, Y.; Choi, K.; Yi, J., Effect of Chemical Stabilizers in Silver Nanoparticle Suspensions on Nanotoxicity. *Bulletin of the Korean Chemical Society* **2011,** *32*.

409. Zaman, M.; Ahmad, E.; Qadeer, A.; Rabbani, G.; Khan, R. H., Nanoparticles in relation to peptide and protein aggregation. *International journal of nanomedicine* **2014,** *9*, 899-912.

410. Thanh, N. T. K.; Rosenzweig, Z., Development of an Aggregation-Based Immunoassay for Anti-Protein A Using Gold Nanoparticles. *Analytical Chemistry* **2002,** *74* (7), 1624-1628.

411. Dzimitrowicz, A.; Bielawska-Pohl, A.; diCenzo, G. C.; Jamroz, P.; Macioszczyk, J.; Klimczak, A.; Pohl, P., Pulse-Modulated Radio-Frequency Alternating-Current-Driven Atmospheric-Pressure Glow Discharge for Continuous-Flow Synthesis of Silver Nanoparticles and Evaluation of Their Cytotoxicity toward Human Melanoma Cells. *Nanomaterials (Basel)* **2018,** *8* (6), 398.

412. Arora, S.; Jain, J.; Rajwade, J. M.; Paknikar, K. M., Interactions of silver nanoparticles with primary mouse fibroblasts and liver cells. *Toxicology and Applied Pharmacology* **2009,** *236* (3), 310-318.

413. Guo, H.; Zhang, J.; Boudreau, M.; Meng, J.; Yin, J.-J.; Liu, J.; Xu, H., Intravenous administration of silver nanoparticles causes organ toxicity through intracellular ROS-related loss of inter-endothelial junction. *Particle and fibre toxicology* **2016,** *13*, 21.

414. Shahmirani, Z.; Irani, S.; Atyabi, S. M.; Mirpour, S.; Shadpour, S.; Ghorannevis, m.; joupari, m. D., Effect of Cold Atmospheric Pressure Plasma and Gold Nanoparticles on Cell Viability. *Annual research and review in biology* **2014**.

415. Fede, C.; Albertin, G.; Petrelli, L.; De Caro, R.; Fortunati, I.; Weber, V.; Ferrante, C., Influence of shear stress and size on viability of endothelial cells exposed to gold nanoparticles. *Journal of Nanoparticle Research* **2017,** *19* (9), 316.

416. Wiegand, I.; Hilpert, K.; Hancock, R. E., Agar and broth dilution methods to determine the minimal inhibitory concentration (MIC) of antimicrobial substances. *Nature protocols* **2008,** *3* (2), 163-75.

417. Vijayakumar, V.; Samal, S. K.; Mohanty, S.; Nayak, S. K., Recent advancements in biopolymer and metal nanoparticle-based materials in diabetic wound healing management. *International Journal of Biological Macromolecules* **2019,** *122*, 137-148.

418. Panacek, A.; Kvitek, L.; Smékalová, M.; Večeřová, R.; Kolář, M.; Röderová, M.; Dyčka, F.; Šebela, M.; Prucek, R.; Tomanec, O.; Zboril, R., Bacterial resistance to silver nanoparticles and how to overcome it. *Nature Nanotechnology* **2018,** *13*.

419. Ardizzoni, A.; Neglia, R.; Baschieri, M.; Cermelli, C.; Caratozzolo, M.; Righi, E.; Palmieri, B.; Blasi, E., Influence of hyaluronic acid on bacterial and fungal species, including clinically relevant opportunistic pathogens. *Journal of materials science. Materials in medicine* **2011,** *22*, 2329-38.

420. Di Cerbo, A.; Aponte, M.; Esposito, R.; Bondi, M.; Palmieri, B., Comparison of the effects of hyaluronidase and hyaluronic acid on probiotics growth. *BMC Microbiology* **2013,** *13* (1), 243.

421. Susanna Vaccaro, M. C., Christian Cuppari, Giovanni Gennari New process for the production and purification of the collagenase enzyme from vibrio alginolyticus CA2870493A1, 2017.

422. Das, A.; Datta, S.; Roche, E.; Chaffee, S.; Jose, E.; Shi, L.; Grover, K.; Khanna, S.; Sen, C. K.; Roy, S., Novel mechanisms of Collagenase Santyl Ointment (CSO) in wound macrophage polarization and resolution of wound inflammation. *Scientific reports* **2018,** *8* (1), 1696.

423. Demidova-Rice, T. N.; Hamblin, M. R.; Herman, I. M., Acute and impaired wound healing: pathophysiology and current methods for drug delivery, part 1: normal and chronic wounds: biology, causes, and approaches to care. *Adv Skin Wound Care* **2012,** *25* (7), 304-14.

La borsa di dottorato è stata cofinanziata con risorse del
Programma Operativo Nazionale Ricerca e Innovazione 2014-2020 (CCI 2014IT16M2OP005),
Fondo Sociale Europeo, Azione I.1 "Dottorati Innovativi con caratterizzazione Industriale"

UNIONE EUROPEA
Fondo Sociale Europeo

Ministero dell'Istruzione,
dell'Università e della Ricerca

PON
RICERCA
E INNOVAZIONE